High-voltage partial-core resonant transformers

Simon Colin Bell

A thesis presented for the degree of
Doctor of Philosophy
in
Electrical and Computer Engineering
at the
University of Canterbury,
Christchurch, New Zealand.

October 2008

ABSTRACT

This thesis first describes the reverse method of transformer design. An existing magnetic model for full-core shell-type transformers, based on circuit theory, is summarised. A magneto-static finite element model is introduced and two sample transformers are analysed. The magnetic model based on finite element analysis is shown to be more accurate than the model based on circuit theory.

Partial-core resonant transformers are then introduced and their characteristics are explained using an equivalent circuit model. A method of measuring the winding inductances under resonant operation is developed and used to investigate the characteristics of two different tuning methods. A finite element model of the partial-core resonant transformer is developed by adopting the model for full-core shell-type transformers. The model results accurately match the measured inductance variation characteristics of three sample transformers and predict the onset of core saturation in both axial-offset and centre-gap arrangements.

A new design of partial-core resonant transformer is arrived at, having an alternative core and winding layout, as well as multiple winding taps. The finite element model is extended to accommodate the new design and a framework of analysis tools is developed. A general design methodology for partial-core resonant transformers with fixed inductance is developed. A multiple design method is applied to obtain an optimal design for a given set of specifications and restrictions. The design methodology is then extended to devices with variable inductance.

Three design examples of partial-core resonant transformers with variable inductance are presented. In the first two design examples, existing devices are replaced. The new transformer designs are significantly lighter and the saturation effects are removed. The third design example is a kitset for high-voltage testing, with the capability to test any hydro-generator stator in New Zealand. The kitset is built and tested in the laboratory, demonstrating design capability. Other significant test results, for which no models have yet been developed, are also presented. Heating effects in the core are reduced by adopting an alternative core construction method, where the laminations are stacked radially, rather than in the usual parallel direction. The new kitset is yet to be used in the field.

LIST OF PUBLICATIONS

The following papers have either been published, accepted or submitted during the course of the research described in this thesis:

JOURNAL PAPERS

1. Bell, S.C., and Bodger, P.S., 'Equivalent circuit for high-voltage partial-core resonant transformers', *IET Electr. Power Appl.*, vol. 2, no. 3, pp. 155-163, May 2008.
2. Bell, S.C., and Bodger, P.S., 'Inductive reactance component model for high-voltage partial-core resonant transformers' *IET Electr. Power Appl.*, vol. 2, no. 5, pp. 288-297, September 2008.
3. Bell, S.C., and Bodger, P.S., 'Power transformer design using magnetic circuit theory and finite element analysis', submitted to IJEEE on 15/8/07.
4. Bell, S.C., and Bodger, P.S., 'New design of high-voltage partial-core resonant transformer', submitted to Electric Power Systems Research, 30/07/08.

CONFERENCE PAPERS

1. Bodger, P.S., and Bell, S.C., 'Power transformer analytical design approaches', paper presented at the *Power Transformer Convention & Workshop*, Christchurch, New Zealand, 2-3 July 2007.
2. Bendre, V.D., Bell, S.C., Enright, W.G., and Bodger, P.S., 'AC high potential testing of large hydro-generator stators using open core transformers', paper presented at the 15^{th} *International Symposium on High Voltage Engineering*, Ljubljana, Slovenia, 27-31 August 2007, paper T3-303.
3. Lynch, K., Bodger, P.S., Enright, W.G., and Bell, S.C., 'Partial core transformer for energisation of high voltage arc-signs', paper presented at the 15^{th} *International Symposium on High Voltage Engineering*, Ljubljana, Slovenia, 27-31 August 2007, paper T3-304.

4. Bell, S.C., and Bodger, P.S., 'Power transformer design using magnetic circuit theory and finite element analysis - a comparison of techniques', paper presented at *Australasian Universities Power Engineering Conference (AUPEC)*, Perth, Western Australia, 9-12 December 2007, pp. 607-612.

5. Bodger, P.S., Enright, W.G., Bell, S.C. and Bendre, V.D, 'Partial core transformers for HV testing and power supplies', Invited paper presented at *Techcon Asia Pacific*, Sydney, Australia, 31 March-2 April, 2008, pp. 67-79.

6. Enright, W.G., Bendre, V.D., Bell, S.C. and Bodger, P.S., 'Field experiences using a prototype open core resonating transformer for A.C. high potential testing of hydro-generator stators', Invited paper presented at *Techcon Asia Pacific*, Sydney, Australia, 31 March-2 April, 2008, pp. 265-277.

Additionally, a 30-minute oral presentation titled 'High-voltage testing of hydro-generator stators using partial-core transformers' was presented at the *Seminar for the next generation of researchers in power systems*, University of Manchester, United Kingdom, 16-19 September 2007.

ACKNOWLEDGEMENTS

The final reading of this thesis has prompted me to review my initial goals and ambitions as a post-graduate student. My original thesis topic was superconducting transformers, which, for reasons beyond my control, I never quite managed to study. My original time-line of 3 years was exceeded by more than 7 months. My anticipated savings over the study period were not quite achieved. Nevertheless, I am very happy with the outcomes of this thesis. The years spent as a post-graduate student have been some of the best of my life so far (but I hope for even better times in the years to come).

None of this would have been possible without the technical and social support of the other students and staff. I would like to give particular thanks to my supervisor Pat Bodger and co-supervisor Wade Enright. Thanks also to the technicians, especially Jac Woudberg and David Healy for building the transformers, and Ken Smart for general advise and constant loaning of equipment. The postgraduate students in the department have also made my life more interesting. Some of the best conversations I had were at the small hours of the morning. I recall, on more than one occasion, having the cleaning ladies tell me to go home when they arrived at 6am.

Special thanks to my friends in the industry who kept telling me to get a real job, and my family, who always managed to appear interested when listening to me talk about my research. Thanks to Geoff Cardwell for informing us about the conference in Slovenia, which I subsequently attended, and for arranging the site visit to an ABB transformer factory in Germany. Thanks also to Mirko, Anna and Rayk for showing me around Germany during my holiday in Europe. I would also like to acknowledge phdcomics.com and dc++ for the much needed distractions from research.

Finally, I would like to acknowledge the financial support I received through Scholarships from the University of Canterbury and the Electric Power Engineering Centre.

CONTENTS

LIST OF FIGURES

LIST OF TABLES

GLOSSARY

The general notation, frequently used terms and abbreviations of this thesis are presented here. Terms used less frequently are defined in the immediate context.

GENERAL NOTATION

V_Q, v_Q	Voltage of Q
I_Q, i_Q	Current of Q
P_Q	Real power of Q
R_Q, L_Q, C_Q	Resistance, inductance, capacitance of Q
X_Q, Z_Q	Reactance, impedance of Q
$\mathrm{Re}(Q)$	Real part of Q
$\mathrm{Im}(Q)$	Imaginary part of Q
$\lvert Q \rvert$	Magnitude of Q
$\angle Q$	Angle of Q
γ_Q	Density of Q
ν_Q	Volume of Q
MC_Q	Material cost of Q
C_Q	Cost of Q
W_Q	Weight of Q
μ_Q	Relative permeability of Q
ρ_Q	Resistivity of Q
T_Q	Temperature of Q
$\Delta\rho_Q$	Thermal resistivity coefficient of Q

FREQUENTLY USED TERMS

Transformers in general

a	Transformer turns ratio

β	Transformer aspect ratio
f	Frequency
k	Coil coupling
l_{eff}	Effective path length for mutual flux
t	Time
τ_{12}	Winding thickness factor
μ_0	Permeability of free space $= 4\pi \times 10^{-7}$ H/m
ω	Angular frequency

Transformer core

A_c	Effective cross-sectional area for magnetic flux
B_{pk}	Peak value of flux-density
δ_c	Skin depth of the core
k_h	Hysteresis loss constant 1
l_c	Core length
LT_c	Lamination thickness
n	Number of laminations
r_c	Core radius
SF_c	Core stacking factor
w_{c1}	Core width 1
w_{c2}	Core width 2
x	Hysteresis loss constant 2

Windings

In the following, i is the winding number, starting from the innermost winding.

A_i	Effective current carrying cross-sectional area
d_i	Winding thickness
J_i	Current-density
l_i	Winding length
l_{w_i}	Wire length
L_{y_i}	Number of layers
N_i	Number of turns

Insulation

COL	Circumferential overlap of inter-layer insulation
Δd	Inter-winding insulation thickness
EOL	End overlap of inter-layer insulation
ft	Former thickness
$OEOL$	Outside end overlap of inter-layer insulation

Finite element model

a_r	Radial length of air-space
a_z	One half of axial length of air-space
f_m	Finite element model upper-frequency
L_{ij}	Inductance between windings i and j
$\mathbf{L}$	Inductance matrix
λ_i	Flux linkage of winding i
P_{ij}	Magnetic permeance between windings i and j
$\mathbf{P}$	Permeance matrix

Resonant circuits

Q	Quality factor
$\omega_{0,m}$	Resonant frequency (maximum impedance definition)
$\omega_{0,u}$	Resonant frequency (unity power factor definition)

ABBREVIATIONS

ac	Alternating current
dc	Direct current
GIS	Gas-insulated switchgear
THD	Total harmonic distortion
HTSPCTX	High temperature superconducting partial-core transformer
hv	High-voltage
lv	Low-voltage
MDPE	Medium density polyethylene
PCRTX	Partial-core resonant transformer
VLF	Very low frequency

Chapter 1

INTRODUCTION

1.1 GENERAL OVERVIEW

High-voltage testing is often performed during commissioning or periodic maintenance of high-voltage equipment such as generators, transformers and underground cables. It is used to test the integrity of the insulation system. If the equipment passes the high-voltage test, it is considered ready to be put into service. If it fails, the damaged insulation can be located and repaired. The damage to the insulation which results from a failed high-voltage test is substantially less than would occur if the equipment had been directly put into service. Testing can be performed at dc, ac very low frequency, ac variable frequency or ac mains frequency. The later is the most representative of in-service conditions, but the equipment is more expensive and heavier than that required for the other test frequencies.

For generator stator testing, a mains frequency test is often a mandatory requirement. However, the volt-amperes required to energise the stator capacitance can be significant, particularly for large hydro-generators, where the volt-ampere requirements can often exceed the capacity of the local supply. Resonant circuits are normally used to reduce supply volt-amperes. Conventional resonant test equipment contains a full-core reactor and a separate exciter transformer. The shipping weight can reach multiple tonnes, making transportation to remote sites difficult and costly.

An alternative design to a full-core transformer is a partial-core transformer. This differs from the conventional design in that the outer limbs and connecting yokes are missing. Partial-core transformers have been used for high-voltage testing of hydro-generator stators [Bodger and Enright, 2004, Enright and Bodger, 2004]. In this application they are referred to as partial-core resonant transformers (PCRTXs). The PCRTX combines the full-core reactor and exciter transformer of conventional test equipment, at a significantly reduced weight and cost.

Since field testing of PCRTXs has already been performed at several power stations in New Zealand, the next technical step towards commercialisation is product refinement.

The emphasis is on accurate design to specification and minimisation of shipping weight.

1.2 THESIS OBJECTIVES

The main thesis objective was to develop a general design methodology for PCRTXs with variable inductance. To demonstrate design capability, a PCRTX kitset for high-voltage testing, with the capability to test any hydro-generator stator in New Zealand, was designed, built and tested.

In order to achieve the main thesis objective, modelling and analysis techniques were first developed and a flexible transformer design and analysis software package was written. The software could also be used to design other PCRTXs for use in other insulation testing applications, such as XLPE cable and switch-gear testing. With modifications, it could also be applied to design partial-core power transformers, having either copper, aluminum or superconducting windings.

1.3 THESIS OUTLINE

Chapter 2 gives a summary of the test procedure and potential issues when performing a high-voltage test on a hydro-generator stator. Conventional methods and test equipment are described. Partial-core inductors are introduced and their use in high-voltage testing applications is reviewed. PCRTXs are then introduced, as a logical extension of the partial-core inductor. Photographs of field tests are shown. Models for partial-core devices are reviewed.

Chapter 3 introduces the reverse method of transformer design and summarises an existing magnetic model for full-core shell-type transformers, based on circuit theory. A magneto-static finite element model is then introduced. Two sample transformers are analysed. The performance of the two magnetic models is compared to the measured performance of the as-built transformers. By first studying full-core transformers, the characteristics of partial-core transformers can be compared to those of conventional design.

Chapter 4 introduces PCRTXs and explains their characteristics using an equivalent circuit model. A method of measuring the winding inductances under resonant operation is developed and used to investigate the tuning characteristics of two different tuning methods.

Chapter 5 details a finite element model of the PCRTX, obtained by adopting the model of Chapter 3. The model is used to calculate the transformer reactances and predict the measured tuning characteristics of Chapter 4. It is also used to predict the onset of core saturation.

Chapter 6 introduces a new design of PCRTX, having an alternative core and winding layout, as well as multiple taps. The finite element model of Chapter 5 is extended for the new design. A framework of analysis tools are developed.

Chapter 7 develops a general design methodology for PCRTXs with fixed inductance. A multiple design method is applied to obtain an optimal design for a given set of specifications and restrictions.

Chapter 8 extends on Chapter 7 by developing a general design methodology for PCRTXs with variable inductance. Three design examples are presented. The first two design examples are replacement transformers for two of the sample devices in Chapter 5. The device weights are significantly reduced and saturation effects are removed. In the third design example, a kitset for high-voltage testing, with the capability to test any hydro-generator stator in New Zealand, is developed.

Chapter 9 verifies the finite element model of Chapter 5, analysis tools of Chapter 6 and the design methods of Chapters 7 & 8 by building the third design example of Chapter 8 and performing tests in the laboratory. Other significant test results, for which no models have yet been developed, are also presented. Heating effects in the core are reduced by adopting an alternative core construction method.

Chapter 10 discusses possible directions for future research and development.

Chapter 11 presents the main conclusions of this thesis.

Chapter 2

BACKGROUND

2.1 INTRODUCTION

The New Zealand electric power system is critically dependent on a majority of hydro-generators that are in excess of 25 years old. In recent times, a continuing process of stator and rotor rewind projects has been in progress. Given the significant effort and outages required for these rewind projects, most asset owners select a rewind and MVA upgrade option [Enright et al., 2008]. Improvements to insulation technology mean that the copper cross-sectional area of the stator bars can be increased without changing the slot size. Since the insulation thickness is reduced, the stator bars are more prone to insulation failure if any damage occurs during installation . High-voltage testing of the stator insulation is typically a contractual requirement of such generator rewind and upgrade projects. Insulation resistance and polarization index tests are normally performed as well. Voltage surge tests, power factor and tip-up tests and partial discharge tests (performed either on-line or off-line) can also be used to assess the health of stator insulation [Warren and Stone, 1998], but are not always performed during commissioning.

Typically one phase of the stator winding is tested at a time and the remaining two phases, along with any resistance temperature detector (RTD) and embedded temperature detector (ETD) wiring, are earthed using fuse wire. The test voltage is manually increased using a variac at a rate of 1 kV per second to 2 times the rated phase-to-phase voltage + 1 kV [IEC60034-1, 2004]. The test voltage is maintained for 60 seconds and then decreased at 1 kV per second back to zero. The supply is isolated and an earth is applied to the phase under test. The test procedure is further detailed in [Bendre et al., 2007]. At first glance, it would appear relatively simple to perform the high-voltage test, and one might be tempted to assume that the test circuit of Figure 2.1 would be adequate.

One problem that can occur with this simple test circuit is that a large stator capacitance C will cause the input impedance of the exciter transformer Z_p to become too low. The volt-ampere rating of the supply could be exceeded. This is illustrated in Table 2.1, which

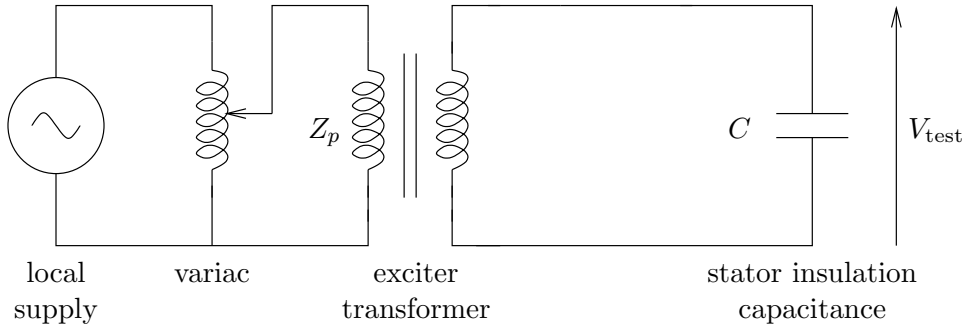

Figure 2.1 Simple test circuit to energise stator insulation capacitance C to voltage V_{test}.

Generator rating	Test voltage, kV	Insulation capacitance, uF	Reactive power, kVAr	Charging current at 230 V[a]
2.35 MVA, 6.6 kV	14.2	0.084	5.32	23
8.82 MVA, 6.6 kV	14.2	0.217	13.7	60
55.55 MVA, 11 kV	13.8	0.234	14	61
88.9 MVA, 11 kV	23	0.422	70.1	305
120 MVA, 15.4 kV	20	0.75	94.2	410
40 MVA, 11 kV	23	0.57	94.7	412
135 MVA, 13.8 kV	32	1.05	338	1470

[a]Calculated assuming zero circuit losses and ideal voltage ratio on exciter transformer.

Table 2.1 Overview of recent hydro-generators tested in New Zealand. (taken from [Enright et al., 2008])

gives an overview of the hydro-generators tested in New Zealand by the University of Canterbury, their test voltages, insulation capacitances, reactive power and the charging current which would be drawn from a 230 V supply using the circuit of Figure 2.1.

The distribution board at a power station is typically rated for at least 200 - 300 A. By obtaining a single-phase supply between any two phases of the three-phase supply, rather than the usual arrangement of between any single phase and neutral, the volt-ampere rating can be increased by $\sqrt{3}$. However, this would still not be enough to test many of the hydro-generators listed in Table 2.1. Larger supply currents also require a larger variac, which is expensive and heavy. To make on-site testing practical, a method of reducing the volt-amperes at the distribution board is required.

2.2 CONVENTIONAL METHODS OF REDUCING SUPPLY kVAr

The loading on the distribution board can be reduced by either reducing the reactive power requirements of the test object, or by inductive reactive power compensation. In the first method, the test frequency is reduced. In the second, resonant circuits are

employed.

2.2.1 Reduced test frequency

Tests were historically performed at dc. Provided that the test object is energised slowly, the current drawn from the supply can be minimised. Once the test voltage has been reached, current is only drawn through the resistive component of the insulation under test. Consequently, the test equipment is cheap and portable. However, experimental data shows that an ac test is more effective in detecting defects or deficiencies than a dc test [Gupta, 1995]. There is also the common criticism that the dc test subjects the insulation to a different electric stress than the ac test [Gillespie et al., 1989]. This is because under dc conditions, the electric field is determined by the insulation resistances, whereas under ac conditions, the electric field is determined by the insulation capacitances [Warren and Stone, 1998]. The minimum dc breakdown voltage for windings under test is typically much higher than the crest voltage of the minimum ac breakdown voltage for similar windings [Gupta, 1995]. Consequently, the dc test voltage is typically set to 1.7 times the ac test voltage.

Very low frequency (VLF) testing is becoming more common. By applying an ac frequency of 0.1 - 0.01 Hz the charging current and thus size of the test equipment can be greatly reduced. However, VLF testing also suffers from the same criticism already noted for the dc test. There is also debate as to what the VLF test voltage should be in relation to the ac test voltage [Bomben et al., 2003].

2.2.2 Resonant circuits

Mains frequency ac testing stresses the components of generator insulation in a manner similar to normal service, except at higher voltages and in a non-induced or non-graded manner. A resonant circuit is formed between the stator insulation capacitance and a tunable inductor. The conventional series and parallel resonant circuits used for high-voltage testing are shown in Figure 2.2. Almost all commercial equipment is based around one of these two circuits. The inductance L is tuned to the stator insulation capacitance C such that the resonant frequency ω_0 $(= 1/\sqrt{LC})$ corresponds to the supply frequency (50 Hz or 60 Hz). Load losses, caused mainly by corona, and inductor and exciter transformer losses limit the circuit quality factor Q to 20-50. Both the series and parallel configurations significantly increase the input impedance of the exciter transformer Z_p.

For the series configuration, the voltage gain of the secondary circuit at ω_0 is equal to Q. This means that the step-up ratio of the exciter transformer is much lower than the required voltage ratio. The series configuration acts as a low-pass filter, producing a clean test voltage even in the presence of supply voltage harmonic distortion [Kuffel

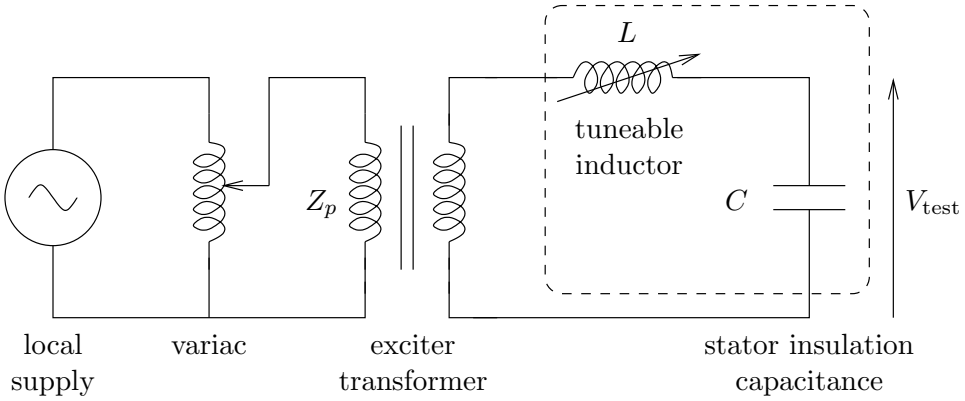

(a) Series resonance between tunable inductor L and stator insulation capacitance C

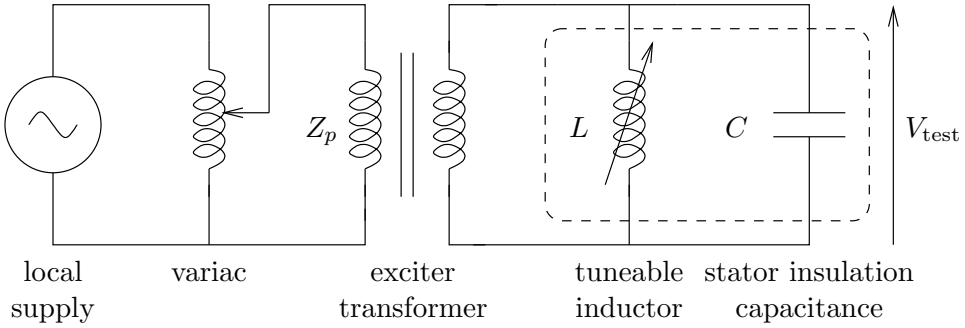

(b) Parallel resonance between tunable inductor L and stator insulation capacitance C

Figure 2.2 Conventional resonant circuits used for high-voltage testing of hydro-generator stators.

et al., 2000]. The short-circuit current of the secondary circuit is much lower than the nominal current, thus minimising any damage to the stator insulation in the event of a flashover.

Stator insulation capacitance is not perfectly linear with voltage [Emery, 2004]. Corona losses are highly non-linear. This can make manual testing difficult, as linear movement of the variac may not result in a linear increase in test voltage. For this reason, the parallel configuration is often used, where the voltage gain is insensitive to minor variations of the load impedance. However, any supply voltage harmonic distortion is directly passed through to the secondary circuit. An output filter may be required to make partial-discharge (PD) measurements. The short-circuit current in the secondary circuit is comparable to the nominal current, and is much higher than in the series configuration.

Since the series and parallel configurations both have their own advantages and disadvantages, some manufacturers provide a tap on the high-voltage inductor. This allows it to be configured for either series or parallel resonance.

2.2.3 Commercial test equipment

Figure 2.3 shows the commercial test equipment that was used to test several of the hydro-generators at the Manapouri power station in New Zealand. The equipment is based on the series resonance principal of Figure 2.2(a). It was designed for PD measurements as well as high-voltage testing. To facilitate this, a double shielded isolation transformer is connected in front of the variac and a filter is connected between the tunable inductor and the test object. Measurement instrumentation is connected to an easy-to-use control panel.

(a) Main view (b) Comparison view

Figure 2.3 Commercial equipment used for high-voltage testing at the Manapouri power station. (obtained from Alstom Power, with permission)

The exciter transformer and tunable inductor are constructed with a full-core magnetic circuit. The inductor is tuned via air-gap adjustment. The cross-section of a typical tunable inductor is shown in Figure 2.4.

By placing the air-gaps inside the high-voltage windings, the stray flux and hence associated core and winding losses are reduced. The two high-voltage windings are connected together in series to obtain the test voltage. The inductor is housed in a metallic tank, which is filled with oil. The air-gap is adjusted via a stepper motor, which is used to rotate the vertical support shafts and hence move the top-half of the core up and down. Tuning ranges of up to 20:1 can be achieved, while still maintaining inductance linearity.

The only downside of the commercial test equipment of Figure 2.3 is the finished weight, approximately 6 tonnes. A more portable solution is desirable when commissioning generators at remote power stations. In many cases, PD testing capability is not required. A more basic system, having just high-voltage testing capability, would be adequate. Since the two heaviest items of the commercial test equipment are the variable inductor and exciter transformer, these components should be the first focus when attempting to

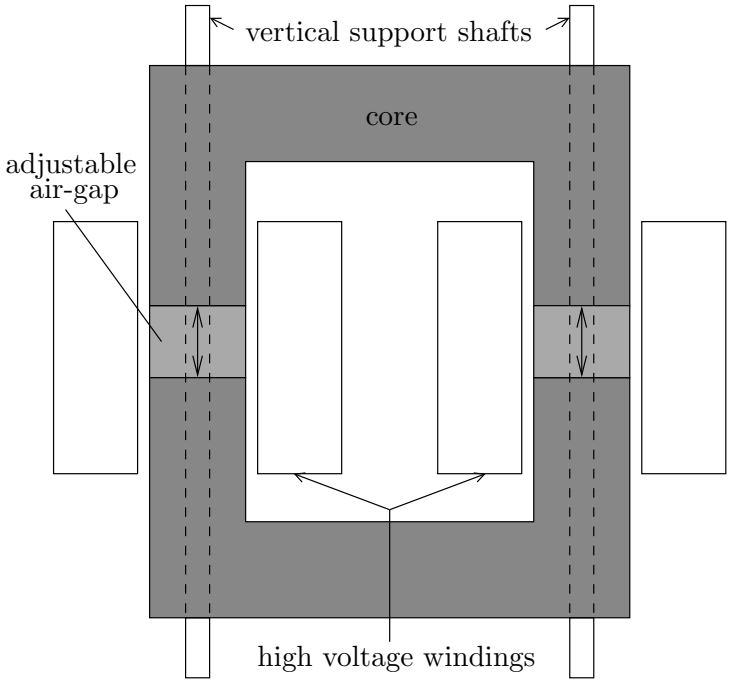

Figure 2.4 Typical winding layout and tuning method of full-core tunable inductors.

reduce the overall weight. Options to achieve this are discussed in the following two sections.

2.3 PARTIAL-CORE INDUCTORS

Partial- or open-core inductors have a higher power-to-weight ratio than full-core inductors with air-gaps [Bernasconi et al., 1979]. The partial-core inductor was first used in a high-voltage testing application in the late 1970s. Several 200 kV, 6 A partial-core inductors of fixed inductance were built and connected together in series / parallel configurations. They were used to form series resonant circuits for testing long underground cables and gas-insulated switchgear (GIS). The circuits were tuned using variable frequency ac, from 30 - 300 Hz. Test voltages of up to 750 kV were achieved. A photograph of an earlier test setup is shown in Figure 2.5.

Further refinements to the basic partial-core design in the 1980s led to frequency-tuned test equipment with partial-core inductors of fixed inductance having specific weight to power ratios of 0.4 - 1.2 kg/kVAr [Gerlach, 1991]. This is a significant reduction over conventional mains frequency ac test equipment, which typically achieve a weight to power ratio of 5 - 10 kg/kVAr. Insulation capacitances having a 50 Hz equivalent reactive power requirement of up to 20 MVAr have been energised using partial-core inductors.

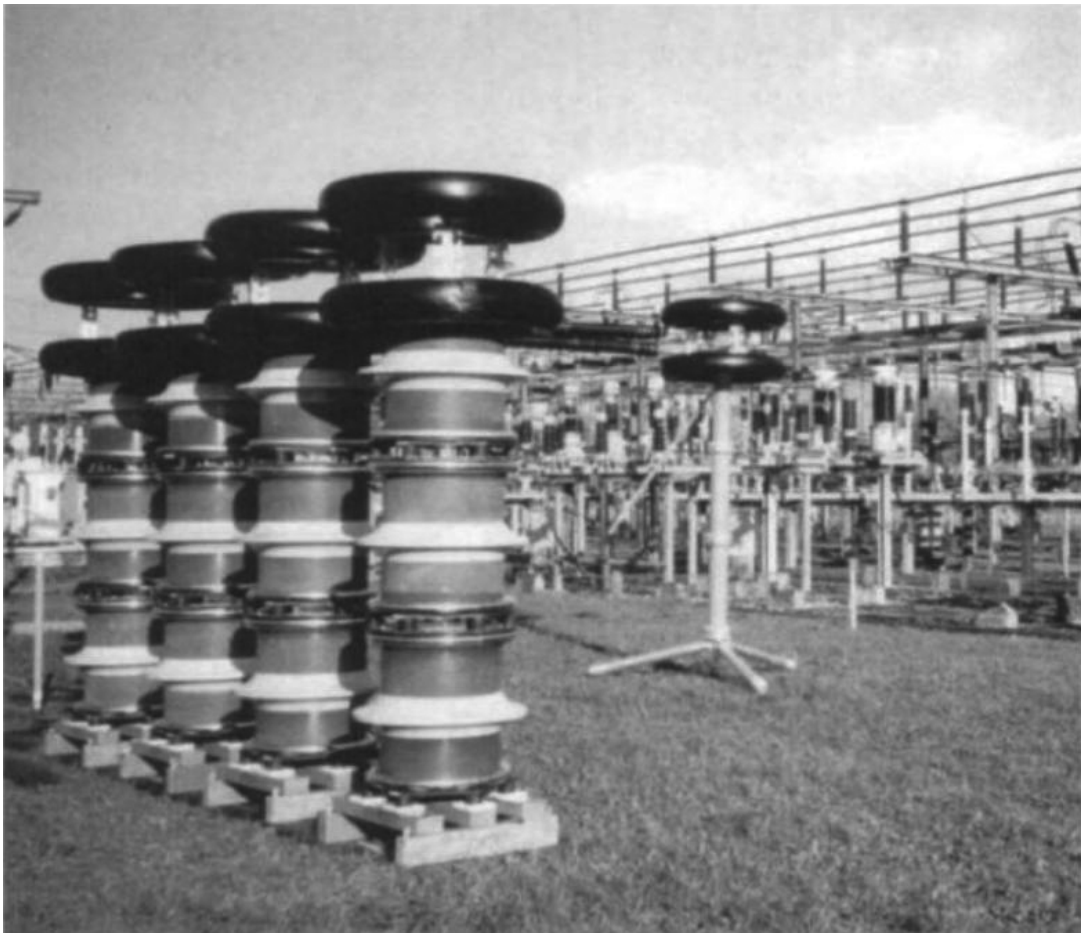

Figure 2.5 Modular partial-core inductors in a series resonant circuit with variable frequency during an on-site test of very long polymeric cables. (taken from [Kuffel et al., 2000])

The partial-core inductor was first used in the application of hydro-generator stator testing in 2002 [Bodger and Enright, 2004]. A tunable partial-core inductor was put in parallel with the stator capacitance. The test voltage was 23 kV and the inductor drew 4.9 A. The specific weight to power ratio of the 120 kg inductor was thus 1.1 kg/kVAr. The test equipment weight can be further reduced, as described in the next section.

2.4 PARTIAL-CORE RESONANT TRANSFORMERS

2.4.1 Theory of operation

A circuit well-known in the field of radio engineering is the inductively coupled circuit with tuned secondary [Terman, 1947]. By making use of this circuit, the exciter transformer and tunable inductor of the conventional resonant circuit can be combined into a single device. When this device is constructed with a partial-core, it is termed a partial-core resonant transformer (PCRTX). Parallel resonance occurs between the

PCRTX secondary winding inductance L and the stator insulation capacitance C. The PCRTX replaces the two heaviest items of conventional test equipment, at a significantly reduced weight and cost. The circuit is shown in Figure 2.6.

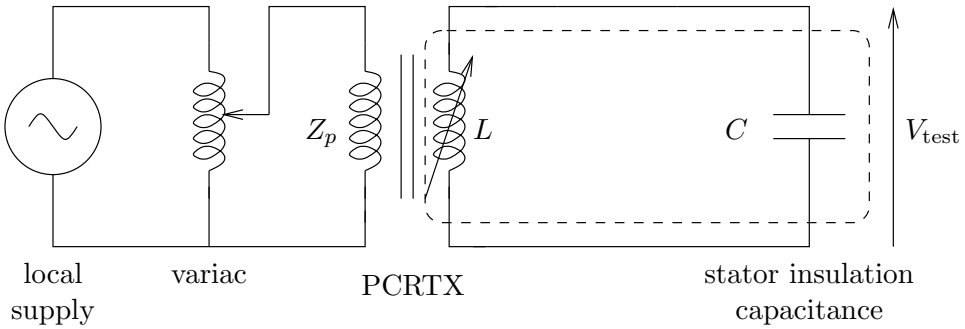

Figure 2.6 The partial-core resonant transformer (PCRTX) in an insulation testing application.

The winding coupling of a PCRTX is lower than an equivalent full-core transformer. Typical winding coupling values are $k = 0.90$ - 0.99. A high input impedance Z_p is still achieved. Adjustment of L through displacement of the partial-core also changes the self-inductance of the primary winding and the mutual inductance between windings. The voltage ratio is therefore a function of the core displacement. The variation of voltage ratio with core displacement over the device operating range is generally small and can be accounted for with the variac.

2.4.2 Field experiences

Several of the hydro-generators listed in Table 2.1 were tested using PCRTXs. Photographs of the test setups for two such examples are shown in Figure 2.7. In these cases, a separate full-core exciter transformer was still required to set the spark-gap. The PCRTXs used for the testing could not be tuned such that operation at rated voltage under open-circuit conditions was possible.

2.5 MODELS FOR PARTIAL-CORE DEVICES

Initial investigations into the magnetic fields of partial-core devices were performed using physical scale-models, such as the one shown in Figure 2.8. The author does not state how the magnetic field was obtained, but it appears that rectangular or cylindrical magnets where used in place of the partial-cores and a field plot was obtained with iron filings.

An analytical model of a partial-core inductor was developed in 1965 [Friedrich, 1965]. This was subsequently used to design the partial-core inductors shown in Figure 2.5.

(a) Manapouri power station (b) Matahina power station

Figure 2.7 High-voltage testing of hydro-generator stators in New Zealand using PCRTXs. (taken from [Enright and Bodger, 2004])

A patent application was filed on a frequency-tuned high-voltage testing system using partial-core inductors [Zaengl and Bernasconi, 1982].

Another model for the partial-core inductor was developed in 1979 [Yamada et al., 1979]. The intended application was smoothing reactors, used in thyristor-controlled equipment. Both of these models take into account the non-uniform magnetic field inside the partial-core and in the surrounding air.

A model for a partial-core transformer was developed in the early 2000s [Liew and Bodger, 2001]. The partial-core transformer was also the topic of a recent PhD thesis [Liew, 2001]. The model assumes a uniform flux-density inside the partial-core and an exponential decay of flux-density in the surrounding air. It was adopted from full-core transformer models, based on circuit theory, and contains empirically derived factors.

PCRTXs have been designed using the model of [Liew, 2001], which was designed for power transformers, not resonant transformers. The model does not take into account core displacement. To meet the main thesis objective of developing a general design methodology for PCRTXs with variable inductance, any of these models could be adopted. Each model has advantages and disadvantages. However, with the advent of modern computer systems, it now becomes practical to use finite element analysis software to analyse and design PCRTXs. Finite element analysis allows for accurate design to specification and removes the need for empirically derived factors.

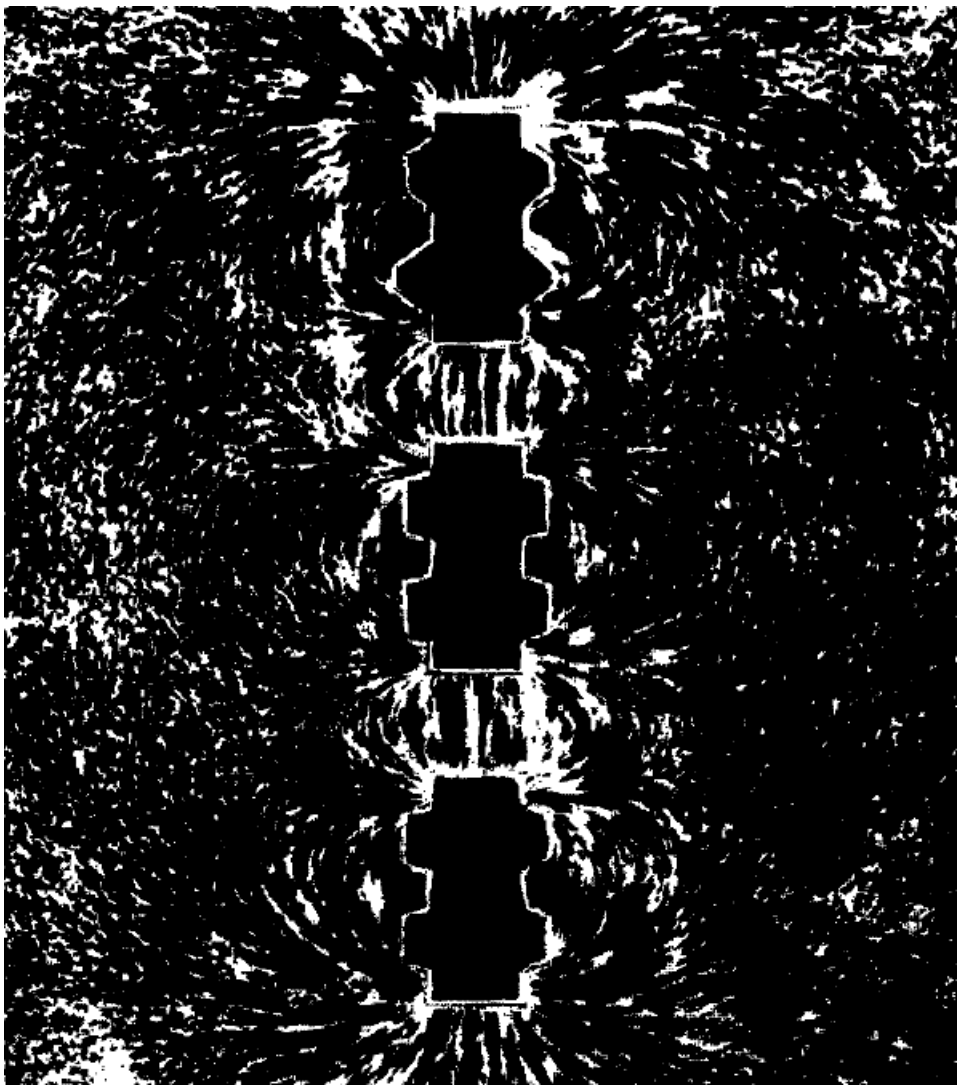

Figure 2.8 Magnetic field of three partial-core inductor units. (taken from [Bernasconi et al., 1979])

2.6 PARTIAL-CORE TERMINOLOGY

Finally, it is worth noting the different terminology which has been used to describe the partial-core magnetic circuit. In high-voltage applications, the partial-core magnetic circuit has also been referred to as open-core [Enright et al., 2008], cylindrical bar-core [Bernasconi et al., 1979], post-type core [Weishu, 1995] and rod-core [Friedrich, 1965]. In RF applications it is often referred to as a slug-type core [Yu et al., 2002], where the core is typically made from ferrite powder rather than individual steel laminations.

Chapter 3

FULL-CORE TRANSFORMER DESIGN USING MAGNETIC CIRCUIT THEORY AND FINITE ELEMENT ANALYSIS

3.1 OVERVIEW

The reverse method of transformer design is described in general and then applied specifically to single-phase full-core shell-type transformers. Models for the resistive and inductive-reactance components of the Steinmetz 'exact' transformer equivalent circuit are developed from fundamental theory, as previously presented in [Bodger and Liew, 2002]. Several anomalies are corrected. Two- and three-dimensional linear and non-linear magneto-static finite element models are introduced as an alternative model for the inductive-reactance components. The reverse design method is used to analyse two sample high-voltage transformers. The performances of the two magnetic models are compared to the measured performance of the as-built transformers. The magnetic model based on finite element analysis is shown to be more accurate than the model based on magnetic circuit theory, though at the expense of complexity of programming.

3.2 INTRODUCTION

From a manufacturer's perspective, it is convenient to design and produce a set range of transformer sizes. Usually, the terminal voltages, VA rating and frequency are specified. In the conventional method of transformer design these specifications decide the materials to be used and their dimensions. This approach to transformer design has been utilised and presented in detail in textbooks [Lowdon, 1989, McLyman, 2004]. It has been used as a design tool for teaching undergraduate power system courses at universities [Rubaai, 1994, Jewell, 1990, Shahzad and Shwehdi, 1997]. In addition, it has also been used extensively in designing switched mode power supplies [Hurley et al., 1998, Petkov, 1995]. Finite element analysis has also been applied, concurrent with the above approach, to aid the overall design process [Asensi et al., 1994, Allcock et al., 1995].

However, by designing to rated specifications, consideration is not explicitly given to what materials and sizes are actually available. It is possible that an engineer, having designed a transformer, may then find the material sizes do not exist. The engineer may then be forced to use available materials. Consequently the performance of the actual transformer built is likely to be different from that of the design calculations.

In the reverse design method, the physical characteristics and dimensions of the core and windings are the specifications. By manipulating the amount and type of material actually to be used in the transformer construction, its performance can be determined. This is essentially the opposite of the conventional transformer design method. It allows for customised design, as there is considerable flexibility in meeting the performance requirements of a particular application.

3.3 REVERSE TRANSFORMER DESIGN

A full-core shell-type transformer profile showing known material characteristics and dimensions is depicted in Figure 3.1. The transformer has a rectangular central limb having length l_c, width w_{c1} and depth w_{c2}. To ensure a uniform core flux-density, the widths of the outer limbs and height of the connecting yokes are equal to $w_{c1}/2$.

In the reverse design method, the transformer is built from the core outwards. The core cross-section dimensions are selected from catalogues of available materials. A core length is chosen. Laminations that are available can be specified in thickness. A core stacking factor can be estimated from the ratio of iron to total volume. The inside winding (usually the low-voltage winding) can then be wound on the former layer by layer. The wire size can be selected from catalogues. They also specify insulation thickness. The designer can then specify how many layers of each winding are wound. Additional insulation may be placed between each layer for high-voltage applications. Insulation can also be placed between each winding. The outer winding (usually the high-voltage winding) is wound over the inside winding, with insulation between layers according to the voltage between them. Additional insulation may be placed between the outside winding and the outer limbs.

Winding current densities and volts per turn become a consequence of the design, rather than a design specification. The only rating requirements are the primary voltage and frequency. The secondary voltage and transformer VA rating are a consequence of the construction of the transformer.

The number of turns on the inside and outside windings are estimated to be:

$$N_1 = \frac{l_1 L_{y1}}{t_1} \tag{3.1}$$

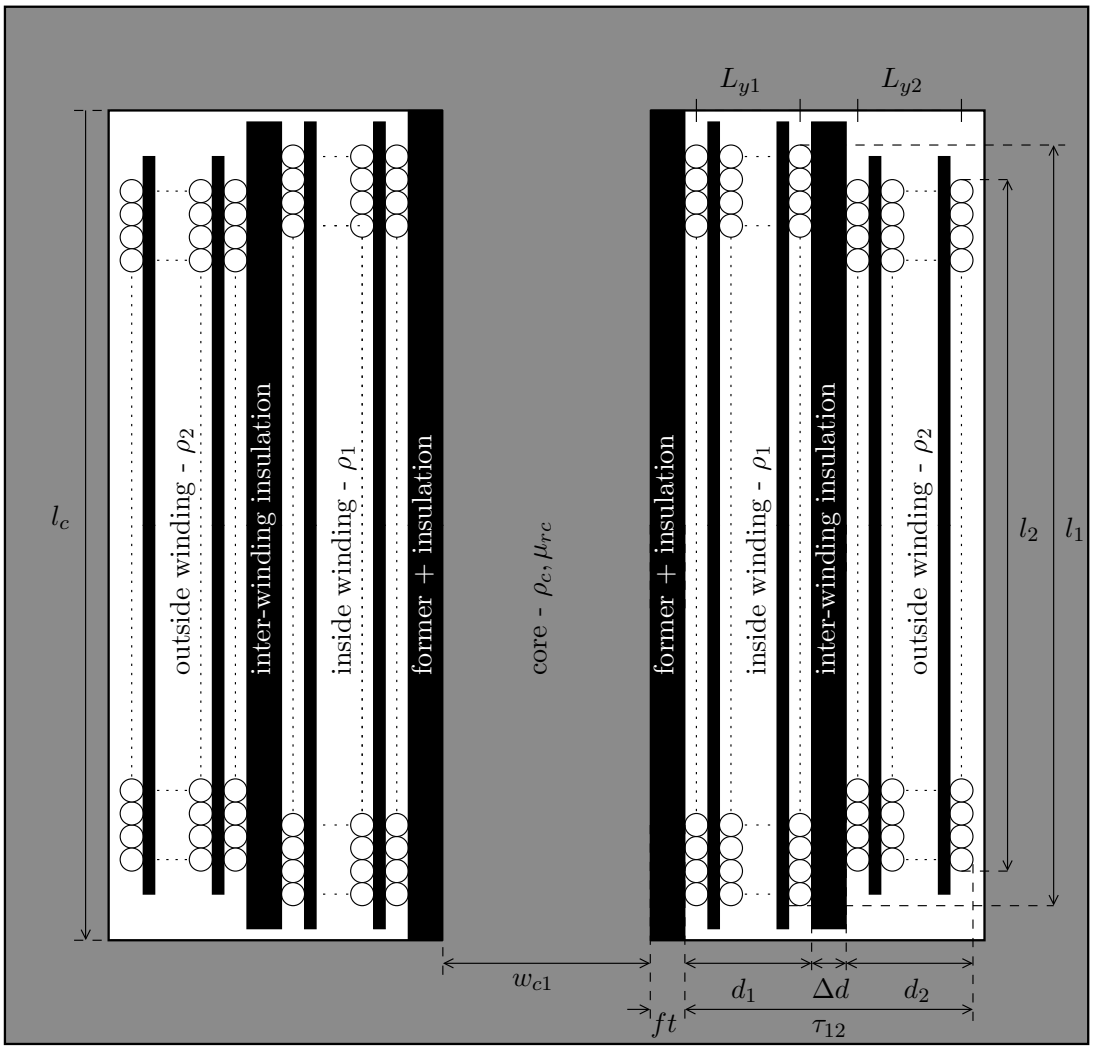

Figure 3.1 Axial view of a full-core shell-type transformer with layer windings, showing component dimensions and material properties.

$$N_2 = \frac{l_2 L_{y2}}{t_2} \tag{3.2}$$

where l_1 and l_2, L_{y1} and L_{y2} and t_1 and t_2 are the lengths, number of layers and wire axial thickness of the inside and outside windings.

The number of primary and secondary winding turns, N_p and N_s, are equal to N_1 and N_2 or N_2 and N_1, respectively, depending on whether the excitation winding is the inside or outside winding.

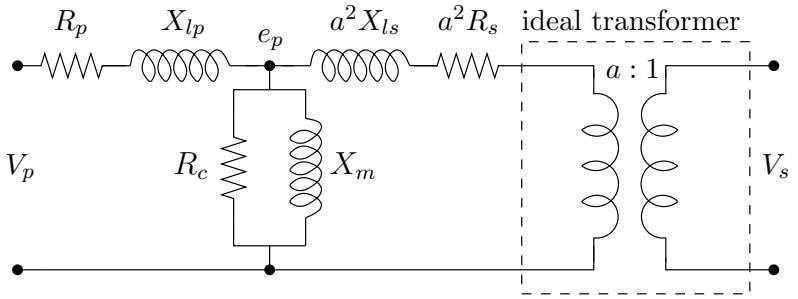

Figure 3.2 Steinmetz 'exact' transformer equivalent circuit, referred to the primary winding.

3.4 EQUIVALENT CIRCUIT MODELS

The Steinmetz 'exact' transformer equivalent circuit shown in Figure 3.2 is often used to represent the transformer at supply frequencies [Paul et al., 1986]. Each component of the equivalent circuit can be calculated from the transformer material characteristics and dimensions.

Where:

V_p	=	Primary voltage
V_s	=	Secondary voltage
e_p	=	Intermediate branch voltage
R_p	=	Primary resistance
R_s	=	Secondary resistance
R_c	=	Core loss resistance
X_{lp}	=	Primary leakage reactance
X_{ls}	=	Secondary leakage reactance
X_m	=	Magnetising reactance
a	=	Transformer turns ratio

3.4.1 Winding resistance components

The resistivity of copper at temperature T °C is calculated as [Liew et al., 2001]

$$\rho_{\text{cu}} = 6.99 \times 10^{-11} T + 1.57 \times 10^{-8} \tag{3.3}$$

Eq. 3.3 is valid for liquid nitrogen and room temperatures. The resistivity of other materials at temperature T °C is calculated as [Davies, 1990]:

$$\rho = (1 + \Delta\rho(T - 20))\rho_{20^\circ\text{C}} \tag{3.4}$$

where $\Delta\rho$ is the thermal resistivity coefficient and $\rho_{20^\circ\mathrm{C}}$ is the material resistivity at 20 °C.

The winding skin depth is calculated as

$$\delta = \sqrt{\frac{2\rho}{\mu_0 \omega}} \tag{3.5}$$

where $\omega = 2\pi f$, f is the supply frequency and $\mu_0 = 4\pi \times 10^{-7}$ H/m is the permeability of free space.

The effective current carrying cross-sectional area of circular wire is calculated as

$$A = \begin{cases} \pi\delta(2r - \delta) & , \delta < r \\ \pi r^2 & , \delta \geq r \end{cases} \tag{3.6}$$

where r is the conductor radius.

For rectangular wire this is calculated as

$$A = \begin{cases} w_1 w_2 - (w_1 - 2\delta)(w_2 - 2\delta) & , 2\delta < w_1 \ \& \ 2\delta < w_2 \\ w_1 w_2 & , \text{otherwise} \end{cases} \tag{3.7}$$

where w_1 and w_2 are the radial and axial widths of the conductor.

The inside and outside winding resistances are calculated using

$$R_1 = \frac{\rho_1 l_{w1}}{A_1} \tag{3.8}$$

$$R_2 = \frac{\rho_2 l_{w2}}{A_2} \tag{3.9}$$

where l_{w1} and l_{w2} are the wire lengths of the inside and outside windings.

The primary and secondary winding resistances, R_p and R_s, are equal to R_1 and R_2 or R_2 and R_1, respectively, depending on whether the excitation winding is the inside or outside winding.

3.4.2 Core loss resistance component

The losses in the core consist of two major components; the hysteresis loss and the eddy current loss. The hysteresis power loss can be calculated using [Paul et al., 1986]:

$$P_h = \nu_c \gamma_c k_h f B_{\mathrm{pk}}^x \tag{3.10}$$

where $\nu_c = A_c l_c$ is the effective volume of the core, γ_c is the core density and k_h and x are constants dependent on the core material, typically 0.11 and 1.85, respectively.

The core peak flux-density is estimated from the 'transformer equation' as

$$B_{\text{pk}} = \frac{\sqrt{2}V_p}{\omega N_p A_c} \tag{3.11}$$

For a rectangular core the effective cross-sectional area for the magnetic flux is calculated as

$$A_c = \begin{cases} w_{c1} w_{c2} SF_c & \delta_c \geq \frac{LT_c}{2} \\ 2\delta_c(nw_{c1} + SF_c w_{c2} - 2\delta_c n) & \delta_c < \frac{LT_c}{2} \end{cases} \tag{3.12}$$

where w_{c1} and w_{c2} are the core widths, SF_c is the stacking factor, LT_c is the lamination thickness and n is the number of laminations in the w_{c2} dimension of the core.

For a circular core this is calculated as

$$A_c = \begin{cases} \pi r_c^2 SF_c & \delta_c \geq \frac{LT_c}{2} \\ 2\delta_c(nw_c + SF_c w_c - 2\delta_c n) & \delta_c < \frac{LT_c}{2} \end{cases} \tag{3.13}$$

where r_c is the core radius and $w_c = 0.5\pi r_c \sqrt{s}$ is the 'equivalent' core width.

The skin depth of the core is calculated as

$$\delta_c = \sqrt{\frac{2\rho_c}{\mu_0 \mu_{\text{rc}} \omega}} \tag{3.14}$$

where ρ_c is core resistivity and μ_{rc} is the relative permeability.

For $\delta_c \geq \frac{LT_c}{2}$ the eddy current loss resistance is calculated as

$$R_{\text{ec}} = \frac{N_p^2 A_c}{l_c} \frac{12\rho_c}{LT_c^2} \tag{3.15}$$

For $\delta_c < \frac{LT_c}{2}$ this is calculated as

$$R_{\text{ec}} = \frac{N_p^2 A_c}{l_c} \frac{3\rho_c}{\delta_c^2} \tag{3.16}$$

The hysteresis loss resistance R_h and core loss resistance R_c are calculated iteratively as

$$R_h = \frac{e_p^2}{P_h} \tag{3.17}$$

$$R_c = \frac{R_h R_{\text{ec}}}{R_h + R_{\text{ec}}} \tag{3.18}$$

where e_p, defined in Figure 3.2, is obtained by subtracting the voltage across the primary winding components ($R_p + jX_{lp}$) from the primary input voltage V_p. These calculations are performed under open-circuit conditions.

3.4.3 Magnetising reactance component

The magnetising reactance component can be calculated as [Slemon, 1966]:

$$X_m = j\omega \frac{N_p^2 \mu_0 \mu_{\text{rc}} A_c}{l_{\text{eff}}} \tag{3.19}$$

where l_{eff} is the effective path length for the mutual flux.

3.4.4 Leakage reactance components

The primary and secondary leakage reactances are assumed to be the same, when referred to the primary, and are each half of the total transformer leakage reactance. One form of expression is [Connelly, 1965]:

$$X_{lp} = a^2 X_{ls} = j\omega \frac{1}{2} \frac{\mu_0 N_p^2}{(l_1 + l_2)/2} \left(\frac{\bar{l}_1 d_1 + \bar{l}_2 d_2}{3} + \bar{l}_{12} \Delta d \right) \tag{3.20}$$

where $\bar{l}_1$, $\bar{l}_2$, $\bar{l}_{12}$ and d_1, d_2, Δd are the mean circumferential lengths and thicknesses of the inside winding, outside winding and inter-winding space, respectively.

Having obtained the component values, the equivalent circuit can be solved. Open circuit, short circuit and loaded circuit performances can be estimated by putting an impedance $Z_L = R_L + jX_L$ across the output and varying its value. Furthermore, performance measures of voltage regulation and power transfer efficiency for any load condition can be readily calculated. Current flows and densities in the windings can be calculated and compared to desired levels.

3.5 INCORPORATING FINITE ELEMENT ANALYSIS INTO THE REVERSE DESIGN METHOD

3.5.1 Transformer design program

A general-purpose transformer design and analysis program was written, based on the reverse design method. Both the circuit theory and finite element magnetic models were implemented. The program is contained in a Microsoft Excel workbook, which is coupled to the commercial finite element analysis software package MagNet [MagNet, 2007]. By automating the process of finite element modelling, much time is saved and the likelihood of user error is reduced.

The workbook acts as a user oriented shell for MagNet, a concept first proposed by Stochnoil [Stochniol et al., 1992]. It contains several worksheets and three stand-alone modules. The modules are written in Visual Basic for Applications (VBA) code. The worksheets contain both cell data (familiar to most Excel users) and VBA code. The program interface consists of data, contained in several input and output worksheets, and command buttons. The command buttons allow the user to execute the program code while the input and output worksheets allow the user to enter-in and read-out program data. The program is further documented in Appendix A.

3.5.2 Model detail

Each winding was modelled as a single block of non-magnetic material encompassing all turns over all layers. Uniform current-density was assumed. The core was modelled as a single non-conducting isotropic material. Both linear and non-linear models were developed. A constant relative permeability of 3000 was used for the linear model. A generic B-H curve for non-oriented steel, which was built into the finite element analysis software package, was used for the non-linear model. The model steel had a saturation flux-density of approximately 1.3 T. This is much lower than the typical value for grain oriented steel of 1.7 - 1.9 T. In this chapter, two sample full-core shell-type transformers FC1 and FC2 were analysed. The transformers are introduced in Section 3.6. It should suffice now to state that their respective operating flux-densities, as calculated using the 'transformer equation' (Eq. 3.11) were 1.23 T and 0.31 T. This generic B-H curve should thus be a suitable first approximation for these sample transformers.

The transformer was enclosed by a rectangular air-space with dimensions twice that of the core, to which a tangential flux boundary condition was applied. The default mesh was automatically refined using the in-built h-adaptation feature and the solution polynomial order was set to 3. Two-dimensional (2D) planar, 2D axisymmetric and three-dimensional (3D) models were developed. For the 2D planar and axisymmetric models, the transformer cross-section of Figure 3.1 was used. The extrusion depth was

set to w_{c2} for the planar model. Rotational symmetry was applied to the right-hand side of the figure for the axi-symmetric model. Solving time was reduced for the 3D model by making use of transformer symmetry, where only one eighth of the device was modelled. The 3D model geometry for an example transformer, FC1, along with the initial mesh, is shown in Figure 3.3.

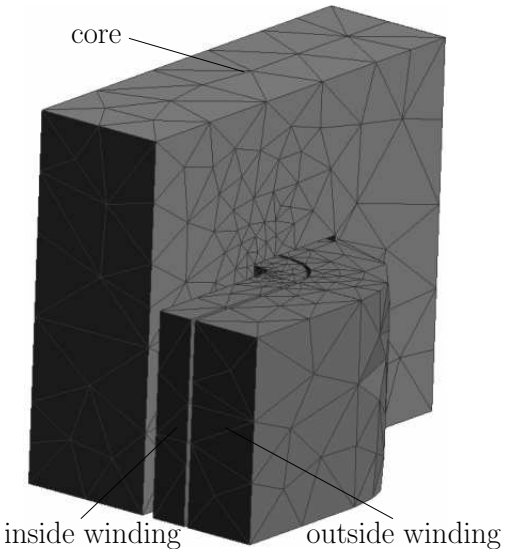

Figure 3.3 3D Geometry and initial mesh for transformer FC1 (air-space mesh not shown).

3.5.3 Reactance calculations

3.5.3.1 Calculation of inductance matrix

The winding inductances are defined as [Ong, 1998]:

$$L_{ij} = N_i N_j P_{ij} \tag{3.21}$$

where N_i, N_j are the number of turns on winding i and j and P_{ij} is the magnetic permeance, defined as

$$P_{ij} = \frac{\lambda_{i'}}{i_{j'}} \tag{3.22}$$

where $\lambda_{i'}$ is the flux linkage of winding i' due to an excitation current $i_{j'}$ in winding j'. Windings i' and j' occupy the same space as winding i and j, respectively, but each have a unity number of turns.

The permeance matrix $\mathbf{P}$ is defined as

$$\mathbf{P} = \begin{bmatrix} P_{11} & P_{12} \\ P_{21} & P_{22} \end{bmatrix} \tag{3.23}$$

where $P_{ij} = P_{ji}$.

$\mathbf{P}$ was obtained from the finite element analysis software by performing two simulations. In each simulation a single winding was excited with unit-current and the flux-linkage of both windings was calculated.

3.5.3.2 Transformation to inductive reactance components

Once the excitation winding has been defined, the winding self- and mutual-inductances are converted into the inductive reactance components of the Steinmetz 'exact' transformer equivalent circuit of Figure 3.2. The transformation equations are derived in [Ong, 1998] and [Ludwig and El-Hamamsy, 1991]. First, a T-equivalent circuit is formed, having primary and secondary leakage inductances as the series components and magnetising inductance as the shunt component. An ideal transformer with turns ratio $a:1$ is placed to the right of the secondary leakage inductance. The equivalent circuit components are then re-written in terms of the self- and mutual inductances. The turns ratio a, required for the transformation, will always be available at the design stage. The inductive reactance components, obtained by multiplying the inductances by $j\omega$, are given by

$$X_m = j\omega(aM_{ps}) \tag{3.24}$$

$$X_{lp} = j\omega(L_p - aM_{ps}) \tag{3.25}$$

$$a^2X_{ls} = j\omega a^2(L_s - \frac{1}{a}M_{ps}) \tag{3.26}$$

where $M_{ps} = L_{12}\ (= L_{21})$ is the primary-secondary mutual inductance.

The self-inductances of the primary and secondary windings, L_p and L_s, are equal to L_{11} and L_{22} or L_{22} and L_{11}, respectively, depending on whether the excitation winding is the inside or outside winding.

3.5.4 Alternative calculation of leakage reactances

An alternative method of calculating the leakage reactances is based on energy techniques [Lindblom et al., 2004]. This provides a simple calculation check, and is less prone to numerical errors than the self- and mutual inductance method, where the (typically small) value of leakage reactance is given by the difference between two large numbers [Edwards, 2005]. However, this method cannot resolve the individual leakage

Transformer	FC1	FC2
Primary voltage (V)	240	14
Secondary voltage (kV)	6.24	4.56
VA rating (VA)	200	617

Table 3.1 Transformer nominal ratings.

reactance values. For transformers with different primary and secondary winding lengths, or incomplete magnetic cores, the common assumption that the leakage reactances are equal when referred to the primary is no longer valid [Margueron and Keradec, 2007].

The total leakage reactance referred to the primary winding is computed from the calculated total stored energy W_s. The number of primary and secondary turns are both set to N_p, the primary winding is energised with current $+i_s$ and the secondary winding is energised with current $-i_s$. The leakage reactance is given by:

$$X_{lp} + a^2 X_{ls} = j\omega(\frac{2W_s}{i_s^2}) \tag{3.27}$$

3.6 TWO EXAMPLES OF TRANSFORMER DESIGN USING THE REVERSE DESIGN METHOD

To illustrate the reverse design method, two single-phase, 50 Hz, high-voltage transformers have been designed, built and tested. The transformers were designed using the magnetic model based on circuit theory and have been subsequently re-analysed using the finite element magnetic model. Their nominal ratings are listed in Table 3.1.

Transformer FC1 was designed for the power supply of an electric water purification device [Johnstone and Bodger, 1997]. Transformer FC2 was a model, designed to evaluate the harmonic performance of capacitive voltage transformers. Both transformers were built as shell types with rectangular cores.

Standard physical values of material permeabilities, resistivities and thermal resistivity coefficients were also entered as data, for the core steel and copper windings, as shown in Table 3.2. The two transformers were constructed using different core steel but the equivalent circuit models do not account for this.

Consideration was given to the wire gauges, insulation material, and core dimensions that were actually available. The dimensions of the various components that were to be used to construct the transformers were entered as data for the reverse design method. They are shown in Table 3.3. The Design Data worksheets of the transformer design program for FC1 and FC2 are listed in Appendix B.

Property	Core	LV winding	HV winding
Relative permeability	3000	1	1
Resistivity at 20 °C (Ω.m)	1.8×10^{-7}	1.76×10^{-8}	1.76×10^{-8}
Thermal resistivity coeff. (/°C)	0.006	0.0039	0.0039
Operating temperature (°C)	50	50	50
Density (kg/m^3)	7870	8960	8960

Table 3.2 Material constants.

Transformer	FC1	FC2
Core		
Length (mm)	68	114
Width 1 (mm)	51	44
Width 2 (mm)	44	152
Core / LV insulation thickness (mm)	2	3.25
LV winding		
Length (mm)	66	114
Number of layers	5	1
Wire diameter (mm)	0.8	3.55
Interlayer insulation thickness (mm)	0.5	0
LV / HV insulation thickness (mm)	0.7	6.5
HV winding		
Length (mm)	66	114
Number of layers	20	20
Wire diameter (mm)	0.125	0.212
Interlayer insulation thickness (mm)	0.5	0.09

Table 3.3 Transformer design data.

3.6.1 Equivalent circuit parameters

The magnetising reactance values were first calculated using 2D and 3D linear finite element models. In both cases, the difference in calculated values was minimal. Then, a non-linear finite element model was used. The magnetising reactance values for the non-linear model were calculated under open-circuit conditions using an iterative procedure. To save computation time, only a 2D model was used. The value of excitation current was adjusted until its product with the calculated value of magnetising reactance was equal to the peak value of the primary voltage. This is an approximation to the actual magnetising reactance value, as measured by true rms meters. A transient solver could have been employed for higher accuracy, at the expense of greatly increased computation time.

The leakage reactance can be calculated with high accuracy using a 2D axi-symmetric finite element model for transformers having circular core limbs and windings [Kulkarni and Khaparde, 2004]. The axi-symmetric model is less accurate for transformers such

Value	Equivalent circuit parameters					
	R_c, Ω	X_m, Ω	$R_p + a^2R_s, \Omega$	X_{lp}, Ω	a^2X_{ls}, Ω	$X_{lp} + a^2X_{ls}, \Omega$
Transformer FC1						
Meas.	3388	1987	10	-	-	2.8
CTM	1342	1383	11.5	0.94	0.94	1.88
l FEM	-	1892/ 1898[a]	-	0.91/ 0.78[b]	0.64/ 0.78[b]	1.55/ 1.55[b]
nl FEM	-	2175	-	-	-	-
Transformer FC2						
Meas.	18	41	0.043	-	-	0.012
CTM	16	20	0.055	0.008	0.008	0.016
l FEM	-	26/ 25[a]	-	0.008/ 0.008[b]	0.007/ 0.008[b]	0.015/ 0.015[b]
nl FEM	-	66	-	-	-	-

[a] 2D model / 3D model.
[b] Self- and mutual-inductance technique / energy technique.

Table 3.4 Measured and predicted equivalent circuit parameters for the sample transformers.

as FC1 and FC2, which have rectangular core limbs and windings. FC1 has a core width to depth ratio w_{c1}/w_{c2} of 3.5, which cannot accurately be represented with an axisymmetric geometry. Consequently, only 3D models were used to calculate the leakage reactance values. Both the self- and mutual-inductance technique, described in Section 3.5.3, and the energy technique, described in Section 3.5.4, were applied.

The calculated transformer equivalent circuit parameters referred to the primary, along with the measured values as determined by open circuit and short circuit tests are presented in Table 3.4. The magnetic models are abbreviated as: 'CTM' - circuit theory model, 'l FEM' - linear finite element model, and 'nl FEM' - non-linear finite element model.

The winding resistance values were calculated with reasonable accuracy. The operating temperature of each model transformer was set to 50°C. The actual winding resistances may have been measured when the transformers were cold, which would explain why the model has slightly over-calculated the values. The calculated value of core loss resistance was below the measured value for both transformers, indicating that the core losses have been over-calculated.

Similar results were obtained for the linear 2D and 3D finite element models when calculating the magnetising reactance value of both transformers. Both models slightly improve on the accuracy of the circuit theory model. The non-linear model has over-calculated the magnetising reactance values. Both the self- and mutual-inductance and energy techniques calculated the same value of total leakage reactance for each transformer, although the self- and mutual-inductance technique has been able to resolve

Performance parameters	Transformer FC1			Transformer FC2		
	CTM	FEM	Measured	CTM	FEM	Measured
V_p, V	240	240	240	14.05	14.05	14.05
I_p, A	0.92	0.91	0.76	1.12	1.04	1.0
V_s, kV	5.9	5.9	6.2	4.7	4.7	4.6
I_s, mA	28	28	27	0	0	0
P_p, W	216	216	181	12	12	8
Efficiency., %	77	77	92	0	0	0
Regulation, %	3.8	3.8	0.7	0.2	0.2	0.1

Table 3.5 Measured and predicted rated performance for the sample transformers.

the individual values, rather than just assuming that they are equal like the energy technique does.

In general, when using the 3D linear finite element model and the self- and mutual-inductance technique to calculate all reactance components, a modest improvement over the circuit theory model is obtained. The reactance component values calculated using this method were then used to perform load tests on the model transformers.

3.6.2 Load tests

A resistance was placed across the secondary of transformer FC1 to obtain the rated load conditions at unity power factor. The model performance was calculated by adjusting the load resistance so that the calculated secondary VA matched the measured value. On the other hand, since transformer FC2 was designed for capacitive loads, an open circuit condition was used to compare calculated and measured values. The results are shown in Table 3.5.

The difference between the two magnetic models is relatively small. It can be concluded that, for the sample transformers, either model could be used to obtain an estimate of the actual performance. For transformer FC1, the core loss model is highly inaccurate, as indicated by the efficiency calculations. This is the reason for the over-estimation of the primary current I_p.

3.7 DISCUSSION

The linear finite element magnetic model calculated higher values of magnetising reactance than the circuit theory model, although both models have the same relative permeability value of 3000. This can be explained by considering the open-circuit magnetic flux plot of transformer FC1, shown in Figure 3.4(a). The flux plot essentially shows the transformer's mutual flux, since the primary leakage is negligible under open-circuit conditions. With the linear model, the flux-density is greatest at the inside

edges of the core, where the highest calculated value exceeds 3.7 T, highlighting the limitations of the linear model. The effect is to reduce the effective path length of the magnetic flux, thereby increasing the magnetising reactance.

The magnetic flux plot of transformer FC1 for the non-linear finite element magnetic model is shown in Figure 3.4(b). The peak flux-density throughout most of the core is approximately 1.2 T, matching the value calculated using the 'transformer equation' (Eq. 3.11). The flux distribution obtained using the non-linear model is more representative of the actual flux distribution and, consequently, the magnetising reactance value is more accurately calculated. The difference in calculated magnetising reactance values between the linear and non-linear finite element models is greatest for transformer FC2. This transformer operates at a reduced flux-density of 0.3 T, where the relative permeability is much greater than the value of 3000 used in the linear model.

In practice, the actual value of magnetising reactance is unimportant, but the magnetic flux plot can be used for loss calculations. More advanced models account for the anisotropic properties of the core and the core construction details. B-H curves and loss data, measured in both the rolling and transverse directions, can be incorporated into the finite element model. Such models are currently used in industry for highly accurate calculation of core losses [Mechler and Girgis, 1998].

Typically, the leakage flux-density is greatest in the duct between the primary and secondary windings, and drops to negligibly low values once inside the core. The value of leakage reactance is therefore mainly determined by the air-path reluctance not the core reluctance, so high accuracy can still be obtained using a linear core model. The leakage flux plot of FC1, calculated using an axi-symmetric model, shown in Figure 3.5, illustrates this concept.

There is a significant difference between the calculated and measured values of core losses. The hysteresis formula of Eq. 3.10 calculates a loss of 13 W/kg for a peak flux-density of 1.6 T. This is a gross overestimation and should be addressed in the future. The intrinsic losses of modern core steel are typically below 1 W/kg and most transformer manufacturers obtain a building factor of less than 1.5 [Qader and Basak, 1982].

3.8 CONCLUSIONS

A finite element magnetic model has been introduced into the reverse method of transformer design. For the example transformers considered, the model was found to be only slightly more accurate than the existing model, which was based on magnetic circuit theory. This comes at the expense of complexity of programming.

On the other hand, the finite element magnetic model is more flexible because it allows

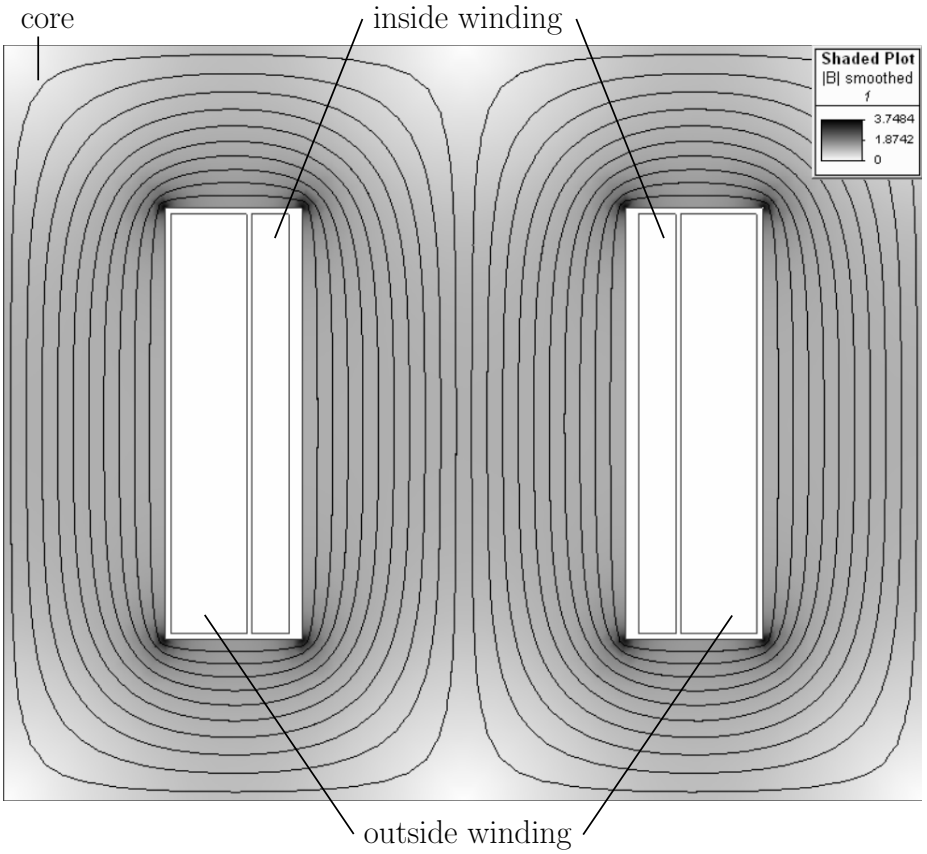

(a) Linear model

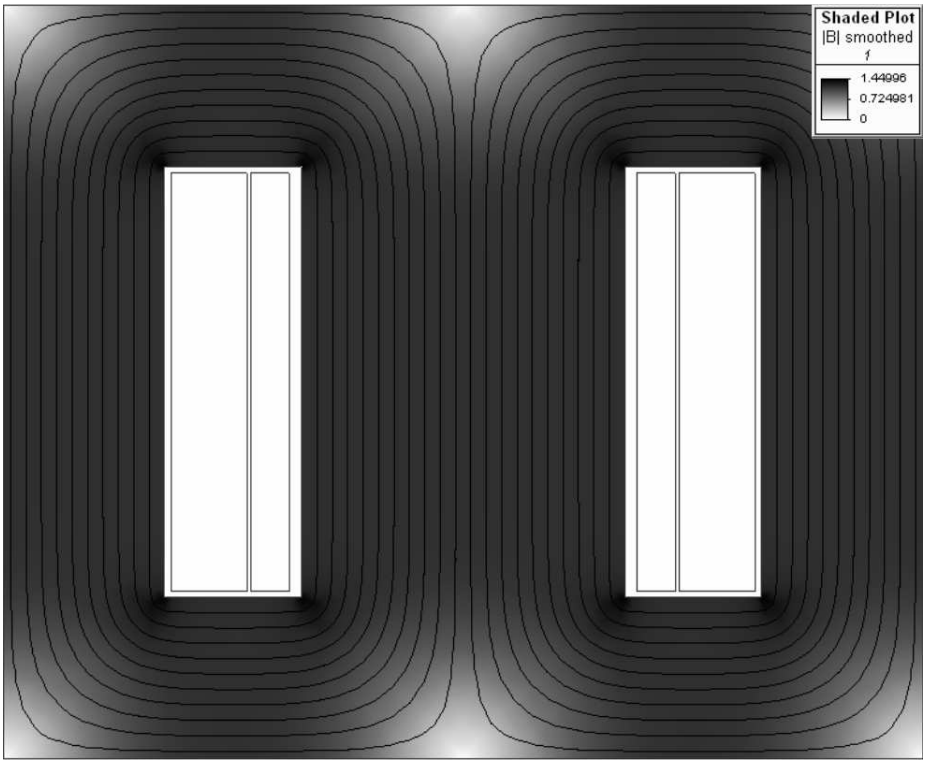

(b) Non-linear model

Figure 3.4 Magnetic flux plot of transformer FC1 under open-circuit conditions, calculated using a 2D planar magneto-static finite element model.

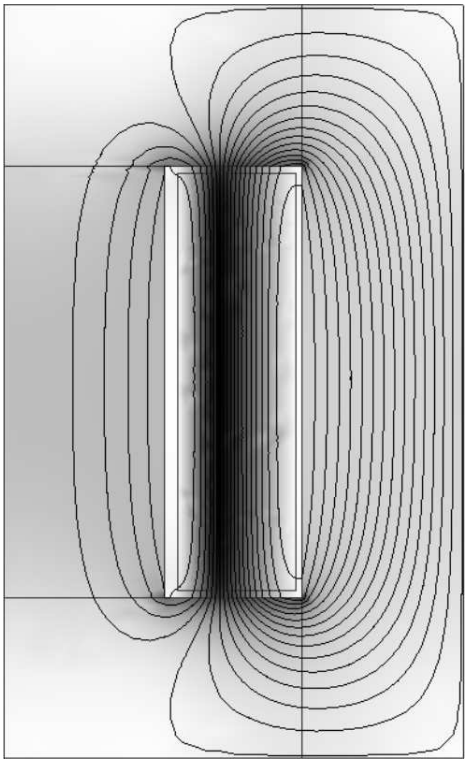

Figure 3.5 Magnetic flux plot of transformer FC1 under short-circuit conditions, calculated using a 2D axi-symmetric magneto-static finite element model.

for other transformer configurations, such as those based on air- or partial-core designs, to be easily considered. Only the model geometry needs to be changed, removing the need for correction factors, which are often based on empirical data. This has strengthened the use of the reverse design method as an entry-level design tool, from which more accurate models can be developed.

Chapter 4

EQUIVALENT CIRCUIT FOR HIGH-VOLTAGE PARTIAL-CORE RESONANT TRANSFORMERS

4.1 OVERVIEW

An equivalent circuit model for the partial-core resonant transformer is developed. A model which omits core losses is first introduced and then verified on a sample air-core resonant transformer. Partial-cores are then introduced into the transformer and the resonant characteristics are re-measured. The model is modified to account for the core losses and verified against measured data. Comparisons and transformations between the model and the Steinmetz 'exact' transformer equivalent circuit are given. A procedure for measuring the equivalent circuit inductances is described and then used to investigate the inductance variation with core displacement characteristics of the sample transformer in both axial-offset and centre-gap arrangements. In a capacitive load test, the sample transformer was linear to a significantly higher voltage when using the centre-gap arrangement.

4.2 INTRODUCTION

An alternative design to a full-core transformer is a partial-core transformer, where the outer limbs and connecting yokes are missing. The magnetic circuit includes both the core and the surrounding air. Consequently, partial-core transformers have a lower value of magnetising reactance than their equivalent full-core counterparts.

Partial-core transformers have been designed as step-up transformers for energising capacitive loads, where they are referred to as partial-core resonant transformers (PCRTXs). By matching the inductive reactance of the secondary winding to the capacitive reactance of the load, the reactive power drawn from the primary winding can be reduced to almost zero. Applications include high-voltage testing of hydro generator stators [Bodger and Enright, 2004, Enright and Bodger, 2004] and energising arc-signs [Bell et al., 2007, Lynch et al., 2007]. In these examples, the advantages over conventional equipment - a full-core step-up transformer and a separate full-core

compensating inductor - are significant reductions in weight and cost, and increased portability. A PCRTX is depicted in Figure 4.1. Further construction details are given in Section 6.2.1.

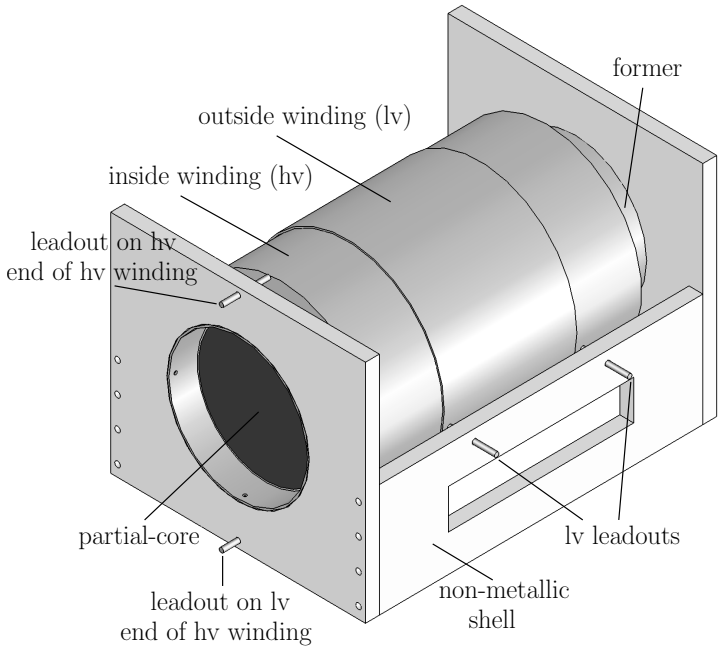

Figure 4.1 Isometric view of a PCRTX, showing core and winding layout.

4.3 BACKGROUND

In insulation testing applications, the key requirement is to energise an insulation capacitance C to a voltage V_s while ensuring the supply current I_{su} is below the capacity of the local supply. A test circuit employing a PCRTX is shown in Figure 4.2.

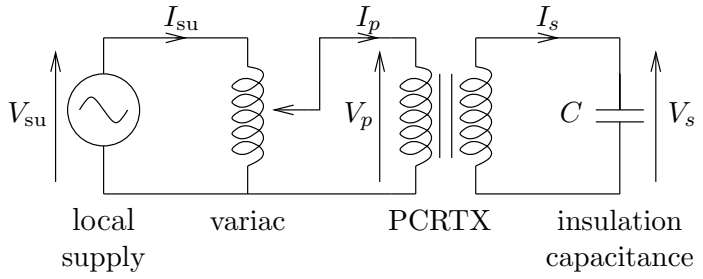

Figure 4.2 The PCRTX in a high-voltage insulation testing application.

PCRTXs have been designed using the reverse method of transformer design [Bodger and Liew, 2002, Liew and Bodger, 2001]. Supply conditions and the physical characteristics and dimensions of the core and windings are used to produce component values for the Steinmetz 'exact' transformer equivalent circuit of Figure 3.2.

Resonance is said to occur when the transformer magnetising reactance X_m is matched to the capacitive reactance of the (primary-referred) load capacitance [Bodger and Enright, 2004]. This description neglects the leakage reactances, which, in PCRTXs, can be significant when compared to the magnetising reactance value. Using the Steinmetz transformer equivalent circuit, the resonant frequencies and loaded-circuit impedance can be calculated for a sample transformer. However, it is difficult to obtain simple analytical expressions for the general case. This can make it difficult to translate design specifications into required values or allowable ranges of values for the equivalent circuit components. The Steinmetz transformer equivalent circuit representation of the PCRTX can also be a source of confusion when it comes to measuring the reactance values. The traditional transformer open-circuit and short-circuit tests may not give an accurate measure of the magnetising and leakage reactance values [Enright and Arrillaga, 1998].

4.4 EQUIVALENT CIRCUIT WITHOUT CORE LOSSES

The return path for the magnetic flux in a PCRTX is air. When compared to equivalent full-core transformers, the coil coupling is reduced and the inductance values are smaller. It is proposed that under normal operating flux densities the coil inductances are essentially linear. Consequently, the PCRTX can be more correctly defined as a coupled inductor than a transformer [Witulski, 1995].

The PCRTX can be analysed in terms of self- and mutual-inductances. In the first analysis the core loss resistance R_c is omitted. The impedance of the insulation under test can be represented as a resistance R_l in series with a capacitance C_l [Emery, 2004]. The supply can be approximated as a Thévenin equivalent circuit. The resulting circuit is shown in Figure 4.3.

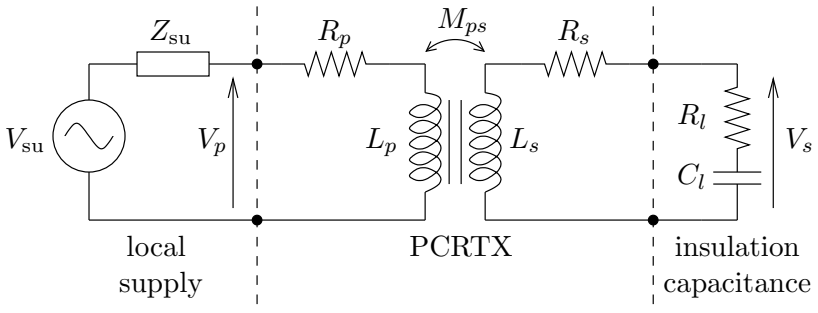

Figure 4.3 Proposed equivalent circuit for the PCRTX.

A general analysis of the circuit in Figure 4.3 has been published by Sherman in 1942 [Sherman, 1942]. The PCRTX with a capacitive load is an example of an inductively coupled circuit with a tuned secondary. The circuit is frequently encountered in radio engineering [Terman, 1947]. The input impedance Z_{in} is equal to the primary winding

impedance Z_p in series with the coupled impedance Z_c. The equivalent circuit is shown in Figure 4.4.

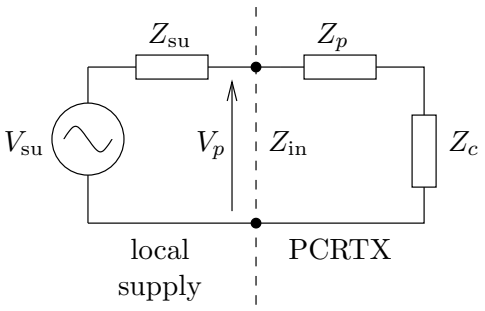

Figure 4.4 Simplified series equivalent circuit for the PCRTX.

The primary winding impedance is given as

$$Z_p = R_p + j\omega L_p \tag{4.1}$$

The coupled impedance is given as [Sherman, 1942]

$$Z_c = \frac{\omega^2 M_{ps}^2}{R_s' + j(\omega L_s - 1/\omega C_l)} \tag{4.2}$$

where $R_s' = R_s + R_l$.

After simplification, the input impedance is

$$\begin{aligned} Z_{\text{in}} = R_p &+ \frac{\omega^2 M_{ps}^2 R_s'}{R_s'^2 + \left(\omega L_s - \frac{1}{\omega C_l}\right)^2} \\ &+ j\left(\omega L_p + \frac{\omega^3 M_{ps}^2 C_l - \omega^5 M_{ps}^2 C_l^2 L_s}{\omega^2 C_l^2 R_s'^2 + (\omega^2 L_s C_l - 1)^2}\right) \end{aligned} \tag{4.3}$$

4.5 MEASUREMENT OF EQUIVALENT CIRCUIT INDUCTANCES

The resonant frequency of the coupled impedance is

$$\omega_{0,c} = \frac{1}{\sqrt{L_p C_l}} \tag{4.4}$$

After simplification, the input impedance at $\omega = \omega_{0,c}$ is

$$Z_{\text{in}} = R_p + \frac{M_{ps}^2}{L_s C_l R_s'} + j\frac{L_p}{\sqrt{L_s C_l}} \tag{4.5}$$

Parallel resonance in tuned circuits can either be defined by the maximum impedance criteria or the unity power factor criteria [Lee, 1933]. For the circuit of Figure 4.4 these two definitions of resonance do not coincide due to the primary winding self-inductance L_p. There are two resonant frequencies for Z_{in}, namely $\omega_{0,m}$ and $\omega_{0,u}$. The following inequality holds

$$\omega_{0,m} \leq \omega_{0,c} \leq \omega_{0,u} \tag{4.6}$$

The inequality gives rise to a procedure for measuring the equivalent circuit inductances of the PCRTX of Figure 4.3. The main advantage of this technique, termed the resonant tuning test, is that it does not require a supply rated for the volt-amperes of the secondary circuit. The insulation capacitance is replaced with a high-voltage capacitor of equivalent value and the circuit is energised from a variable frequency sinewave generator. The resonant frequencies $\omega_{0,m}$ and $\omega_{0,u}$ and the corresponding terminal conditions of the PCRTX are measured. The test results, along with the measured values of winding resistance and load capacitance, are used to determine the secondary winding self-inductance and mutual-inductance values, given by

$$L_s = \frac{1}{\omega^2 C_l} \tag{4.7}$$

$$M_p = \frac{\sqrt{(\text{Re}\{Z_{\text{in}}\} - R_p)R'_s}}{\omega} \tag{4.8}$$

Ideally, Eqs. 4.7 & 4.8 would be evaluated at $\omega = \omega_{0,c}$, but this frequency is not directly measured in the resonant tuning test. However, minimum and maximum values of L_s and M_p can be found by evaluating Eqs. 4.7 & 4.8 at $\omega = \omega_{0,u}$ and $\omega = \omega_{0,m}$, respectively. The uncertainty in inductance values ΔL_s and ΔM_p is a function of the equivalent circuit component values. The percentage uncertainty in these values will determine the usefulness of the resonant tuning test as a method of measuring the equivalent circuit inductances. This can be determined by experimenting with a sample PCRTX.

The resonant tuning test can also be used to measure the primary winding self-inductance L_p. A capacitive load is applied to the low-voltage winding and the high-voltage winding is energised using a sinewave generator and conventional full-core step-up transformer. The coil coupling can then be calculated as

$$k = \frac{M_p}{\sqrt{L_p L_s}} \tag{4.9}$$

4.6 EQUIVALENT CIRCUIT WITH CORE LOSSES

Core losses in full-core power transformers can be calculated using magneto-static finite element analysis in combination with magnetisation and loss data, measured on single sheets of material [Moses, 1998]. The magnetic field is typically computed under open-circuit conditions [Alonso and Antonio, 2001]. The primary leakage flux and mutual flux both have an influence on the magnetic field and hence core losses. To account for this, it has been proposed that the core loss resistance R_c in the transformer equivalent circuit of Figure 3.2 should be moved to the left side of the primary leakage reactance branch [Alonso and Antonio, 2001].

However, for the magneto-static case, the magnetic field in any transformer is a function of the instantaneous values of both the primary and secondary ampere-turns. For the PCRTX, the magnetic field is mainly due to the secondary ampere-turns, particularly for a circuit quality factor $Q > 10$. The core loss resistance R_c should therefore be accounted for by a parallel resistance over the secondary winding self-inductance, changing the load impedance from Z_L to Z'_L, as shown in Figure 4.5.

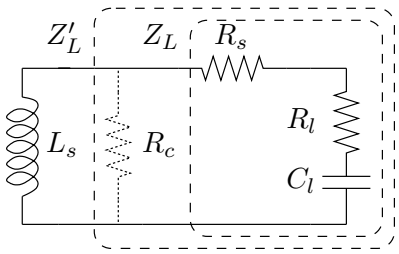

Figure 4.5 Equivalent circuit of load: Z_L - without core loss resistance, Z'_L - with core loss resistance.

The new load impedance is given by

$$Z'_L = |Z'_L| \angle \phi_{Z'_L} \tag{4.10}$$

where

$$|Z'_L| = \sqrt{\frac{(R_c R'_s)^2 + (R_c X_c)^2}{(R_c + R'_s)^2 + X_c^2}} \tag{4.11}$$

$$\phi_{Z'_L} = \tan^{-1}(\theta_1) - \tan^{-1}(\theta_2) \tag{4.12}$$

$$\theta_1 = \frac{X_c}{R'_s} \tag{4.13}$$

$$\theta_2 = \frac{X_c}{R_c + R'_s} \tag{4.14}$$

The effect of introducing core loss resistance on the resonant behavior of the transformer can be determined by experimenting with a sample PCRTX.

4.7 T-EQUIVALENT CIRCUIT WITH CORE LOSSES

The series equivalent circuit of Figure 4.4 can be used to calculate the loaded-circuit input impedance but not the voltage ratio because the secondary terminals are absent. This can be calculated using a T-equivalent circuit. The circuit, shown in Figure 4.6, is similar to the Steinmetz 'exact' transformer equivalent circuit, but the reactance values change from $\{X_{lp}, X_m, X_{ls}\}$ to $\{X'_{lp}, X'_m, X'_{ls}\}$ and the core loss resistance is moved to the right hand side of the secondary leakage reactance branch.

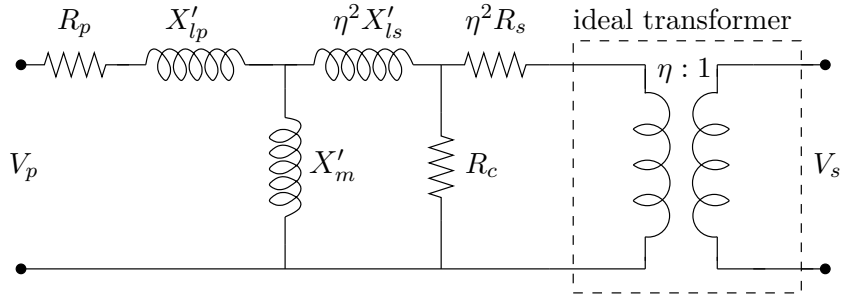

Figure 4.6 T-equivalent circuit for the PCRTX, referred to the primary winding.

The reactance values and coupling factor are given by [Margueron and Keradec, 2007]

$$X'_{lp} = j\omega L_p(1 - xk) \tag{4.15}$$

$$X'_m = j\omega L_p xk \tag{4.16}$$

$$\eta^2 X'_{ls} = j\omega L_p x(x - k) \tag{4.17}$$

$$\eta = x\sqrt{\frac{L_p}{L_s}} \tag{4.18}$$

The coupling factor η (not to be confused with the coil coupling k) replaces the transformer turns ratio a, which is not measured in the above described tests. The choice of x is arbitrary, but one leakage reactance will become negative if x is chosen outside the range $k < x < \frac{1}{k}$. According to $x = k$, 1 or $1/k$, leakage reactances appear on the primary side, split into two equal parts, or on the secondary side.

4.8 EXPERIMENTAL RESULTS

4.8.1 Transformer specifications

A sample PCRTX was used to verify the proposed equivalent circuit model. The transformer was designed for energising arc-signs [Lynch et al., 2007]. The specifications are shown in Table. 4.1. The Design Data worksheet of the transformer design program for the sample PCRTX (PC3) is listed in Appendix B. The core was constructed in a single 604 mm length and then divided into two 300 mm axial lengths using a water-jet cutter. Open-circuit tests, performed before and after the core cutting, showed no difference in measured terminal conditions. The split core allowed for inductance variation via centre-gap tuning as well as axial-offset tuning, used in previous PCRTXs [Bodger and Enright, 2004].

Ratings	
Primary voltage, V	230
Secondary voltage, kV	80
Operating frequency, Hz	50
Core	
Length, mm	600
Diameter, mm	72
Lamination thickness, mm	0.50
Inside (hv) winding	
Length, mm	700
Number of layers	37
Leadouts on layers	1,37
Number of turns	59,200
Maximum current[a], A	0.55
Outside (lv) winding	
Length, mm	600
Number of layers	2
Number of turns	160
Maximum current[a], A	126

[a] At a (short-time-rated) current-density of 5 A/mm^2.

Table 4.1 Specifications of sample PCRTX (PC3).

4.8.2 Resonant tuning test in air-core configuration

The resonant tuning test was first performed on the PCRTX in the air-core configuration, at a reduced secondary voltage of 10 kV. The winding resistances were measured at dc using a MPK 254 digital micro ohmmeter. The dc resistance measurements were assumed to be representative of the ac resistances of the sample PCRTX at the supply

frequency, where the calculated skin depths of the primary and secondary winding materials were much greater than the conductor thicknesses. A calibrated Fluke-41B harmonic analyser was used to take primary-side measurements. The secondary voltage was measured using a 10,000:1 capacitive voltage divider and Escort '97 multimeter. A Universal Technic "M1.UB02" 5A/5V CT and additional Escort '97 multimeter were used to measure the secondary current. The load capacitance was formed from series or parallel combinations of capacitors from an inverted Marx impulse generator. The capacitance value was chosen so that resonance occurred at approximately 50 Hz. The load resistance was considered negligible and the load capacitance was estimated from secondary voltage, current and frequency measurements as

$$C_{\text{meas}} = \frac{I_s}{2\pi f V_s} \tag{4.19}$$

The resonant tuning test was not repeated with the PCRTX in the reverse configuration, due to the difficulty in acquiring low-voltage capacitors of sufficient rating. The required load capacitance could have been obtained by impedance matching high-voltage capacitors with a conventional full-core step-up transformer, at the expense of circuit complexity.

In this instance, the PCRTX was rated for the open-circuit current at the reduced test voltage so the primary winding self-inductance was obtained from open-circuit test results. The equivalent circuit impedance under open circuit was assumed to be $R_p + j\omega L_p$. The primary winding self-inductance was calculated as

$$L_p = \frac{\sqrt{\left(\frac{V_{oc}}{I_{oc}}\right)^2 - R_p^2}}{\omega} \tag{4.20}$$

The measured parameters are shown in Table 4.2. These were used to model the resonant tuning test by calculating the loaded-circuit input impedance (via Eq. 4.3) over the tested frequencies. The model and test results are compared in Figure 4.7.

Parameter	Value
R_p, Ω	0.14
R_s, kΩ	3.63
L_p, mH	1.23
M_{ps}, H	0.21 ± 7%
L_s, H	58.1 ± 9%
k	0.78 ± 3%

Table 4.2 Measured parameters of sample PCRTX in air-core configuration.

The uncertainties in the measured inductance values highlight the limitations of the

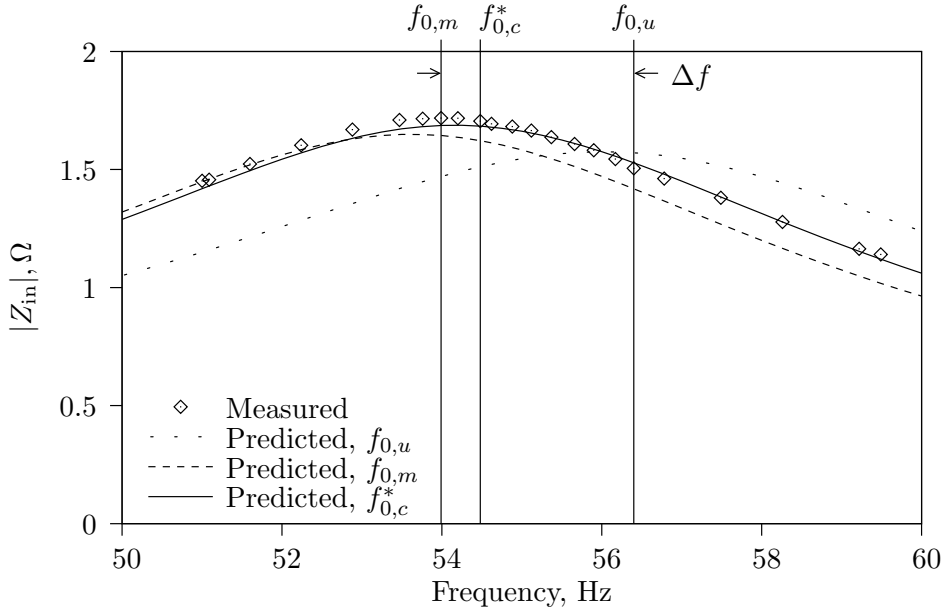

(a) Magnitude

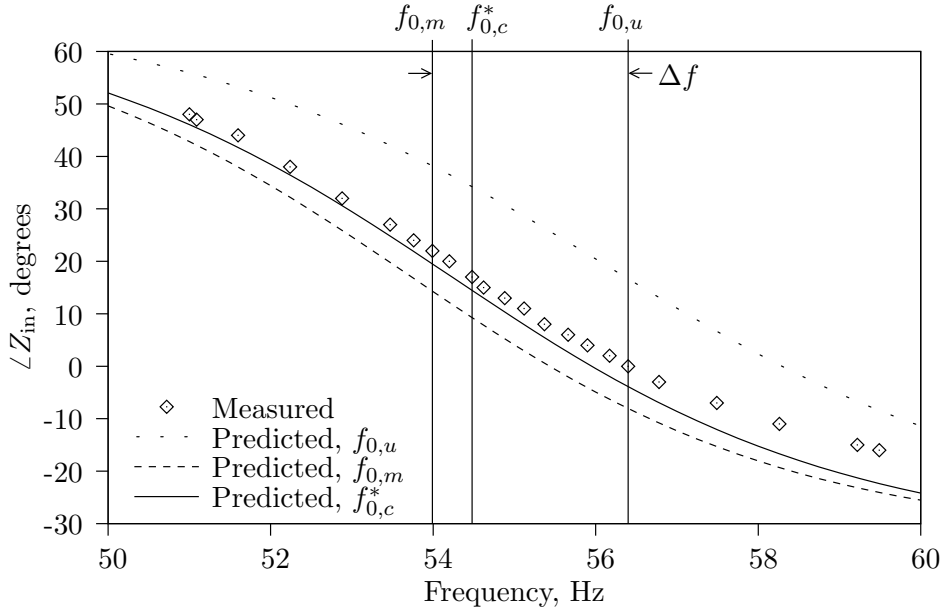

(b) Phase

Figure 4.7 Measured and predicted resonant characteristics of sample PCRTX in air-core configuration at $V_s = 10$ kV. $\Delta f = 2.41$ Hz.

resonant tuning test as a method of measuring the equivalent circuit inductances in air-core resonant transformers.

The uncertainties can be reduced by obtaining a better estimation of $\omega_{0,c}$ (and corresponding $f_{0,c}$). Model resonant characteristics were plotted for each set of measured terminal conditions for all the measured frequencies from $f_{0,m}$ to $f_{0,u}$. The best estimate of $f_{0,c}$, denoted $f^*_{0,c}$, was defined as the frequency whose corresponding model resonant characteristic best matched the measured terminal conditions.

There is a high level of correlation between the test and model results when using $f^*_{0,u}$ in the model. The shape of the resonant characteristic, and hence the circuit Q, has been accurately predicted. This indicates that the proximity losses and capacitor losses, which were not modelled, are negligible when compared to the winding resistance losses.

4.8.3 Open-circuit test in partial-core configuration

The sample PCRTX was configured to maximise the winding inductance values by placing the two core sections inside the former and setting the centre-gap to zero. The device saturation characteristics were measured in an open-circuit test. The results, shown in Figure 4.8, indicate that saturation started to occur at a secondary voltage of 62.6 kV. The core peak flux-density, calculated using the 'transformer equation' (Eq. 3.11) at this voltage was 1.43 T, significantly lower than the typical saturation flux-density for silicon steel of 1.7 T. In this instance, the 'transformer equation' cannot be used to accurately predict the onset of core saturation. As the 'transformer equation' assumes a uniform core flux-density, this may indicate that the sample PCRTX has a non-uniform core flux-density and that parts of the core steel are in saturation at a secondary voltage of 62.6 kV.

Harmonic voltages and currents were also measured. The results, shown in Table 4.3, indicate that the introduced core steel has not caused significant third harmonic currents, confirming the assumption that the device can be modelled using linear circuit elements provided that the operating flux-density is below the saturation level.

4.8.4 Resonant tuning test in partial-core configuration

The procedures used to measure the inductance values for the air-core configuration were first repeated for the partial-core transformer in several different core configurations. The measured values of secondary winding-self inductance were then used to calculate load capacitance values for each configuration such that $f_{0,c} = 50$ Hz. The effect of introducing core losses was then investigated theoretically by plotting the ratios of the real and imaginary components of $\frac{Z'_L}{Z_L}$ against specific core losses using Eqs. 4.11-4.14, as shown in Figure 4.9.

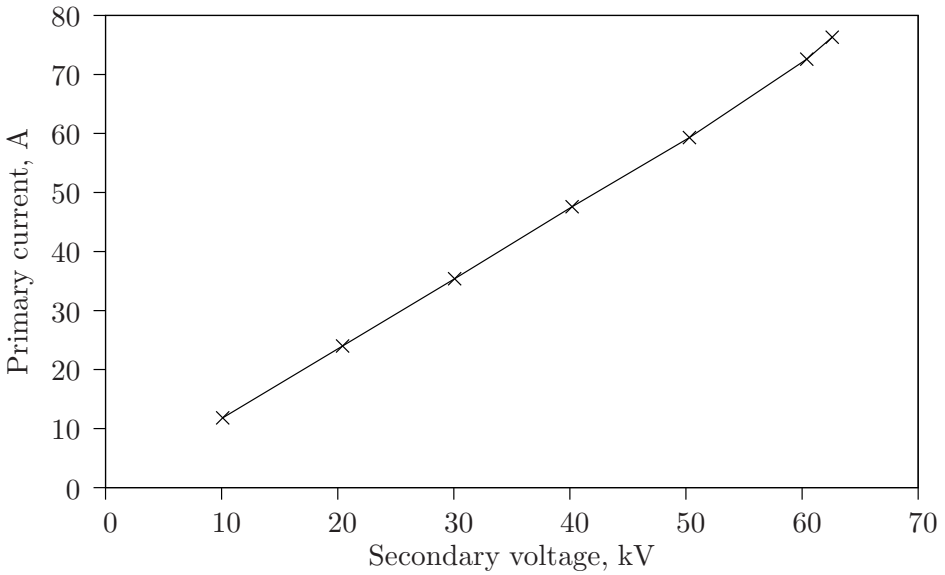

Figure 4.8 Open-circuit test of sample PCRTX.

Secondary voltage, kV	Total harmonic distortion	
	Voltage	Current
10.1	3.6	0.8
20.4	3.6	0.8
30.1	3.9	0.8
40.2	4.4	1.0
50.3	4.0	0.9
60.4	3.8	2.3
62.6	3.7	3.2

Table 4.3 Primary-side total harmonic distortion measurements for sample PCRTX with 2 * 300 mm core pieces and centre-gap = 0 mm under open-circuit conditions.

The plots indicate that, at a typical value of specific core loss of 1 W/kg, for the considered configurations, the effect of the introduced core losses is to increase the real component of Z_L and leave the imaginary component unchanged. Hence the core loss resistance can be incorporated into the circuit model by increasing the value of R'_s to $R''_s = Re\{Z'_L\}$. With reference to Eqs. 4.7 & 4.8, the results also show that omitting the core loss resistance will have a small impact on the measured value of secondary winding self-inductance, but a much larger impact on the measured value of mutual-inductance.

The resonant tuning test was repeated on the sample PCRTX in two different partial-core configurations. The first was an artificial case with a single core of length $l_c = 100$ mm and the second was a more realistic case with two cores of 300 mm length and a centre-gap of cg = 195 mm. The capacitor and proximity losses were not accounted for in the model.

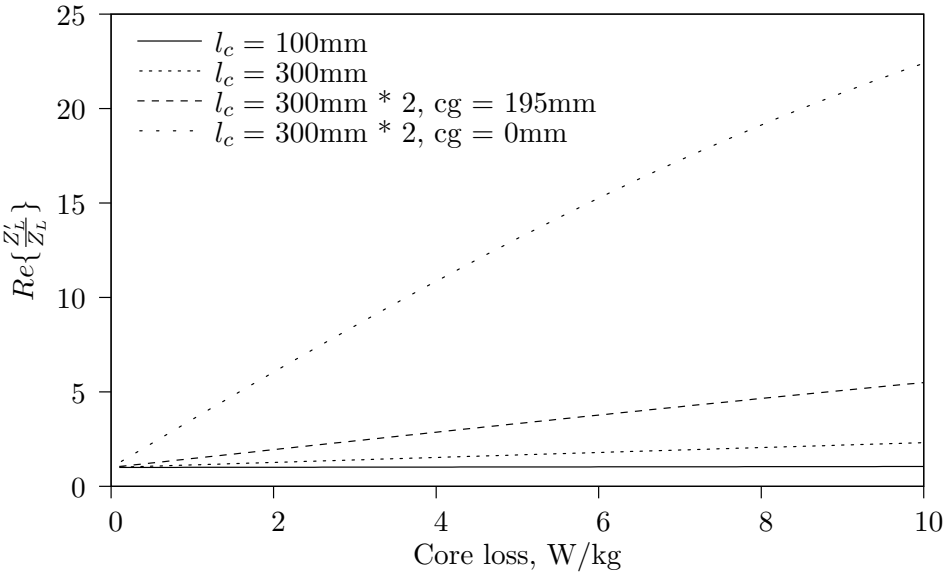

(a) Real component

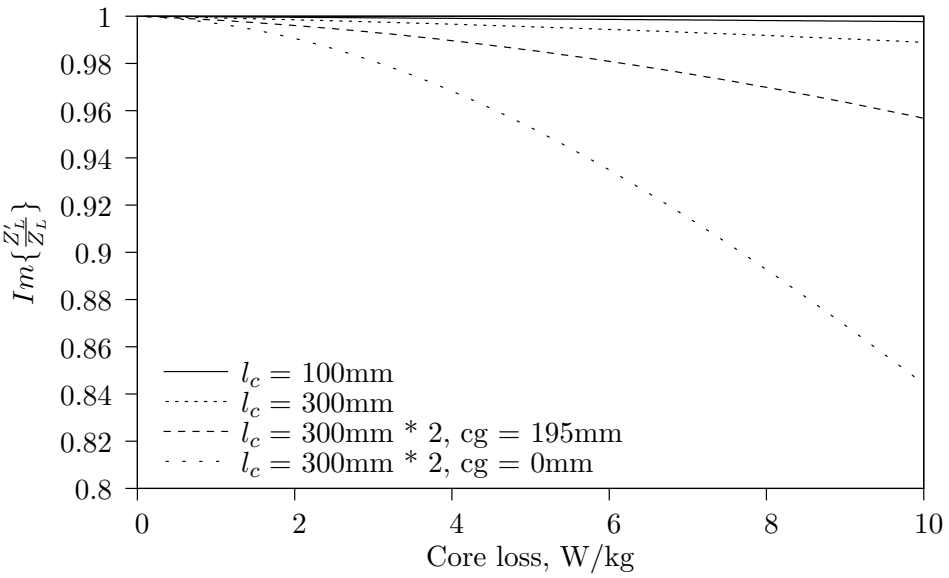

(b) Imaginary component

Figure 4.9 The effect of introducing core losses on the load impedance for the sample PCRTX for several core configurations.

As indicated in Figure 4.9, the introduced core loss will have a minimal impact on performance for the first configuration and do not need to be modelled. The test and model results are compared in Figure 4.10. The introduced core steel has reduced the difference in resonant frequencies Δf and the winding inductances and coil coupling have increased. The circuit model accurately matches the test results.

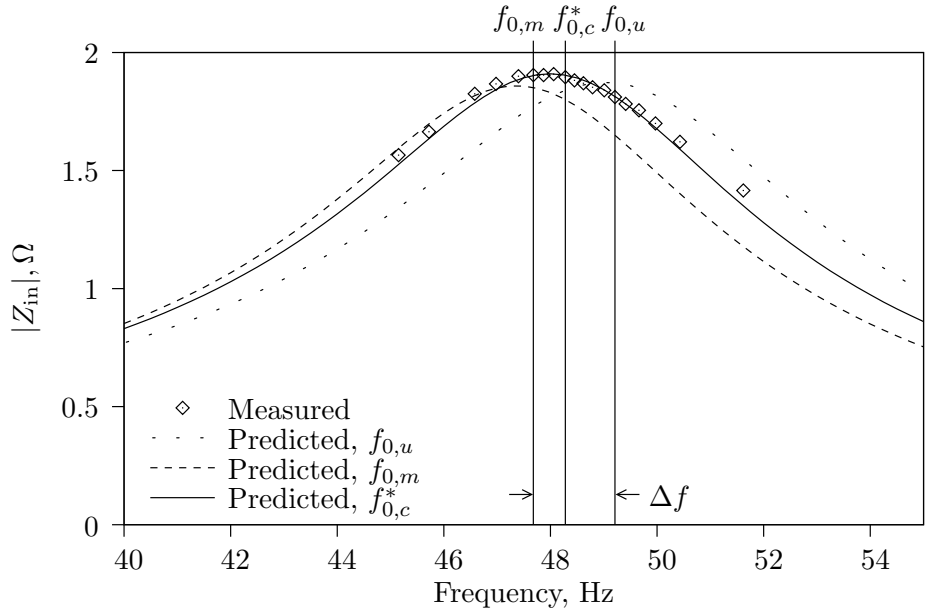

(a) Magnitude

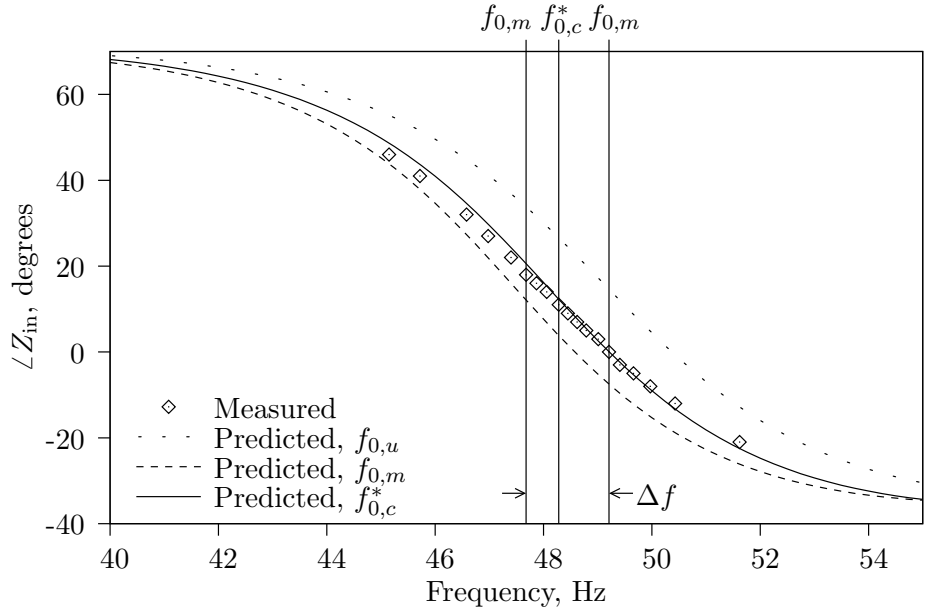

(b) Phase

Figure 4.10 Measured and predicted resonant characteristics of sample PCRTX with 100 mm core at $V_s = 10$ kV. $\Delta f = 1.53$ Hz.

For the second case, the introduced core losses were larger and needed to be modelled.

The core losses were estimated by subtracting the i^2R winding losses from the measured input power. A specific loss value of 0.4 W/kg was obtained at $f = f^*_{0,c}$ at $V_s = 10$ kV. The resulting core loss resistance value of $R_c = 13.3 \times 10^6\ \Omega$ was used to compute the effective secondary winding resistance value of $R''_s = 4384\ \Omega$. The model input impedance was then calculated using Eq. 4.3 with R''_s in place of R'_s. The test and model results are compared in Figure 4.11.

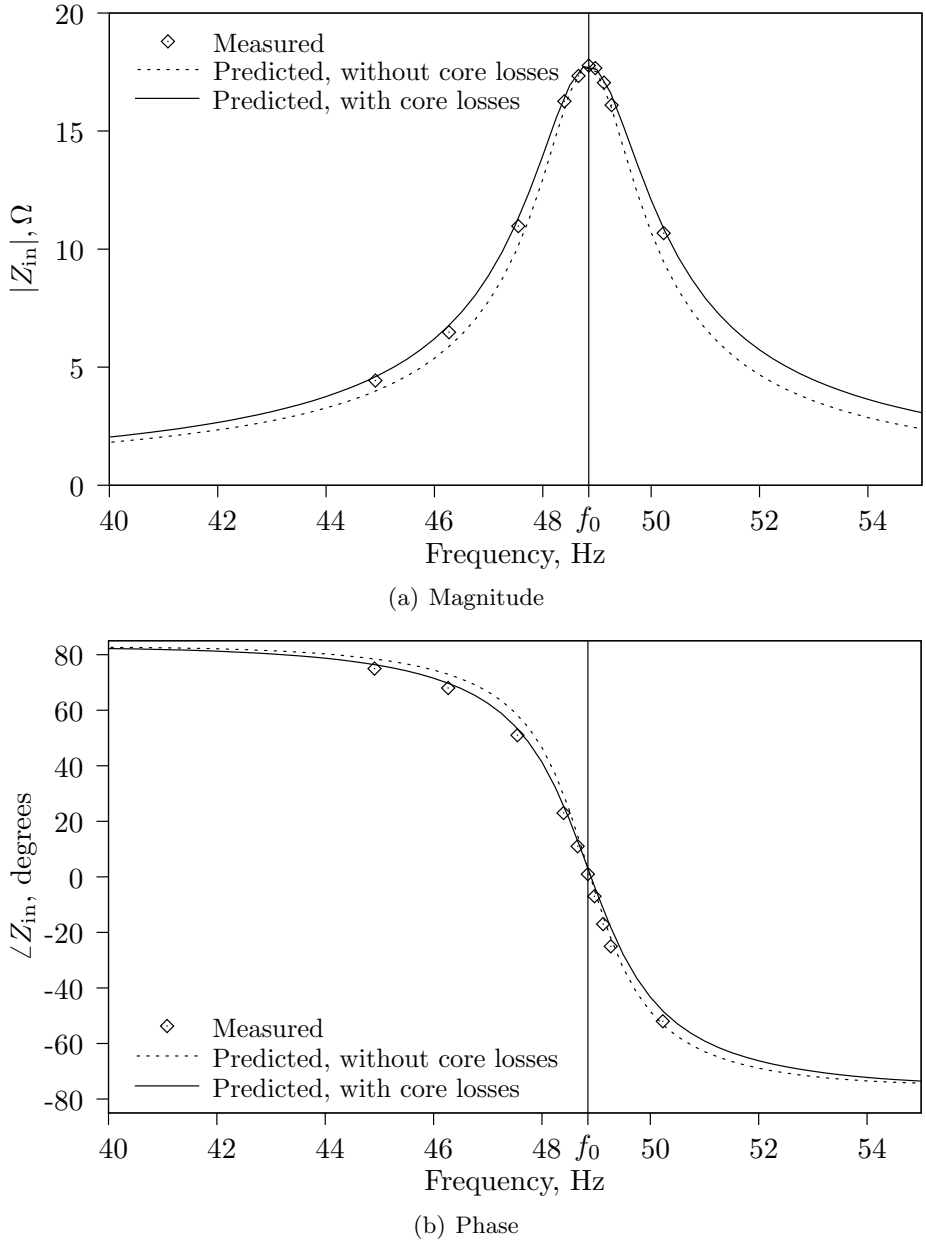

(a) Magnitude

(b) Phase

Figure 4.11 Measured and predicted resonant characteristics of sample PCRTX with 2 * 300 mm cores with a centre-gap of 195mm at $V_s = 10$ kV.

By including the core loss resistance, the equivalent circuit model is again verified over the limited frequency range. The model may not hold for other frequencies since the

core loss resistance is a function of frequency. The difference in resonant frequencies Δf in this configuration has reduced to an immeasurably low value and the coil coupling has increased to 0.92.

4.8.5 Inductance variation characteristics

The resonant tuning test was used to measure the secondary winding self-inductance value of the sample PCRTX in both centre-gap and axial-offset arrangements for several different core displacements. The results are shown in Figure 4.12. Centre-gap tuning provides more variation for the same offset. It is therefore preferred, and also has the advantage of producing no net axial magnetic forces between the core and windings, which was an issue for previous designs.

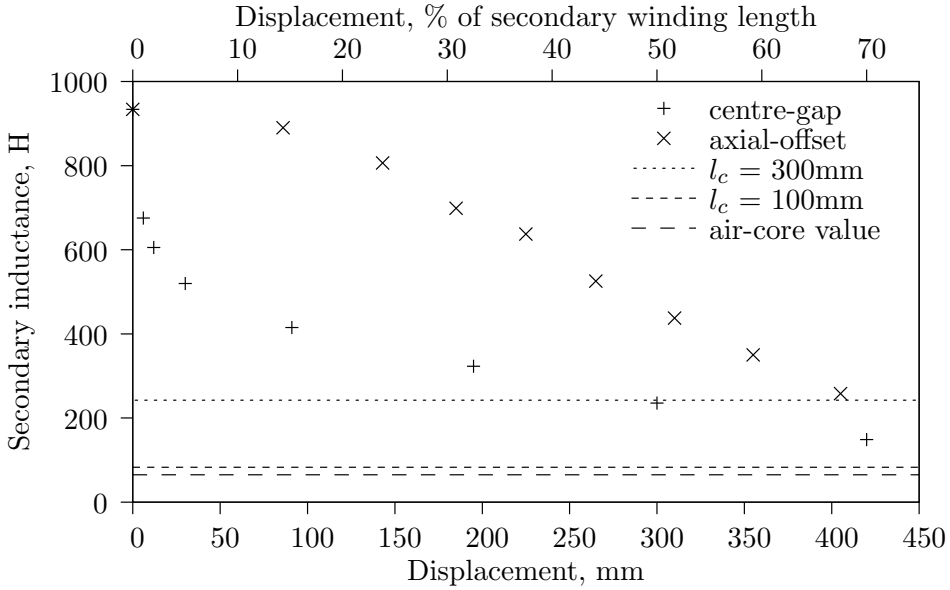

Figure 4.12 Secondary winding self-inductance variation with core displacement characteristics for the sample PCRTX with 2 * 300 mm cores.

4.8.6 Capacitive load test

A capacitive load test was performed on the sample PCRTX in two different configurations. In the first, the two 300 mm core pieces were placed together and offset axially 355 mm from the winding centre. In the second configuration, the two core pieces were centered with respect to the winding and a 195 mm gap was placed in the centre of the core pieces. Both configurations gave approximately the same value of secondary winding self-inductance, as shown in Figure 4.12. The load capacitance value was the same in both cases and was chosen so that the power factor was leading below the saturation voltage. The results are shown in Figure 4.13, where $I_{p,\mathrm{rms}}$ and $I_{p,\mathrm{fund}}$ are the root-mean-squared and fundamental components of primary current.

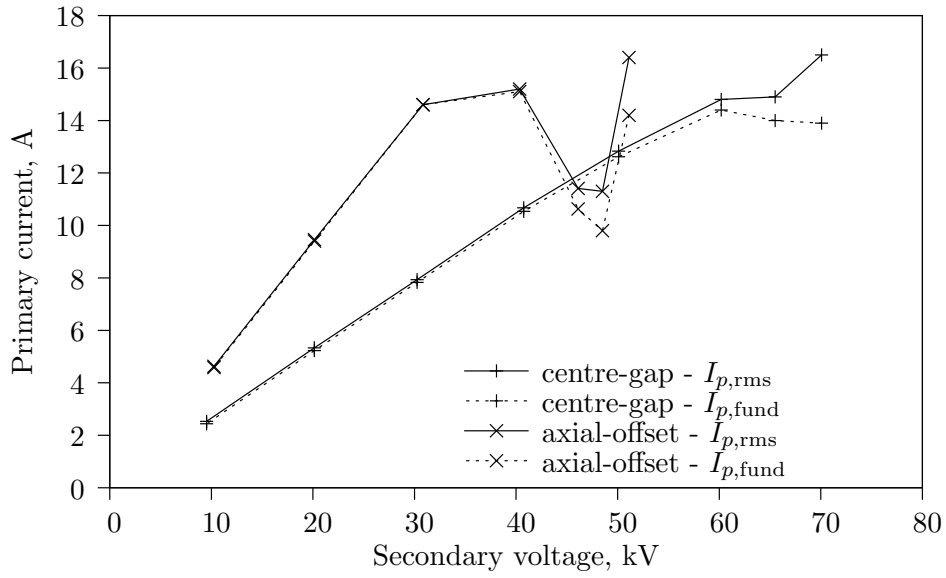

(a) Magnitude

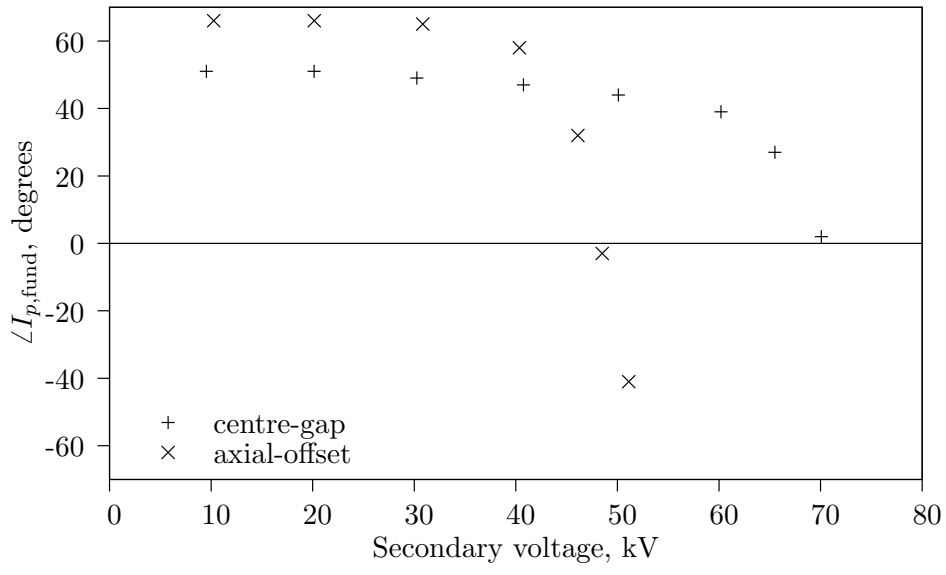

(b) Phase

Figure 4.13 Capacitive load test for the sample PCRTX in two different core configurations with the same value of load capacitance.

The difference in primary currents between the two configurations in the linear region of the graph is due to the 8% difference in the value of secondary winding self-inductance, illustrating the sensitivity of the tuned circuit. Core saturation is first indicated by a small decrease in primary current at higher voltages, followed by a sharp increase in primary current as the voltage is further increased. As the core saturates, the winding inductance values decrease. Because the circuit was initially slightly capacitive-tuned, the decreasing inductance values initially brings the loaded-circuit closer to resonance, increasing circuit impedance. Saturation occured at a significantly higher voltage in the centre-gap configuration, indicating a more uniform flux-density. In both cases, measurable levels of harmonic distortion appear in the primary current waveform as the saturation voltage is reached.

4.9 CONCLUSIONS

An equivalent circuit model for the PCRTX has been developed. The model is mathematically identical to the Steinmetz 'exact' transformer equivalent circuit but the core loss resistance has been moved to the right hand side of the secondary leakage reactance branch. The main advantage of the new model is that the input impedance can be more simply expressed. This allows design specifications to be more easily translated into required values or allowable ranges of values of equivalent circuit components. A method has been presented for measuring the winding self- and mutual-inductances using a variable-frequency sinewave generator and a load capacitance. Secondary winding self-inductance variation with core displacement characteristics have been measured for the sample transformer in the centre-gap and axial-offset arrangements. Centre-gap tuning was found to be the most sensitive method of inductance variation and allowed for operation at a higher voltage before the onset of saturation.

Chapter 5

INDUCTIVE REACTANCE COMPONENT MODEL FOR HIGH-VOLTAGE PARTIAL-CORE RESONANT TRANSFORMERS

5.1 OVERVIEW

A model for the inductive reactance components of an equivalent circuit for high-voltage partial-core resonant transformers is developed. The self- and mutual-inductances of the transformer windings are calculated using a two-dimensional linear magneto-static finite element model. Provisions are made for axial-offset and centre-gap tuning. The model can also predict the secondary voltage at which core saturation occurs under resonant conditions. Its performance was verified against test results of three sample transformers.

5.2 INTRODUCTION

A photograph of one completed PCRTX is shown in Figure 5.1 [Bendre et al., 2007]. The device offers a proven 40 kV rms, 50 Hz voltage rating with at least 286 kVAr of inductive-reactive compensation. The finished weight is approximately 500 kg.

PCRTXs have been designed using the reverse method of transformer design [Bodger and Liew, 2002, Liew and Bodger, 2001]. Supply conditions and the physical characteristics and dimensions of the core and windings are used to produce component values for the Steinmetz 'exact' transformer equivalent circuit of Figure 3.2.

An alternative equivalent circuit for PCRTXs was described in Chapter 4. The model analytically describes resonant characteristics, which gives rise to a technique for measuring the equivalent circuit inductances under resonant operation, and better represents core losses on a physical basis. Ignoring core and proximity losses, the model results are identical to those obtained by numerically solving the Steinmetz 'exact' transformer equivalent circuit. Since core and proximity losses are not critical in short-term rated devices and existing core loss models [Liew and Bodger, 2001] are

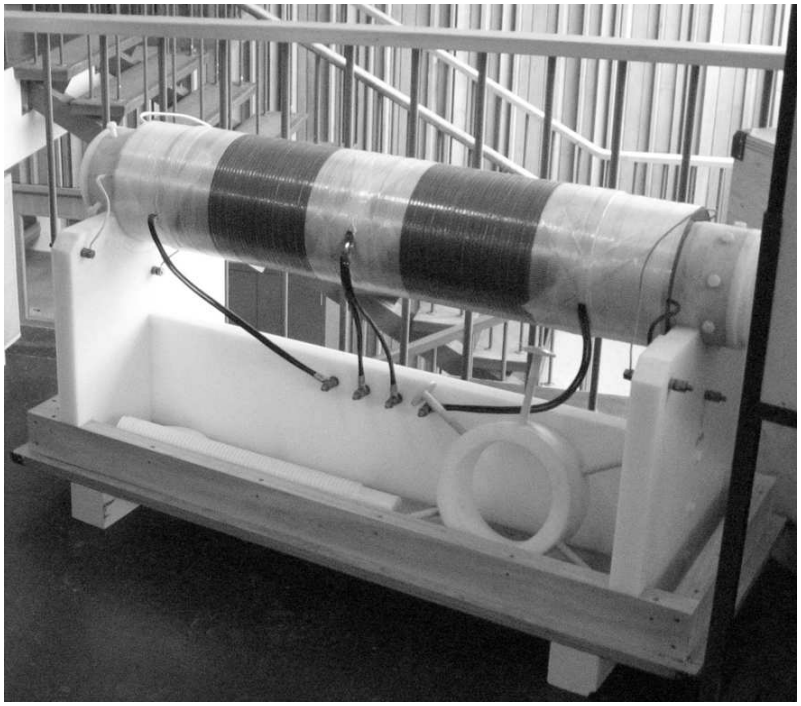

Figure 5.1 A PCRTX designed for high-voltage testing of hydro-generator stators.

now known to be inadequate, the Steinmetz circuit is a suitable model for preliminary analysis and design. The advantage of this model is that it can also be used to calculate performance under open-circuit and short-circuit conditions, and applied to non-resonant transformers.

Models for the inductive reactance components X_{lp}, X_{ls} and X_m of the Steinmetz 'exact' transformer equivalent circuit have been developed for power transformers, where the magnetic circuit is designed to provide efficient transfer of real power and the coil coupling approaches unity. They are based on magnetic circuit theory and contain empirically derived factors. Derived from full-core transformer models, a leakage-based approach is used to analyse the magnetic circuit, where the magnetising reactance and leakage reactance values are calculated separately. With the exception of the number of turns, no consideration is given to the geometry of the primary winding when calculating the magnetising reactance value. The leakage reactance is assumed to be contained entirely in the air and is split equally between the primary and secondary windings.

The magnetic circuit in resonant transformers is designed to provide inductive-reactive compensation as well as voltage transformation. Linear inductances are required, necessitating the use of air-gaps. Consequently the coil coupling is reduced and it becomes possible to analyze the coil in terms of self- and mutual-inductances. This approach is not normally employed in full-core transformers because the individual leakage reactance values are typically only a small fraction of the magnetising reactance value. Thus, any errors in calculating the self- and mutual-inductance values are amplified enormously

when computing the individual leakage reactance values [Edwards, 2005]. The self- and mutual-inductance approach also reflects the way that resonant transformers are designed, where the secondary winding self-inductance value is determined by the load capacitance and the primary winding is designed such that the resulting self- and mutual-inductance values provide the required voltage ratio.

An inductive reactance component model for PCRTXs based on the self- and mutual-inductance approach is required. The model must account for both axial offsets between the core and windings and multiple core-sections with centre-gaps, the two current practices of circuit tuning. It also must calculate the core flux-density with sufficient accuracy to predict the onset of core saturation under resonant conditions.

5.3 NEW INDUCTIVE REACTANCE COMPONENT MODEL

The new inductive reactance component model is based on magneto-static finite element analysis. This does away with the assumption of uniform flux-density and empirically derived factors of the previous model [Liew and Bodger, 2001].

5.3.1 Development of finite element model

A cross-section of a PCRTX is shown in Figure 5.2. The transformer is constructed with layer windings and has a circular core. For clarity only one quarter of the device is shown.

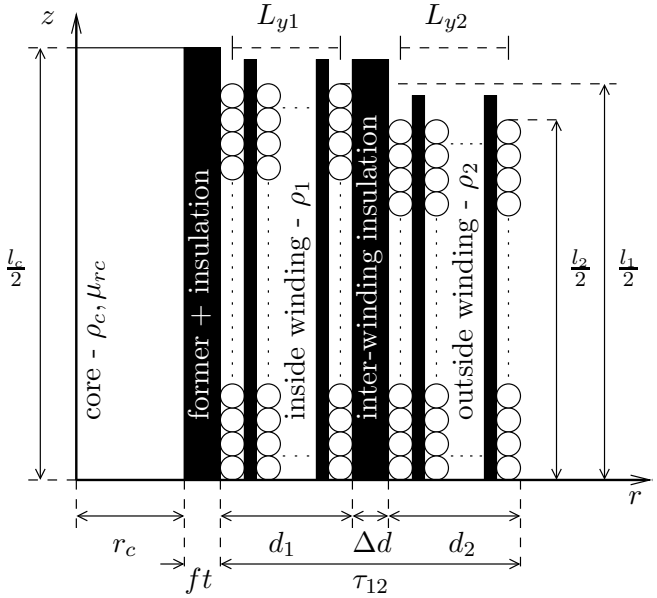

Figure 5.2 Axial view of a partial-core transformer with layer windings, showing component dimensions and material properties.

5.3.1.1 Winding model

As in Section 3.5.2, each winding was modelled as a single block of non-magnetic material encompassing all turns over all layers. The model is thus more suitable for tightly packed windings, where the inter-layer insulation is of smaller thickness than the individual conductors. Winding excitation was with uniform current-density. Any eddy currents induced in the winding wire were assumed to have a negligible effect on the global field distribution.

5.3.1.2 Core model

The magnetic properties of grain-oriented transformer steel are highly non-linear and anisotropic. A typical value of relative permeability in the rolling direction for non-saturated transformer steel is approximately 28,000 [Holland et al., 1992]. This value is greatly reduced for magnetisation in other directions. Within the lamination plane, the lowest value of relative permeability occurs at an angle of 55° between the rolling and transverse directions [Shirkoohi and Arikat, 1994]. The relative permeability in the direction normal to the lamination plane is further reduced because of the inter-laminar insulation and can be less than 100, depending on the stacking factor, insulation thickness and clamping pressure [Pfützner et al., 1994].

The return-path for magnetic flux in a partial-core transformer is air. There are no flux guides to ensure that the air-core boundary is restricted to the core-ends. If the laminations are oriented in the usual parallel way, any flux leaving the core radially along the length of the core is no longer restricted to the lamination plane. Inter-laminar flux, reduced somewhat by the lower relative permeability value, produces large planar eddy currents. In one PCRTX temperature differences of approximately 30°C were measured around the outer perimeter of one end of the partial-core [Bodger and Enright, 2004]. A similar problem can occur in shunt reactors with large air-gaps [Christoffel, 1967]. The solution here, a radially laminated transformer core [Meyerhans, 1956], is investigated in Chapter 9.

Rather than trying to model these three-dimensional non-linear effects, a simple isotropic linear model was employed. Eddy currents induced in the core laminations were assumed to have a negligible effect on the global field distribution.

5.3.1.3 Boundaries

The return path for magnetic flux in a full-core transformer is restricted mostly to the ferromagnetic material of the outer limbs and connecting yokes. The flux-density in the surrounding air drops rapidly to near-zero values. Finite element models of full-core

transformers typically employ closed boundary conditions, where it is necessary to model only a small amount of the surrounding air [Brauer, 1993].

The partial-core transformer is an example of an open-bounded problem. Because the return-path for magnetic flux is air, there is no clear distinction between the problem and exterior domains. Finite element modelling techniques for such problems are reviewed in [Chen and Konrad, 1997].

The simple truncation method was employed, where the outer air-space boundary was located far away from the transformer. A large exterior domain is required for high accuracy in the problem domain, making this one of the most computationally expensive techniques [Bettess, 1988]. A popular technique based on the Kelvin transform [Freeman and Lowther, 1989] could have been employed to improve the computational efficiency. This must be weighed against the extra effort of implementation and the potential time savings. The models presented in this paper are magneto-static and limited to two-dimensions. Typical solving times on a standard desktop PC were in the order of seconds.

5.3.1.4 Constraints

The Dirichlet (flux tangential) constraint was applied along the z-axis boundary to account for model symmetry. As an approximation, the Dirichlet constraint was also applied to the remaining air-space boundaries, effectively constraining all flux to inside the model.

5.3.1.5 Implementation

The transformer design program is briefly described in Section 3.5.1. Further documentation is given in Appendix A. The two-dimensional axi-symmetric model is shown in Figure 5.3 and the model parameters are summarised in Table 5.1. Axial movement of the core was accounted for by introducing a displacement parameter Δ which measures the core offset from the centre position. Provisions were also made for multiple core sections with centre-gaps between them.

The air-space ratios were initially both chosen as 5, using the general rule of thumb given in [Chen and Konrad, 1997], and then increased until any changes in field shape and inductance values between successive increments were negligible.

5.3.2 Maximum frequency of model

The device was modelled with magneto-static analysis, using the low frequency approximation. This is valid for all frequencies for which the following inequality applies to all conductors in the model

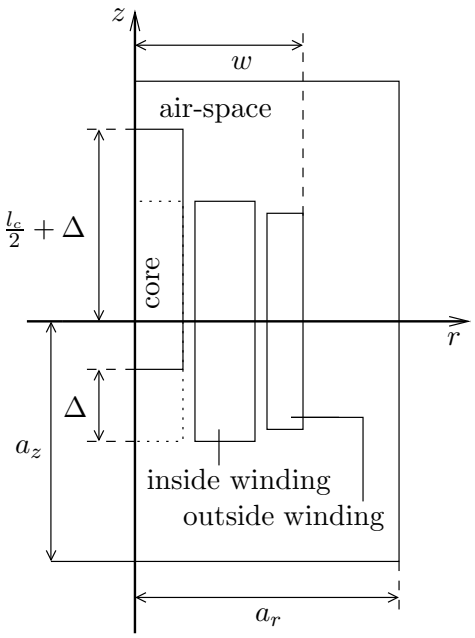

Figure 5.3 Finite element model of PCRTX with circular core utilising axial-offset tuning.

Solving Options	
Method	Newton-Raphson
Polynomial order	3
Max. Newton iterations	20
Newton tolerance	0.5%
CG tolerance	0.01%
Adaptation Options	
Type	h-adaptation
% of elements to refine	40
Tolerance	0.5%
Max. steps	10
Air-space Ratios	
a_r/w	15
$a_z/$ max $(\frac{l_c}{2} + \Delta, \frac{l_1}{2}, \frac{l_2}{2})$	8

Table 5.1 Summary of finite element model parameters.

$$d < x\delta \tag{5.1}$$

where x is 1.6 or 2.0 depending on the author [Van den Bossche et al., 2006, Sullivan, 2001], d is the conductor thickness and δ is the skin depth, calculated as

$$\delta = \sqrt{\frac{2\rho}{\mu_0 \mu_{\mathrm{rc}} \omega}} \tag{5.2}$$

where ρ is the material resistivity, $\mu_0 = 4\pi \times 10^{-7}$ H/m is the permeability of free space, μ_{rc} is the relative permeability, $\omega = 2\pi f$ and f is the supply frequency.

The model upper-frequency f_m for each conductor can be calculated by substituting Eq. 5.2 into Eq. 5.1, equating Eq. 5.1 and then solving for ω (and hence f). This is given by

$$f_m = \frac{\rho x^2}{\pi \mu_0 \mu_{\mathrm{rc}} d^2} \tag{5.3}$$

5.3.3 Obtaining reactance parameters

The method of calculating the inductive reactance components X_m, X_{lp} and X_{ls} from the finite element model is described in Section 3.5.3.

5.3.4 Calculating the onset of core saturation

PCRTXs are designed with linear inductances. The air return-path for the magnetic flux ensures that, provided the transformer steel remains non-saturated, variations in the relative permeability value of the transformer steel over the magnetisation cycle have a minimal effect on the inductance values.

For the magneto-static case, the magnetic field in any transformer is a function of the instantaneous values of both the primary and secondary ampere-turns. Under resonant conditions however, the magnetic field is mainly due to the secondary ampere-turns, particularly for a circuit quality factor Q > 10.

An estimate of the secondary voltage at the onset of core saturation can be obtained using

$$V_{s,\mathrm{sat}}^{\mathrm{model}} = \frac{B_{\mathrm{sat}}}{\sqrt{2}\alpha_u} V_{s,u} \tag{5.4}$$

where B_{sat} is the saturation peak flux-density of the transformer steel and α_u is the calculated maximum core flux-density at a secondary voltage of $V_{s,u}$, typically set to 1

Transformer	PC1	PC2	PC3
Ratings			
Primary voltage, V	230	400	230
Secondary voltage, kV	30	30	80
Operating frequency, Hz	50	50	50
Core			
Length, mm	715	1200	600
Diameter, mm	125	175	75
Lamination thickness, mm	0.50	0.50	0.23
Peak flux-density[a], T	1.4	1.3	1.5
Inside (hv) winding			
Length, mm	735	920	700
Number of layers	13	9	37
Leadouts on layers[b]	1,2,4,5,13	1,3,6,7,8,9	1,37
Number of turns	8,840	4,518	59,200
Maximum current[c], A	3.9	12.7	0.55
Outside (lv) winding			
Length, mm	680	875	600
Number of layers	1	1	2
Number of turns	65	62	160
Maximum current[c], A	125	233	126
Aspect ratio[d]	27	34	13

[a]Calculated using the 'transformer equation' (Eq. 3.11) at the indicated primary voltage.
[b]Layers numbered from the inside.
[c]At a (short-time-rated) current-density of 5 A/mm^2.
[d]As defined by Eq. 5.5.

Table 5.2 As-built specifications of sample PCRTXs.

volt, obtained from the finite element model by exciting the secondary winding with $V_{s,u}N_2/2\pi f L_s$ ampere-turns.

5.4 EXPERIMENTAL RESULTS

5.4.1 Transformer specifications

The model performance was verified against test results of three sample PCRTXs. PC1 and PC2 were designed as high-voltage test transformers [Bodger and Enright, 2004, Enright and Bodger, 2004] while PC3 was designed to energise arc-signs [Bell et al., 2007, Lynch et al., 2007]. The specifications are shown in Table 5.2. PC1 and PC2 were tested using the maximum tap on the high-voltage winding. The core in PC3 was designed in two 300 mm axial lengths, to allow for both axial-offset and centre-gap tuning.

5.4.2 Model-value core relative permeability

The finite element model was used to calculate the effect of core relative permeability on the winding inductance values of the sample PCRTXs. The results are shown in Figure 5.4. The inductances are expressed as a percentage of their value at a relative permeability of 10^5. The inductance values saturate as the relative permeability approaches 10^4. They are limited by the reluctance of the air return-path.

The ratios of partial-core inductance to air-core inductance ($L_{\mu_{\rm rc}=10^4}/L_{\mu_{\rm rc}=1}$) differ for each transformer but appear to be positively correlated with the transformer aspect ratio, defined as

$$\beta = \frac{l_1 + l_2}{2\tau_{12}} \tag{5.5}$$

where τ_{12} is the winding thickness factor, as defined in Figure 5.2.

For the sample PCRTXs the ratios $\frac{L_{p,\mu_{\rm rc}=10^4}}{L_{p,\mu_{\rm rc}=1}}$ were less than the ratios $\frac{L_{s,\mu_{\rm rc}=10^4}}{L_{s,\mu_{\rm rc}=1}}$, indicating that the primary winding self-inductance value is less influenced by the core. This can be attributed to the fact that the primary winding is wound over the secondary and is thus further away from the core.

The isotropic relative permeability value was chosen as 3000, a compromise between the expected relative permeability values in the rolling, traverse and inter-laminar directions. Using this value, the maximum difference in inductance from the $\mu_{\rm rc} = 10^4$ value for the sample PCRTXs was less than 1%.

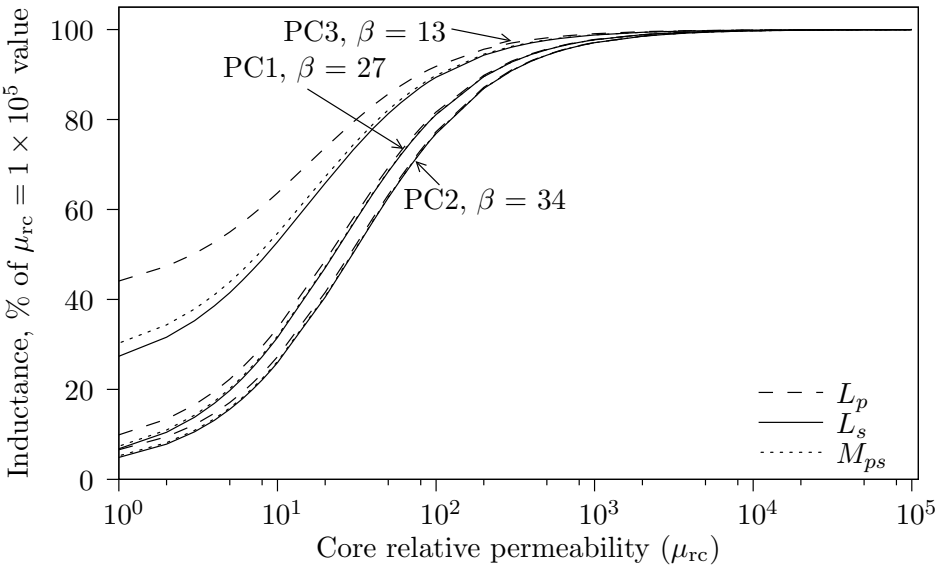

Figure 5.4 Variation of inductance with core relative permeability.

Property	Value		
	Core	HV winding	LV winding
μ_{rc}	3000	1	1
$\rho_{20^\circ\text{C}}$, $\Omega.m$	1.80×10^{-7}	1.76×10^{-8}	2.76×10^{-8}
$\Delta\rho$, /°C	6.0×10^{-3}	3.9×10^{-3}	4.3×10^{-3}
T, °C	50	50	50

Table 5.3 Material constants.

5.4.3 Maximum frequency of model

The maximum frequency of the magneto-static finite element model was calculated using Eq. 5.3 with $x = 2.0$ for each of the sample PCRTXs. Standard physical values of material permeabilities, resistivities and thermal resistivity coefficients were used for the core steel, aluminium primary windings and copper secondary windings, as shown in Table 5.3.

The results, shown in Table 5.4, indicate that the core upper-frequency of 287 Hz was the limiting frequency for all of the sample PCRTXs. The exact value is determined by the core relative permeability, a non-linear anisotropic quantity. However, for the assumed (isotropic) relative permeability value of 3000, the upper-frequency limit was significantly above the supply (and resonant) frequency of 50 Hz. The exact value is unimportant when operating from undistorted supplies. It could be measured experimentally by finding the frequency at which the inductance values start to decrease.

Voltage total harmonic distortion levels of up to 2.1% have been measured at the local supply of one power station in New Zealand. Energisation under these conditions can result in third and fifth harmonic components of primary current which exceed the fundamental, significantly increasing the rms supply current. This may cause a fuse or circuit breaker to operate, which would not have operated if the same circuit was energised from an undistorted supply. The model upper-frequency would be required to analyse this situation. For PCRTXs with very high turns ratios, it may also be necessary to model the capacitive effects of insulation [Liew and Bodger, 2002], which have been ignored in this chapter.

5.4.4 Coil coupling and reactance calculations

The finite element model was used to calculate the inductive reactance component values and coil coupling for the sample PCRTXs. The results are shown in Table 5.5. For the sample PCRTXs, the self- and mutual-inductance and energy methods both calculated almost the same value of primary-referred leakage reactance, confirming that the PCRTX can be analysed in terms of self- and mutual-inductances. The coil coupling

Conductor	Upper-frequency, Hz		
	PC1	PC2	PC3
Core	287	287	287
Primary[a]	5,050 / 316	2,510 / 327	2,510 / 626
Secondary	20,000	6,147	13,800
Overall	287	287	287

[a]Radial direction / axial direction.

Table 5.4 Calculated upper frequency of magneto-static finite element model.

Parameter	PC1	PC2	PC3
$1/a$	136.0	72.9	370.0
X_m	0.6126	1.1007	2.1082
X_{lp}	0.0377	0.0238	0.3627
a^2X_{ls}	-0.0225	-0.0108	-0.1938
$X_{lp} + a^2X_{ls}{}^a$	0.0152	0.0129	0.1689
$X_{lp} + a^2X_{ls}{}^b$	0.0154	0.0129	0.1689
k	0.9889	0.9943	0.9693

[a]Self- and mutual-inductance technique.
[b]Energy technique.

Table 5.5 Calculated reactance and coil coupling values.

values were calculated at almost unity, but will reduce as axial-offsets or centre-gaps are introduced.

The calculated value of secondary leakage reactance was negative for each of the sample PCRTXs. This was because $P_{22} < P_{12}$ in these examples. Negative leakage reactance may be a characteristic of the partial-core magnetic topology, but can also occur in full-core transformers if one winding is much longer than the other [Margueron and Keradec, 2007]. Only P_{11} or P_{22} can be less than P_{12}, since the inequality $k = \frac{P_{12}}{\sqrt{P_{11}P_{22}}} < 1$ must still remain. It is possible to form an alternative T-equivalent circuit where both leakage reactance values remain positive even if $P_{22} < P_{12}$ or $P_{11} < P_{12}$ [Margueron and Keradec, 2007]. This may be useful for some simulation packages, where negative leakage reactance values can cause numerical instability. Accordingly, the turns ratio of the ideal transformer in this T-equivalent circuit will differ from the actual turns ratio of $a : 1$.

5.4.5 Inductance variation characteristics

The secondary winding self-inductance values of the sample PCRTXs were measured using the resonant tuning test of Section 4.5. The inductances were measured for several different axial-offsets for PC1 and PC2. For PC3, the winding inductances were

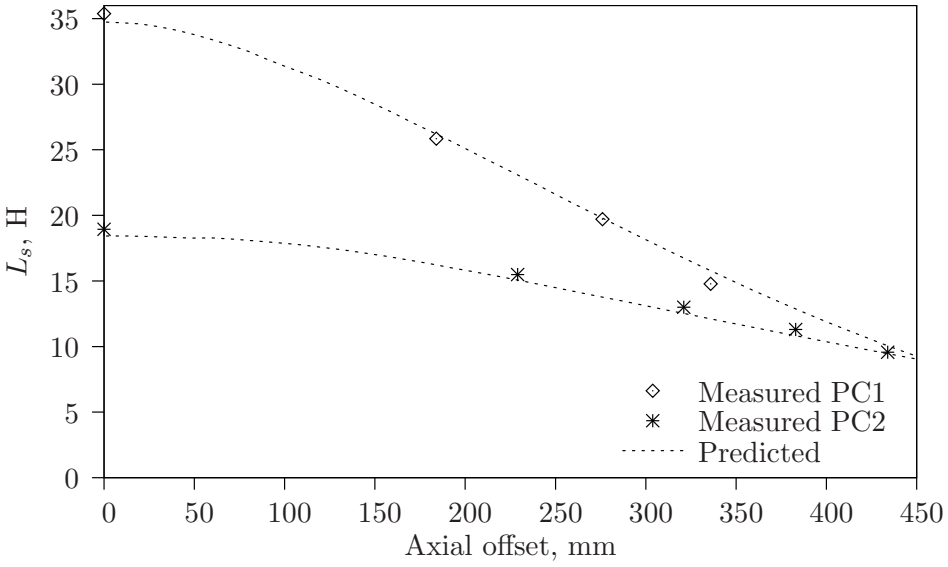

(a) PC1 & PC2

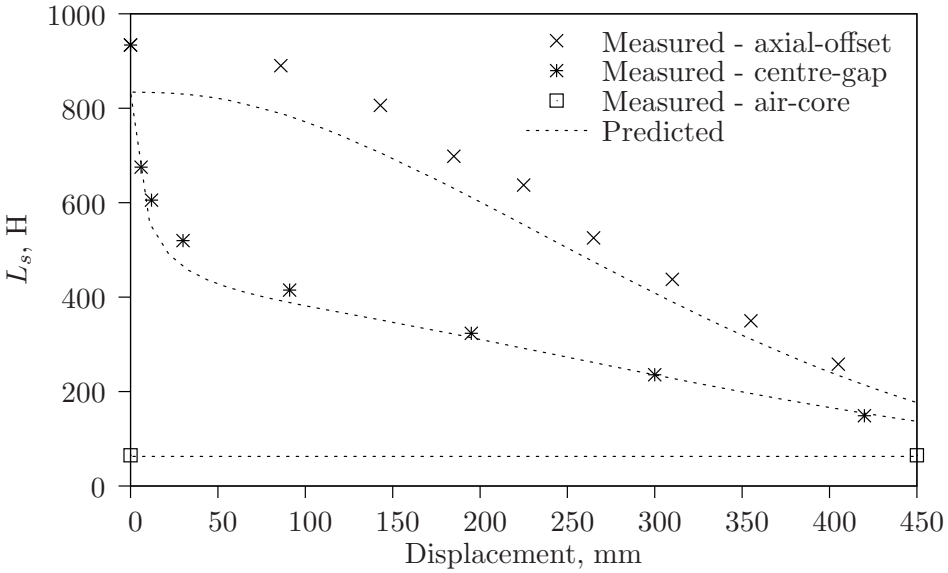

(b) PC3

Figure 5.5 Measured and predicted secondary winding self-inductance variation characteristics.

measured in both axial-offset and centre-gap arrangements. The inductance variation characteristics are shown in Fig 5.5.

The finite element model accurately calculated the secondary winding self-inductance values of PC1 and PC2. It was less accurate at calculating the inductance values of PC3, where the maximum difference between test and model results was 12%. The error may be due to differences between the design and as-built data, or approximations in the finite element model. The secondary winding self-inductance of PC3 was also measured in the air-core configuration, where there was an excellent correlation between

test and models results. Primary winding self-inductance and mutual inductance values were also measured for the sample PCRTXs in some configurations. The results are not shown here, but a similar level of accuracy as the secondary winding self-inductances was obtained.

5.4.6 Core saturation characteristics

Capacitive load tests were performed on the sample PCRTXs for several different values of load capacitance to determine the secondary voltage at which the onset of core saturation occurred. All three PCRTXs were slightly off-tuned to the load capacitance so that the supply factor was leading at lower voltages. Some sample test results are shown in Figures 5.6 & 5.7.

Figure 5.6 shows test results for PC1 and PC2 using axial-offset tuning. Figure 5.7 shows test results for PC3 in axial-offset and centre-gap arrangements, both having the same value of load capacitance. In both PC1 and PC3 the primary current components $I_{p,\mathrm{rms}}$ and $I_{p,\mathrm{fund}}$ are almost the same value but for PC2 $I_{p,\mathrm{fund}}$ is lower than $I_{p,\mathrm{rms}}$. The harmonic currents are due to harmonic voltages in the mains supply. The voltage harmonic components are small but the current harmonic components are much larger because the impedance of the resonant circuit is greatly reduced at harmonic frequencies.

The secondary voltages at the onset of core saturation for PC1 and PC2 were determined visually from the magnitude and phase plots of Figure 5.6 as 22.2 kV and 25.7 kV, respectively. For PC3 the saturation voltages for the axial-offset and centre-gap arrangements were 30.8 kV and 65.5 kV, respectively, as determined from Figure 5.7. The difference between the secondary winding self-inductance values for the two arrangements of PC3 was 8% (see Figure 5.5(b)) but more than twice the secondary voltage was obtained before the onset of core saturation in the centre-gap arrangement.

Core saturation in PC3 is first indicated by a small decrease in primary current at higher voltages, followed by a sharp increase in primary current as the voltage is further increased. As the core saturates, the winding inductance values decrease. Because the circuit was initially slightly capacitive-tuned, the decreasing inductance values initially brings the loaded-circuit closer to resonance, increasing circuit impedance. The same phenomenon is not observed for PC1 and PC2, owing to higher circuit quality factors and a lack of measurements near the zero phase point. The phase response of PC3 most closely matches the ideal characteristic of linear phase up to the saturation voltage. The lower aspect and $L_{\mu_{\mathrm{rc}}=10^4}/L_{\mu_{\mathrm{rc}}=1}$ ratios of PC3 make it less sensitive to the inherent non-linear characteristics of the core steel, which occur in the unsaturated region of the B-H curve.

The finite element model was used to predict the peak core flux-density at the measured secondary voltage where the onset of core saturation occurred. The model secondary

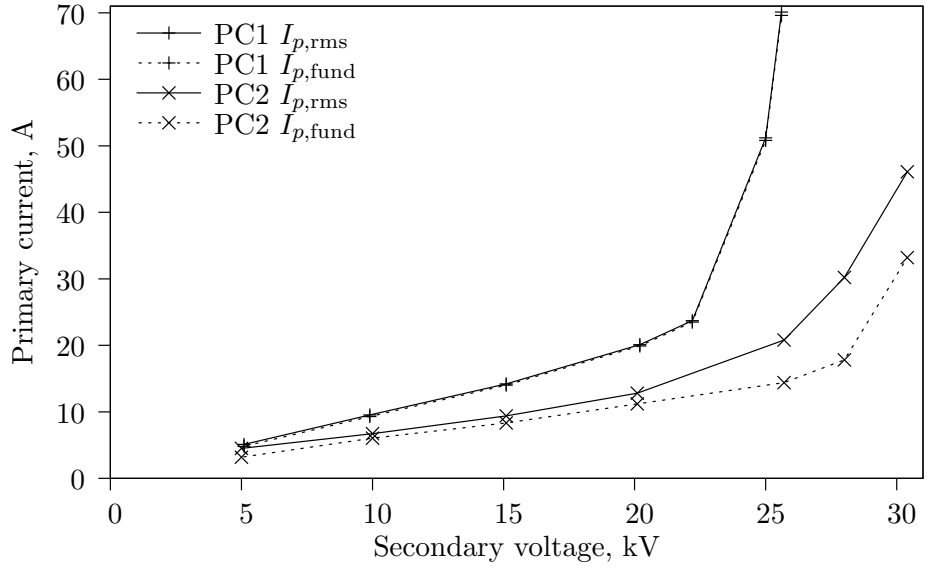

(a) Magnitude

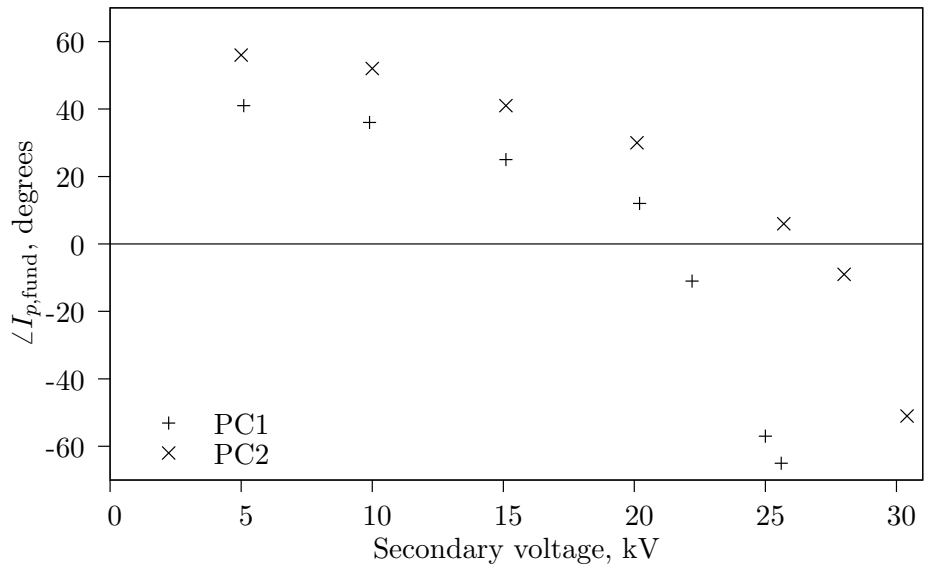

(b) Phase

Figure 5.6 Sample capacitive load test results for PC1 (axial-offset = 336 mm, C = 664 nF) and PC2 (axial-offset = 434 mm, C = 1.07 uF).

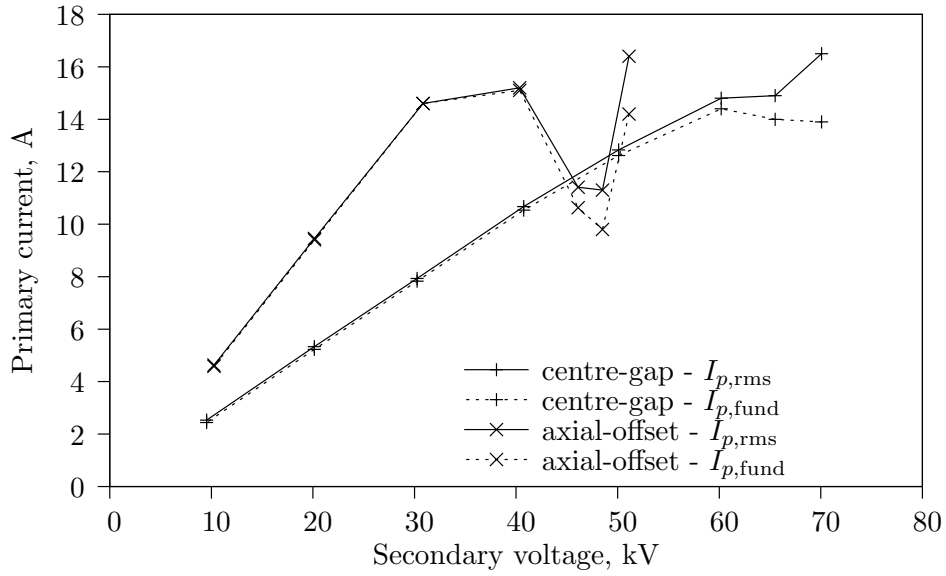

(a) Magnitude

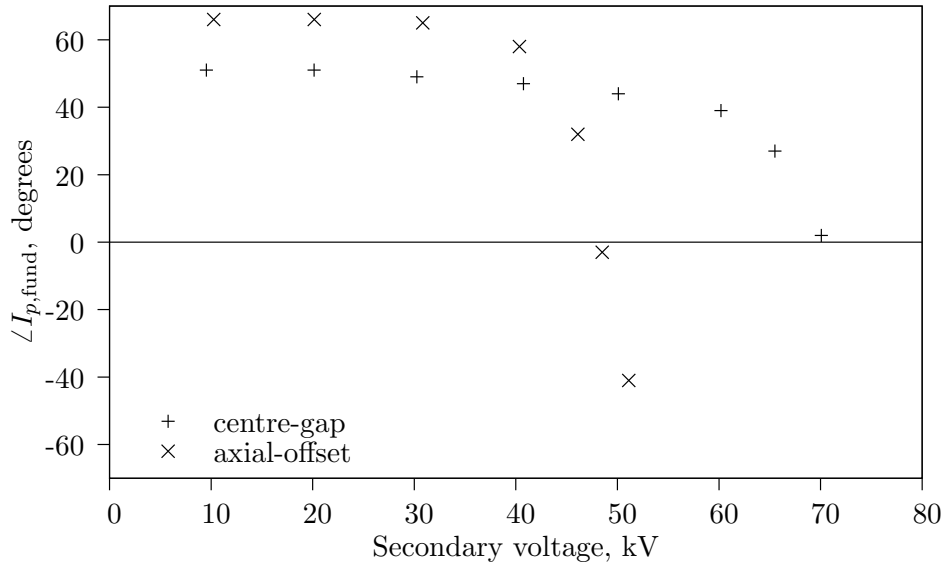

(b) Phase

Figure 5.7 Sample capacitive load test results for PC3 (axial-offset = 355 mm and centre-gap = 195 mm, C = 33.0 nF).

	PC1	PC2	PC3[a]
$V_{s,\mathrm{sat}}^{\mathrm{model}}$, kV	20.7	25.0	63.0 / 38.8
$V_{s,\mathrm{sat}}^{\mathrm{meas}}$, kV	22.2	25.7	65.5 / 30.8
$V_{s,\mathrm{sat}}^{\mathrm{model}}/V_{2,\mathrm{sat}}^{\mathrm{meas}}$	0.93	0.97	0.97 / 1.26

[a]Centre-gap / axial-offset.

Table 5.6 Measured and predicted core saturation voltages.

winding was excited with the measured ampere-turns. The ratios of secondary to primary ampere-turns for the PCRTXs over all test voltages was between 8.1 and 39.0. The contribution of the primary winding ampere-turns to the model core flux-density was thus negligible and was ignored. The flux plots are shown in Figures 5.8 & 5.9.

In all cases the peak flux-density was calculated at around 1.75-1.80 T, a typical value of core saturation flux-density for transformer steel. For PC3, a more uniform flux-density was obtained in the centre-gap arrangement, which explains why a higher voltage was obtained at the onset of core saturation.

To further investigate the finite element model as a tool for predicting the onset of core saturation Eq. 5.4 was applied to the sample PCRTXs in the same configurations using $B_{\mathrm{sat}} = 1.7$ T. In this case, the model value ampere-turns was determined from the calculated inductance value rather than the measured secondary current. The differences in ampere-turns will be small provided that the PCRTXs are tuned to the load capacitance. The test and model results are shown in Table 5.6.

Table 5.6 shows that the finite element model has predicted the onset of core saturation with a reasonable level of accuracy. The difference between test and model results may be even smaller than implied by Table 5.6, due to the difficulty in determining the exact value of $V_{s,\mathrm{sat}}^{\mathrm{meas}}$ from the limited resolution of the experimental data.

5.5 CONCLUSIONS

A model for the inductive reactance components of an equivalent circuit for high-voltage partial-core resonant transformers has been developed. It was based on two-dimensional linear magneto-static finite element analysis. Provisions were made for axial-offset and centre-gap tuning. The model was also used to predict the onset of core saturation. The model could be used for design as well as analysis because the solving time is in the order of seconds on a standard desktop PC. More advanced models, which take into account the three-dimensional effects of the laminated core, are required to calculate planar eddy current losses.

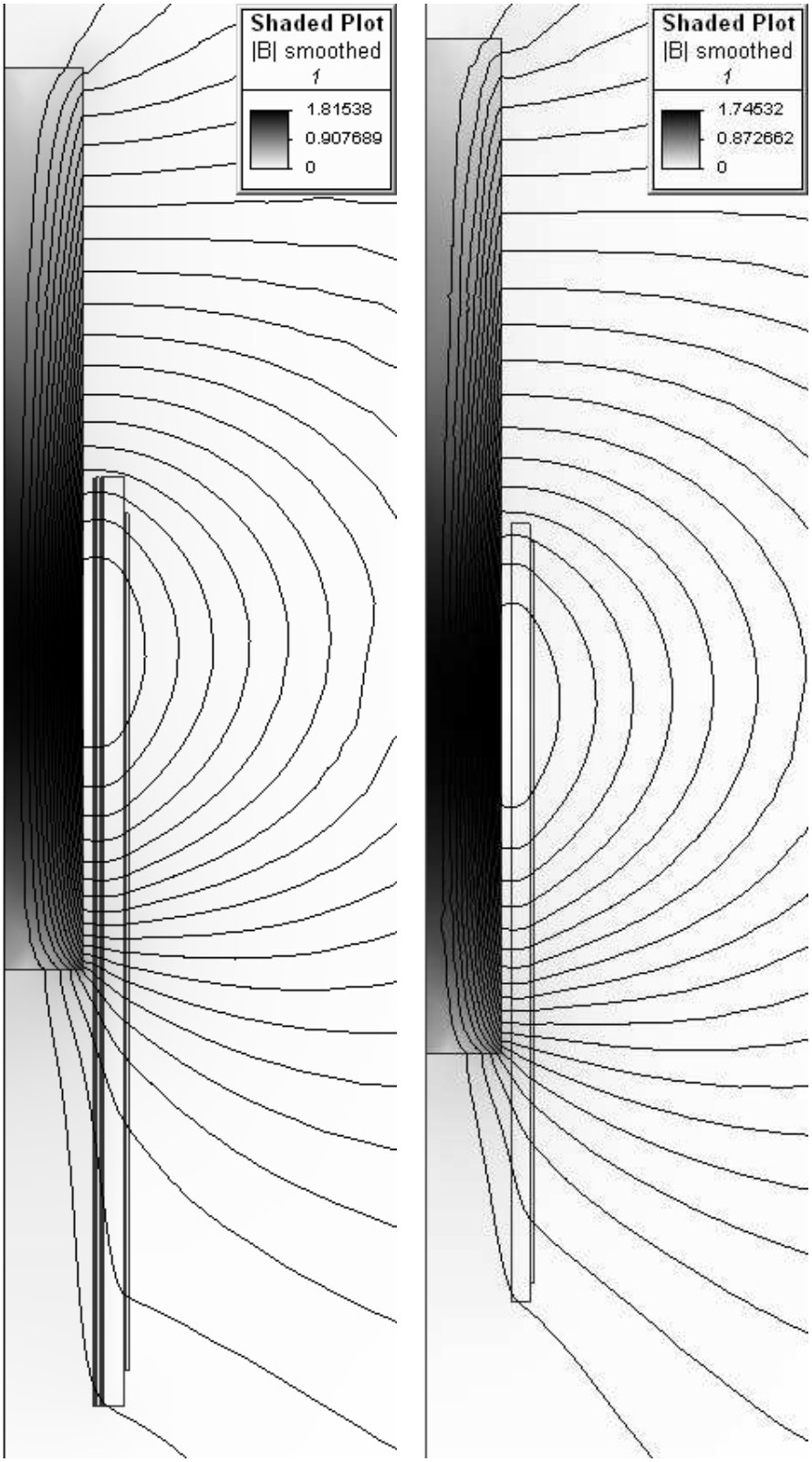

(a) PC1, axial-offset = 336 mm, V_s = 22.2 kV.

(b) PC2, axial-offset = 434 mm, V_s = 25.7 kV.

Figure 5.8 Magnetic field plots of PC1 and PC2 at the onset of measured core saturation.

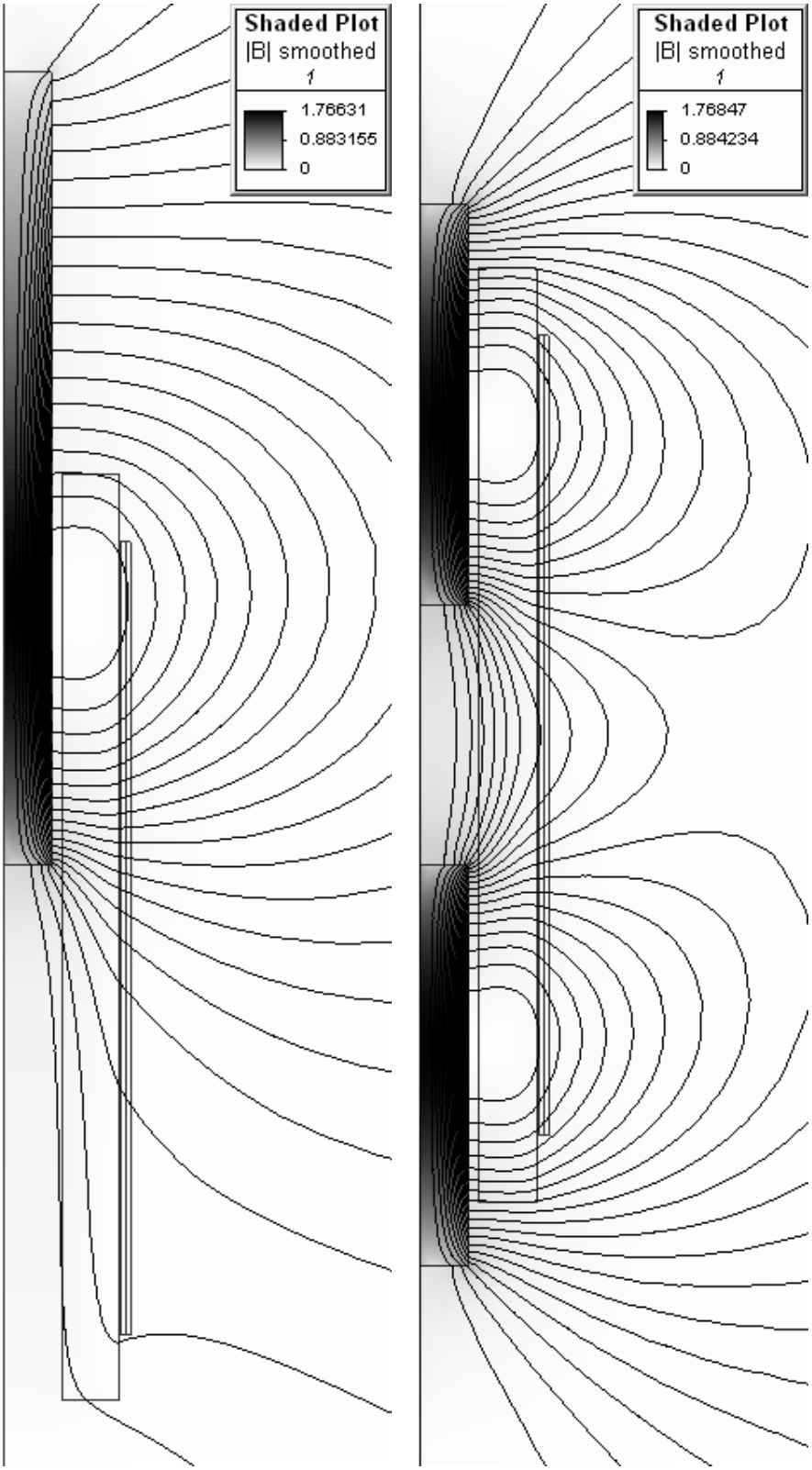

(a) Axial-offset = 355 mm, $V_s = 30.8$ kV. (b) Centre-gap = 195 mm, $V_s = 65.5$ kV.

Figure 5.9 Magnetic field plot of PC3 at the onset of measured core saturation.

Chapter 6

NEW DESIGN OF HIGH-VOLTAGE PARTIAL-CORE RESONANT TRANSFORMER

6.1 OVERVIEW

A new design of high-voltage partial-core resonant transformer is described. A framework of analysis tools is developed for the new design, which has multiple core and winding sections and employs centre-gap tuning. A previously developed finite element model is extended. An approximate formula for the loaded-circuit input impedance, which can be used at the design stage, is derived from an analytical formula. This is used to calculate the maximum allowable secondary winding resistance for a given set of load and supply characteristics. A thermal upper-limit of current-density for the secondary winding is calculated from the device on-time. Optimal winding shape with regard to obtaining maximum inductance per metre of wire is discussed. Consideration is given to the design of the insulation system and minimum clearances in air between winding leadouts. Weight and cost calculations are presented in programmable form.

6.2 NEW PCRTX DESIGN

A PCRTX of new design is depicted in Figure 6.1. The winding layout, method of induction variation and the resulting magnetic field variation characteristic are described in this section.

6.2.1 Winding layout

PCRTXs are constructed with layer windings. The first layer of the high-voltage winding is wound directly on the former. Insulation is placed between subsequent layers. Wave wiring is employed, meaning that wire joins are only required when a wire spool runs out, rather than after each layer [Blachie et al., 1994]. The completed high-voltage winding is encapsulated and the low-voltage winding is wound over this, further shielding the electric field of the high-voltage winding from ground [Bodger and Enright, 2004].

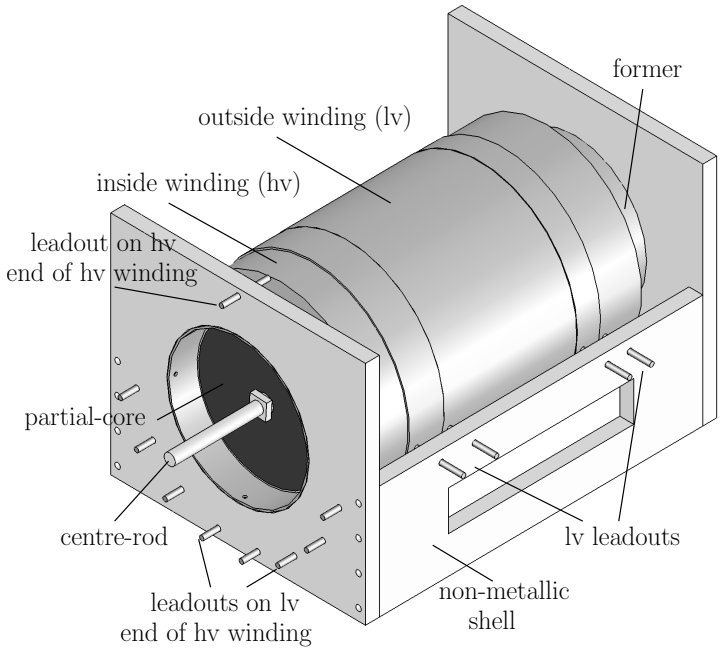

Figure 6.1 Isometric view of a PCRTX of new design, showing core and revised winding layout.

The winding layout is the opposite of a conventional full-core step-up transformer. One advantage is that the high-voltage winding, comprising most of the total winding weight, can be designed directly from the load specifications and supply restrictions without having to first estimate the space occupied by the low-voltage winding. The low-voltage winding can then be designed around the high-voltage winding to achieve the required step-up ratio.

The existing PCRTX design utilises axial-offset tuning. This can produce large axial forces between the core and windings. In one field test, a second PCRTX, connected as a high-voltage inductor, was employed to reduce the core offset and axial forces of the first PCRTX, which were otherwise estimated to be too large at the test voltage [Bendre et al., 2007]. Centre-gap tuning is the preferred method of tuning because there are no net axial forces between the core and windings. It also provides a greater inductance range for the same core displacement.

The inductance range of the high-voltage winding can be further increased by adding a tapping section. Accurate finite element models allow for designs with graded wire sizes, where the design-value current-density is maintained over the tapping section. The number of layers in the tapping section is limited by leadout clearances in air and operational complexity.

In the existing PCRTX design, the tapping section is placed on the high-voltage end of the high-voltage winding. The layers of the tapping section were connected in series, meaning that induced voltage in the unused layers of the tapping section would build-up. Higher-than-rated voltage would occur on some taps when using an other-than-maximum

tap.

The new PCRTX design has the tapping sections placed on the low-voltage end of the high-voltage winding. Leadouts are required at both ends of all the layers in the tapping section. One end of each layer is earthed to stop voltage build-up. Fabrication becomes easier because the main winding section is unaffected by build-up from the leadouts on the tapping section. The winding layout and tuning method of new PCRTX designs is shown in Figure 6.2.

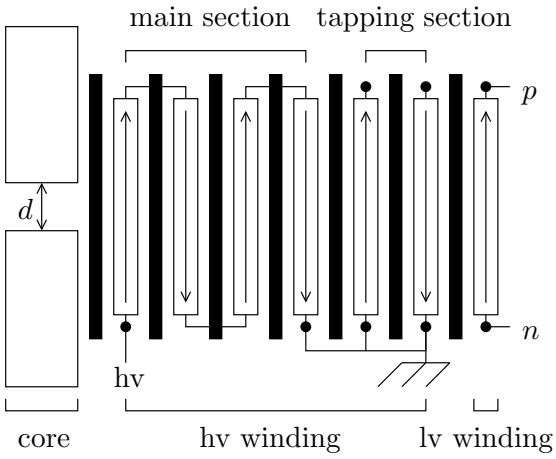

Figure 6.2 Winding layout and tuning method for the new PCRTX design. In this example the secondary winding is formed using just the main winding section of the high-voltage winding and the tapping winding sections are earthed at one end. (↑↓ = winding direction, • = winding leadout)

6.2.2 Inductance variation

Inductance variation in the main winding section of the high-voltage winding is achieved via centre-gap displacement. The maximum secondary winding self-inductance value $L_{s(\mathrm{WS1,max})}$ occurs when the centre-gap d is set to zero. The minimum inductance value $L_{s(\mathrm{WS1,min})}$ approaches the air-core value $L_{s(\mathrm{WS1,ac})}$ as d becomes large.

As shown in Section 5.4.2, the ratio $L_{s(\mathrm{WS1,max})}/L_{s(\mathrm{WS1,min})}$ is positively correlated with the winding aspect ratio. Designs with higher aspect ratios require fewer layers to achieve the same target inductance. The maximum ratio $L_{s(\mathrm{WS1})}/L_{s(\mathrm{WS1,min})}$ is therefore limited by the voltage rating of the inter-layer insulation.

Inductance variation in the tapping section is achieved via suitable tap selection and centre-gap displacements. The displacements are much smaller than those used for the main winding section. The inductance increase for each additional layer in the tapping section is higher for designs with a smaller number of layers in the main winding section. Thus, regardless of whether tapping sections are used, more inductance variation is achieved in designs with a higher aspect ratio. However, higher aspect ratios also increase the sensitivity of the PCRTX to the inherent non-linear characteristics of the

core steel, which occur over the unsaturated region of the BH curve. The effect is a more pronounced departure from the response of an ideally tuned circuit, where the power factor is maintained at unity for all voltages up to the saturation voltage.

The inductance range for a sample PCRTX of new design whose high-voltage winding is comprised of 8 winding sections is shown in Figure 6.3.

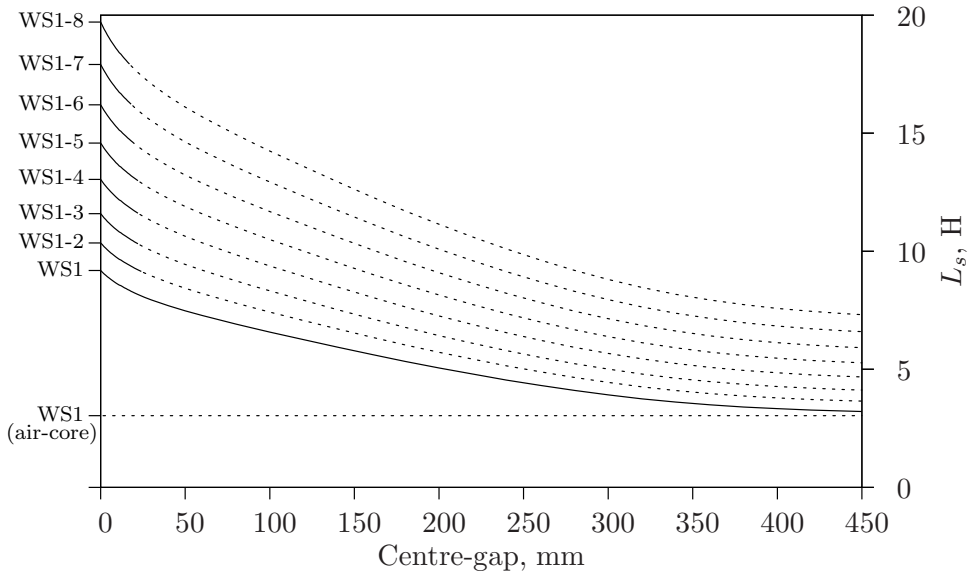

Figure 6.3 Calculated inductance variation characteristics of a sample PCRTX of new design.

The inductance set-point at voltage V_s for the design-value current-density of the main winding section $WS1$ may be chosen as either $L_{s(\mathrm{WS1,max})}$ or $L_{s(\mathrm{WS1,min})}$. If the first set-point is chosen, the maximum operating voltage at smaller inductance values must be reduced so as to maintain the design-value current-density. The inductance set-point for the design-value current-density of the n^{th} tapping winding section, having inductance $L_{s(\mathrm{WS1\text{-}n+1})}$, is $L_{s(\mathrm{WS1\text{-}n,\ max})}$. The operating voltage must be reduced if $L_{s(\mathrm{WS1\text{-}n+1})}$ is set below $L_{s(\mathrm{WS1\text{-}n,\ max})}$ (this region is indicated with dashed lines in Figure 6.3).

6.2.3 Magnetic field variation

Both the core flux-density and winding inductance values are a function of the centre-gap between the partial-cores. If the device is rated at a constant secondary voltage for all values of inductance then, to avoid the possibility of core saturation when operating with large centre-gaps, it is necessary to evaluate the variation of peak flux-density with centre-gap. It is assumed that for all centre-gap values, the load capacitance value is chosen such that resonance with the secondary winding self-inductance is maintained. Under these conditions, the contribution of the primary winding ampere-turns to the overall core flux-density can be neglected, particularly for a circuit quality factor $\mathrm{Q} > 10$.

Flux-density and secondary winding ampere-turns variation characteristics were calculated for PC3 of Chapter 5. Although a linear model was employed, the results should still be accurate provided that the peak flux-density remains below the saturation flux-density of the steel for all centre-gap values. The same model has already proved successful at predicting the secondary voltage at which core saturation occurs. A normalised plot showing the variation characteristics is shown in Figure 6.4.

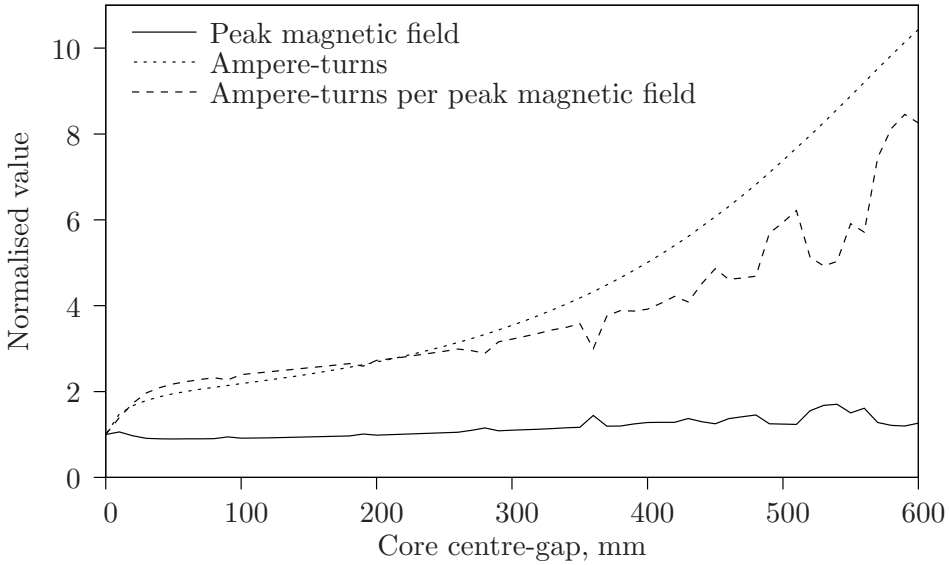

Figure 6.4 Core peak flux-density and secondary winding ampere-turns as a function of core centre-gap for a sample PCRTX.

Figure 6.4 shows that inductance variation via centre-gap tuning can be achieved without significantly increasing the peak value of magnetic field. This is because at larger centre-gaps the core flux-density becomes more uniform. A better utilisation of the steel is obtained.

6.3 EXTENSION OF FINITE ELEMENT MODEL

A finite element model for PCRTXs was developed in Chapter 5. The model is extended to accommodate the new PCRTX design. The primary and secondary windings are divided into winding sections, defined as one or more layers of the same wire size and type with a consistent inter-layer insulation thickness and leadouts at each end. Provisions were made for n winding sections of length $l_{\mathrm{WS}i}$ and m core sections of length $l_{\mathrm{CS}i}$, inner radius $r_{1,\mathrm{CS}i}$ and outer radius $r_{2,\mathrm{CS}i}$. The axial air-space ratio was re-defined as $a_z/\max(l_{CSt}, l_{WSi})$. The new model geometry is shown in Fig 6.5.

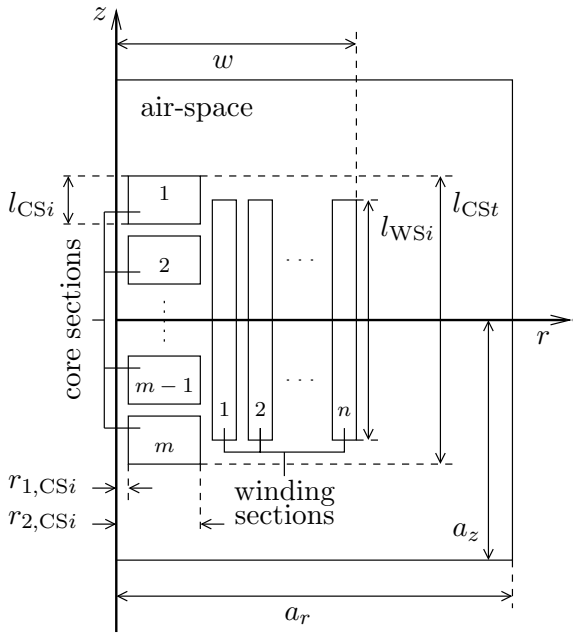

Figure 6.5 Model geometry for new PCRTX designs.

6.3.1 Calculation of inductance matrix

The winding section permeance matrix is defined as

$$\mathbf{P} = \begin{bmatrix} P_{11} & \dots & P_{1n} \\ \vdots & \ddots & \vdots \\ P_{n1} & \dots & P_{nn} \end{bmatrix} \tag{6.1}$$

where $P_{ij} = P_{ji}$.

$\mathbf{P}$ can be obtained from the finite element model by performing n simulations. In each simulation a single winding section, assigned with a unity number of turns, is excited with unit-current and a row of $\mathbf{P}$ is calculated.

The winding section inductance matrix $\mathbf{L}$ can be obtained from $\mathbf{P}$. The elements of $\mathbf{L}$ are calculated as [Ong, 1998]

$$L_{ij} = N_i N_j P_{ij} \tag{6.2}$$

where N_i and N_j are the number of turns of the i^{th} and j^{th} winding sections.

6.4 CALCULATION OF EQUIVALENT CIRCUIT COMPONENTS

The equivalent circuit model for the PCRTX is the Steinmetz 'exact' transformer equivalent circuit of Figure 3.2. The model is extended to accommodate the new PCRTX design. The unused winding sections are not shown in the equivalent circuit, but the induced voltage in these layers needs to be taken into account when designing the insulation. This is discussed in Section 6.9.1.

6.4.1 Primary and secondary self- and mutual-inductances

The primary and secondary windings are formed via series connections of one or more winding sections. Let $W = \{WS_1, \ldots, WS_n\}$ be the set of n winding sections (numbered from the inside) and P and S be subsets of W containing n_P and n_S elements, respectively. Let $P(i)$ and $S(j)$ denote the i^{th} and j^{th} elements of P and S. The primary and secondary winding self-inductances are given by [Wirgau, 1976]

$$L_p = \sum_{i=1}^{n_P} \mathbf{L}_{P(i)P(i)} + \sum_{i=1}^{n_P} \sum_{\substack{j=1 \\ i \neq j}}^{n_P} \mathbf{L}_{P(i)P(j)} \tag{6.3}$$

$$L_s = \sum_{i=1}^{n_S} \mathbf{L}_{S(i)S(i)} + \sum_{i=1}^{n_S} \sum_{\substack{j=1 \\ i \neq j}}^{n_S} \mathbf{L}_{S(i)S(j)} \tag{6.4}$$

The primary-secondary mutual-inductance is given by

$$M_{ps} = \sum_{i=1}^{n_P} \sum_{j=1}^{n_S} \mathbf{L}_{P(i)S(j)} \tag{6.5}$$

Eqs. 3.24 - 3.26 of Section 3.5.3.2 are used to transform the above inductances into the reactance components of the Steinmetz 'exact' transformer equivalent circuit.

6.4.2 Mutual inductances from primary and secondary to unused winding sections

Let U be a subset of W containing all elements not in P or S (i.e. the unused winding sections). The mutual inductances from the $U(k)^{\text{th}}$ unused winding section to the primary and secondary windings are given by

$$M_{PU(k)} = \sum_{i=1}^{n_P} \mathbf{L}_{P(i)U(k)} \tag{6.6}$$

$$M_{SU(k)} = \sum_{i=1}^{n_S} \mathbf{L}_{S(i)U(k)} \tag{6.7}$$

6.4.3 Primary and secondary winding resistances

The primary and secondary winding resistances are given by

$$R_p = \sum_{i=1}^{n_P} \mathbf{R}(P(i)) \tag{6.8}$$

$$R_s = \sum_{i=1}^{n_S} \mathbf{R}(S(i)) \tag{6.9}$$

where the row vector $\mathbf{R} = \{R_1, \ldots, R_n\}$ contains the winding section resistances R_i.

6.5 ESTIMATE OF INPUT IMPEDANCE AT DESIGN STAGE

As shown in Section 4.5, the input impedance of a PCRTX with capacitive load C_l at frequency $\omega_0 = 1/\sqrt{L_s C_l}$ is given by

$$Z_{\text{in}} = R_p + \frac{M_{ps}^2}{L_s C_l R_s'} + j\frac{L_p}{\sqrt{L_s C_l}} \tag{6.10}$$

where $R_s' = R_s + R_l$ and R_l is the resistive component of the insulation under test. Core losses could have also been included in R_s', as described in Section 4.6. However, these are typically much lower than the winding and load losses, and existing core loss models are known to be inaccurate.

Z_{in} can also be obtained numerically by solving the Steinmetz 'exact' transformer equivalent circuit. Both methods can be used for analysis of existing PCRTXs. An approximate formula for Z_{in} which can be used at the design stage, where equivalent circuit component values are unknown, is derived from Eq. 6.10. PCRTXs are typically designed such that ω_0 corresponds to the supply frequency ω_s. Substituting $\omega_s = 1/\sqrt{L_s C_l}$ into Eq. 6.10 gives

$$Z_{\text{in}} = R_p + \left(\frac{\omega_s^2}{R_s'}\right)\left(M_{ps}^2\right) + j\omega_s L_p \tag{6.11}$$

M_{ps} can be expressed in terms of the coil coupling $k = M_{ps} / \sqrt{L_p L_s}$:

$$Z_{\text{in}} = R_p + \left(\frac{\omega_s^2}{R_s'}\right)\left(k^2 L_p L_s\right) + j\omega_s L_p \tag{6.12}$$

Rewriting L_p as $L_s(L_p/L_s)$ gives:

$$\begin{aligned} Z_{\text{in}} = R_p &+ \left(\omega_s^2 L_s^2\right)\left(\frac{1}{R_s'}\right)\left(k^2\right)\left(\frac{L_p}{L_s}\right) \\ &+ j\left(\omega_s L_s\right)\left(\frac{L_p}{L_s}\right) \end{aligned} \tag{6.13}$$

Substituting $1/(\omega_s^2 C_l)$ for L_s gives:

$$\begin{aligned} Z_{\text{in}} = &R_p + \left(\frac{1}{\omega_s^2 C_l^2}\right)\left(\frac{1}{R_s'}\right)\left(k^2\right)\left(\frac{L_p}{L_s}\right) \\ &+ j\left(\frac{1}{\omega_s C_l}\right)\left(\frac{L_p}{L_s}\right) \end{aligned} \tag{6.14}$$

L_p and L_s can be expressed in terms of their definitions:

$$\begin{aligned} Z_{\text{in}} = R_p &+ \left(\frac{1}{\omega_s^2 C_l^2}\right)\left(\frac{1}{R_s'}\right)\left(k^2\right)\left(\frac{N_p}{N_s}\right)^2\left(\frac{P_p}{P_s}\right) \\ &+ j\left(\frac{1}{\omega_s C_l}\right)\left(\frac{N_p}{N_s}\right)^2\left(\frac{P_p}{P_s}\right) \end{aligned} \tag{6.15}$$

where P_p and P_s are the permeances of the primary and secondary windings.

The following assumptions are applied to Eq. 6.15 to obtain an approximate formula for Z_{in}:

1: Ideal coil coupling
$(k = 1,\ \frac{P_p}{P_s} = 1,\ N_p/N_s = V_p/V_s)$
$\therefore \left(k^2\right)\left(\frac{N_p}{N_s}\right)^2\left(\frac{P_p}{P_s}\right) = \left(\frac{V_p}{V_s}\right)^2$

2: $(\frac{1}{\omega_s^2 C_l^2})(\frac{1}{R_s'})(\frac{V_p}{V_s})^2 >> R_p$

3: $\text{Re}\{Z_{\text{in}}\} >> \text{Im}\{Z_{\text{in}}\}$

Parameter	PC1[a]	PC2[b]	PC3[c]
SF_1	0.99 / 0.73	1.00 / 0.91	0.98 / 0.75
SF_2	1.00 / 1.15	1.00 / 1.04	1.01 / 1.10
SF_3	1.00 / 1.01	1.00 / 1.00	1.00 / 1.05
SF_{eff}	1.00 / 0.86	1.00 / 0.96	0.99 / 0.87

[a] Axial-offset = 336 mm / air-core.
[b] Axial-offset = 434 mm / air-core.
[c] Centre-gap = 195 mm / air-core.

Table 6.1 Calculated input impedance scale-factors for sample PCRTXs.

$$\tilde{Z}_{\text{in}} \approx \left(\frac{1}{\omega_s^2 C_l^2}\right)\left(\frac{1}{R'_s}\right)\left(\frac{V_p}{V_s}\right)^2 \tag{6.16}$$

where V_p and V_s are the primary and secondary voltages of the PCRTX.

The exact and approximate formulas for the input impedance are related by

$$Z_{\text{in}} = \tilde{Z}_{\text{in}} SF_{\text{eff}} \tag{6.17}$$

where

$$SF_1 = (k^2)\left(\frac{N_p}{N_s}\right)^2\left(\frac{P_p}{P_s}\right) / \left(\frac{V_p}{V_s}\right)^2 \tag{6.18}$$

$$SF_2 = \left[R_p + \left(\frac{1}{\omega_s^2 C_l^2}\right)\left(\frac{1}{R'_s}\right)\left(\frac{V_p}{V_s}\right)^2 SF_1\right] / \left[\left(\frac{1}{\omega_s^2 C_l^2}\right)\left(\frac{1}{R'_s}\right)\left(\frac{V_p}{V_s}\right)^2 SF_1\right] \tag{6.19}$$

$$SF_3 = Z_{\text{in}}/\text{Re}\{Z_{\text{in}}\} \tag{6.20}$$

$$SF_{\text{eff}} = SF_1 SF_2 SF_3 \tag{6.21}$$

The scale factors were calculated for PC1, PC2 and PC3 of Chapter 5 in typical partial-core and air-core configurations. The results are shown in Table 6.1.

Table 6.1 shows that the effective scaling factor is always less than one, implying that the actual input impedance is always lower than calculated by Eq. 6.16. However, for the sample PCRTXs in typical partial-core configurations, the difference was negligible. Assuming an effective scale factor of 1 is acceptable.

Effective scaling factors may be required for different applications where the frequency, load capacitance or resistive components are significantly different than for the sample

PCRTXs. Once an effective scale factor has been established for a particular application it can be applied to subsequent designs.

6.6 MAXIMUM SECONDARY WINDING RESISTANCE

The minimum allowable input impedance is calculated as

$$Z_{\text{in,min}} = \frac{V_p}{I_{p,\max}} SF_Z \tag{6.22}$$

where $I_{p,\max}$ is the maximum allowable supply current and $SF_Z > 1$ is a scale factor to account for the decrease in input impedance due to deviation from resonance, variations from the ideal voltage ratio and harmonic currents.

Deviation from resonance will occur if the PCRTX is operated above the saturation voltage, the centre-gap between the partial-cores is incorrectly set (due to human error or quantisation of the air-gap setting) or if the load capacitance starts to increase at higher voltages. This phenomenon is known as capacitance tip-up in stator coils [Emery, 2004] and has also been observed in lightning arc signs [Bell et al., 2007].

Variations from the ideal voltage ratio are due to an effective change in the primary-secondary turns ratio which occurs as the secondary winding self-inductance value is adjusted to the load capacitance via suitable winding tap and partial-core centre-gap selection. The variations can be modelled for using the finite element model and the Steinmetz 'exact' transformer equivalent circuit. They can be reduced to within acceptable limits by placing additional taps on the low-voltage winding.

Harmonic currents can occur when operating from a distorted supply. The loaded-circuit is tuned to the supply frequency and the input impedance is reduced at harmonic frequencies. The harmonic current levels can be calculated using the Steinmetz 'exact' transformer equivalent circuit of the PCRTX and load, along with the voltage harmonic levels and impedance of the supply. However, voltage harmonic levels are different at each site and the supply impedance is normally unknown. Furthermore, the harmonic voltages may not scale linearly through the variac, making predictions even more difficult.

To best account for all of these factors, a conservative scale factor should be applied, for example $SF_Z = 2.5$. In general, higher values of SF_z will result in a more conservative design, of higher weight and cost, but the risk of overloading the supply during testing is reduced. The variac must also be rated for the maximum primary current of the resonant circuit. For short-duration tests, the variac rating may be overloaded, as per manufacturers' rating curves.

An upper-limit on R'_s can be obtained by substituting Z_{in} with $Z_{\text{in,min}}$ in Eq. 6.17. The

equation is rewritten using the expression for $\tilde{Z}_{\text{in}}$ given in Eq. 6.16 and then solved for R'_s:

$$R'_{s,\max} = \left(\frac{1}{\omega_s^2 C_l^2}\right)\left(\frac{V_p}{V_s}\right)^2\left(\frac{1}{Z_{\text{in,min}}}\right) SF_{\text{eff}} \tag{6.23}$$

$R_{s,\max}$ is calculated at the maximum load capacitance value $C_{l,\max}$. It is assumed that Z_{in} will increase as additional winding sections are added. This can be checked by adding extra winding sections to the finite element model and then re-evaluating Z_{in} using Eq. 6.10 with the new values of winding resistance and inductance.

R_l can be calculated from the estimated load quality factor Q_l as

$$R_l = \frac{1}{\omega_s Q_l C_{l,\max}} \tag{6.24}$$

Q_l depends on the test object. For XLPE cables, Q_l is usually so much higher than the quality factor of the test equipment that the losses of the test object can be neglected [Hauschild et al., 2002]. For hydro generator stators, Q_l can be as low as 20 or 10.

The upper-limit for the winding resistance is

$$R_{s,\max} = R'_{s,\max} - R_l \tag{6.25}$$

6.7 CURRENT-DENSITY UPPER-LIMIT

PCRTXs are designed for short-term rather than continuous operation. Testing times are relatively short and tests are carried out infrequently. A conduction heating formula was applied to find the thermal upper-limit of current-density for the secondary winding [Davies, 1990]:

$$J_{\text{ul}} = \sqrt{\frac{\theta_m}{t_{\text{on,des}}}\left(\frac{C\gamma}{\rho}\right)} \tag{6.26}$$

where θ_m is the maximum allowable temperature rise, $t_{\text{on,des}}$ is the design-value on-time, $C\gamma$ is the volume specific heat and ρ is the resistivity.

Eq. 6.26 also assumes zero radiation, convection and conduction losses, so the actual temperature rise will be less than θ_m, given by

$$\theta_m = T_{\max} - T_{\text{ambient}} - T_{\text{sf}} \tag{6.27}$$

where $T_{\max}$ is the thermal rating of the insulation system, T_{ambient} is the worst-case ambient temperature and T_{sf} is a safety factor to account for variations of $C\gamma$ and ρ over the temperature range and localised heating effects of the wire at the ends of the inner-most layer due to proximity losses.

The thermal duty cycle $D = \frac{t_{\text{on}}}{t_{\text{on}}+t_{\text{off}}}$ can be determined from experiments with sample PCRTXs or with thermal modelling, although neither of these techniques have yet been applied. In [Gerlach, 1991], an inductor operating near the current-density upper-limit, housed in a minimum-oil tank, took six to twelve hours to cool-down after a three-minute on-time. A similar duty cycle (of $< 1\%$) is expected for PCRTXs with an encapsulated high-voltage winding.

The device maximum on-time depends on the design-value current-density J_{des} (which may be $< J_{\text{ul}}$), operating voltage V_{op} and inductance L_{op} according to:

$$T_{\text{on,max}}(J_{\text{des}}, V_{\text{op}}, L_{\text{op}}) = \left(\frac{J_{\text{ul}}}{J_{\text{des}}} \times \frac{V_s}{V_{\text{op}}} \times \frac{L_{\text{op}}}{L_{\text{des}}} \right)^2 T_{\text{on,des}} \tag{6.28}$$

where L_{des} is the inductance of the connected winding sections with the centre-gap set to zero (refer to Figure 6.3).

Further experimentation or modelling would be required to establish a current-density suitable for continuously-rated devices.

6.8 OPTIMAL WINDING SHAPE

A finite element model was used to evaluate the magnetic permeance over each square millimetre of the winding window of full-core shell-type transformer FC1 (see Chapter 3). A linear two-dimensional planar model was employed. The sample transformer was then converted into a partial-core transformer. The dimensions of the partial-core were the same as the central-limb of the full-core transformer but the core was made circular. The magnetic permeance per square millimetre was then re-evaluated over the winding space, which was now extended past the dimensions of the original winding window. The transformer cross-sections and regions where the magnetic permeances were evaluated are shown in Figure 6.6. The magnetic permeance plots for the sample full-core and partial-core transformers are shown in Figures 6.7 & 6.8. Both permeance and permeance per metre plots are included. The field quantities are expressed as a percentage of the maximum value for that plot.

Figure 6.7 shows that the magnetic permeance is almost uniform over the winding window in the sample full-core transformer. The results are consistent with elementary magnetic models, based on circuit theory, which assume that the mutual-flux permeance is independent of the winding position. Maximum permeance per metre can be obtained

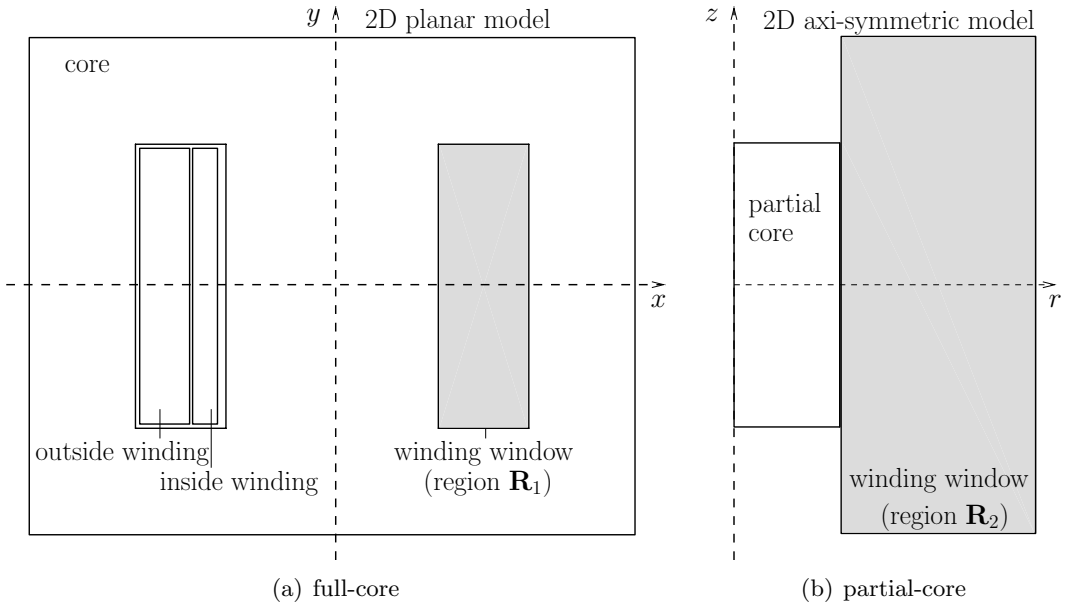

(a) full-core (b) partial-core

Figure 6.6 Transformer cross-sections and regions to evaluate the permeance plots.

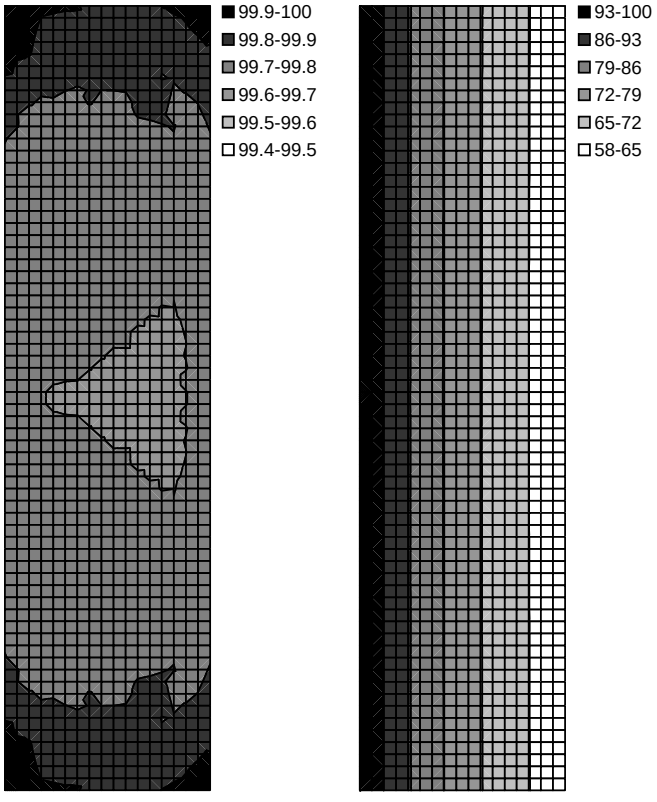

(a) permeance (b) permeance per metre

Figure 6.7 Permeance plots for sample full-core transformer, evaluated over region $\mathbf{R}_1$. Maximum permeance and permeance per metre values are 3.59 $\times 10^{-5}$ H and 1.71 $\times 10^{-4}$ H/m.

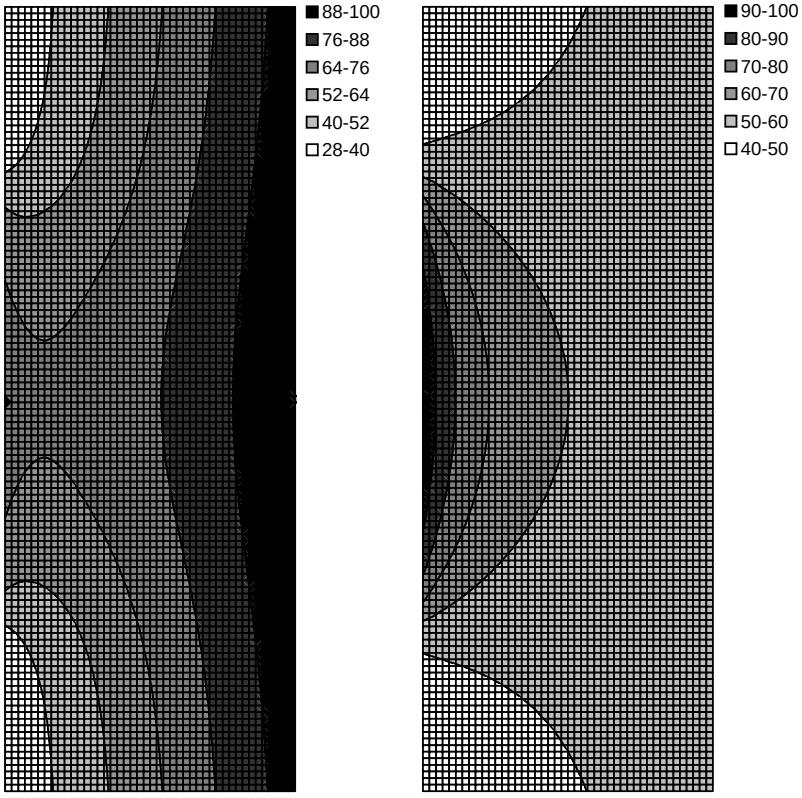

(a) permeance (b) permeance per metre

Figure 6.8 Permeance plots for sample partial-core transformer, evaluated over region $\mathbf{R}_2$. Maximum permeance and permeance per metre values are 5.04 $\times 10^{-7}$ H and 1.99 $\times 10^{-6}$ H/m.

by positioning each turn as close as possible to the inside of the winding window. The optimal winding shape, in regard to obtaining maximum inductance for a given length of wire, is thus rectangular in cross-section with the winding length equal to the height of the winding window.

The distribution of magnetic permeance over the winding space is much less uniform in the sample partial-core transformer, as shown in Figure 6.8. The optimal winding shape is no longer rectangular in cross-section. For practical reasons, a rectangular cross-section is still maintained but the optimal winding length is no longer equal to the core length. For layer windings, the optimal ratio of winding length to core length is a function of the magnetic permeance over the winding space and the ratio of inter-layer insulation thickness to wire thickness.

6.9 VOLTAGE DISTRIBUTION IN HIGH-VOLTAGE WINDING

Consideration must be given to the individual layer voltages of the high-voltage winding when designing the insulation system. Voltage will be induced in all winding sections

of the high-voltage winding, including those in the tapping section which do not form part of the secondary winding in all configurations. Within the secondary winding, the voltage per layer is not strictly uniform as it depends on the individual layer inductances and resistances. With reference to Figure 6.8(a), it can be inferred that the variation of layer inductance over the high-voltage winding depends on the shape of the winding window. For a winding whose length is approximately equal to the core length and thickness is less than the core radius, the inductance variation is minimal. The winding resistance per layer will increase for each additional layer because of the increasing wire length.

Analysis is only performed for the case of normal resonant operation. Transient analysis is not required because the secondary voltage is manually raised to the rated voltage using a variac. Momentary over-voltage and different voltage distributions within the secondary winding may occur if the test object fails. Analysis of this situation is difficult because the exact value of load impedance is unknown and becomes time-varying due to arcing effects. Any transient effects calculated using the Steinmetz 'exact' transformer equivalent circuit, based on a constant fault impedance, may still be inaccurate if short time-constants are involved because the circuit omits winding capacitances. In practice, the fault-current following a test object failure will cause the fuse on the low-voltage winding to operate within a few cycles. Sphere-gaps are placed in parallel with the test object to limit the secondary voltage during the transient period. They are typically set to flashover at 20% above the test voltage.

6.9.1 Unconnected winding sections

The voltage induced in the $U(k)^{\text{th}}$ unused winding section is given by

$$v_{U(k)} = M_{PU(k)} \frac{di_p}{dt} + M_{SU(k)} \frac{di_s}{dt} \tag{6.29}$$

where i_p and i_s are the primary and secondary winding currents.

Assuming that the supply has zero input impedance and zero harmonic distortion and that the variac is ideal, the primary voltage can be written as $V_p \sin(\omega t + \phi)$, where ϕ is the initial phase angle. Ignoring transient effects, The primary and secondary currents can be written as

$$i_p = I_{p,f} \sin(\omega t + \phi + \theta_{I_{p,f}}) \tag{6.30}$$

$$i_s = -I_{s,f} \sin(\omega t + \phi + \theta_{I_{s,f}}) \tag{6.31}$$

where the subscript 'f' denotes the forced response and $I_{p,f}$, $I_{s,f}$, $\theta_{I_{p,f}}$ and $\theta_{I_{s,f}}$ can

be found by numerically solving the Steinmetz 'exact' transformer equivalent circuit with the appropriate load impedance. In the transformer equivalent circuit, primary current is normally defined as positive when flowing into the winding, whereas secondary current is normally defined as positive when flowing out of the winding. The negative sign on the secondary current ensures that both currents are aligned with respect to their winding direction.

The voltage induced in the $U(k)^{\text{th}}$ unused winding section can be obtained by differentiating Eqs. 6.30 and 6.31 and substituting them into Eq. 6.29, giving

$$V_{U(k)} = j\omega[M_{PU(k)} I_{p,f} \angle(\phi + \theta_{I_{p,f}}) - M_{SU(k)} I_{s,f} \angle(\phi + \theta_{I_{s,f}})] \tag{6.32}$$

At first glance, it would appear that a much larger voltage would be induced in the unused winding sections when a short-circuit occurs, owing to higher-than-normal currents. However, the ampere-turns are almost equal in magnitude and opposite in phase under short-circuit conditions, so the induced voltage is minimal. Unlike full-core transformers, the ampere-turn balance is not exact in PCRTXs because the leakage reactance values are typically a significant fraction of the magnetising reactance value.

6.9.2 Connected winding sections

With reference to Figure 6.2, the location of maximum inter-layer voltage is at the winding ends, alternating between one end and the other for each additional layer. Assuming constant resistance and inductance per layer, the rms inter-layer voltage is given by

$$V/L = \frac{2V_s}{n_{Ls}} \tag{6.33}$$

where n_{Ls} is the total number of layers used to form the high-voltage winding.

For high-voltage windings which have graded wire sizes or non-rectangular cross-sections, the individual layer voltages must be calculated. This requires the finite element model to be extended so that each layer of each winding section of the high-voltage winding is represented individually. Eq. 6.32 can be used to calculate the individual layer voltages by substituting $M_{PU(k)}$ and $M_{SU(k)}$ with M_{PLyi} and M_{SLyi}, where M_{PLyi} and M_{SLyi} are the mutual inductances from layer i to the primary and secondary windings.

6.9.3 Example calculation

The individual layer voltages were calculated for PC1 of Chapter 5. The high-voltage winding consists of one main winding section and three tapping winding sections, which are located on the high-voltage end of the high-voltage winding. The wire size is constant throughout the winding. The secondary voltage was maintained at 20 kV and the centre-gap set to zero for each of the four tapping configurations, where the calculated load capacitances for resonant operation at 50 Hz are 291 uF, 342 uF, 493 uF and 608 uF, respectively. The layer voltages are shown in Figure 6.9.

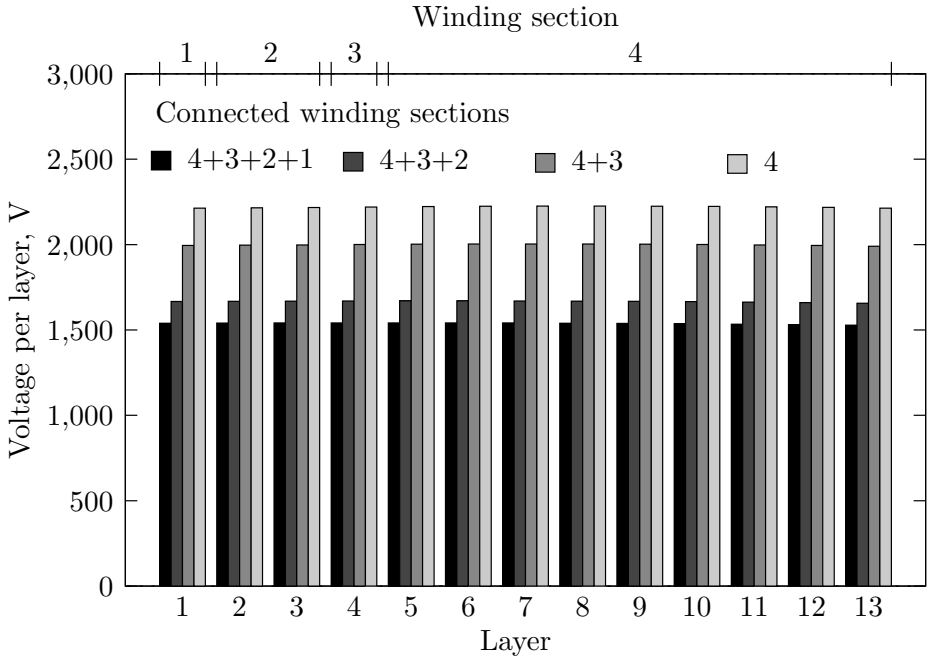

Figure 6.9 Calculated layer voltages in the high-voltage winding of a sample PCRTX with secondary voltage maintained at 20 kV for each configuration.

Figure 6.9 shows that the variation of layer voltage over the high-voltage winding is almost zero for each configuration. The induced voltages in the unconnected winding sections are essentially the same magnitude as in the connected winding sections, owing to the similar mutual inductance values. In this case, Eq. 6.33 can be used to calculate the maximum volts per layer, equal to 4.44 kV for $n_{Ls} = 9$ (with only the main winding section connected).

6.10 INSULATION AND LEAD-OUT DESIGN

A detailed view of a sample PCRTX is shown in Figure 6.10. Consideration must be given to the electric fields within the device and in the surrounding air when designing the inter-layer insulation system and determining the spacing between winding leadouts.

Accurate field calculations could be obtained using an electro-static finite element model. This method has been applied to dry-type transformers to study the electric field at the winding ends [Hong et al., 2005].

A more elementary method has been applied here. As a general rule of thumb, the breakdown electric field strength of air is $\approx 3 \times 10^6$ V/m under standard atmospheric conditions [Kuffel et al., 2000]. As a first approximation, breakdown of air between two needle electrodes along an insulating surface will occur when the ratio of the ac voltage to distance is $\approx 5 \times 10^5$. For the same voltage, needle electrodes will create much higher localised electric fields (and hence corona) than the conductor geometries employed in the PCRTX. Minimum distances between electrodes and insulation overlaps are calculated by using the above figure, with an additional safety factor applied to the distance. This method has proved adequate for designing PCRTXs for indoor operation with secondary voltages up to 80 kV. No direct consideration has been given to the over-voltage and impulse tests which would be required to meet transformer standards.

6.10.1 Layer insulation

The inter-layer insulation material is selected based on the required dielectric strength and temperature rating. The 5-10-5 grade of Nomex-Mylar-Nomex (NMN), having a dielectric strength of 22 kV and temperature rating of 180°C, has been used successfully in previous designs.

6.10.1.1 Circumferential overlap

The circumferential overlap of the inter-layer insulation is calculated using

$$COL = \frac{(V/L)_{\max}}{E_b} SF_e \tag{6.34}$$

where $(V/L)_{\max}$ is the maximum voltage between any single layer, as determined from Section 6.9, $E_b = 5 \times 10^5$ V/m and $SF_e = 2.5$ is an additional safety factor to account for manufacturing tolerances and uneven voltage distributions which may occur when the insulation under test fails.

For simplicity, the same circumferential overlap is applied to all layers, even if graded wire has been used. A flashover between the circumferential overlap is unlikely because the maximum electric field occurs at the winding ends, which are fully encapsulated.

6.10.1.2 End overlaps

With reference to Figure 6.10(a) the end overlaps EOL and $OEOL$ are chosen to obtain the required creepage distance $d_{1,\text{hv-lv}}$. EOL is made a short as practically possible,

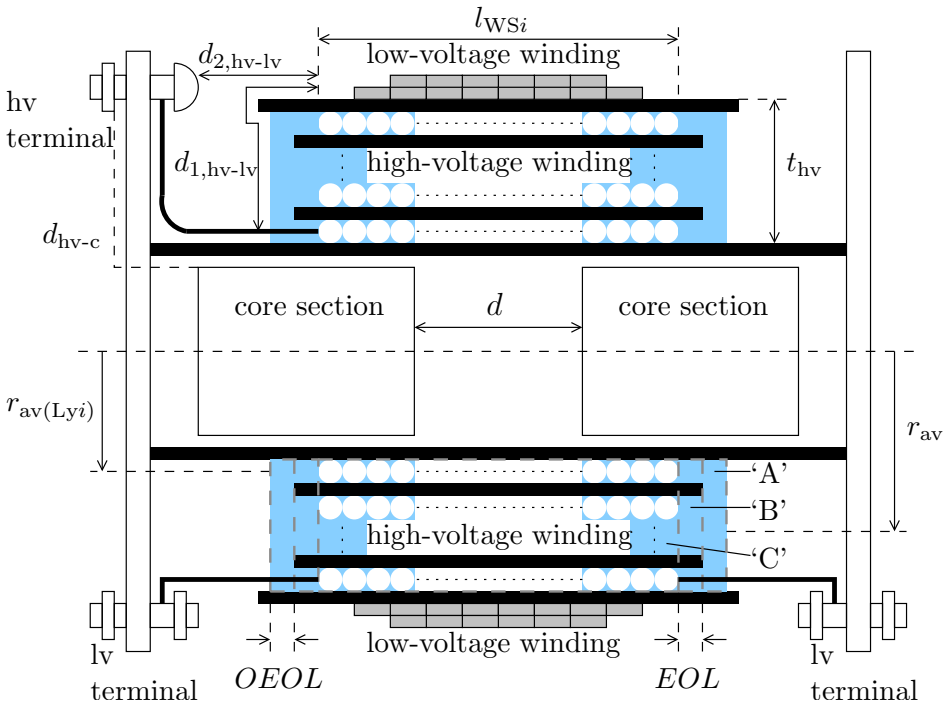

(a) Cross-section

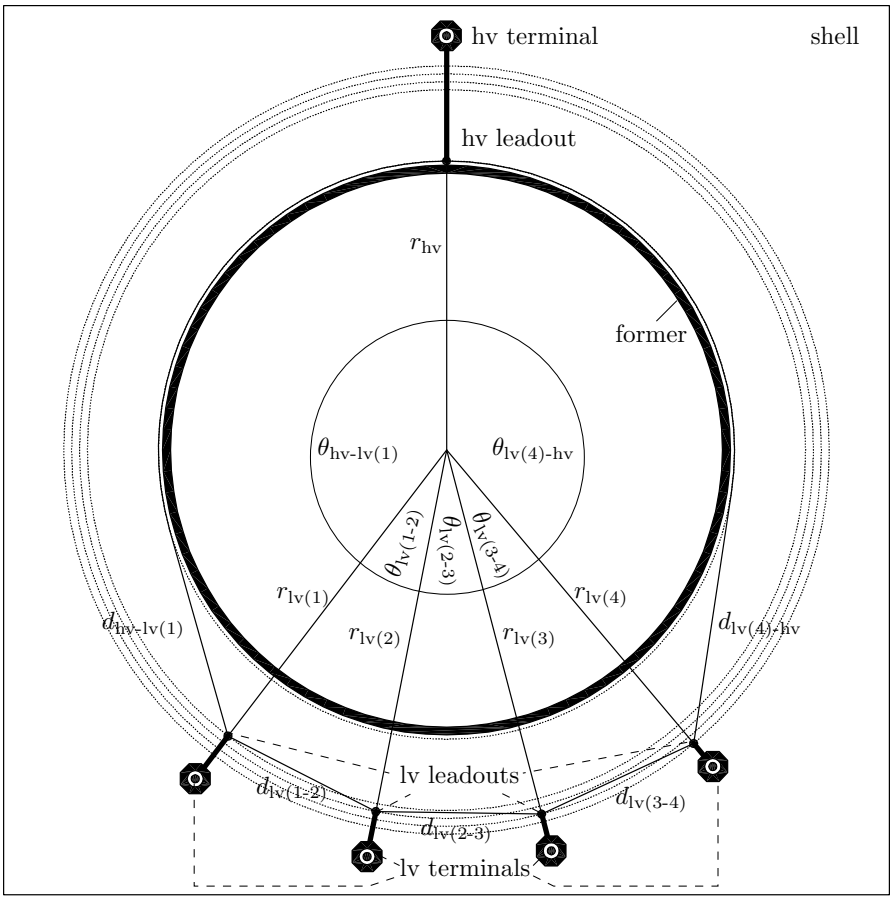

(b) End view (for clarity the low-voltage winding is not shown)

Figure 6.10 Detailed view of a sample PCRTX, showing the insulation system and leadout clearances.

typically 15-25 mm and $OEOL$ is given by

$$OEOL = \frac{V_s}{E_b} SF_e - EOL - t_{\text{hv}} \tag{6.35}$$

where t_{hv} is the thickness of the high-voltage winding.

Eq. 6.35 assumes that the length of the low-voltage winding is less than the length of the high-voltage winding. It is impractical to wind over the encapsulated region anyway, as this would reduce the mechanical strength of the winding.

6.10.2 Leadouts

6.10.2.1 High-voltage leadout

Terminals on the high-voltage winding have been made using M8 threaded rod. A dome washer is placed on the inside of the terminal to reduce the electric field gradient about the terminal. Since the creepage distance $d_{2,\text{hv-lv}}$ includes both a surface and air, this value can be made somewhat lower than $d_{1,\text{hv-lv}}$. Consideration must also be given to the creepage distance $d_{\text{hv-c}}$. For the PCRTX described in [Lynch et al., 2007], which had a secondary voltage of 80 kV, the core was bonded to the hv terminal to reduce the corona around the core.

6.10.2.2 Angles between leadouts

As shown in Figure 6.1 the high-voltage leadout on the high-voltage winding is located at the top of one end of the transformer shell. Leadouts on the low-voltage end of the high-voltage winding are located at the bottom of each end of the shell and are spaced apart radially. Assuming that there are several layers in the main winding section and a single layer in each of the tapping winding sections, the creepage distance between each of the low-voltage leadouts will include only a straight-line component, whereas the creepage distances between the high-voltage leadout and the two closest low-voltage leadouts will include part of an arc as well as a straight-line component. The angles between leadouts are calculated such that equal voltage per creepage distance is obtained between all of the leadouts. The creepage distances are given by

$$d_{\text{hv}-\text{lv}(1)} = r_{\text{hv}}(\theta_{\text{hv-lv}(1)} - \cos^{-1}(r_{\text{hv}}/r_{\text{lv}(1)})) + \sqrt{r_{\text{lv}(1)}^2 - r_{\text{hv}}^2} \tag{6.36}$$

$$d_{\text{lv}(i)-\text{lv}(i+1)} = \sqrt{r_{\text{lv}(i)}^2 + r_{\text{lv}(i+1)}^2 - 2r_{\text{lv}(i)} r_{\text{lv}(i+1)} \cos(\theta_{\text{lv}(i)-\text{lv}(i+1)})} \tag{6.37}$$

$$d_{\text{lv}(n)-\text{hv}} = r_{\text{hv}}(\theta_{\text{lv}(n)-\text{hv}} - \cos^{-1}(r_{\text{hv}}/r_{\text{lv}(n)})) + \sqrt{r_{\text{lv}(n)}^2 - r_{\text{hv}}^2} \tag{6.38}$$

Eqs. 6.36-6.38 are solved (using numerical methods) for all θ_i subject to the restrictions

$$\theta_{\text{hv}-\text{lv}(1)} + \sum_{i=1}^{\alpha} \theta_{\text{lv}(i)-\text{lv}(i+1)} + \theta_{\text{lv}(n)-\text{hv}} = 2\pi \tag{6.39}$$

$$d_{\text{hv}-\text{lv}(1)} = d_{\text{lv}(n)-\text{hv}} = \frac{V_{\text{hvl}}}{V_s} d_{\text{lv}(i)-\text{lv}(i+1)} \tag{6.40}$$

where V_{hvl} is the maximum voltage between any two layers in the tapping winding sections, $\alpha = n_{\text{tap}}$ or $n_{\text{tap}} - 1$ depending on whether the number of layers in the main winding section is even or odd and n_{tap} is the number of tapping winding sections in the high-voltage winding.

The same angles are then used for the low-voltage leadouts on the other side of the high-voltage winding.

The safety factor of the leadout spacing is calculated as

$$SF_{\text{leadouts}} = V_s / d_{\text{hv-lv}(1)} \tag{6.41}$$

For devices which have a relatively high secondary voltage (> 100 kV) and relatively small core cross-sectional area, such as testing transformers designed to operate under open-circuit conditions, it may be impossible to obtain a sufficiently high value of SF_{leadouts}. An alternative insulation medium such as oil or SF_6 may be required.

6.10.3 Example calculation

Table 6.2 shows the calculated parameters of the inter-layer insulation and leadout spacing for the sample PCRTX described in Section 6.9.3. It is assumed that the tapping winding section is placed on the low-voltage end of the high-voltage winding. A scaled drawing of the end view of the transformer is shown in Figure 6.10(b).

6.11 WEIGHT AND COST CALCULATIONS

For a given set of electrical specifications and restrictions, multiple design solutions exist from within the PCRTX topology. Each design has a unique set of material dimensions. The criteria for the 'optimal' solution is typically based on minimum total weight or minimum total cost. Weight and cost calculations for the key components of the PCRTX - core, wire, inter-layer insulation and encapsulant - are presented in programmable form. Other components, such as the fibre-glass shell and leadouts, can be added as required.

Parameter	Value	Unit
V_s	20	kV
$(V/L)_{\max}$	4.44	kV
COL	22	mm
EOL	25	mm
$OEOL$	50.4	mm
t_{hv}	24.6	mm
$d_{1,\text{hv-lv}}$	100	mm
$d_{2,\text{hv-lv}}$	75	mm
$\theta_{\text{hv-lv(1)}}$	142.5	degrees
$\theta_{\text{lv(1-2)}}$	26.4	degrees
$\theta_{\text{lv(2-3)}}$	25.8	degrees
$\theta_{\text{lv(3-4)}}$	25.5	degrees
$\theta_{\text{lv(4)-hv}}$	139.8	degrees
SF_{leadouts}	4.6	-

Table 6.2 Inter-layer insulation and leadout spacing parameters calculated for a sample PCRTX.

6.11.1 Core

The weight and cost of the j^{th} core section is given by

$$W_{\text{CS}j} = \pi(r_{2,\text{CS}j}^2 - r_{1,\text{CS}j}^2) l_{\text{CS}j} \gamma_{\text{C}} \tag{6.42}$$

$$C_{\text{CS}j} = W_{\text{CS}j} \times MC_{\text{C}} \tag{6.43}$$

where γ_{C} and MC_{C} are the density and material cost of the core steel.

6.11.2 Wire

The wire length of the j^{th} winding section is given by

$$l_{\text{WS}j} = (T/L)_j \sum_{i=1}^{n_{\text{Ly},j}} 2\pi r_{\text{av(Ly},i)} \tag{6.44}$$

where $(T/L)_j$ and $n_{\text{Ly,j}}$ are the number of turns per layer and number of layers in winding section j and $r_{\text{av(Ly},i)}$ is the radial distance to the axial-centre of the conductors in the i^{th} layer.

The wire weight and cost of the j^{th} winding section is given by

$$W_{\mathrm{WS}j} = A_{\mathrm{WS}j} \times l_{\mathrm{WS}j} \times \gamma_{\mathrm{WS}j} \tag{6.45}$$

$$C_{\mathrm{WS}j} = W_{\mathrm{WS}j} \times MC_{\mathrm{WS}j} \tag{6.46}$$

where $\gamma_{\mathrm{WS}j}$ and $MC_{\mathrm{WS}j}$ are the density and material cost and $A_{\mathrm{WS}j}$ is the conductor cross-sectional area.

6.11.3 Inter-layer insulation

The cross-sectional area of insulation in the j^{th} winding section is given by

$$A_{\mathrm{I,WS}j} = \sum_{i=1}^{n_{\mathrm{Ly}}} (2\pi r_{\mathrm{av(Ly}i)} + COL)(l_{\mathrm{WS}i} + 2EOL) \tag{6.47}$$

where $r_{\mathrm{av(Ly}i)}$ is the radial distance to the axial-centre of the inter-layer insulation of the i^{th} layer.

The weight and cost of the insulation in the j^{th} winding section is given by

$$W_{\mathrm{I,WS}j} = A_{\mathrm{I,WS}j} \times t_{\mathrm{I,WS}j} \times \gamma_{\mathrm{I,WS}j} \tag{6.48}$$

$$C_{\mathrm{I,WS}j} = W_{\mathrm{I,WS}j} \times MC_{\mathrm{WS}j} \tag{6.49}$$

where $t_{\mathrm{I,WS}j}$, $\gamma_{\mathrm{I,WS}j}$ and $MC_{\mathrm{I,WS}j}$ are the thickness, density and material cost of the insulation.

6.11.4 Encapsulant

The three regions for encapsulant in the high-voltage winding ('A', 'B' and 'C') are shown in Figure 6.10(a). The region volumes are calculated as

$$V_{`A'} = 2\pi r_{\mathrm{av}} \times t_{\mathrm{hv}} \times OEOL \tag{6.50}$$

$$V_{`B'} = \sum_{j=1}^{n_S} wd_{S(j)} \times EOL \sum_{i=1}^{n_{Ly,S(j)}} 2\pi r_{\mathrm{av(Ly},i)} \tag{6.51}$$

$$V_{`C'} = \sum_{j=1}^{n_S} wd_{S(j)}^2 (1 - \frac{\pi}{4})(T/L)_{S(j)} \sum_{i=1}^{n_{Ly,S(j)}} 2\pi r_{\mathrm{av(Ly},i)} \tag{6.52}$$

where the high-voltage winding is formed by subset $S \in W$, having n_S elements, as defined in Section 6.4.1.

The encapsulant weight and cost are calculated as

$$W_{\mathrm{e}} = \gamma_e(2V_{`A'} + 2V_{`B'} + FF_eV_{`C'}) \tag{6.53}$$

$$C_{\mathrm{ep}} = W_{\mathrm{e}} \times MC_{\mathrm{e}} \tag{6.54}$$

where γ_e and MC_{e} are the density and material cost of the encapsulant and $FF_e < 1$ is the estimated fill-factor of region 'C'.

6.12 CONCLUSIONS

The tools developed in this chapter can be used for analysis and design. The presented equations have been coded into a purpose-built transformer design and analysis program. At the most basic level, the design process is user-driven, where the dimensions of the core and windings are adjusted using an iterative procedure in order to meet device specifications and restrictions. The final device is thus highly dependent on the designer's experience.

The established interface between the transformer design and analysis program and the finite element analysis software package (as described in Chapter 3 and Appendix A) also brings about the possibility of design via scripting. This would allow multiple designs to be evaluated with little or no user-interaction, making it possible to find optimal material dimensions, with regards to either minimum weight or minimum cost, for a given set of device specifications and restrictions. This process is described in Chapters 7 & 8.

Chapter 7

DESIGN METHODOLOGY FOR HIGH-VOLTAGE PARTIAL-CORE RESONANT TRANSFORMERS WITH FIXED INDUCTANCE

7.1 OVERVIEW

Magnetic field and inductance characteristics for transformers having different core aspect and winding length to core length ratios are investigated using a finite element model. These are used to place restrictions on field values and device dimensions. A design methodology for fixed inductance devices is then introduced, where supply frequency, load capacitance, primary and secondary voltage, on-time, load quality factor and minimum impedance are the main specifications. Restrictions such as maximum flux-density, volts per layer, number of layers and winding length to core length ratios are defined. The problem is written in general form, ready for optimisation, where the target to minimise is weight. A multiple design method is implemented. The methodology is illustrated with a design example, where the first stage of a transformer kitset for high-voltage testing of hydro-generator stators is developed.

7.2 INTRODUCTION

PCRTXs can be designed with fixed or variable inductance. Inductance can be varied by changing a tap setting, the air-gap between partial-cores, or a combination of both techniques. In the present application of stator testing a large inductance range is required. However, there are some applications for which a PCRTX with fixed inductance could be employed. One example is frequency-tuned resonance. Cable testing is often performed using this method. The reactors are normally oil-filled and have a full-core magnetic circuit. They are typically configured for series resonance [Hauschild et al., 2002]. Partial-core reactors have also been used in some test circuits [Bernasconi et al., 1979] , [Weishu, 1995] with the main advantage being a reduction in the specific weight per volt-ampere. Modern arc-suppression coils are often designed with fixed inductance. The effective value of inductance is changed via thyristor switched capacitors, connected

to tertiary windings [Jia et al., 2005]. A partial-core arc-suppression coil may also be practical, although consideration must be given to any eddy-current heating effects of the winding wire from the stray magnetic field, since a continuous rating is required.

A general design method for partial-core resonant transformers with fixed inductance is developed. While intended to be useful in its own right, the method is also a lead-in to the development of variable inductance devices. As a design example, a fixed inductance PCRTX is designed as the first stage of a transformer kitset for high-voltage testing of hydro-generator stators.

7.3 MAGNETIC FIELD AND INDUCTANCE CHARACTERISTICS

Magnetic field and inductance characteristics for transformers having different core aspect and winding length to core length ratios are investigated using a finite element model. These are used to place restrictions on field values and device dimensions.

7.3.1 Magnetic field calculation

The secondary voltage at which core saturation occurs in PCRTXs was calculated using a linear magneto-static finite element model in Chapter 5. In that chapter the method was applied to three sample PCRTXs, each having relatively long and thin partial cores. Consequently, the magnetic field distribution within the cores of the three devices was quite similar. However, as the dimensions of the partial-core are changed so that the core becomes shorter and wider, the magnetic field distribution within the core is significantly altered. To illustrate this concept, the core radius of a sample PCRTX was adjusted to obtain two different ratios of core length to core radius. For each case, the peak magnetic field was normalised to 1.7 T, the approximate value at which core saturation occurred for the sample PCRTXs in Chapter 5. The field plots for the two cases are shown in Figure 7.1.

For the first case, shown in Figure 7.1(a), the peak value of magnetic field is located at the axial centre-line, just inside the core outer-radius. Figure 7.1(b) shows the second case, where there are two peak values, located at the top and bottom of the core, just inside the core outer-radius. The two peak values, which are much higher than the average value, were initially thought to be caused by insufficient refinements in the finite element mesh or the use of a linear core model. However, refining the mesh and using a non-linear core model did not significantly change the field distribution under normal operating flux densities. The field plots suggest that the magnetic utilisation of the core is much poorer for cores which are shorter and wider. This does not mean that such designs should be immediately rejected. They should still be evaluated as part of the design process.

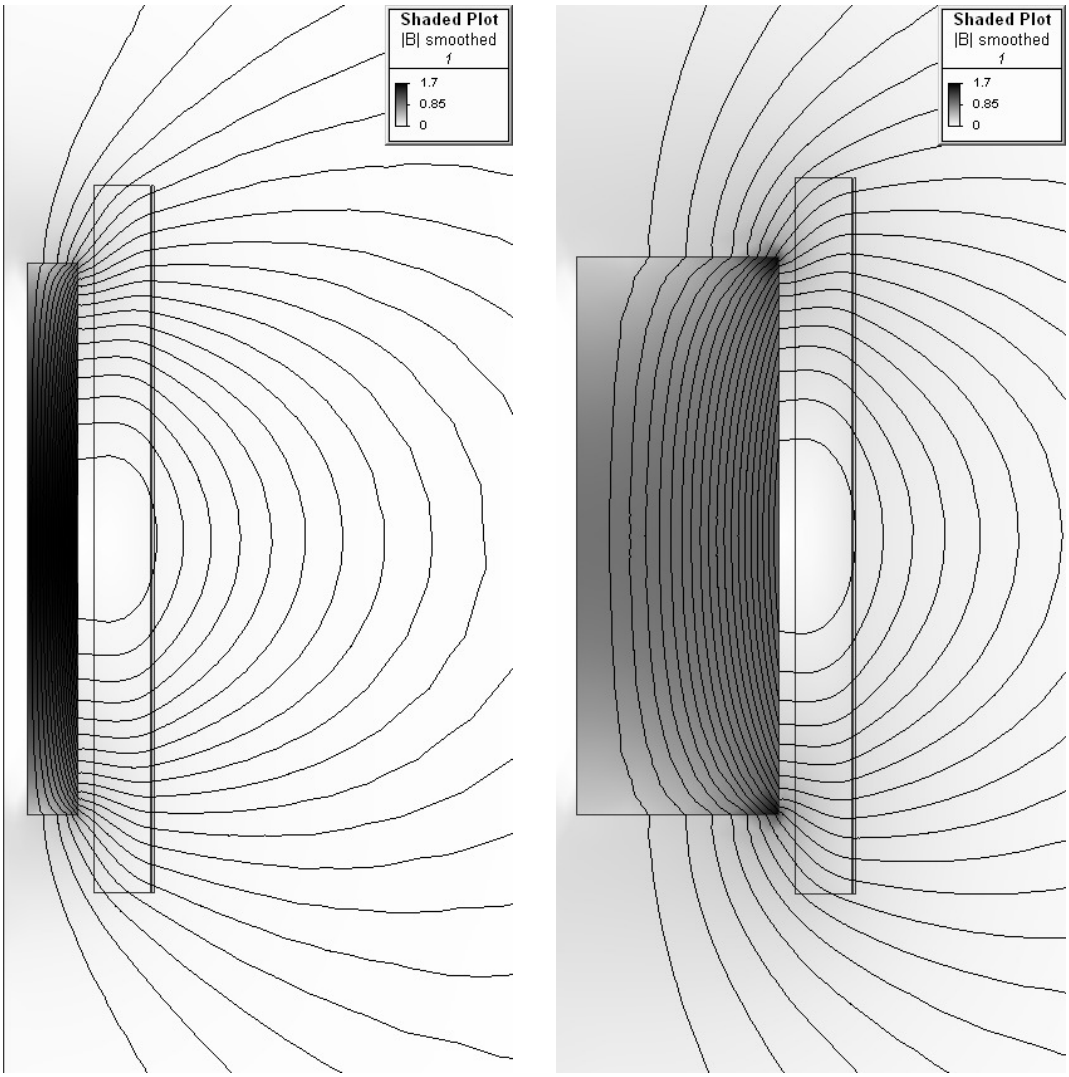

(a) core length / core radius = 7.4. (b) core length / core radius = 2.5.

Figure 7.1 Magnetic field of a sample PCRTX for two different values of core radii with the peak magnetic field value maintained at 1.7 T.

A suitable method of magnetic field calculation needs to be established which can be applied to both types of field distributions. In the interests of reducing programming complexity and computation time, it would be desirable for the criterion on the magnetic field to be based on an upper-limit of a single magnetic field value. Furthermore, in order to reduce operating noise, this upper-limit should be significantly lower than the saturation flux-density of the core steel.

Linear and non-linear core models were evaluated to see if a linear model could be applied to both types of field distributions for a design-value flux-density of 1.2 T. In the absence of the actual B-H curve for the grain oriented steel normally used in PCRTXs, a B-H curve for non-oriented steel which was built into the finite element analysis

software package was used. This was the same curve used in Chapter 3. The steel has a saturation flux-density level of approximately 1.3 T, much lower than the typical value for grain oriented steel of 1.7 - 1.9 T. This will mean that any correlations found between the linear and non-linear core models will hold to even higher flux-densities in the actual core steel. The results are shown in Figure 7.2.

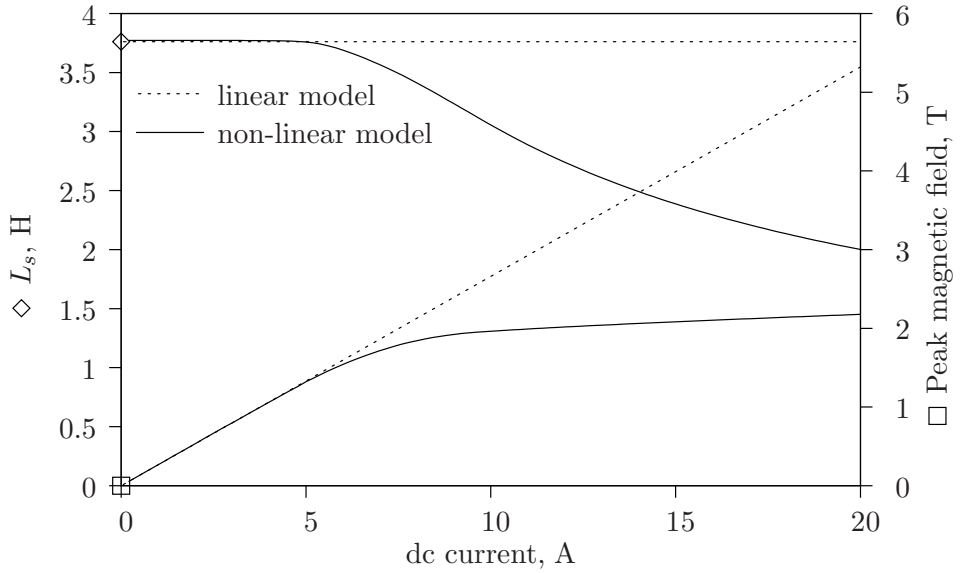

(a) core length / core radius = 7.4.

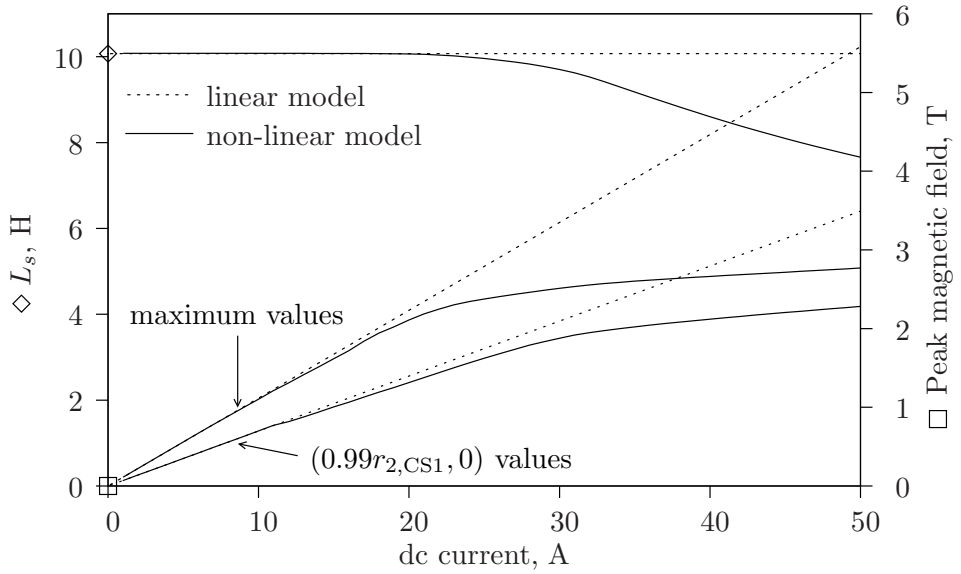

(b) core length / core radius = 2.5.

Figure 7.2 Linear and non-linear core models compared for a sample PCRTX with two different values of core radii.

Figure 7.2(a) shows there is an excellent correlation between the peak field values calculated with the linear and non-linear models for PCRTXs with long thin cores, when operating below the saturation flux-density. The difference between field values increases

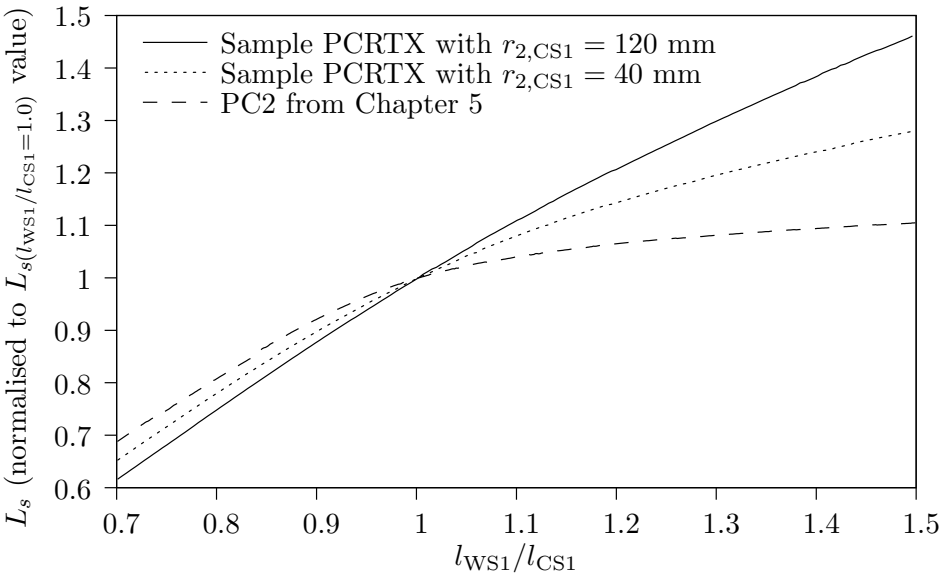

Figure 7.3 Calculated secondary inductance to ratio of winding length to core length characteristic for two different PCRTXs.

to 5% at a flux-density of ∼1.60 T. Figure 7.2(b) shows the correlation between field values for PCRTXs with short, wide cores. Both the maximum field value and the field value at the axial centre-line of the core, just inside the core outer-radius, were calculated for each level of excitation current. The difference between the linear and non-linear field values increases to 5% at a flux-density of ∼2.0 T and ∼1.05 T for the two different cases. The tendancy for the linear model is to slightly over-estimate the flux-density. Setting an upper-limit of 1.2 T for the flux-density, which is calculated using a linear model and sampled at the axial centre-line, just inside the core outer-radius, will ensure highly linearity and low operating noise for PCRTXs having either core shape.

7.3.2 Inductance as a function of winding length to core length ratio

Having already specified the core dimensions, current-density and number of layers of a trial design, the next task is to adjust the winding length to meet the target inductance. Limits are placed on the minimum and maximum ratio of winding length to core length. If the target inductance lies within the allowable range, a method of narrowing in on the correct number of turns per layer is required. A normalised plot of the calculated inductance as a function of the ratio of winding length to core length for the same sample PCRTX for which the field plots were generated is shown in Figure 7.3. The results are compared to PC2 of Chapter 5.

Figure 7.3 shows that the function is different for each PCRTX and is strongly dependent on the ratio of core length to radius. It cannot easily be determined via analytical methods. Hence a general method of narrowing in on the correct number of turns per

layer is required, which mimimises the number of times the finite element model is executed. A binary search technique was chosen.

The reason for the restriction on the ratio of winding length to core length can be understood from the permeance per metre plots of Section 6.8. Unlike a full-core transformer, the optimal winding shape for a partial-core transformer is non-rectangular. For practical reasons, rectangular shaped windings are normally employed. Inter-layer insulation scales the radial axis of the permeance per metre plot, making the optimal winding length longer than the core length. The higher the ratio of inter-layer insulation to radial wire thickness, the greater this effect.

7.4 DESIGN METHODOLOGY FOR FIXED INDUCTANCE

PCRTXs have been designed using the reverse design method. The final design is non-unique, and a product of the designer's experience. Example devices which were developed using this method are listed in [Bodger and Enright, 2004] and [Lynch et al., 2007]. A more rigorous design method is described here which allows for optimal design with regard to a particular cost function, normally defined as the total weight or cost. An overview of the new design method for PCRTXs with fixed inductance is shown in Figure 7.4 and explained in the following sections.

7.4.1 Initial considerations

7.4.1.1 Function specifications

The functional specifications are obtained from the load requirements and supply characteristics. Secondary voltage V_s, load capacitance C_l, maximum on-time $t_{\text{on,max}}$ and load quality factor Q_l are determined by the load. Primary voltage V_p, supply frequency f_s and minimum input impedance $Z_{\text{in,min}}$ are determined from the supply. The maximum ambient temperature T_{ambient} is also specified. $Z_{\text{in,min}}$ is calculated using Eq. 6.22 of Section 6.6.

7.4.1.2 Other specifications

Other specifications include the inside radius of the core $r_{1,\text{CS1}}$ and the end over-lap of the inter-layer insulation EOL. A core centre-hole of radius $r_{1,\text{CS1}}$ is required if the laminations are stacked in the radial direction. For PCRTXs having multiple core sections a threaded rod is used to clamp the core sections together to minimise vibration. EOL is made as short as practically possible, typically 15-25 mm.

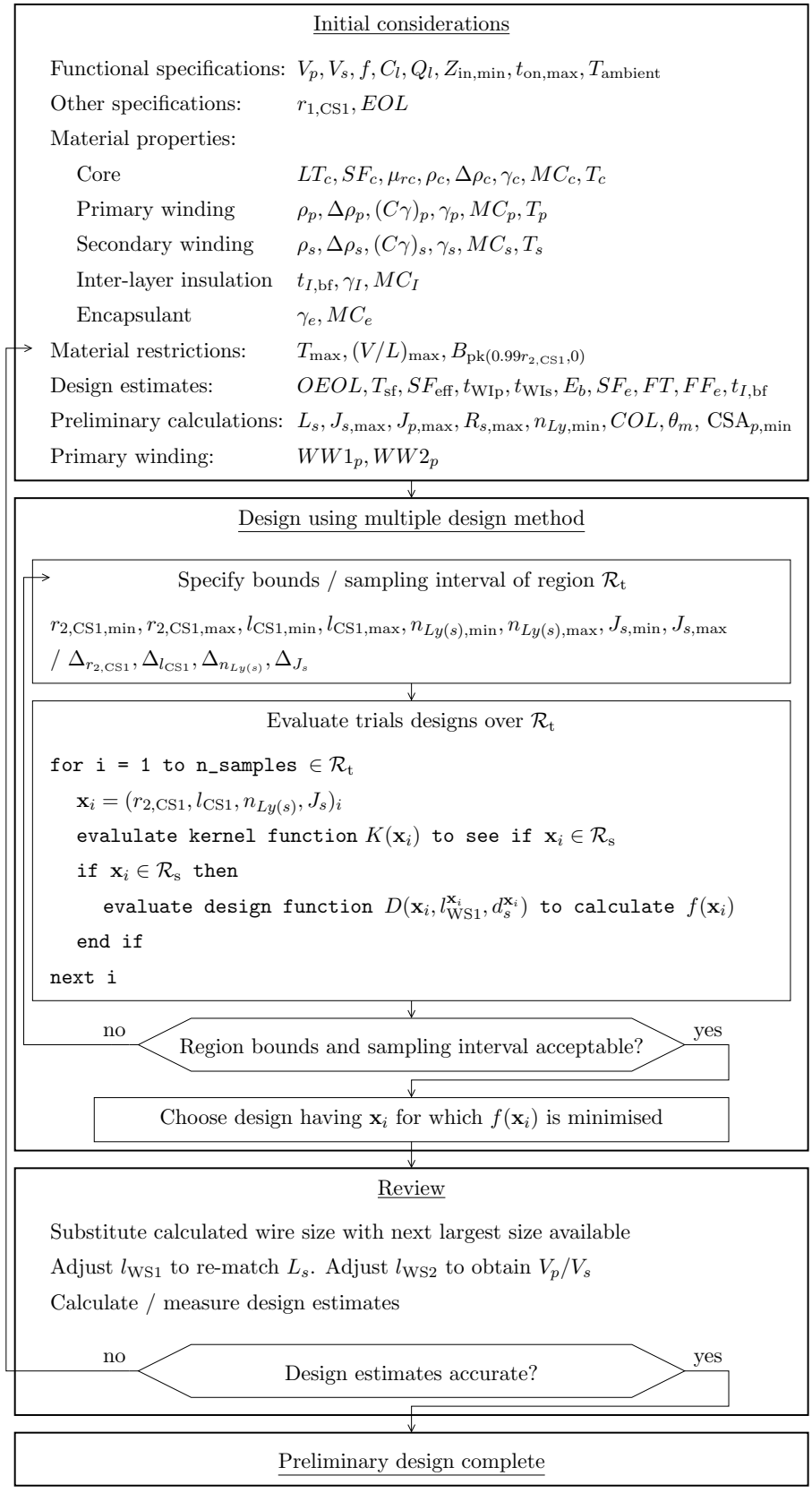

Figure 7.4 Overview of design process for PCRTXs with fixed inductance.

7.4.1.3 Material properties

Material properties of the core, primary and secondary windings, inter-layer insulation and encapsulant are specified. Material properties common to all materials are density γ and material cost MC. Material properties common to the core and windings are resistivity ρ, thermal resistivity coefficient $\Delta\rho$ and operating temperature T. Material properties specific to the core are lamination thickness LT_c, stacking factor SF_c and relative permeability $\mu_{\text{rc}} = 3000$ (as chosen in Section 5.4.2). Volume specific heat $C\gamma$ is required for the windings only.

7.4.1.4 Material restrictions

Material restrictions include the thermal rating of the insulation system $T_{\max}$, maximum voltage per layer of insulation $(V/L)_{\max}$ and peak value of core flux-density $B_{\text{pk}(0.99r_{2,\text{CS1}},0)}$, sampled at the axial centre-line, just inside the core outer-radius.

7.4.1.5 Design estimates

Estimates are made of the end overlap of the outer-most layer of insulation $OEOL$, the safety factor applied to the thermal rating of the insulation system T_{sf}, scale factor between the design-value and analytical input impedance $SF_{\text{eff}} < 1.0$, thickness of insulation on primary and secondary winding wire t_{WI}, approximate value of electric field strength for breakdown of air between two needle electrodes along a surface $E_b = 5 \times 10^5$ V/m, former thickness FT, fill-factor for the encapsulant in the central winding region $FF_e < 1$ and build factor for the thickness of the inter-layer insulation $t_{I,\text{bf}}$.

$OEOL$ is calculated using Eq. 6.35 of Section 6.10.1, assuming that the secondary winding is as thin as possible (i.e., constructed using the smallest allowable wire size and minimum number of layers). Recent experience suggests that the safety factor on the breakdown field strength of 2.5 is no longer required.

7.4.1.6 Preliminary calculations

The secondary winding self-inductance value L_s, maximum current-density of primary and secondary windings $J_{p,\max}$ and $J_{s,\max}$, maximum secondary winding resistance $R_{s,\max}$, minimum number of layers on the secondary winding $n_{Ly,\min}$, circumferential overlap of the inter-layer insulation COL, worst-case temperature rise of winding wire θ_m and minimum cross-sectional area of primary winding wire $CSA_{p,\min}$ are calculated prior to the main design process.

L_s is given by

$$L_s = \frac{1}{\omega_s^2 C_l} \tag{7.1}$$

where $\omega_s = 2\pi f_s$.

$J_{\max}$ and $R_{s,\max}$ are calculated using Eq. 6.26 of Section 6.7 and Eq. 6.25 of Section 6.6, respectively. COL is calculated assuming that the minimum number of layers is chosen, using Eq. 6.34 of Section 6.10.1. $n_{Ly,\min}$ and $CSA_{p,\min}$ are calculated using:

$$n_{Ly,\min} = \frac{2V_s}{(V/L)_{\max}} \tag{7.2}$$

$$CSA_{p,\min} = \frac{V_{\text{su}}}{I_{\text{su,max}} J_{p,\max}} \tag{7.3}$$

7.4.1.7 Primary winding

Rectangular wire is normally used for the primary winding, having radial and axial widths $WW1_p$ and $WW2_p$, respectively. The choice of wire size is normally more based on what is available in stock rather than exactly meeting the minimum wire cross-sectional area requirements of Eq. 7.3. The weight of the primary winding wire is typically only a small fraction of the total device weight.

7.4.2 Multiple design method

7.4.2.1 Overview

Optimisation problems of computational electro-magnetics can be reduced to the following form [Preis et al., 1991]:

Minimize

$$f(\mathbf{x}) \tag{7.4}$$

subject to

$$g_p(\mathbf{x}) = 0 \tag{7.5}$$

$$h_q(\mathbf{x}) \leq 0 \tag{7.6}$$

where $\mathbf{x} = (x_1, \ldots, x_n)$ are degrees of freedom, and the functions f, g_p and h_q define an optimisation criterion, constraint equations and constraint inequalities, respectively.

For this problem, $f(\mathbf{x})$ is defined as the total weight of the device, given by

$$f(\mathbf{x}) = \sum_{i=1}^{n_{\mathrm{CS}}} W_{\mathrm{CS}i} + \sum_{j=1}^{n_{\mathrm{WS}(s)}} (W_{\mathrm{WS}j} + W_{\mathrm{I,WS}j}) + W_{\mathrm{e}} + \sum_{k=1}^{n_{\mathrm{WS}(p)}} W_{\mathrm{WS}k} \tag{7.7}$$

where $W_{\mathrm{CS}i}$ is the weight of the i^{th} core section, $W_{\mathrm{WS}j}$ and $W_{\mathrm{I,WS}j}$ are the wire and inter-layer insulation weight of the j^{th} secondary (high-voltage) winding section, W_{e} is the weight of the encapsulant, $W_{\mathrm{WS}k}$ is the wire weight of the k^{th} primary (low-voltage) winding section, n_{CS} is the number of core sections and $n_{\mathrm{WS}(s)}$ and $n_{\mathrm{WS}(p)}$ are the number of winding sections on the primary and secondary windings, respectively.

Eq. 7.7 contains only the basic components of the transformer. Weight calculations for the individual elements are given in Section 6.11. They can be expanded to include other components once a first cycle of the design process has been completed and the materials for the transformer housing have been decided on. For example, the weight of the former, shell and packing box can easily be calculated once the materials and their respective thicknesses have been chosen, since all other dimensions are completely determined from the transformer design.

The Monte-Carlo iteration method has been applied for optimal transformer design [Andersen, 1967]. Other general methods include the higher-order deterministic optimisation and zeroth-order stochastic optimisation methods, which have been applied to 2-D and 3-D linear and non-linear finite element models [Preis et al., 1991]. A simpler approach was applied to PCRTXs, known as the multiple design method [Saravolac, 1998]. Both the computational requirements of the two-dimensional magneto-static finite element model and the degrees of freedom for this problem are small. This makes it more practical to sample over an entire region, rather than spending additional time implementing more advanced algorithms, which would presumably reach the same solution in far fewer iterations.

The minimum value of $f(\mathbf{x})$ is determined by calculating $f(\mathbf{x}_i)$ at a specified sampling interval Δ over a specified region $\mathcal{R}$. The region bounds and sampling interval are adjusted in a user-driven iterative process, so as to locate the $\mathbf{x}_i$ for which $f(\mathbf{x})$ is minimised. It is assumed that there exists only one such minimum for this type of geometry.

There are four degrees of freedom, namely

$$\mathbf{x} = r_{2,\mathrm{CS}i}, l_{\mathrm{CS}i}, n_{Ly(s)}, J_s \tag{7.8}$$

The single constraint equation is

$$L_s^{\mathbf{x}_i} = L_\mathrm{s} \tag{7.9}$$

where the superscript $\mathbf{x}_i$ represents the calculated value of L_s for the parameter set $\mathbf{x}_i$.

The basic method of obtaining the target inductance for a given $\mathbf{x}_i$ is to adjust the winding length l_{WS1}, using a binary search technique, until a match is obtained, to the nearest integer number of turns. The core dimensions can be manually adjusted to more closely meet the target inductance once the optimal solution has been found.

There are three constraint inequalities, given by

$$R_s^{\mathbf{x}_i} \leq R_{s,\max} \tag{7.10}$$

$$B_{\mathrm{pk}(0.99r_{2,\mathrm{CS1}},0)}^{\mathbf{x}_i} \leq B_{\mathrm{pk}(0.99r_{2,\mathrm{CS1}},0),\max} \tag{7.11}$$

$$(\frac{l_{\mathrm{WS1}}}{l_{\mathrm{CS1}}})_{\min} \leq \frac{l_{\mathrm{WS1}}}{l_{\mathrm{CS1}}}^{\mathbf{x}_i} \leq (\frac{l_{\mathrm{WS1}}}{l_{\mathrm{CS1}}})_{\max} \tag{7.12}$$

7.4.2.2 Specify bounds / sampling interval of region $\mathcal{R}_t$

Minimum and maximum values of core outer radius $r_{2,\mathrm{CS1,min}}$ and $r_{2,\mathrm{CS1,max}}$, core length $l_{\mathrm{CS1,min}}$ and $l_{\mathrm{CS1,max}}$, number of layers $n_{Ly(s),\min}$ and $n_{Ly(s),\max}$, secondary winding current-density $J_{s,\min}$ and $J_{s,\max}$ and their respective sampling intervals $\Delta_{r_{2,\mathrm{CS1}}}$, $\Delta_{l_{\mathrm{CS1}}}$, $\Delta_{n_{Ly(s)}}$ and Δ_{J_s} are specified, forming a trial region $\mathcal{R}_t$. $J_{s,\min}$ is equal to the typical current-density value used in continuously rated devices of 1-2 A/mm^2.

After evaluating a set of trial designs (all $\mathbf{x}_i \in \mathcal{R}_t$), the user can check how many solutions were obtained and which of the constraint inequalities (Eqs. 7.10 - 7.12) were not met. The bounds can then be adjusted accordingly.

7.4.2.3 Evaluate trial designs over $\mathcal{R}_t$

7.4.2.3.1 Evaluate kernel function The kernel function $K(\mathbf{x})$, shown in Figure 7.5, determines if a solution can be obtained for a particular $\mathbf{x}_i$. The function attempts to design the secondary (high-voltage) winding, from which it can be determined if the complete transformer could be designed for the given $\mathbf{x}_i$. If $\mathbf{x}_i \in \mathcal{R}_s$, the

solution region, another function, called the design function, is executed to complete the PCRTX design and calculate $f(\mathbf{x}_i)$.

Assuming that circular wire is used for the secondary winding and that $2\pi L_s >> R_{s,\max}$, the wire diameter is calculated using

$$d_s = \frac{\sqrt{2}}{\pi}\sqrt{\frac{V_s}{f L_s^{\mathbf{x}_i} J_s^{\mathbf{x}_i}}} \tag{7.13}$$

Next, it is determined if L_s can be obtained for the given $\mathbf{x}_i$ within the minimum and maximum allowable winding lengths (Eq. 7.12). The correct winding length, to the nearest integer turn, is then calculated using a binary search algorithm. The winding resistance is calculated to check the inequality of Eq. 7.10. Finally, the magnetic field value $B_{\mathrm{pk}(0.99r_{2,\mathrm{CS1}},0)}$ is calculated from the finite element model by driving the inductor with the peak value of ampere-turns excitation, calculated as

$$\text{A-t}_{\mathrm{pk}} = \frac{\sqrt{2}V_s}{R_s^{\mathbf{x}_i} + \omega L_s^{\mathbf{x}_i}} N_s^{\mathbf{x}_i} \tag{7.14}$$

where $N_s^{\mathbf{x}_i}$ is the calculated number of secondary turns for $\mathbf{x}_i$.

The number of times the finite element model is executed per trial design is given by

$$n_{\mathrm{simulations}} = \begin{cases} 3 + \log_2\left[\frac{l_{\mathrm{CS1}}[(\frac{l_{\mathrm{WS1}}}{l_{\mathrm{CS1}}})_{\max} - (\frac{l_{\mathrm{WS1}}}{l_{\mathrm{CS1}}})_{\min})]}{d+2t_{\mathrm{WI}}}\right] & \mathbf{x}_i \in \mathcal{R}_s \\ 2 & \mathbf{x}_i \notin \mathcal{R}_s \end{cases} \tag{7.15}$$

The running time of each simulation is approximately constant. It is impossible to know in advance if the chosen bounds are suitable (i.e. how many $\mathbf{x}_i \in \mathcal{R}_s$) but a worst-case estimate of the total number of simulations required for a particular $\mathcal{R}_t$ can be made.

7.4.2.3.2 Evaluate the design function The number of turns on the primary winding is estimated using the ideal transformer equation $V_p/V_s = N_p/N_s$. The number of full-length layers and the length of the partial-layer (if required) is calculated from the wire dimensions. The error in this approximation is shown for two sample PCRTXs in Table 7.1. Due to leakage flux, the ideal transformer equation tends to over-estimate the number of primary turns required, meaning that the required step-up ratio is not quite obtained. The introduction of a more realistic load quality factor $Q_l = 20$ tends to increase this effect. The correct number of turns can be obtained by re-running the finite element model, but this is not done for each trial solution to save computation time.

Once the design has been completed, $f(\mathbf{x}_i)$ is calculated using Eq. 7.7.

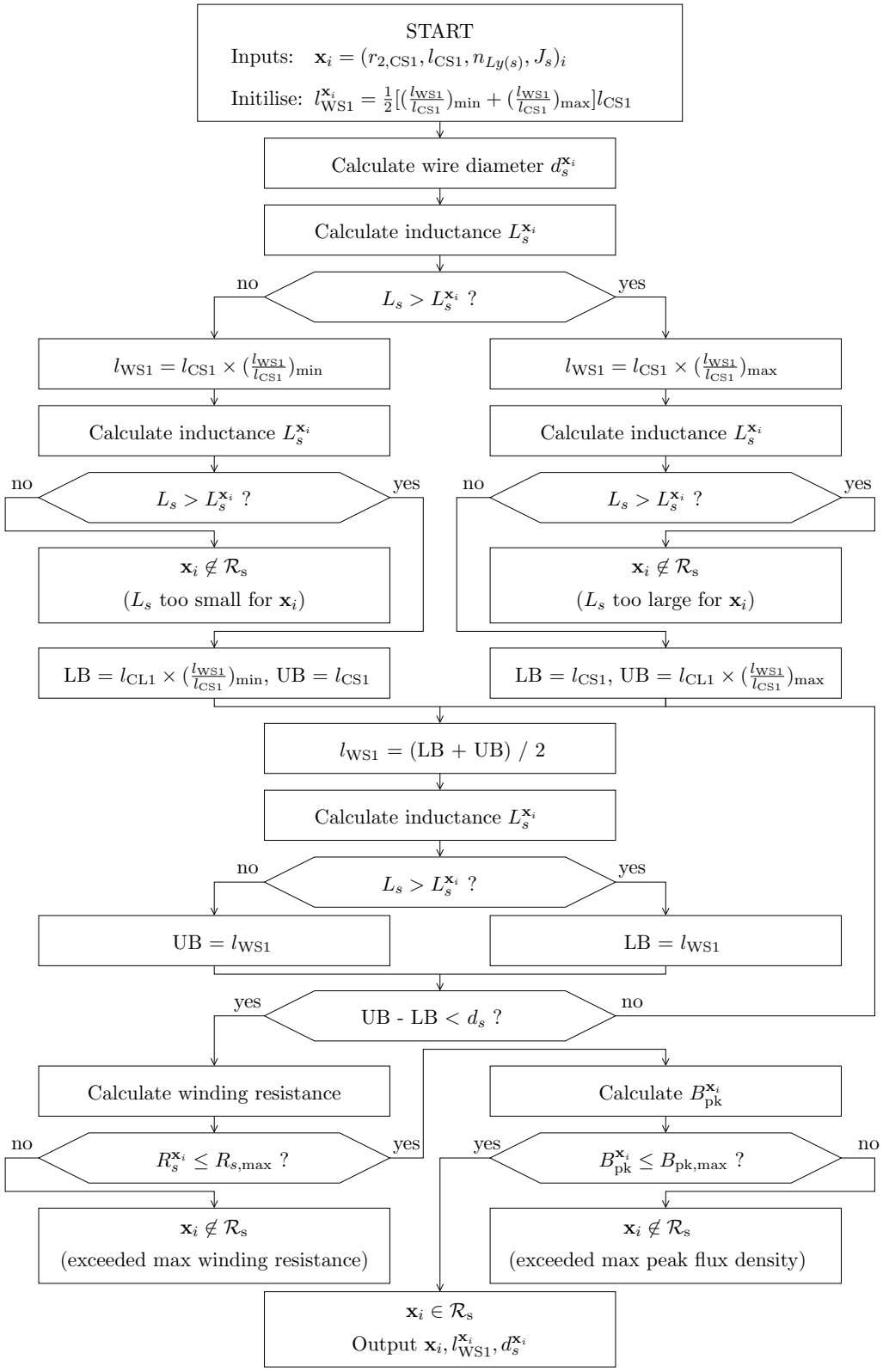

Figure 7.5 Evaluation of the kernel function $K(\mathbf{x})$ for a sample parameter set $\mathbf{x}_i \in \mathcal{R}_{\mathrm{t}}$ to determine if $\mathbf{x}_i \in \mathcal{R}_{\mathrm{s}}$.

Transformer	$(V_p/V_s)/(N_p/N_n)$	
	$Q_l = \infty$	$Q_l = 20$
Sample PCRTX with $r_{2,\mathrm{CS1}} = 120$ mm	1.24	1.25
Sample PCRTX with $r_{2,\mathrm{CS1}} = 40$ mm	1.15	1.17
PC2 from Chapter 5	1.01	1.01

Table 7.1 Calculated voltage to turn ratios for two different PCRTXs.

7.4.3 Review

After the optimisation process is complete, the next largest available wire size for the high-voltage winding should be chosen, rather than working with fictitious wire sizes. The winding length can be manually adjusted until the target inductance is obtained. The number of turns on the low-voltage winding can then be adjusted to meet the voltage ratio.

The design estimates can be compared to their initial values. $OEOL$ and SF_{eff} can be calculated using Eq. 6.35 of Section 6.10.1 and Eq. 6.17 of Section 6.5, respectively. T_{sf}, $t_{\mathrm{WI}p}$, $t_{\mathrm{WI}s}$, E_b, SF_e, FF_e and $t_{I,\mathrm{bf}}$ could be obtained experimentally, by constructing a mock-up device, or from previous experience. The former thickness FT can be adjusted to the nearest available standard size once the approximate core dimensions have been obtained. If any significant changes to the design estimates have been made, the design cycle can be repeated to find the new optimal solution.

7.4.4 Preliminary design complete

For short-term rated devices practical considerations to the construction can now be given. For devices with an on-time of more than a few minutes, eddy-current heating effects in the winding wire due to the stray magnetic field should be calculated. If these are too great, actions such as making the core length greater than the winding length, placing a larger gap between the core and inside winding, or reducing the core flux-density may be required. Continuously transposed conductor may be another option for high-current devices. Eddy-current losses can also be calculated using a magneto-static finite element model [Sullivan, 2001].

7.5 DESIGN EXAMPLE

7.5.1 Overview

The design methodology was applied to the first stage of a transformer kitset for high-voltage testing of hydro-generator stators. The key requirement was to energise stators in the capacitance range of 0 - 1.1 uF up to 36 kV from a 50 Hz supply. For this fixed

inductance design example, L_s was matched to the largest value of load capacitance, where the secondary volt-amperes and core cross-sectional area requirements are the greatest. The paper design produced is to be considered a starting point for the final device. L_s could be made variable by adding tapping winding sections and / or by constructing the core in two axial pieces and adjusting the centre air-gap. However, since it was designed for minimum weight with fixed inductance, not minimum weight over a specified inductance range, the core dimensions may not be optimal for this application. A revised design methodology is developed for variable inductance devices in Chapter 8.

7.5.2 Initial considerations

A nominal primary voltage of 400 V was chosen, which can be obtained across two phases of a three-phase supply. The inter-layer insulation and on-time requirements were based around performance demonstrations, requested for another PCRTX by the client prior to stator testing [Bodger and Enright, 2004]. The device was required to energise capacitors from an inverted Marx impulse generator to 40 kV and maintain the test voltage for three minutes.

The 5-10-5 grade of Nomex-Mylar-Nomex (NMN) was chosen for the inter-layer insulation due to its high dielectric strength of 22 kV, temperature rating of 180°C and success in previous designs. A fiberglass cylinder with a 3 mm wall thickness is to be used for the former. A local manufacturer was found with capability to produce to specification, meaning that a compromise to the nearest available standard size would not be required. An additional 5.5 mm was added between the core outer-radius and former to account for the core binding process and to allow for easy insertion of the core into the former. Sylgard 170 Silicone Elastomer was the chosen encapsulant, with a dielectric strength of 18.9 kV/mm and temperature rating of 200°C. The copper wire to be used is insulated with polyesterimide resin, having a temperature rating of 180°C.

$Z_{\text{in,min}}$ was calculated using Eq. 6.22 of Section 6.6 with $I_{\text{su,max}} = 160$ A and $SF_Z = 2$. The variac normally used for testing has a rated current of 70 A, but, as per manufacturer's guidelines, it can be overloaded to 190 A for up to four minutes. It would be supplied with a 160 A fuse in this case. Q_l and T_{ambient} were set to 20 and 35°C, respectively. The complete list of variables in the Initial Considerations section of Figure 7.4 are shown in Table 7.2. For clarity, material properties are omitted.

7.5.3 Multiple design method

The multiple design method is demonstrated for the design example in Table 7.3. Two trial regions, $\mathcal{R}_{t,1}$ and $\mathcal{R}_{t,2}$, were required to obtain a good estimate of the optimal solution. The bounds were made relatively wide and the sampling intervals were made

Functional specifications			Design estimates (cont.)		
V_p	400	V	$t_{\mathrm{WI}p}$	0.1	mm
V_s	36	kV	$t_{\mathrm{WI}s}$	0.04	mm
F	50	Hz	E_b	500	kV/m
C_l	1.1	uF	SF_e	2.5	-
Q_l	20	-	FT	8.5	mm
$Z_{\mathrm{in,min}}$	5	Ω	FF_e	0.5	-
$t_{\mathrm{on,max}}$	180	s	$t_{I,\mathrm{bf}}$	0.6	-
T_{ambient}	35	°C	Preliminary calculations		
Other specifications			L_s	9.21	H
$J_{s,\mathrm{min}}$	2	A/mm^2	$J_{s,\mathrm{max}}$	10.1	A/mm^2
$r_{1,\mathrm{CS1}}$	12.5	mm	$J_{p,\mathrm{max}}$	6.9	A/mm^2
EOL	25	mm	$R_{s,\mathrm{max}}$	62.1	Ω
Material restrictions			$n_{Ly,\mathrm{min}}$	15	-
T_{max}	180	°C	COL	25	mm
$(V/L)_{\mathrm{max}}$	5	kV	θ_m	95	°C
$B_{\mathrm{pk}(0.99r_{2,\mathrm{CS1}},0)}$	1.2	T	$CSA_{p,\mathrm{min}}$	11.5	mm^2
Design estimates			Primary winding		
$OEOL$	26.6	mm	$WW1_p$	2.5	mm
T_{sf}	50	°C	$WW2_p$	4.0	mm
SF_{eff}	1	-			

Table 7.2 Initial considerations for the design example.

relatively coarse in the first region. In the second, the region bounds were reduced and the sampling intervals were increased, to narrow in on the optimal solution.

Prior to evaluating the trial designs over $\mathcal{R}_{t,1}$ the average time per simulation was measured at approximately 4 seconds on a standard desktop PC. The maximum number of simulations per trial design was calculated to be 11, using Eq. 7.15 with $(\frac{l_{\mathrm{WS1}}}{l_{\mathrm{CS1}}})_{\mathrm{min}} = 1.0$, $(\frac{l_{\mathrm{WS1}}}{l_{\mathrm{CS1}}})_{\mathrm{max}} = 1.5$ and $d_{\mathrm{min}} = 1.25$ mm, giving an estimated worst-case execution time of 18 hours. The task was split over three personal computers, allowing the complete simulation to be completed overnight. The actual CPU time required to evaluate regions $\mathcal{R}_{t,1}$ and $\mathcal{R}_{t,2}$ was 10 and 13 hours respectively. $\mathcal{R}_{t,2}$ had less trial designs than $\mathcal{R}_{t,1}$, 2079 compared to 2970, but more of them were $\in \mathcal{R}_s$.

7.5.4 Review

The calculated wire size $d_s = 1.2534$ mm was reduced slightly to the nearest available size of 1.25 mm. The length of the high-voltage winding did not require adjustment to account for this change. The calculated voltage ratio for a load quality factor $Q_l = 20$ was correct to the nearest turn, so the length of the primary winding did not need to be adjusted either. The input impedance was calculated to be 4.83 Ω, giving an input impedance scale-factor of $SF_{\mathrm{eff}} = 0.97$. Using the design estimate of $OEOL$ the associated safety factor was 1.22. These two parameters were judged to be acceptable.

Trial region $\mathcal{R}_{t,1}$ (total samples = 2970)							
Bounds and sampling interval							
Variable	Minimum			Maximum		Interval	
$r_{2,\mathrm{CS1}}$, mm	100			150		10	
l_{CS1}, mm	200			600		50	
$n_{Ly(s)}$	15			25		1	
J_s, A/mm^2	2			10.1		2	
Five most optimal solutions							
$\mathbf{x}_i$				Restrictions			$f(\mathbf{x}_i)$, kg
$r_{2,\mathrm{CS1}}$, mm	l_{CS1}, mm	$n_{Ly(s)}$	J_s, A/mm^2	R_s, Ω	B_{pk}, T	$l_{\mathrm{CS1}}/r_{2,\mathrm{CS1}}$	
120	250	20	10.1	60.3	1.20	1.1	136.1
120	200	25	8.1	56.3	1.15	1.3	141.5
120	200	24	8.1	56.9	1.15	1.4	142.0
120	250	22	8.1	50.1	1.19	1.1	150.1
120	300	16	10.1	58.7	1.20	1.1	150.7
Trial region $\mathcal{R}_{t,2}$ (total samples = 2079)							
Bounds and sampling interval							
Variable	Minimum			Maximum		Interval	
$r_{2,\mathrm{CS1}}$, mm	118			122		2	
l_{CS1}, mm	200			300		5	
$n_{Ly(s)}$	15			25		1	
J_s, A/mm^2	8.1			10.1		2	
Five most optimal solutions							
$\mathbf{x}_i$				Restrictions			$f(\mathbf{x}_i)$, kg
$r_{2,\mathrm{CS1}}$, mm	l_{CS1}, mm	$n_{Ly(s)}$	J_s, A/mm^2	R_s, Ω	B_{pk}, T	$l_{\mathrm{CS1}}/r_{2,\mathrm{CS1}}$	
122	210	25	10.1	61.8	1.20	1.0	127.7
118	200	24	9.1	61.4	1.19	1.3	129.9
122	220	24	10.1	60.8	1.20	1.0	130.1
118	205	24	9.1	60.1	1.20	1.3	130.3
120	200	25	9.1	59.8	1.18	1.2	130.9

Table 7.3 Design example illustrating the multiple design method.

A mock-up device would need to be built in order to determine the validity of the other design estimates.

7.6 CONCLUSIONS

A design methodology for high-voltage partial-core resonant transformers with fixed inductance has been developed. Magnetic field and inductance characteristics for transformers having different core aspect and winding length to core length ratios were calculated using a finite element model. These were used to place restrictions on field values and device dimensions. A design methodology was introduced and then illustrated with a design example, where the first stage of a transformer kitset for high-voltage testing of hydro-generator stators was developed. The design example is modified to allow for tuning capability in Chapter 8.

Chapter 8

DESIGN METHODOLOGY FOR HIGH-VOLTAGE PARTIAL-CORE RESONANT TRANSFORMERS WITH VARIABLE INDUCTANCE

8.1 OVERVIEW

A design methodology for high-voltage partial-core resonant transformers with variable inductance is described. The methods include centre-gap tuning, tap selection or a combination of both techniques. Larger variations can be obtained using multiple devices. Design strategies are developed for each method, building on previous work in the design of fixed inductance devices. The methodology is illustrated with three design examples, each having a different inductance range. Devices utilising each method of inductance variation are obtained for each inductance range and the device weights are compared. The design examples include two replacement transformers and a new kitset for high-voltage testing, with the capability to test any hydro-generator stator in New Zealand as well as set the sphere gaps, replacing the multi-tonne equipment normally used.

8.2 DESIGN METHODOLOGY FOR VARIABLE INDUCTANCE

Modifications to the design methodology for fixed inductance devices of Chapter 7 which are applicable to all types of variable inductance devices are described in this section.

8.2.1 Initial considerations

8.2.1.1 Functional specifications

Minimum and maximum values of load capacitance $C_{l,\min}$ and $C_{l,\max}$ are specified. The minimum and maximum secondary winding self-inductance values are given by

$$L_{s,\min} = \frac{1}{\omega_s^2 C_{l,\max}} \tag{8.1}$$

$$L_{s,\max} = \frac{1}{\omega_s^2 C_{l,\min}} \tag{8.2}$$

where $\omega_s = 2\pi f_s$.

For some devices, operation under open-circuit conditions may also be a requirement. For example, in high-voltage insulation testing applications, spheres are usually employed, with the gap set to 20% above the test voltage, to protect equipment against accidental overvoltage. By designing for operation under resonant and open-circuit conditions, a single device can be used for both insulation testing and sphere-gap setting.

The minimum value of $L_{s,\max}$ for operation under open-circuit conditions can be calculated by considering the input impedance of $L_{s,\max}$ referred through an ideal transformer, having voltage ratio V_p/V_s, giving:

$$L_{s,\max} = \left(\frac{V_s}{V_p}\right)^2 \frac{Z_{\text{in,min}}}{\omega_s} SF_{\text{oc}} \tag{8.3}$$

where V_p and V_s are the primary and secondary voltages, $Z_{\text{in,min}}$ is the minimum input impedance for the resonant circuit and $SF_{\text{oc}} = 2$ is a scale factor to ensure that the primary current under open-circuit conditions is approximately one-half of the largest value under resonant conditions.

The maximum secondary winding resistance $R_{s,\max}$ (Eq. 6.25 of Section 6.6) is modified to

$$R_{s,\max} = \frac{1}{\omega_s^2 C_{l,\max}^2} \left(\frac{V_p}{V_s}\right)^2 \frac{1}{Z_{\text{in,min}}} SF_{\text{eff}} - \frac{1}{\omega_s Q_l C_{l,\max}} \tag{8.4}$$

where SF_{eff} is the scale factor between the design-value and analytical input impedance, and Q_l is the load quality factor.

8.3 CORE CENTRE-GAP TUNING

Modifications to the design methodology for fixed inductance devices which are applicable to centre-gap tuned variable inductance devices are described in this section.

8.3.1 Magnetic field calculations

As shown in Section 7.3, for partial-core transformers having fixed inductance and one core section, there are two different types of magnetic field distributions that can occur within the core. In devices having relatively long thin partial-cores, the peak value of magnetic field is located at the axial centre-line, just inside the core outer-radius. As the partial-core becomes shorter and wider, the magnetic field distribution changes significantly. There are now two peak values, located at the top and bottom of the core, just inside the core outer-radius. A design-value for the peak magnetic field, sampled at the axial centre-line, just inside the core outer radius, was established for either type of field distribution as $B_{\mathrm{pk}(0.99r_{2,\mathrm{CS1}},0)} = 1.2$ T.

Of interest is the change in magnetic field shape which occurs when a PCRTX of fixed inductance is made variable by dividing the partial-core into two axial sections and placing an air-gap between the two sections. This is known as centre-gap tuning. Field plots were generated for the same sample PCRTX used in Section 7.3, which was modified to allow for centre-gap tuning. The plots, shown in Figure 8.1, indicate that there are still two different types of magnetic field distributions that can occur in devices which are centre-gap tuned. In Section 6.2.3 it was found that the peak value of magnetic field did not increase significantly in a sample PCRTX when the air centre-gap was increased, provided that the device remained tuned and the secondary voltage was constant. This suggests that the design-value and sampling location of the peak magnetic field which was used for fixed inductance devices may also be applicable to devices which are centre-gap tuned.

For a fixed inductance device with one core section, the operating point is defined as the peak value of ac current which produces a peak value of magnetic field equal to the design-value, typically 1.2 T. The operating point is defined in the same way for a centre-gap tuned variable inductance device when the centre-gap is set to zero. For all other centre-gap values, the operating point is defined as the above calculated peak value of ac current multiplied by the ratio of inductances for a centre-gap of zero to the given centre-gap. The operating points and inductance / current characteristics for the two different configurations of the sample PCRTX of Figure 8.1 were calculated for different values of air centre-gap using linear and non-linear core models. The same B-H curve used in Chapters 3 and 7 was employed for the non-linear model. The results, shown in Figure 8.2, indicate that all of the operating points on both of the sample centre-gap tuned devices are below the saturation level. The method of field sampling and design-value of peak magnetic field for fixed-inductance devices was thus applicable to these example centre-gap tuned devices.

This characteristic is assumed to hold for all centre-gap tuned devices and is used as part of the design process. Once an optimal solution of a given design has been obtained, the

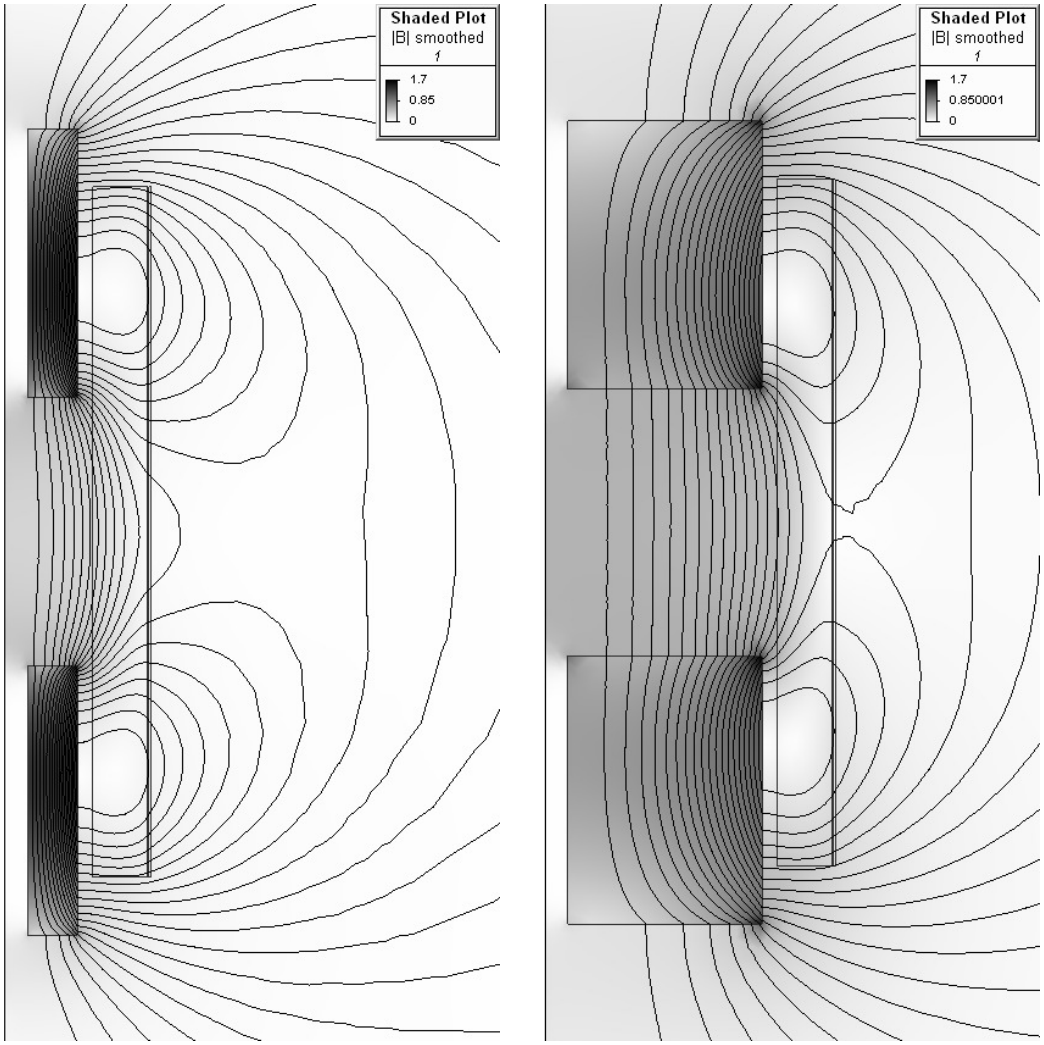

(a) core length / core radius = 7.4, centre-gap = 148 mm

(b) core length / core radius = 2.5, centre-gap = 148 mm

Figure 8.1 Magnetic field of a sample PCRTX having two core sections with a large centre-gap for two different values of core radii with the peak magnetic field value maintained at 1.7 T.

secondary inductance can be calculated at the operating points of several different air centre-gap values. If saturation occurs at any of these points, the assumed characteristic is false. This can be compensated for by repeating the same design process with a reduced design-value of peak magnetic field.

8.3.2 Initial considerations

8.3.2.1 Other specifications

The minimum and maximum allowable air centre-gaps $d_{\min}$ and $d_{\max}$ are specified. $d_{\min}$ is typically 3-5 mm to allow for a layer of resin to be applied to the core faces. For smaller

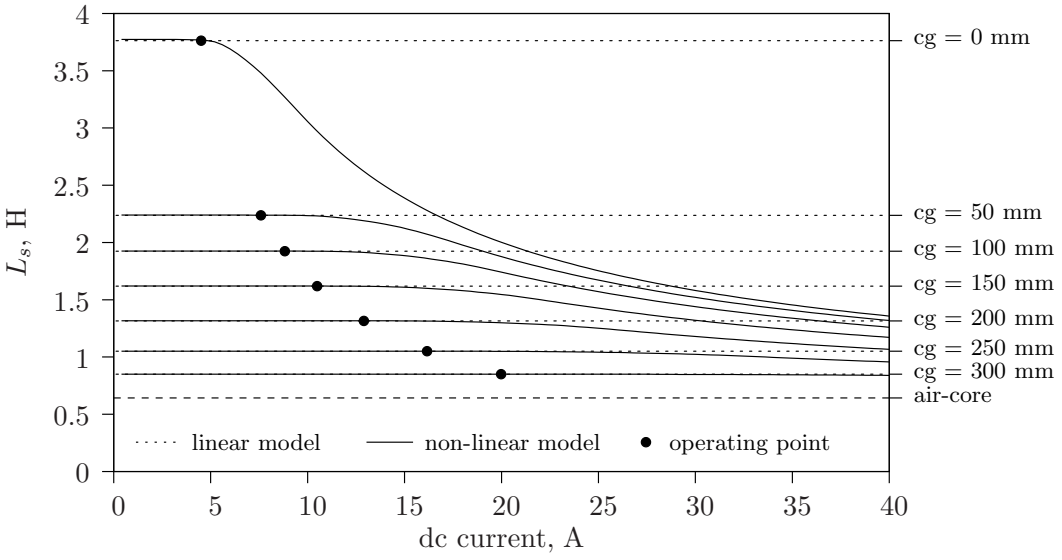

(a) core length / core radius = 7.4.

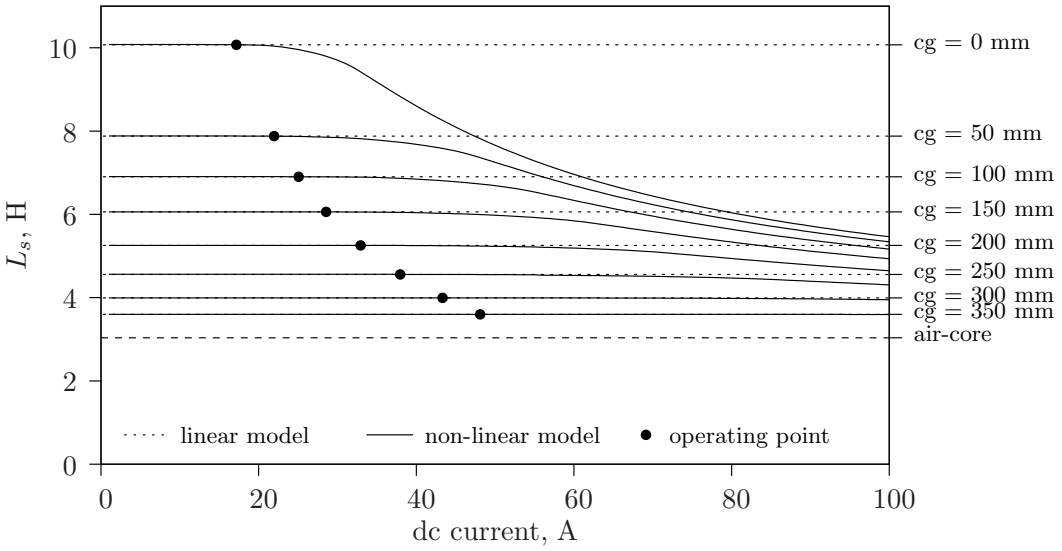

(b) core length / core radius = 2.5.

Figure 8.2 Linear and non-linear core models compared for a sample PCRTX having two core sections with two different values of core radii for different air centre-gap (cg) values.

cores, whose individual core sections can be moved by hand, a set of polyethylene spacers can be used to manually adjust the centre-gap. For larger cores or for automated tuning systems, the air-gap can be made adjustable using a spindle with left- and right-handed threads on the ends, as used on some earlier arc-suppression coils [Meyerhans, 1945]. $d_{\max}$ is expressed as a percentage of the core length and is normally set to 50-100%.

8.3.3 Multiple design method

8.3.3.1 Overview

The single constraint equation (Eq. 7.9 of Section 7.4.2.1) is modified to

$$L_{s(d=d_{\min})} = L_{s,\max} \tag{8.5}$$

An extra constraint inequality is added:

$$L_{s(d=d_{\max})} \leq L_{s,\min} \tag{8.6}$$

8.3.3.2 Evaluate trial designs over $\mathcal{R}_t$

The kernel function of the fixed inductance design methodology is modified to account for the changes. The target inductance becomes $L_{s,\max}$, designed around $d = d_{\min}$. The peak value of magnetic field is calculated with $d = 0$, for the reasons described in Section 8.3.1. The inductance at $d = d_{\max}$ is calculated to ensure that it is less than $L_{s,\min}$. The revised kernel function $K(\mathbf{x})$ is shown in Figure 8.3. It requires two more executions of the finite element model than the fixed inductance one.

8.3.3.3 Review

As discussed in Section 7.4.2.3.2, the voltage ratio is not exactly equal to the turns ratio in PCRTXs. For centre-gap tuned devices, the voltage ratio is a function of centre-gap. This characteristic is shown for two sample PCRTXs in Figure 8.4. The voltage ratio is reduced by the load quality factor $Q_l = 20$ and the leakage reactance. The reduction of voltage ratio and variation over centre-gap displacements is least for PC2 which has the largest aspect ratio and smallest leakage reactance. The voltage gain of the other sample PCRTX could be increased by removing turns from the primary winding. Taps could be placed on the primary winding to reduce the variation in voltage gain over the centre-gap operating range.

8.4 CENTRE-GAP + TAP TUNING

Modifications to the design methodology for fixed inductance devices which are applicable to centre-gap + tap tuned variable inductance devices are described in this section.

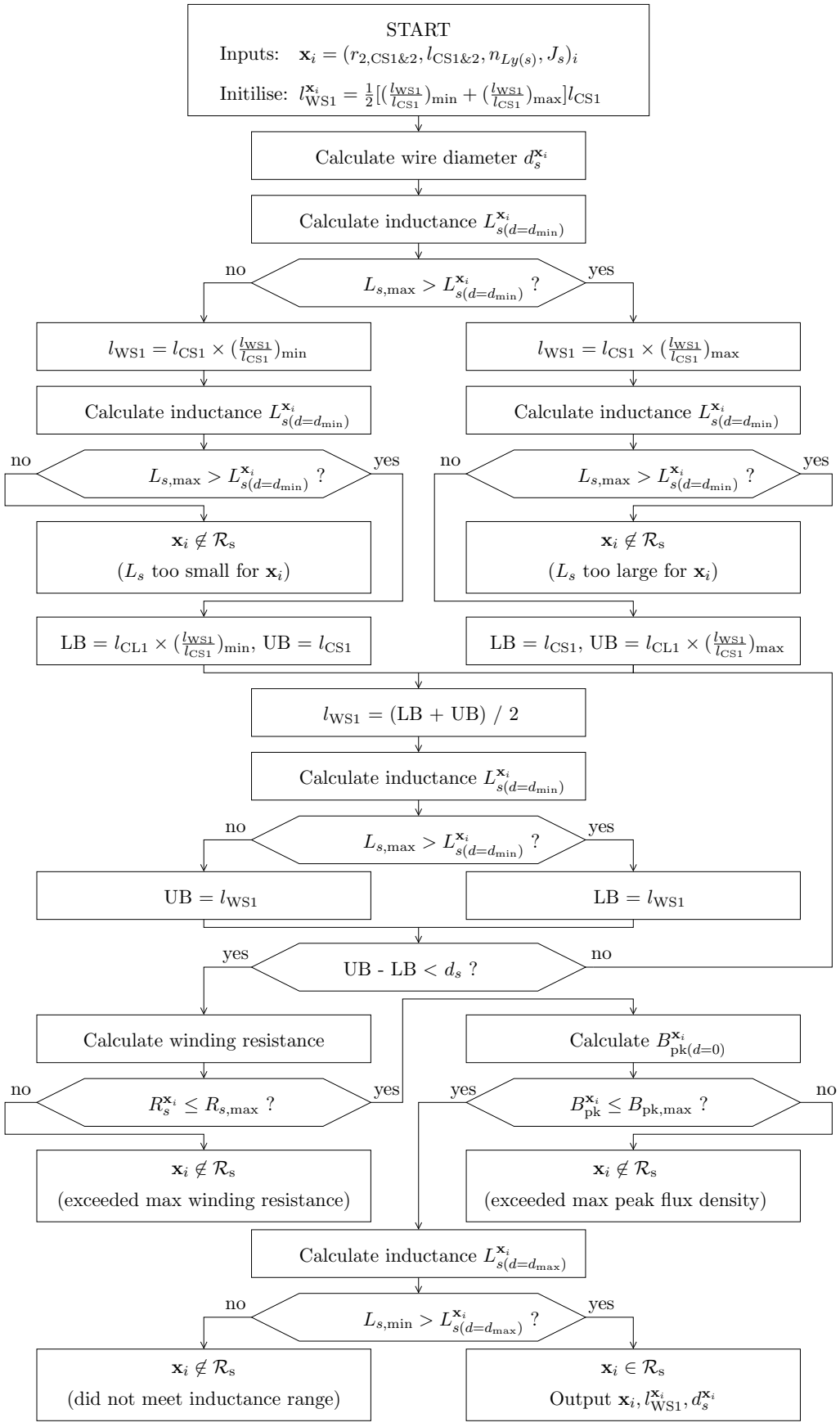

Figure 8.3 The kernel function $K(\mathbf{x})$ for centre-gap tuned devices. A sample parameter set $\mathbf{x}_i \in \mathcal{R}_{\mathrm{t}}$ is evaluated to determine if $\mathbf{x}_i \in \mathcal{R}_{\mathrm{s}}$. (LB = lower bound, UB = upper bound)

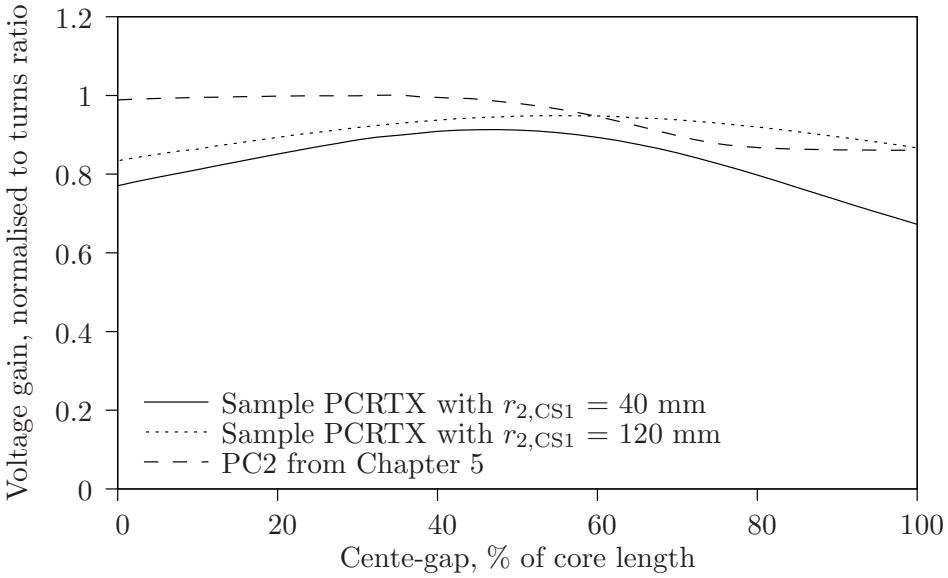

Figure 8.4 Calculated voltage gain as a function of centre-gap for two different PCRTXs.

8.4.1 Extension of tuning range

Consider a PCRTX having a resonant capacitance range ($C_{l,\mathrm{min}}$ — $C_{l,\mathrm{max}}$) which is achieved using centre-gap tuning. The range can be extended by decreasing the minimum resonant capacitance from $C_{l,\mathrm{min}}$ to $C'_{l,\mathrm{min}}$ by adding a tapping winding section to the secondary winding. The advantage of doing so is that, in some cases, it allows for a significant reduction in the device weight $f(\mathbf{x})$ (defined by Eq. 7.7 of Section 7.4.2.1) from what would be achieved with a centre-gap tuned device having the same total range ($C'_{l,\mathrm{min}}$ — $C_{l,\mathrm{max}}$). This is because the layers in the tapping winding section do not contribute to the wire resistance restriction, allowing for higher current-densities and a reduced core aspect ratio. However, centre-gap + tap tuned devices are more complex to manufacture and operate. Both options should be evaluated as part of the design process so that the most suitable design can be obtained.

There is also the possibility of using tap tuning only. The mismatch of reactive power could be compensated for by connecting a Statcom to the primary winding [Bendre et al., 2008] and thyristor-based switches could be used to select the taps. This would allow for an automated tuning system to be developed with no moving parts.

Assuming that the secondary winding is formed using just the main winding section of the high-voltage winding (denoted WS1) and that $\omega L_{WS1} >> R_{WS1}$, the voltages induced in the main winding section and the first layer of the tapping winding section (denoted WS2) are given by

$$v_{\mathrm{WS1}} \ \ (= V_s) = L_{\mathrm{WS1}}\frac{di_s}{dt} + M_{\mathrm{WS1}-p}\frac{di_p}{dt} \tag{8.7}$$

$$v_{\mathrm{WS2}} = M_{\mathrm{WS1\text{-}WS2}}\frac{di_s}{dt} + M_{\mathrm{WS2}-p}\frac{di_p}{dt} \tag{8.8}$$

where L and M are self- and mutual-inductances, i_p and i_s are the primary and secondary currents and $M_{\mathrm{WS}i-p}$ is the mutual inductance between WSi and the primary winding.

Assuming that the secondary circuit is loaded with a capacitance C_l which is tuned to the supply frequency ω_s such that $\omega_s = 1/\sqrt{L_{\mathrm{WS1}}C_l}$ and that the circuit quality factor Q is greater than 10, the contribution of the primary current to the induced voltage in the high-voltage winding can be neglected. Assuming ideal coil coupling ($M_{\mathrm{WS1\text{-}WS2}}/\sqrt{L_{\mathrm{WS1}}L_{\mathrm{WS2}}} = 1$), an expression for L_{WS2} can be obtained by rearranging Eqs. 8.7 & 8.8 for $\frac{di_s}{dt}$ and equating them, giving

$$L_{\mathrm{WS2}} = L_{\mathrm{WS1}}\left(\frac{V_{\mathrm{WS2}}}{V_s}\right)^2 \tag{8.9}$$

The upper-limit for V_{WS2} is $(V/L)_{\max}/2$, where $(V/L)_{\max}$ is the maximum allowable voltage per layer of insulation. Hence the following inequality must be satisfied

$$L_{\mathrm{WS2}} \leq L_{\mathrm{WS1}}\frac{(V/L)^2_{\max}}{4V_s^2} \tag{8.10}$$

Assuming a constant permeance P over the winding window, an approximation in partial-core transformers (see Section 6.8), L_{WS2} ($= N^2_{\mathrm{WS2}}P$) can be written in terms of L_{WS1} as

$$L_{\mathrm{WS2}} = L_{\mathrm{WS1}}\frac{(T/L)^2_{\mathrm{WS2}}}{(T/L)^2_{\mathrm{WS1}}n^2_{\mathrm{Lys(WS1)}}} \tag{8.11}$$

where $(T/L)_{\mathrm{WS1}}$ and $(T/L)_{\mathrm{WS2}}$ are the turns per layer in winding sections 1 and 2 and $n_{\mathrm{Lys(WS1)}}$ is the number of layers in winding section 1.

An upper-limit for $(T/L)_{\mathrm{WS2}}$ can be obtained by equating Eqs. 8.10 & 8.11:

$$(T/L)_{\mathrm{WS2,max}} = (T/L)_{\mathrm{WS1}}\frac{n_{\mathrm{Lys(WS1)}}(V/L)_{\max}}{2V_s} \tag{8.12}$$

In order to encapsulate the high-voltage winding, the length of the tapping winding section must be the same as the main winding section (i.e. $l_{\mathrm{WS2}} = l_{\mathrm{WS1}}$). An initial estimate of the wire diameter on the first layer of the tapping winding section is obtained by assuming $(T/L)_{\mathrm{WS2}} = (T/L)_{\mathrm{WS2,max}}$, giving

$$d_{\mathrm{WS2}}^{\mathrm{est}} = \frac{l_{\mathrm{WS1}}}{(T/L)_{\mathrm{WS2,max}}} - 2WIT \tag{8.13}$$

where WIT is the wire insulation thickness.

The minimum wire diameter on the first layer of the tapping winding section $d_{\mathrm{WS2,min}}$ can be obtained from the thermal upper-limit of current-density $J_{\max}$ and the maximum winding current when voltage V_s is applied. This is equal to the secondary current in the high-voltage winding when just winding section 1 is connected, since $L_{\mathrm{WS1\text{-}2}}$ must be tunable to $L_{\mathrm{WS1}(d=d_{\min})}$. The maximum current through winding section 2 is thus

$$I_{\mathrm{WS1\text{-}2,max}} = \frac{V_s}{j\omega((T/L)_{\mathrm{WS1}} n_{\mathrm{Lys(WS1)}})^2 P} \tag{8.14}$$

P can be calculated from the first winding section of the optimal centre-gap tuned solution, obtained from the multiple design method. $d_{\mathrm{WS2,min}}$ is calculated for circular wire from $I_{\mathrm{WS1\text{-}2,max}}$ and $J_{\max}$ as

$$\begin{aligned} d_{\mathrm{WS2,min}} &= \sqrt{\frac{4I_{\mathrm{WS1\text{-}2,max}}}{\pi J_{\max}}} \\ &= \frac{2}{(T/L)_{\mathrm{WS1}} n_{\mathrm{Lys(WS1)}}} \sqrt{\frac{V_s}{\pi\omega P J_{\max}}} \end{aligned} \tag{8.15}$$

d_{WS2} and $(T/L)_{\mathrm{WS2}}$ are given by

$$d_{\mathrm{WS2}} = \begin{cases} d_{\mathrm{WS2}}^{\mathrm{est}}, & d_{\mathrm{WS2}}^{\mathrm{est}} \geq d_{\mathrm{WS2,min}} \\ d_{\mathrm{WS2,min}}, & \text{otherwise} \end{cases} \tag{8.16}$$

$$(T/L)_{\mathrm{WS2}} = \begin{cases} (T/L)_{\mathrm{WS2,max}}, & d_{\mathrm{WS2}}^{\mathrm{est}} \geq d_{\mathrm{WS2,min}} \\ l_{\mathrm{WS1}}/(d_{\mathrm{WS2,min}} + 2WIT), & \text{otherwise} \end{cases} \tag{8.17}$$

L_{WS2} is limited by the voltage rating of the inter-layer insulation $(V/L)_{\max}$ if $d_{\mathrm{WS2}}^{\mathrm{est}} \geq d_{\mathrm{WS2,min}}$, or by thermal upper-limit of current-density $J_{\max}$ otherwise.

Assuming there are $n_{\mathrm{Lys(TWS)}}$ layers in the tapping winding section, the upper-limit of which is determined by lead-out clearances in air (discussed in Section 6.10.2) and that $d_{\mathrm{WS2}}^{\mathrm{est}} \geq d_{\mathrm{WS2,min}}$, $C'_{l,\min}$ is given by

$$C'_{l,\min} = C_{l,\min} \frac{1}{(1 + n_{\mathrm{Lys(TWS)}} \frac{(V/L)_{\max}}{2V_s})^2} \tag{8.18}$$

The first part of the kernel function for centre-gap + tap tuned devices is the same

as the kernel function for centre-gap tuned devices, with $L_{s,\min}$ being calculated from $C_{l,\min}$ not $C'_{l,\min}$. $n_{\text{Lys(TWS)}}$ 1-layer winding sections are then added to the high-voltage winding.

8.4.2 Input impedance over tapping winding sections

As shown in Section 4.5, the input impedance of a PCRTX with capacitive load C_l tuned to the supply frequency ω_s such that $\omega_s = 1/\sqrt{L_s C_l}$, is given by

$$Z_{\text{in}} = R_p + \left(\frac{\omega_s^2}{R'_s}\right)\left(M_{ps}^2\right) + j\omega_s L_p \tag{8.19}$$

where R_p is the primary winding resistance and $R'_s = R_s + \frac{1}{\omega C_l Q_l}$ is the resistance of the secondary circuit.

Assuming that $(\frac{\omega_s^2}{R'_s})(M_{ps}^2) >> R_p$ and $\text{Re}\{Z_{\text{in}}\} >> \text{Im}\{Z_{\text{in}}\}$, the input impedance when the secondary circuit is formed from winding sections 1 to n is given by

$$Z_{\text{in(WS1-}n\text{)}} = Z_{\text{in(WS1-1)}}\frac{(M_{ps}^2/R'_s)_{\text{WS1-}n}}{(M_{ps}^2/R'_s)_{\text{WS1-1}}} \tag{8.20}$$

Intuitively, M_{ps} will increase as additional winding sections are connected because the space between the primary and secondary windings decreases. Assuming that $V_p/V_s = N_p/N_s$, the voltage gain will increase as additional winding sections are connected to form the secondary circuit. These two concepts together suggest that as additional taps are connected, the input impedance increases and the primary voltage required to maintain a constant secondary voltage decreases. This implies that, for the purposes of ensuring that the variac fuse does not operate, taps are not required on the low-voltage winding for devices which employ centre-gap + tap tuning.

Z_{in} and V_s/V_p were calculated at each tap for the sample PCRTX analysed in Section 6.2 with the centre-gap set to its minimum value. The results, shown in Figure 8.5, agree with the above assumptions. This characteristic is assumed to hold true for all centre-gap + tap tuned devices and is used as part of the design process. Once the optimal solution for a particular design has been obtained, Z_{in} and V_s/V_p can be calculated to check that the assumption holds.

In accordance with Eq. 8.3, taps are still required on the low-voltage winding if the device is designed to operate under open-circuit conditions as well as resonant conditions.

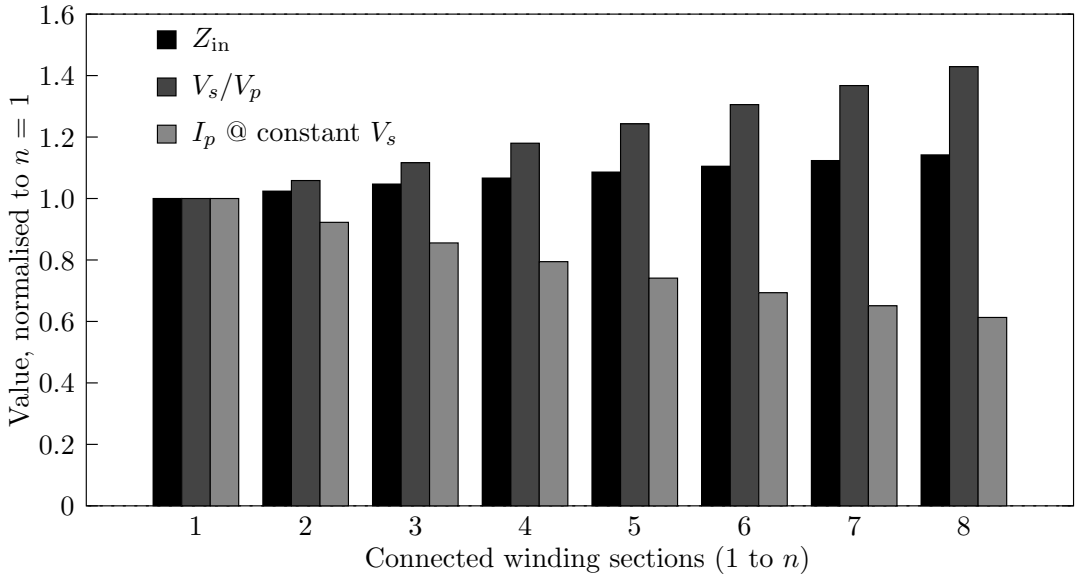

Figure 8.5 Input impedance, voltage gain and primary current for a sample PCRTX having 7 tapping winding sections with the centre-gap set to the minimum value.

8.5 MULTIPLE DEVICES

Full-core reactors can be designed with a tuning ratio of up to 20:1 [Hauschild et al., 2002]. As the ratio becomes larger, the minimum air-gap becomes smaller and the device starts to become non-linear, even when operating at reduced flux-densities. Similar effects were observed in partial-core transformers in Chapter 5. Multiple devices are required to achieve larger tuning ratios. There is also the possibility of reducing $f(\mathbf{x})$ by using multiple devices even for smaller ratios.

The resonant capacitance range ($C_{l,\min}$ — $C_{l,\max}$) can be divided into n sub-ranges, each corresponding to a separate PCRTX. It is assumed that $f(\mathbf{x})$ for the n PCRTXs will be minimised if the tuning ratio is the same for each PCRTX, equal to $\sqrt[n]{C_{l,\max}/C_{l,\min}}$:1. Overlaps in the tuning range between PCRTXs are not explicitly specified. They can be accounted for by working outside the air centre-gap range ($d_{\min}$ — $d_{\max}$).

8.6 DESIGN EXAMPLES

The fixed design example of Section 7.5 was modified to have variable inductance. $C_{l,\max}$ was maintained at 1.1 uF and three different values of $C_{l,\min}$ were considered. For each target range ($C_{l,\min}$ — $C_{l,\max}$), the different methods of inductance variation were applied and the optimal solution for each method was obtained. For the centre-gap tuned devices, $d_{\min}$ was set to 5 mm and $d_{\max}$ was set to 80% of the total core length. For the centre-gap + tap tuned devices, a tap-tuning ratio $C_{l,\min}/C'_{l,\min}$ of 2 was chosen. This ratio was chosen as a compromise between achieving a significant reduction in

$f(\mathbf{x})$ without greatly increasing operational complexity. Given $V_s = 36$ kV and $(V/L)_{\max} = 5$ kV, a minimum of 6 layers are required to achieve this ratio (using Eq. 8.18). In order to maintain the inequality $15 \leq n_{\text{Lys}} \leq 25$, which was applied to the fixed inductance and centre-gap tuned variable inductance devices, it is required that $15 \leq n_{\text{Lys(MWS)}} \leq 19$ for the centre-gap + tap tuned devices.

For each design example, the multiple design method was first applied with a peak magnetic field value of 1.2 T. After the optimal design was obtained, the assumption of Section 8.3.1 was tested by calculating the inductance at the operating point for several different centre-gap values using linear and non-linear models. The assumption was considered false if the inductance of the non-linear model dropped below the inductance of the linear model. If this occurred, the design process was repeated with a reduced value of peak magnetic field, in increments of 0.1 T, until the inductance of the non-linear model was higher than the inductance of the linear model for all centre-gap values over the centre-gap tuning range.

For centre-gap + tap tuned devices, the target $C'_{l,\min}$ will not be obtained if $d^{\text{est}}_{\text{WS2}} < d_{\text{WS2,min}}$ (which is unknown at design-time), meaning that one or more layers must be added to the tapping winding section. The wire size of the main winding section (and tapping winding section for centre-gap + tap tuned devices) is increased to the next largest available wire size. An attempt is made to maintain the same inductance in the main winding section by increasing the winding length so that the number of turns is maintained. This is strictly only valid if the permeance of the winding cross-section does not change as the length increases.

For each design, the number of primary winding turns was modified so that the design-value voltage ratio was maintained as closely as possible over the centre-gap tuning range. The safety factor for the distance between the low-voltage winding and the high-voltage leadout on the high-voltage winding (SF_e) was calculated. If this was less than 1.2, the insulation end overlap $OEOL$ was increased in increments of 25 mm until the required safety factor was obtained. The ratio $Z_{\text{in}}/Z_{\text{in,min}}$ was calculated. If the ratio was too low, the design process could be repeated with a reduced value of $R_{s,\max}$, although this was not required for the design examples. The lowest value of 0.73 occurred in the device with the largest centre-gap tuning ratio, where the voltage ratio was -21.5% / +21.4% of the target value. For centre-gap + tap tuned devices, the safety factor of the leadouts SF_{leadouts} was calculated. The lowest value of 2.4 was just acceptable and would require greater manufacturing tolerances. $f(\mathbf{x})$ was re-calculated for each design after all of the changes had been made.

Parameter	Device			
	500 nF $\leq C_l \leq$ 1100 nF		250 nF $\leq C_l \leq$ 1100 nF	
	cg	cg + tap	cg	cg + tap
$f(\mathbf{x})$, kg	173.2	160.5	284.2	209.6
$B_{\mathrm{pk}(0.99r_{2,\mathrm{CS1}},0)}$, T	1.2	1.2	1.0	1.2
$L_{\mathrm{WS1,linear}}$ - $L_{\mathrm{WS1,non\text{-}linear}}$, %	0.08 / 0.02	0.11 / 0.10	0.24 / 0.03	0.27 / 0.10
$d^{\mathrm{est}}_{\mathrm{WS2}} \geq d_{\mathrm{WS2,min}}$?[a]	-	no	-	yes
No. extra layers added if "no"	-	2	-	-
Wire diameter increase (MWS), %	-0.1	-0.3	0.2	0.1
New wire diameter (MWS), mm	1.45	1.25	1.7	1.4
Wire diameter increase (TWS)[a], %	-	4.7	-	1.6
New wire diameter (TWS), mm[a]	-	1.25	-	1.12
$C'_{l,\mathrm{min}}$[a], nF	-	505.7	-	254.6
Primary winding turns reduced by	4	2	0	2
V_s/V_p, deviation from target, %	-2.3 / 1.7	0.6 / 1.1	-13.8 / 12.5	-7.2 / 8.2
SF_e	1.26	1.34	1.41	1.31
$Z_{\mathrm{in}}/Z_{\mathrm{in,min}}$	0.93	0.98	0.84	0.81
SF_{leadouts}	-	4.1	-	3.8
$f(\mathbf{x})$ (revised), kg	172.8	167.6	284.8	210.2

[a]cg + tap tuned devices only.

Table 8.1 Results of the design process to obtain the target range (500 nF — 1100 nF) and (250 nF — 1100 nF) in one centre-gap (cg) tuned or one centre-gap + tap (cg + tap) tuned PCRTX.

8.6.1 500 nF $\leq C_l \leq$ 1.1 uF

This target range is equivalent to the usable range of PC2 in Chapter 5, having $f(\mathbf{x}) = 303.8$ kg. Saturation occurred in that device below the design voltage of 36 kV. This was because the transformer was designed around an existing core of inappropriate dimensions and axial-offset tuning was employed instead of centre-gap tuning. A user-based iterative design method, known as reverse design [Bodger and Liew, 2002], was used in conjunction with a magnetic model, based on circuit theory and empirical data [Liew and Bodger, 2001]. Compared to this device, the new designs presented here offer weight savings and ensure linearity up to the rated voltage.

The results of the design process are shown in Table 8.1. The centre-gap tuned device is the preferred option. It is the most simple to manufacture and operate. The weight saving of the centre-gap + tap tuned device over this is only 3%. $f(\mathbf{x})$ is 43% lower than the original device. The cross-sections of the two new designs are compared with the existing variable inductance device and the fixed inductance design example of Section 7.5 in Figure 8.6.

8.6.2 250 nF $\leq C_l \leq$ 1.1 uF

This target range is equivalent to the usable range of PC1 and PC2 of Chapter 5, having a combined $f(\mathbf{x})$ value of 411.3 kg. The new designs presented here offer weight savings and the convenience of having just one device.

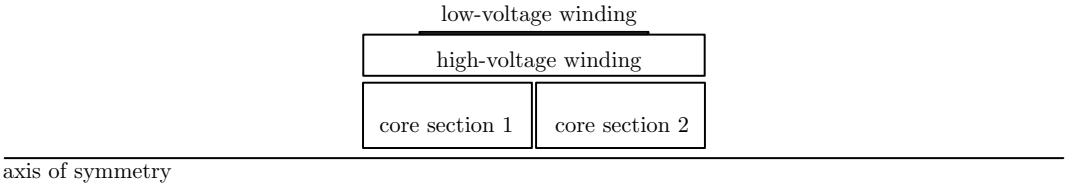

(a) New design (centre-gap tuned): $C_{l,\min} = 500$ nF, $C_{l,\max} = 1.1$ uF, $f(\mathbf{x}) = 172.8$ kg.

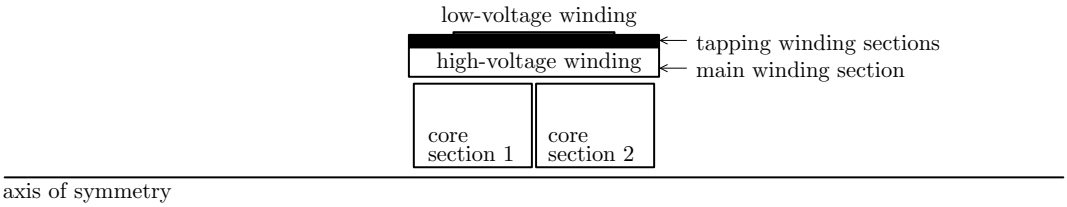

(b) New design (centre-gap + tap tuned): $C'_{l,\min} = 500$ nF / 505.7 nF (estimated / actual value), $C_{l,\min} = 1.00$ uF, $C_{l,\max} = 1.1$ uF, $f(\mathbf{x}) = 167.6$ kg.

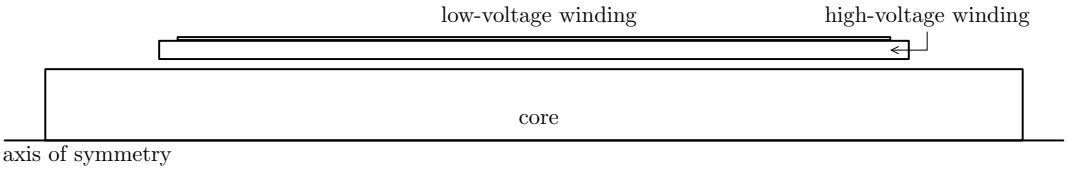

(c) Existing design (centre-gap tuned): $f(\mathbf{x}) = 303.8$ kg.

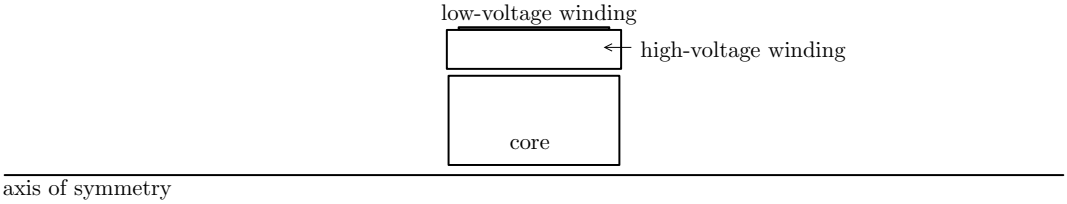

(d) Fixed inductance design: $C_l = 1.1$ uF, $f(\mathbf{x}) = 127.7$ kg.

Figure 8.6 Cross-sections of two new PCRTX designs each having a tuning range of 500 nF — 1.1 uF compared to an existing device and a fixed inductance design.

The results of the design process are shown in Table 8.1. Centre-gap + tap tuning is now a viable option, offering a weight saving of 26% over the centre-gap tuning device. Using this device, $f(\mathbf{x})$ is 49% lower than the original two devices. The cross-sections of the two new designs are compared with the two existing variable inductance devices, which together cover the same inductance range, in Figure 8.7.

8.6.3 39.3 nF $\leq C_l \leq$ 1.1 uF

$C_{l,\min} = 39.3$ nF was calculated using Eq. 8.3, allowing for resonant operation down to $C_{l,\min}$, as well as operation under open-circuit conditions, with a supply current of less than 40 A. A PCRTX kitset having this tuning range could be used to test any hydro-generator stator in New Zealand, as well as set the sphere gaps, replacing the multi-tonne equipment normally used. The high tuning ratio $\frac{L_{s,\max}}{L_{s,\min}}$ of 28.0 means that

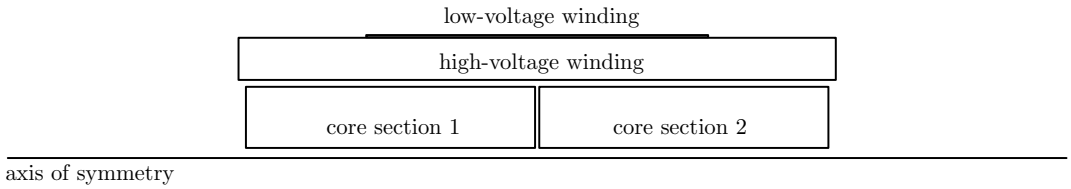

(a) New design (centre-gap tuned): $C_{l,\min} = 250$ nF, $C_{l,\max} = 1.1$ uF, $f(\mathbf{x}) = 284.8$ kg.

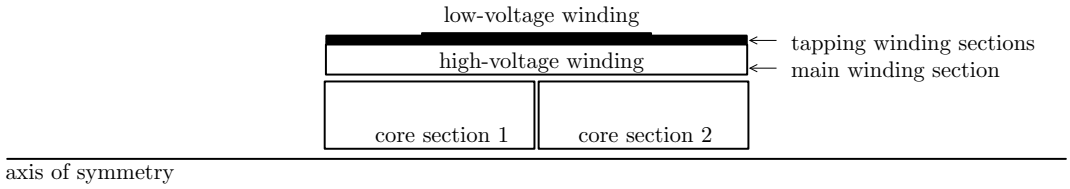

(b) New design (centre-gap + tap tuned): $C'_{l,\min} = 250$ nF / 255 nF (estimated / actual value), $C_{l,\min} = 501.7$ nF, $C_{l,\max} = 1.1$ uF, $f(\mathbf{x}) = 210.2$ kg.

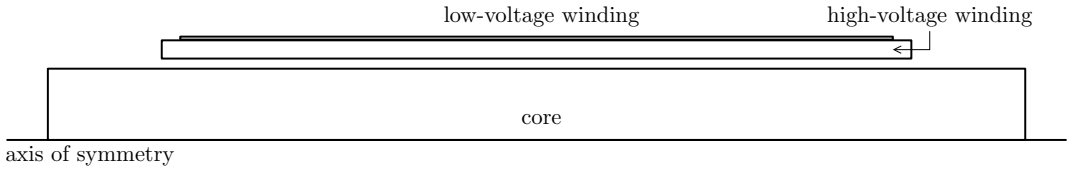

(c) Existing design (centre-gap tuned, covering top-half of range): $f(\mathbf{x}) = 303.8$ kg.

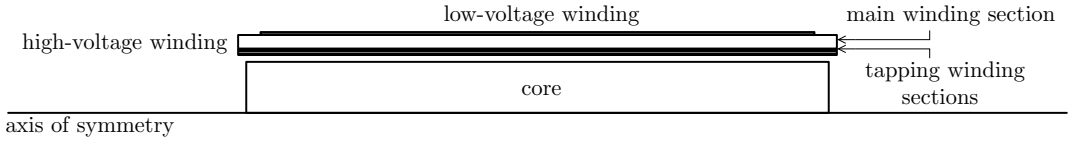

(d) Existing design (centre-gap + tap tuned, covering bottom-half of range): $f(\mathbf{x}) = 107.5$ kg.

Figure 8.7 Cross-sections of two new PCRTX designs each having a tuning range of 250 nF — 1.1 uF compared to two existing devices which (together) cover the same range.

a minimum of two devices are required to achieve the tuning range.

The geometric mean of $C_{l,\max}$ and $C_{l,\min}$ gives the tuning breakpoint for the two-device option as 207.9 nF. The results of the design process are shown in Tables 8.2 & 8.3 for the core sharing and non core sharing options respectively. In both the centre-gap and centre-gap + tap tuned devices, $f(\mathbf{x})$ was reduced by approximately 40 kg when the core was shared between the two devices. Using core sharing for both options, $f(\mathbf{x})$ was reduced by 18% when using the centre-gap + tap tuned devices instead of the centre-gap tuned devices. The cross-sections of the centre-gap and centre-gap + tap tuned designs are compared in Figures 8.8 & 8.9.

The geometric one-third and two-third points of $C_{l,\max}$ and $C_{l,\min}$ gives the tuning break points for the three-device option as 362.3 nF and 119.3 nF. The core was shared between each of the three centre-gap and centre-gap + tap tuned devices. From the experience of the two-device option, without core sharing, the safety factor SF_{leadouts} would be too low on the device covering 39.3 nF $\leq C_l \leq$ 119.3 nF. The results of the

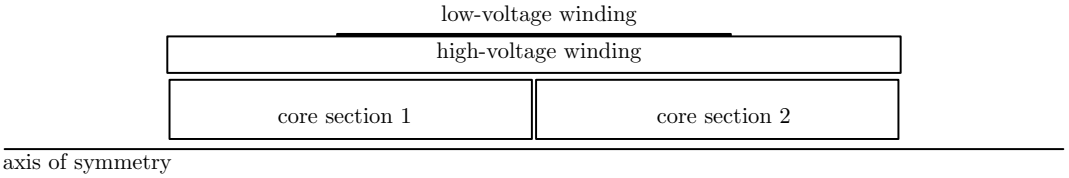

(a) Variable inductance example, centre-gap tuned: $C_{l,\min}$ = 207.9 nF, $C_{l,\max}$ = 1.1 uF, $f(\mathbf{x})$ = 308.2 kg.

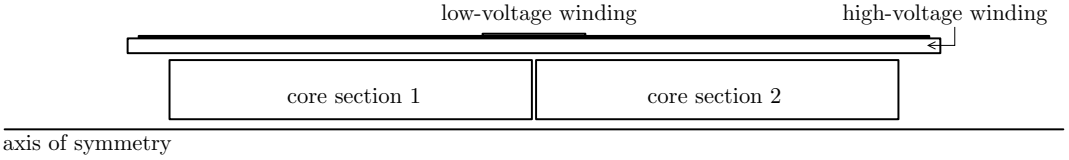

(b) Variable inductance example, centre-gap tuned: $C_{l,\min}$ = 39.3 nF, $C_{l,\max}$ = 207.9 uF, $f(\mathbf{x})$ = 196.6 kg. The 149.3 kg core is shared with (a).

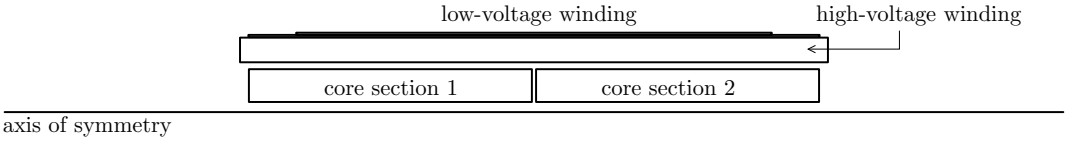

(c) Variable inductance example, centre-gap tuned: $C_{l,\min}$ = 39.3 nF, $C_{l,\max}$ = 207.9 uF, $f(\mathbf{x})$ = 85.6 kg.

Figure 8.8 Cross-sections of the possible centre-gap tuned designs for achieving 39.6 nF — 1.1 uF in two devices. Option 1 - (a) + (b): $f(\mathbf{x})$ = 355.5 kg, with core sharing. Option 2 - (a) + (c): $f(\mathbf{x})$ = 393.8 kg, with no core sharing.

Parameter	Device			
	207.9 nF $\leq C_l \leq$ 1100 nF		39.3 nF $\leq C_l \leq$ 207.9 nF	
	cg	cg + tap	cg	cg + tap
$f(\mathbf{x})$, kg	307.1	242.3	193.7	162.8
$B_{\text{pk}(0.99r_{2,\text{CS1}},0)}$, T	1.0	1.1	-	-
$L_{\text{WS1,linear}}$ - $L_{\text{WS1,non-linear}}$, %	0.34 / -0.01	0.33 / 0.09	-	-
$d_{\text{WS2}}^{\text{est}} \geq d_{\text{WS2,min}}$?[a]	-	yes	-	yes
No. extra layers added if "no"	-	-	-	-
Wire diameter increase (MWS), %	0.3	0.5	2.8	2.8
New wire diameter (MWS), mm	1.7	1.5	0.56	0.56
Wire diameter increase (TWS)[a], %	-	0.5	-	5.6
New wire diameter (TWS), mm[a]	-	1.12	-	0.475
$C'_{l,\min}$[a], nF	-	211.1	-	41.2
Primary winding turns reduced by	-9	2	-2	0
V_s/V_p, deviation from target, %	-21.5 / 21.4	-8.8 / 10.0	-5.5 / 5.2	-4.2 / 3.6
SF_e	1.31	1.36	1.29[b]	1.37[b]
$Z_{\text{in}}/Z_{\text{in,min}}$	0.73	0.78	2.8	3.2
SF_{leadouts}	-	3.8	-	3.6
Turns on low-voltage winding tap[c]	-	-	none	48
Primary current (sec. O/C)[c], A	-	-	39.4 @ 432 V	43.9 @ 401 V
$f(\mathbf{x})$ (revised), kg	308.2	243.4	196.6	167.7

[a] cg + tap tuned devices only.
[b] After increasing $OEOL$ by 25 mm to 50 mm.
[c] Devices rated for operation under open-circuit (O/C) only.

Table 8.2 Results of the design process to obtain target range (39.3 nF — 1100 nF) in two centre-gap (cg) tuned or two centre-gap + tap (cg + tap) tuned PCRTXs. For each tuning method the core is shared between the two devices.

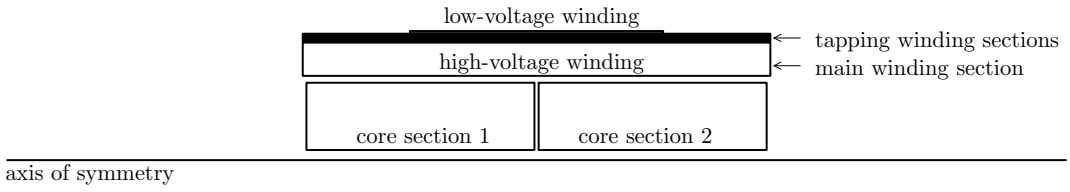

(a) Variable inductance example, centre-gap + tap tuned: $C'_{l,\min}$ = 207.9 / 211.1 nF (estimated / actual value), $C_{l,\min}$ = 417.2 nF, $C_{l,\max}$ = 1.1 uF, $f(\mathbf{x}) = 243.4$ kg.

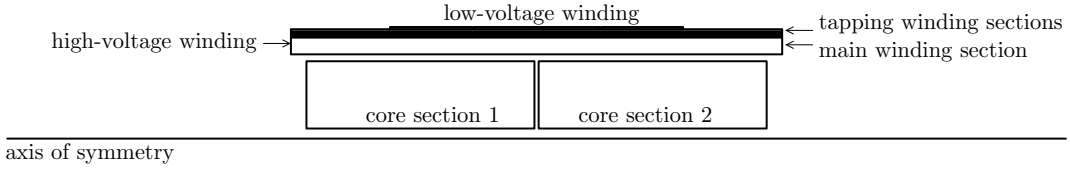

(b) Variable inductance example, centre-gap + tap tuned: $C'_{l,\min}$ = 39.3 / 41.2 nF (estimated / actual value), $C_{l,\min}$ = 78.9 nF, $C_{l,\max}$ = 207.9 nF, $f(\mathbf{x})$ = 167.7 kg. The 117.9 kg core is shared with (a).

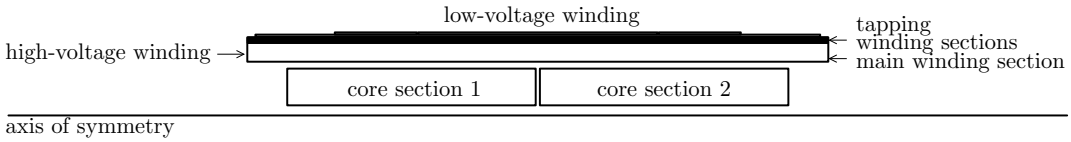

(c) Variable inductance example, centre-gap + tap tuned: $C'_{l,\min}$ = 39.3 / 44.0 nF (estimated / actual value), $C_{l,\min}$ = 78.9 nF, $C_{l,\max}$ = 207.9 nF, $f(\mathbf{x})$ = 89.6 kg.

Figure 8.9 Cross-sections of the possible centre-gap + tap tuned designs for achieving 39.3 nF — 1.1 uF in two devices. Option 1 - (a) + (b): $f(\mathbf{x}) = 293.2$ kg, with core sharing. Option 2 - (a) + (c): $f(\mathbf{x}) = 333.0$ kg, with no core sharing.

design process are shown in Tables 8.3 & 8.4.

$f(\mathbf{x})$ was reduced by 10% when using the centre-gap + tap tuned devices instead of the centre-gap tuned devices. $f(\mathbf{x})$ has reduced by 12% and 3% for the centre-gap and centre-gap + tap tuned devices, respectively, when moving from the two-device option to the three-device option. Since $f(\mathbf{x})$ does not include the shell and box weight, the shipping weight may still be reduced with the two-device option, but the individual package weights would be lower in the three-device options. The cross-sections of the new centre-gap and centre-gap + tap tuned designs are compared in Figures 8.10 & 8.11.

8.7 CONCLUSIONS

A design methodology for centre-gap and centre-gap + tap tuned PCRTXs was developed. The methodology was illustrated with three design examples. In the two replacement transformer examples, a reduction in $f(\mathbf{x})$ of 43% and 49% was achieved. In the third design example, a new kitset with the capability to test any hydro-generator stator in New Zealand was developed. The lightest option was realised with three centre-gap + tap tuned PCRTXs which share a common core. $f(\mathbf{x})$ was 285.5 kg, giving a specific weight-to-power ratio of 0.63 kg/kVAr. This is a significant reduction

Parameter	Device			
	39.3 nF $\leq C_l \leq$ 207.9 nF		39.3 nF $\leq C_l \leq$ 119.3 nF	
	cg	cg + tap	cg	cg + tap
$f(\mathbf{x})$, kg	83.8	84.7	130.2	129.3
$B_{\mathrm{pk}(0.99r_{2,\mathrm{CS1}},0)}$, T	1.0	1.1	-	-
$L_{\mathrm{WS1,linear}}$ - $L_{\mathrm{WS1,non\text{-}linear}}$, %	1.30 / 0.20	1.23 / 0.40	-	-
$d^{\mathrm{est}}_{\mathrm{WS2}} \geq d_{\mathrm{WS2,min}}$?[a]	-	yes	-	no
No. extra layers added if "no"	-	-	-	0
Wire diameter increase (MWS), %	2.8	2.8	15.1	15.1
New wire diameter (MWS), mm	0.56	0.56	0.475	0.475
Wire diameter increase (TWS)[a], %	-	20.6	-	5.8
New wire diameter (TWS), mm[a]	-	0.475	-	0.355
$C'_{l,\mathrm{min}}$[a], nF	-	44.0	-	46.6
Primary winding turns reduced by	7	0	12	14
V_s/V_p, deviation from target, %	-2.8 / 2.9	-8.6 / 10.0	-5.1 / 5.2	-2.2 / 1.7
SF_e	1.46[b]	1.41[b]	1.37[b]	1.37[b]
$Z_{\mathrm{in}}/Z_{\mathrm{in,min}}$	3.0	2.9	4.8	6.0
SF_{leadouts}	-	2.4	-	3.8
Turns on low-voltage winding tap[c]	none	48	none	38
Primary current (sec. O/C)[c], A	40.4 @ 426 V	46.6 @ 402.1	45.2 @ 438 V	51.9 @ 400 V
$f(\mathbf{x})$ (revised), kg	85.6	89.6	138.6	138.4

[a] cg + tap tuned devices only.
[b] After increasing $OEOL$ by 25 mm to 50 mm.
[c] Devices rated for operation under open-circuit (O/C) only.

Table 8.3 Results of the design process to obtain the second device of the 2-device option to achieve target range (39.3 nF — 1100 nF) with no core sharing and the third device of the 3-device option to achieve target range (39.3 nF — 1100 nF) with core sharing (the other two devices are shown in Table 8.4).

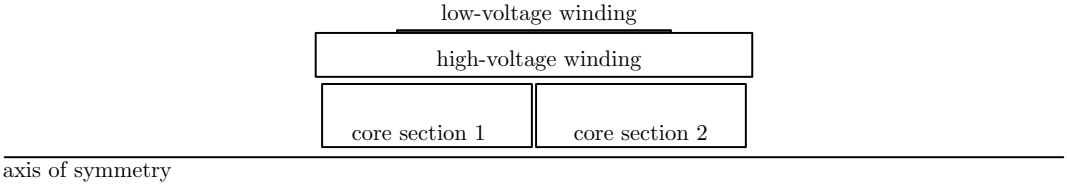

(a) Variable inductance example, centre-gap tuned: $C_{l,\mathrm{min}} = 362.3$ nF, $C_{l,\mathrm{max}} = 1.1$ uF, $f(\mathbf{x}) = 221.7$ kg.

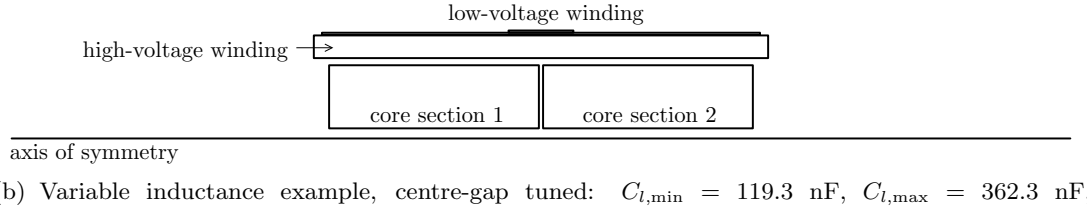

(b) Variable inductance example, centre-gap tuned: $C_{l,\mathrm{min}} = 119.3$ nF, $C_{l,\mathrm{max}} = 362.3$ nF, $f(\mathbf{x}) = 147.5$ kg.

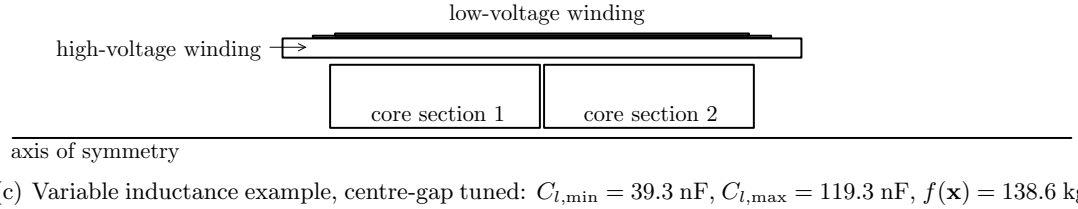

(c) Variable inductance example, centre-gap tuned: $C_{l,\mathrm{min}} = 39.3$ nF, $C_{l,\mathrm{max}} = 119.3$ nF, $f(\mathbf{x}) = 138.6$ kg.

Figure 8.10 Cross-sections of the centre-gap tuned designs for achieving 39.3 nF — 1.1 uF in three devices. $f(\mathbf{x}) = 313.6$ kg. The 97.1 kg core is shared between all three devices.

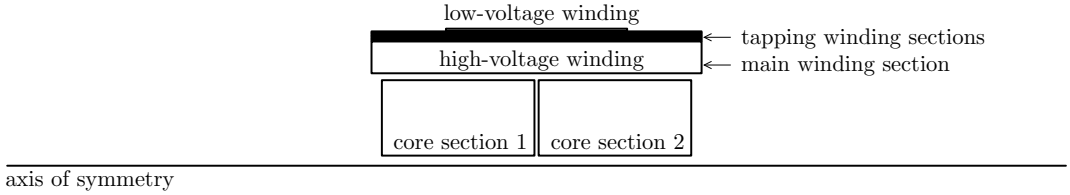

(a) Variable inductance example, centre-gap tuned: $C'_{l,\min}$ = 362.3 / 367.5 nF (estimated / actual value), $C_{l,\min}$ = 727.1 nF, $C_{l,\max}$ = 1.1 uF, $f(\mathbf{x})$ = 191.9 kg.

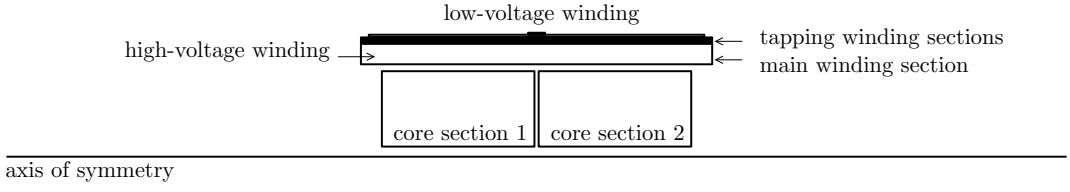

(b) Variable inductance example, centre-gap tuned: $C'_{l,\min}$ = 119.3 / 127.0 nF (estimated / actual value), $C_{l,\min}$ = 239.4 nF, $C_{l,\max}$ = 362.3 nF, $f(\mathbf{x})$ = 148.6 kg.

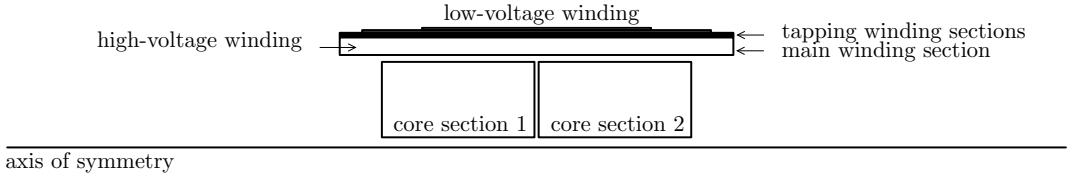

(c) Variable inductance example, centre-gap tuned: $C'_{l,\min}$ = 39.3 / 46.6 nF (estimated / actual value), $C_{l,\min}$ = 119.3 nF, $C_{l,\max}$ = 239.4 nF, $f(\mathbf{x})$ = 138.4 kg.

Figure 8.11 Cross-sections of the centre-gap + tap tuned designs for achieving 39.3 nF — 1.1 uF in three devices. $f(\mathbf{x})$ = 285.5 kg. The 96.7 kg core is shared between all three devices.

Parameter	Device			
	362.3 nF $\leq C_l \leq$ 1100 nF		119.3 nF $\leq C_l \leq$ 362.3 nF	
	cg	cg + tap	cg	cg + tap
$f(\mathbf{x})$, kg	215.6	178.0	142.7	143.4
$B_{\text{pk}(0.99r_{2,\text{CS1}},0)}$, T	1.1	1.2	-	-
$L_{\text{WS1,linear}}$ - $L_{\text{WS1,non-linear}}$, %	0.14 / 0.01	0.17 / 0.11	-	-
$d^{\text{est}}_{\text{WS2}} \geq d_{\text{WS2,min}}$?[a]	-	no	-	no
No. extra layers added if "no"	-	1	-	0
Wire diameter increase (MWS), %	2.6	6.0	4.3	4.3
New wire diameter (MWS), mm	1.6	1.4	0.75	0.75
Wire diameter increase (TWS)[a], %	-	10.1	-	2.7
New wire diameter (TWS), mm[a]	-	1.12	-	0.6
$C'_{l,\min}$[a], nF	-	367.5	-	127.0
Primary winding turns reduced by	5	4	2	0
V_s/V_p, deviation from target, %	-6.0 / 5.1	-2.0 / 3.9	-2.5 / 2.6	-0.5 / 0.1
SF_e	1.45	1.35	1.43[b]	1.44[b]
$Z_{\text{in}}/Z_{\text{in,min}}$	0.91	0.92	2.1	2.4
SF_{leadouts}	-	4.1	-	3.9
$f(\mathbf{x})$ (revised), kg	221.7	191.9	147.5	148.6

[a] cg + tap tuned devices only.
[b] After increasing $OEOL$ by 25 mm to 50 mm.

Table 8.4 Results of the design process to obtain target range (39.3 nF — 1100 nF) in three centre-gap (cg) tuned or three centre-gap + tap (cg + tap) tuned PCRTXs. For each tuning method the core is shared between all three devices. The first two devices are shown here and the third is shown in Table 8.3.

over what is normally obtained using full-core variable inductors of 5-10 kg/kVAr and starts to approach that of frequency-tuned fixed inductance devices. Without the need for a frequency converter, mains frequency testing becomes as economical as variable frequency testing, while being more representive of the generator in-service conditions.

Chapter 9

LABORATORY TEST RESULTS OF RESONANT TRANSFORMER KITSET FOR HIGH-VOLTAGE TESTING OF HYDRO-GENERATOR STATORS

9.1 OVERVIEW

A kitset for high-voltage testing of hydro-generator stators was designed, built and tested. The kitset, consisting of three-partial-core transformers and a common core, was designed to energise stator insulation capacitances of up to 1.1 uF to 36 kV from a 400 V, 50 Hz supply. It can also be configured to operate under open-circuit conditions, to allow for sphere-gap setting. The short-term rating of 448 kVAr was achieved with a shipping weight of 480 kg. Design and construction methods are briefly described. Loaded and open-circuit tests were performed at rated voltage. Voltage linearity was greatly improved over an existing device. Short-circuit tests were performed at rated voltage to demonstrate stator insulation failure withstand capability. Winding resistance and inductance values, along with the tuned-circuit frequency response, were measured and compared to model values. The effect of supply-side voltage harmonic distortion on circuit impedance was investigated experimentally using a programmable ac source and compared to model results. The voltage induced in each winding section of the high-voltage winding of one transformer was measured and compared to model results. Good correlation between measurements and models was obtained in all cases. Heat-runs were performed on each transformer to determine the thermal duty-cycle. A partial-core with radially-stacked laminations was constructed. Significant reduction of planar eddy-current heating effects and power losses over the parallel-stacked partial-core was experimentally shown through thermal images and terminal measurements.

9.2 DESIGN OF KITSET

The specifications of the kitset are the same as the third design example in Chapter 8, having primary voltage $V_p = 400$ V, secondary voltage $V_s = 36$ kV and minimum and maximum values of resonant load capacitance $C_{l,\min}$ and $C_{l,\max}$ of 50 nF and 1.1 uF

at 50 Hz. Ideally, one of the designs from Chapter 8 would have been built, such as the centre-gap tuned kitset consisting of three PCRTXs and a common core, having metal, insulation and encapsulant weight of $f(\mathbf{x}) = 316.6$ kg, or the same design, but utilising centre-gap + tap tuning, having $f(\mathbf{x}) = 285.5$ kg. However, time constraints meant that the kitset had to be designed before the methodology was fully developed. Consequently, while meeting all of the requirements, the kitset is sub-optimal in terms of weight.

The fixed inductance design methodology of Chapter 7 was used to design the first two PCRTXs. Tap tuning was added to achieve inductance variation, with centre-gap tuning only to be used for fine tuning. The third device was designed using a combination of centre-gap and tap tuning, but the design was obtained mainly using intuition rather than strictly following the design methodology for variable inductance. $f(\mathbf{x})$ of the kitset was 305.0 kg, 7% higher than the optimal centre-gap + tap tuned design and only 4% lighter than the optimal centre-gap tuned design. The centre-gap tuned design would probably be used in the future, as the operational complexity is considerably reduced.

The formers were made from three custom-made fibre-glass cylinders, each having inner diameter 250 mm, wall thickness 3 mm and length 1 m. The shells were formed using 25 mm thick medium density polyethylene (MDPE). Slots were cut so that each PCRTX could be lifted by hand between two people. Leadout spacing was determined as per Section 6.10.2 and 8 mm threaded-rod was used to form the leadouts on the high- and low-voltage windings. A dome washer was fitted on the inside of the high-voltage leadout on the high-voltage winding of each PCRTX to reduce corona. Shipping boxes were constructed from 18 mm thick marine plywood. Space heaters were installed to remove any condensation that may occur during shipping. An external socket and switch were fitted to each box. A fourth box was made to hold the core, spacers, MDPE threaded-rod and connecting bars. The core was constructed in four 25 kg sections, making setup and circuit tuning practical with just one person. The finished kitset, having a shipping weight of 480 kg, is shown in Figure 9.1.

The winding layout and terminal labels of the PCRTXs are shown in Figure 9.2. PC4, PC5 and PC6 have a 50 Hz-resonant capacitive tuning range of approximately $0.51 \text{ uF} < C_l < 1.1 \text{ uF}$, $0.25 \text{ uF} < C_l < 0.56 \text{ uF}$ and $0.05 \text{ uF} < C_l < 0.25 \text{ uF}$, respectively. C_l of PC4 can be extended to 2 uF for V_s up to 19.8 kV, where the reduced voltage is required to ensure that the design-value current-density is not exceeded. The low-voltage winding taps of PC4, PC5 and PC6 can generally be left on A2-A3, A1-A4 and A1-A2, respectively. The other low-voltage winding taps on PC4 and PC5 can be used to more closely match the voltage ratio 400 V / 36 kV but, as shown in Section 8.4.2, are not required to ensure that the supply-current will not exceed the design-value. The low-voltage winding tap on PC6 is required for operation under open-circuit conditions,

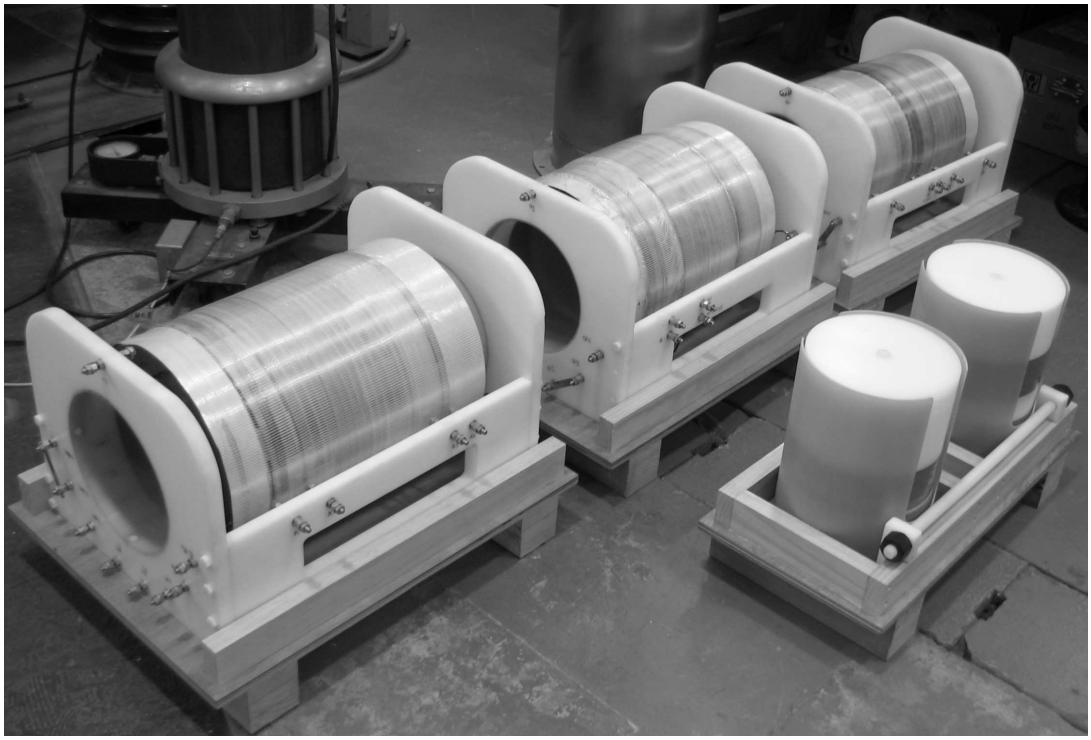

Figure 9.1 Prototype kitset for high-voltage testing of hydro-generator stators.

as discussed in Section 9.3.2.

9.3 KEY PERFORMANCE INDICATORS

The laboratory tests performed in this section were designed to replicate in-field conditions. High-voltage capacitors were used in-place of stator capacitance. The capacitors are expected to be more linear and have lower losses than a real generator stator. Consequently, the supply currents drawn in field-tests are expected to be somewhat higher than obtained in the laboratory.

9.3.1 Load and insulation test

The insulation integrity of an earlier PCRTX was demonstrated to a client prior to stator testing by energising a load capacitance to 40 kV and maintaining the voltage for three minutes [Bodger and Enright, 2004]. The same test was performed on PC4, PC5 and PC6 with no insulation failures encountered. The voltage-per-layer in the new PCRTXs is almost 50% lower than in the earlier device. The dome washer on the high-voltage leadout of the high-voltage winding of each PCRTX ensured that corona levels were relatively low at 40 kV. Even at a reduced flux-density of 1.2 T, the operating noise and vibration levels of PC4 with $C_l = 1.1$ uF were still relatively high.

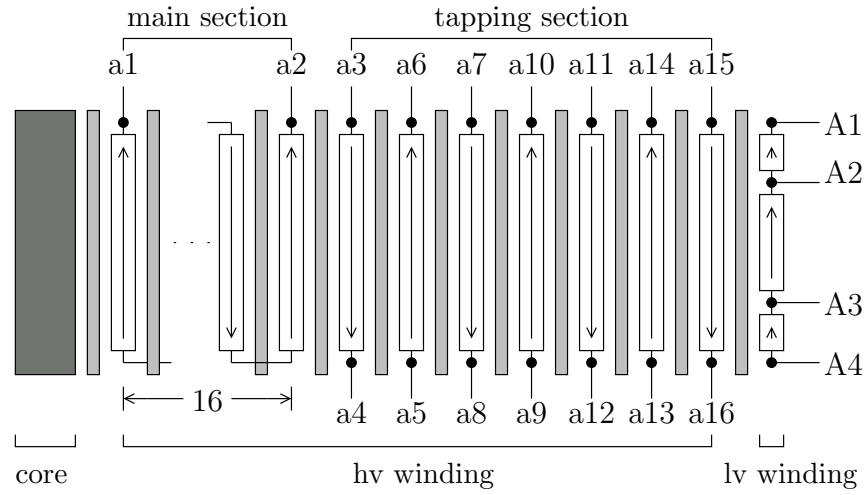

(a) PC4

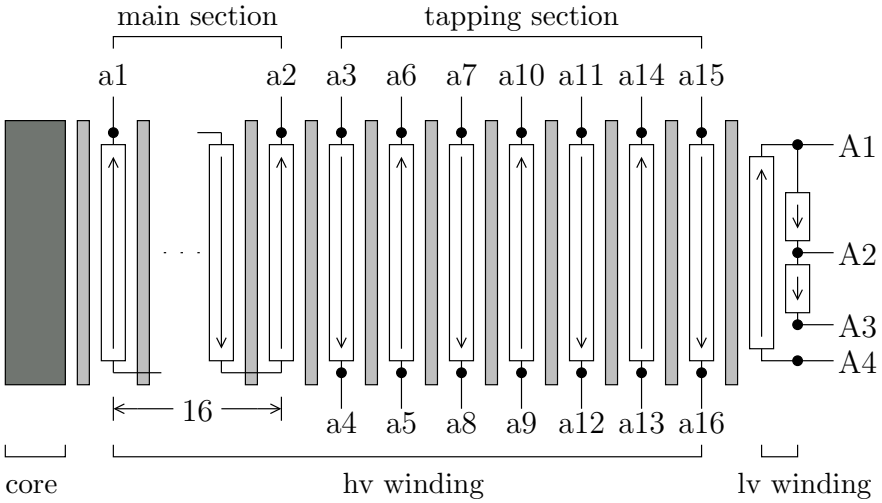

(b) PC5

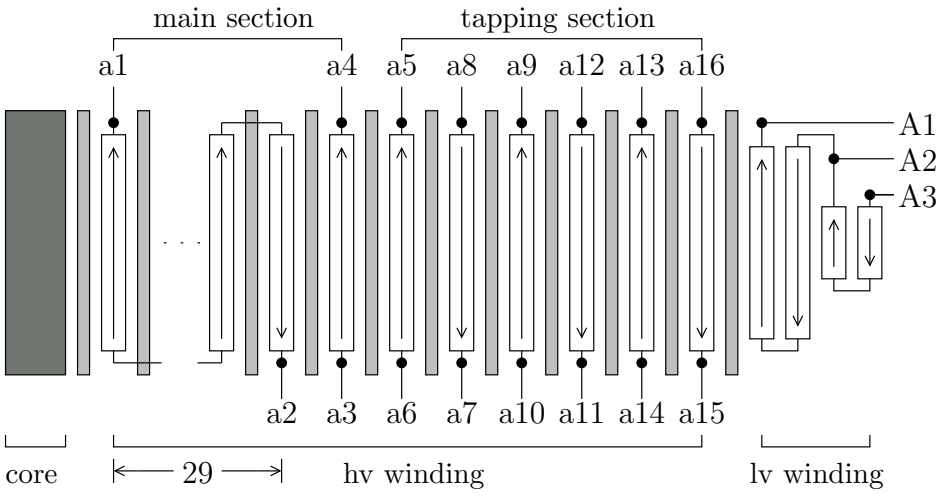

(c) PC6

Figure 9.2 Winding layout and terminal labels of the PCRTXs. (↑↓ = winding direction, • = winding leadout)

Vibration was reduced by adding lock-nuts to the threaded-rod which held the core sections together. These are tightened after circuit tuning.

9.3.2 Energisation under open-circuit conditions

A sphere gap, set to 20% above the test voltage, is normally placed in the secondary circuit to protect the stator from accidental over-voltage. One requirement of the kitset is that it can be used to set the sphere gap, removing the need for a separate high-voltage test transformer. PC6 was configured with the core centre-gap set to zero and the high- and low-voltage winding taps set to a1-a16 and A1-A3, respectively. A primary voltage of 487 V and current of 68.4 A was required to obtain a secondary voltage of 43.2 kV, 20% over the rated voltage. The required primary voltage could be achieved from a 415 V supply using a variac with a regulation range of 120%. Alternatively, low-voltage winding tap A1-A2 could be selected, giving a calculated primary voltage and current of 315.5 V and 110.9 A, respectively. The fifth core section, discussed in Section 9.5.3, could also be used in this configuration to further reduce the magnetising current. The kitset has not yet been used to set sphere gaps, but it looks practical, except prehaps at the highest voltage. The example PCRTXs designed in Section 8.6.3 have an even lower value of $C_{l,\min}$, which would also reduce the magnetising current.

9.3.3 Device linearity

PC4 was configured with the core centre-gap set to 13.5 mm and the high- and low-voltage winding taps set to a1-a4 and A2-A3, respectively. Device linearity was measured by energising a load capacitance $C_l = 1.1$ uF to 40 kV from the laboratory mains supply. Primary current readings were taken at 5 kV intervals. The same test was repeated using PC2 of Chapter 5, which was also designed for 36 kV. The results are shown in Figure 9.3. PC4 has a very linear response over the designed operating range. The existing device started to saturate at a secondary voltage of 25 kV and the rated voltage could not be obtained, despite the circuit being purposely off-tuned at 5 kV so that mild saturation would initially bring the circuit closer to resonance.

9.3.4 Short-circuit test at rated voltage

Stator insulation failure during high-voltage testing is a relatively common occurrence. Earlier PCRTX designs have been subjected to many such failures in field tests without sustaining any obvious damage from the resulting short-circuit forces. In one instance, repeated failures were requested by the client so that the damaged bar could be located [Bendre et al., 2007].

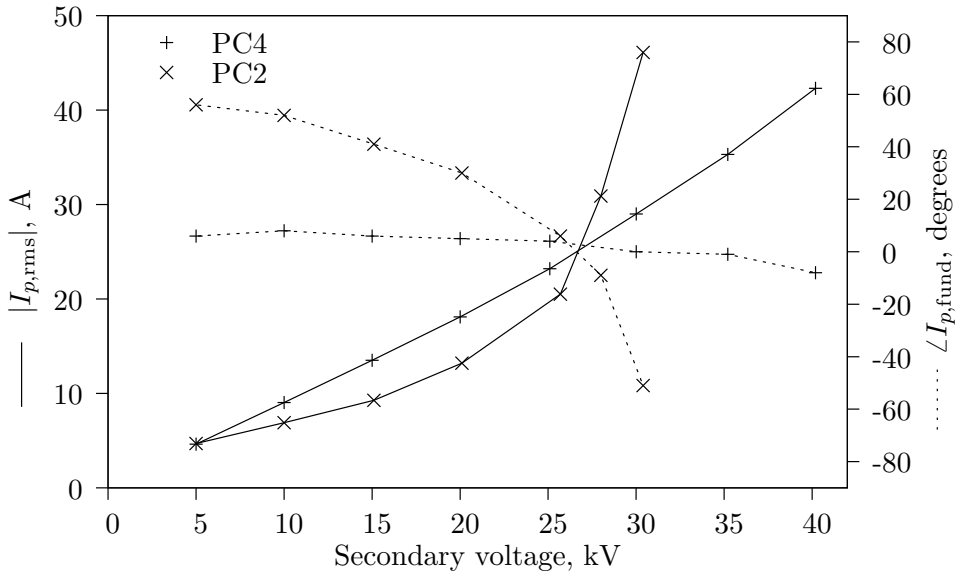

Figure 9.3 Voltage linearity of PC4 compared with an existing device, both having C_l = 1.1 uF.

Transformer	Configuration				Loaded / SC currents @ V_s = 36 kV	
	hv tap	lv tap	cg, mm	C_l, nF	I_p, A	I_s, A
PC4	a1-a2	A3-A4	12	1186	31.9 / 2497	13.4 / 27.0
PC5	a1-a2	A1-A4	0	558	19 / 1678	6.3 / 18.6
PC6	a1-a2	A1-A2	297[a]	248	24 / 560	2.8 / 5.1

[a]Only 2 core sections were used in this configuration.

Table 9.1 Calculated loaded-circuit and short-circuit currents for each PCRTX in the configurations that the short-circuit tests were performed.

Short-circuit tests were performed at rated voltage on the three new PCRTXs in an attempt to replicate the in-field condition of stator insulation failure. Confidence was held that the new PCRTXs would survive the tests intact as the manufacturing process was similar to the previous devices. However, the alternative winding layout, tuning method and reduced winding aspect ratio of the new PCRTXs meant that the prospective short-circuit currents and forces could be significantly different.

The PCRTX under-test was first used to energise a load capacitance to 36 kV. A remotely operated mechanical drop-switch, designed for use in an exploding wire circuit [Smith et al., 2007], was then manually closed by the operator to initiate a short-circuit. The steady-state loaded-circuit and short-circuit winding currents were calculated for each PCRTX in the tested configuration. The model-value load capacitance was set to $1/\omega_s^2 L_s$, where L_s was the calculated inductance value and $\omega_s = 2\pi \times 50$ Hz. Transient effects, which are dependent on the supply phase angle, were ignored. The results are shown in Table 9.1.

Table 9.1 shows that the short-circuit to loaded-circuit current ratios are much higher

on the primary side than the secondary. Therefore, the most likely action following a short-circuit is operation of the low-voltage fuse, or opening of the voltage regulator circuit breaker, set to 600 A for the tests. Consequently, no fuse was fitted to the high-voltage circuit, although these are normally fitted in practice.

The variac had four separate coils, each having its output slider fitted with a 63 A fuse. The coils were connected in a series / parallel configuration, meaning that the expected current through each coil was equal to one-half of the transformer primary current. Using the calculated primary currents and the manufacturer's fuse characteristic, the expected fuse operation time for PC4, PC5 and PC6 was less than 0.01 s (0.5 cycles), 0.04 s (2 cycles) and approximately 4 s (200 cycles), respectively.

Three short-circuit tests were performed on both PC4 and PC5 and one short-circuit test was performed on PC6. Each test was captured on video. Waveforms were not recorded. Short-circuit tests of PC4 and PC5 went without incidence. There was no obvious insulation failure or winding movement. With one exception on PC4, the circuit breaker opened before any of the variac fuses operated. The fuses did not operate and the circuit breaker remained closed after a short-circuit was applied to PC6. Nine seconds after the short was applied the circuit breaker was manually opened. It was noted that the output current of the voltage regulator was approximately 400 - 500 A during the short-circuit. Given that the primary voltage was 339 V and the voltage regulator was set to 400 V, this figure is in good agreement with the calculated value of 474 A. The short-circuit current and resulting forces caused no obvious damage to the insulation or winding movement. A thermal image of the primary winding, taken approximately one minute after the test, showed a maximum winding temperature of 78°C.

While the PCRTXs appear capable of enduring a short-circuit for several seconds, the low-voltage fuse should still be selected to minimise fault duration in field testing because the arc energy of a sustained flashover could further exacerbate the damage to the failed stator winding.

9.4 COMPARISON WITH MODEL

Test results obtained in this section are directly compared to the analytical models described in Chapters 5 & 6. Differences between test and model results are generally within 5% and demonstrate a good ability to design to specification. The differences are due to approximations in the finite element model, as well as incorrect design estimates of parameters such as wire insulation thickness, build-value of inter-layer insulation thickness and the resin thickness on the face of each core section.

hv terminals	dc resistance, Ω		
	Measured	Predicted[a]	Error, %
PC4			
a1-a2	56.58	57.34	1
a3-a4	3.94	3.99	1
a5-a6	4.00	4.04	1
a7-a8	5.46	5.65	3
a9-a10	5.52	5.71	3
a11-a12	5.59	5.77	3
a13-a14	5.64	5.83	3
a15-a16	5.72	5.89	3
PC5			
a1-a2	157.84	158.30	0
a3-a4	10.81	10.84	0
a5-a6	12.546	12.92	3
a7-a8	12.661	13.05	3
a9-a10	12.775	13.18	3
a11-a12	12.911	13.30	3
a13-a14	26.472	26.83	1
a15-a16	26.685	27.05	1
PC6			
a1-a2	834.02	831.19	0
PC6 (continued)			
a3-a4	66.14	63.36	-4
a5-a6	66.1	63.80	-4
a7-a8	66.63	64.24	-4
a9-a10	159.16	147.74	-8
a11-a12	161.83	148.64	-9
a13-a14	161.06	149.55	-8
a15-a16	163.16	150.45	-8
lv terminals	dc resistance, mΩ		
	Measured	Predicted[a]	Error, %
PC4			
A1-A2	29.64	28.90	-3
A2-A3	112.00	110.78	-1
A3-A4	20.60	19.27	-7
PC5			
A1-A4	176.20	172.23	-2
A1-A2	18.56	16.34	-14
A2-A3	26.84	25.67	-5
PC6			
A1-A2	341.30	324.59	-5
A2-A3	169.7	163.49	-4

[a]At 20°C.

Table 9.2 Measured and predicted winding resistances of the PCRTXs.

9.4.1 Wire resistance measurements

Wire resistance measurements were made using a digital micro-ohmmeter (model MPK-254). The design-values are compared to the measured values in Table 9.2. The differences are generally within a few percent and can mainly be attributed to incorrect estimation of the wire insulation thickness WIT. Since, for practical reasons, each layer on the high-voltage winding was made the same length, any error in WIT meant that the actual number of turns wound differed from the design value. The winding sections most affected by this were those having terminal labels a9-a10, a11-a12, a13-a14, a15-a16 on PC6.

9.4.2 Inductance measurements

The secondary winding self-inductance values L_s were measured across the tuning range using the resonant tuning test of Section 4.5. A resonant circuit was formed with each value of load capacitance C_l within the tuning range which could be formed using simple series or parallel combinations of capacitors from an inverted Marx impulse generator. The design-values are compared to the measured values in Figure 9.4. The differences are generally within a few percent and can be attributed to the differing number of turns, as well as the uncertainty in the air-gap between each core face. The solid lines in Figure 9.4 indicate the region of normal operation. Operation in the region indicated by dashed lines is also possible, but the secondary voltage would have to be reduced to

ensure that the design-value current-density is not exceeded.

9.4.3 Frequency response of tuned circuit

The frequency response of each PCRTX was measured in selected configurations using a Chroma 61504 2 kVA programmable ac source. The phase and magnitudes of the primary and secondary waveforms were measured using two Tektronix TDS220 100 MHz oscilloscopes. The case of energising the same load capacitance C_l from two different PCRTXs is considered here. Ideally, C_l would have been chosen such that a resonant frequency $f_0 = 1/2\pi\sqrt{L_s C_l}$ of 50 Hz could be obtained for both PCRTXs for some secondary winding self-inductance value L_s, which lies in the inductance overlap region of the two devices.

The two inductance overlap regions of the kitset are between PC4 and PC5 and between PC5 and PC6. The later region was chosen because the input impedance of the tuned circuit is much higher here, meaning that a higher output voltage could be obtained from the limited kVA rating of the ac source. For this region, the nearest available value of C_l which could be formed from the impulse generator capacitors was 265 nF. An attempt was made to adjust the winding tap and core centre-gap of each PCRTX such that $f_0 = 50$ Hz. However, since C_l did not lie exactly in the inductance overlap region of the two PCRTXs, a f_0 value for PC6 of < 50 Hz was obtained, even when the centre-gap was set to its maximum value. The measured input impedance and voltage gain characteristics of the two PCRTXs are compared with the model results in Figures 9.5 & 9.6.

Figures 9.5 & 9.6 show that, in general, the model accurately predicted the input impedance and voltage gain characteristics of the two PCRTXs. The largest discrepancies occur at f_0, where the calculated input impedance of PC5 and PC6 was 38% and 20% higher than the measured values, respectively. The model does not include core, proximity and capacitor losses, which may account for the over-estimation of the input impedance.

In Section 5.4.3 the upper-frequency of the finite element model f_m was calculated as 287 Hz, the exact value depending on the core relative permeability $\mu_{\rm rc}$, assumed to be 3000. However, for the two sample configurations, good correlation between the measured and predicted frequency response was obtained up to 1 kHz, the maximum frequency of the ac source. According to Eq. 5.3, $\mu_{\rm rc} = 861$ for $f_m = 1$ kHz. Such a low value would not occur in the rolling direction of grain oriented steel unless the core steel was saturated. This indicates a limitation of the two-dimensional model, which does not take into account the anisotropic properties of the core.

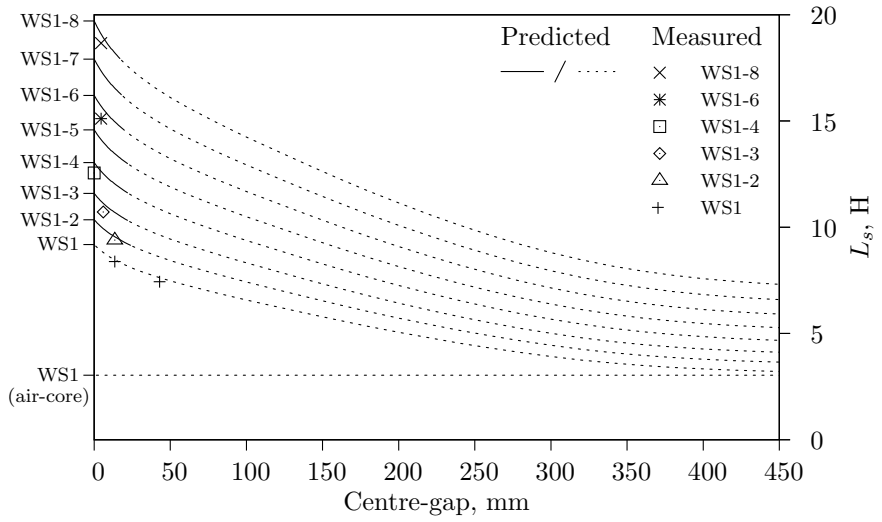

(a) PC4

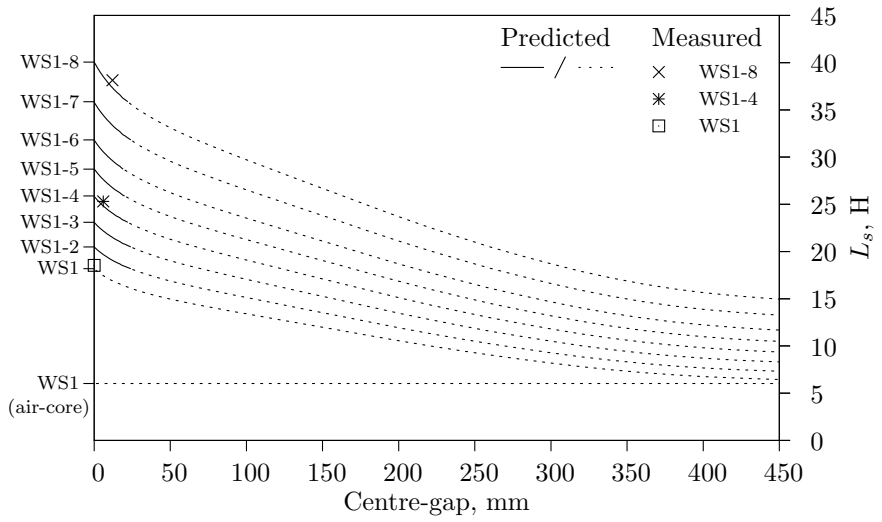

(b) PC5

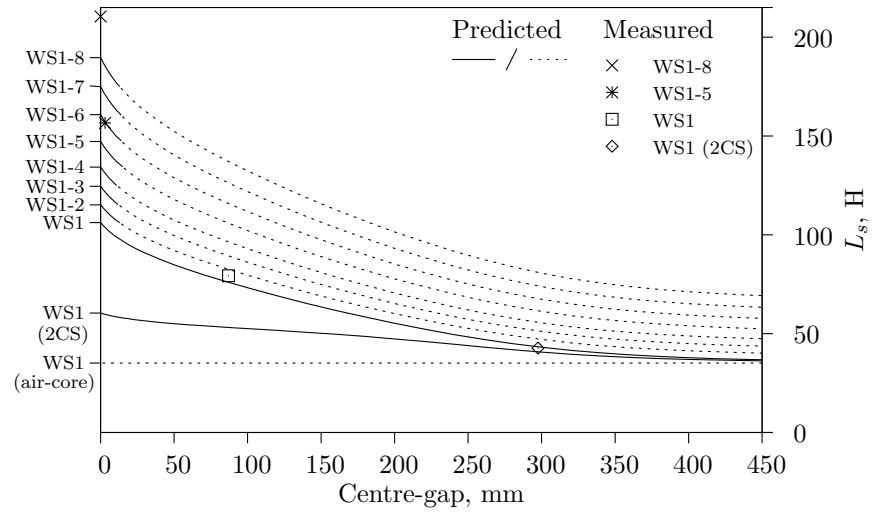

(c) PC6

Figure 9.4 Measured and predicted secondary winding self-inductance variation characteristics.

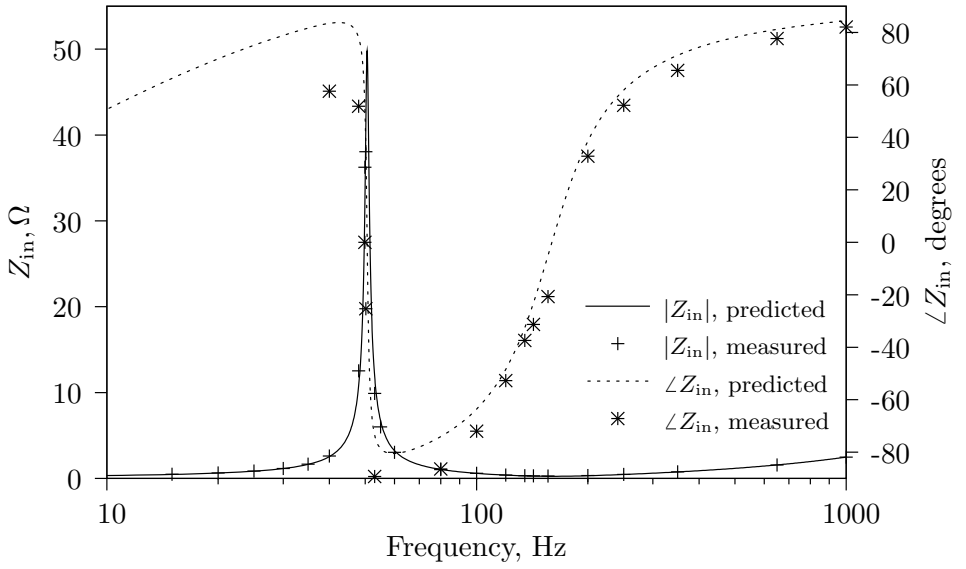

(a) Input impedance

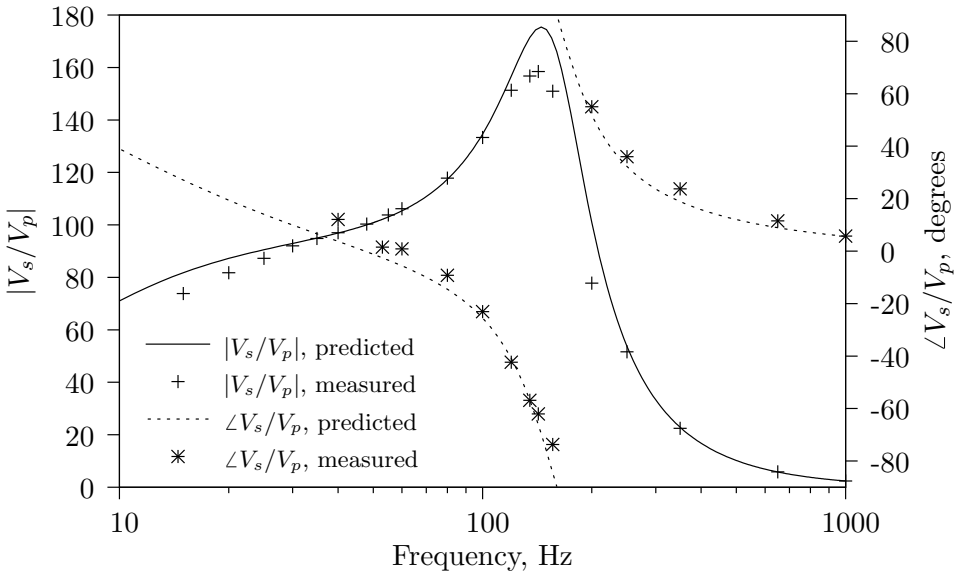

(b) Voltage ratio

Figure 9.5 Measured and predicted frequency response of PC5. (high-voltage winding tap a1-a16, low-voltage winding tap A3-A4, centre-gap = 12 mm, $f_{0,\text{meas}} = 49.88$ Hz, $C_l = 265$ nF)

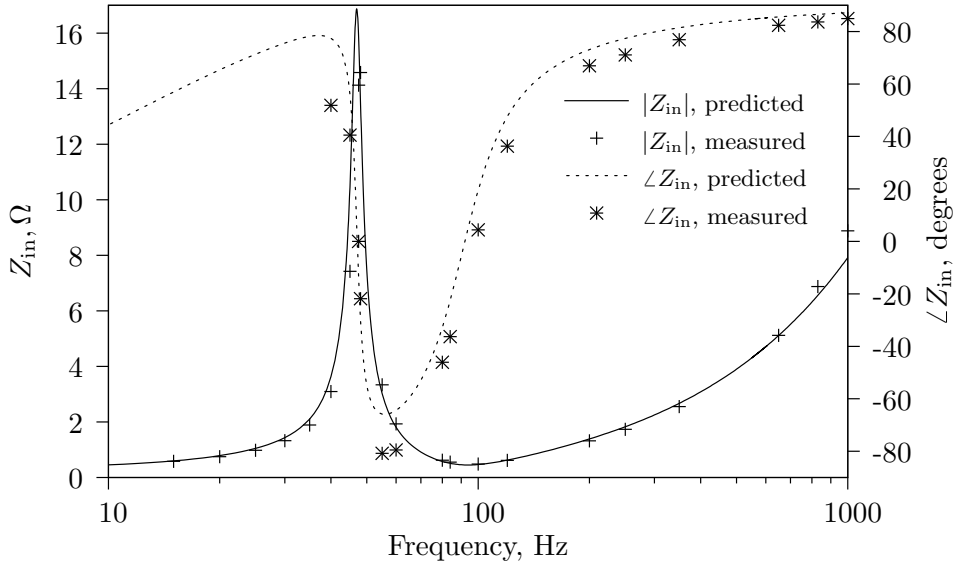

(a) Input impedance

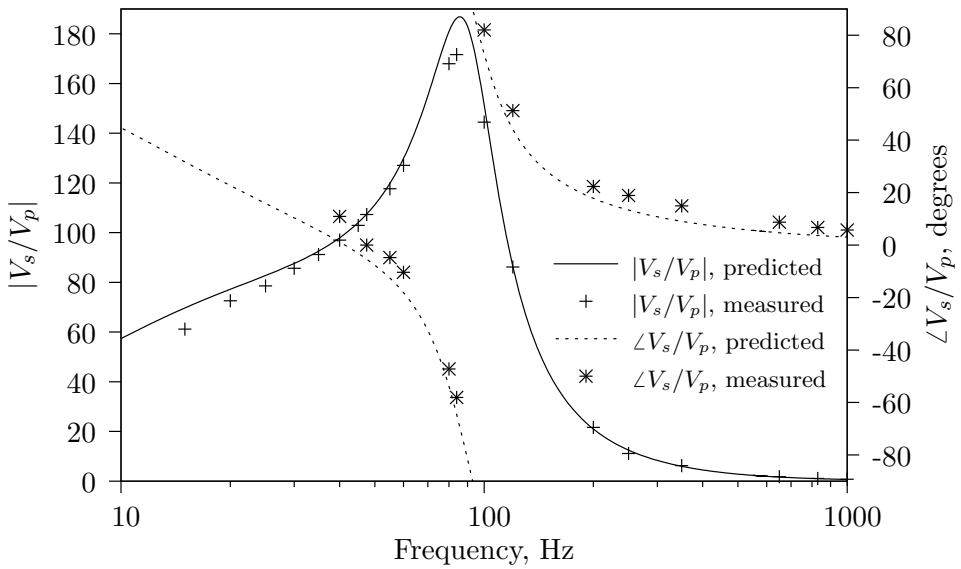

(b) Voltage ratio

Figure 9.6 Measured and predicted frequency response of PC6. (high-voltage winding tap a1-a2, low-voltage winding tap A1-A2, centre-gap = 297.5 mm, $f_{0,\text{meas}} = 47.49$ Hz, $C_l = 265$ nF)

9.4.4 Operation from a distorted supply

The test results of Section 9.4.3 indicate that $f_m > 1$ kHz. This means that the model can be used to calculate the lower-order harmonic currents, which occur when energising the PCRTX from a distorted supply. The effect of current harmonic distortion is to reduce supply impedance. This may cause the variac fuse to operate, disrupting the high-voltage test. The tuned circuit also acts as a filter, which could either increase or decrease the total harmonic distortion (THD) of the secondary voltage, depending on the voltage gain characteristic. It is important to model the voltage gain characteristic because, according to IEC IEC60060 [IEC60060-1, 1989], the test voltage must have a THD of less than 5%, and THD levels of up to 2.1% have been measured at the local supply of one power station in New Zealand.

The harmonic content of a typical waveform from the laboratory mains supply was measured using a Fluke 41 meter. The waveform was then programmed into the ac source. The waveform had 3^{rd}, 5^{th}, 7^{th}, 9^{th} and 11^{th} harmonic components of 1.3%, 3.8%, 1.3%, 0.4% and 0.4%, respectively, giving a THD of 4.3%. The waveform was applied to PC5 and PC6, in the configurations described in Section 9.4.3. The magnitude was adjusted such that an output voltage of 10 kV rms was obtained for both PCRTXs.

The fifth harmonic voltage component at the output of the ac source was measured as 2.8% and 3.4% when PC5 and PC6 were used to energise C_l to 10 kV, respectively, even though the same harmonic component of 3.8% was programmed in each case. The different magnitudes may be due to the supply impedance of the ac source. The measured voltage harmonics were applied to the model to calculate the harmonic currents. The results are shown in Figure 9.7.

Figure 9.7 shows that the model has accurately calculated the harmonic currents using the transformer design-data. The fundamental component of current was calculated with good accuracy for PC5 but only with reasonable accuracy for PC6. The high circuit quality factor Q makes it difficult to predict the input impedance near f_0. In practice the circuit would be tuned such that f_0 closely matches the supply frequency. The harmonic currents are less for PC6 than PC5 even though both devices were energised from the same source. This occurs because the secondary circuit is formed using only the first winding section of the high-voltage winding in PC6 but is formed using all eight winding sections in PC5. The unconnected winding sections in PC6 act like a large air-gap, increasing leakage reactance and impedance at harmonic frequencies.

The measured THD of the primary and secondary voltages was 3.2% and 3.1%, respectively, for PC5 and 3.8% and 1.4%, respectively, for PC6. Some filtering of the distorted supply waveform was thus achieved, with a larger reduction in THD for PC6. This brings about the possibility of designing a PCRTX with improved operation on a distorted supply, where the tuned impedance at f_0 can be traded off for increased

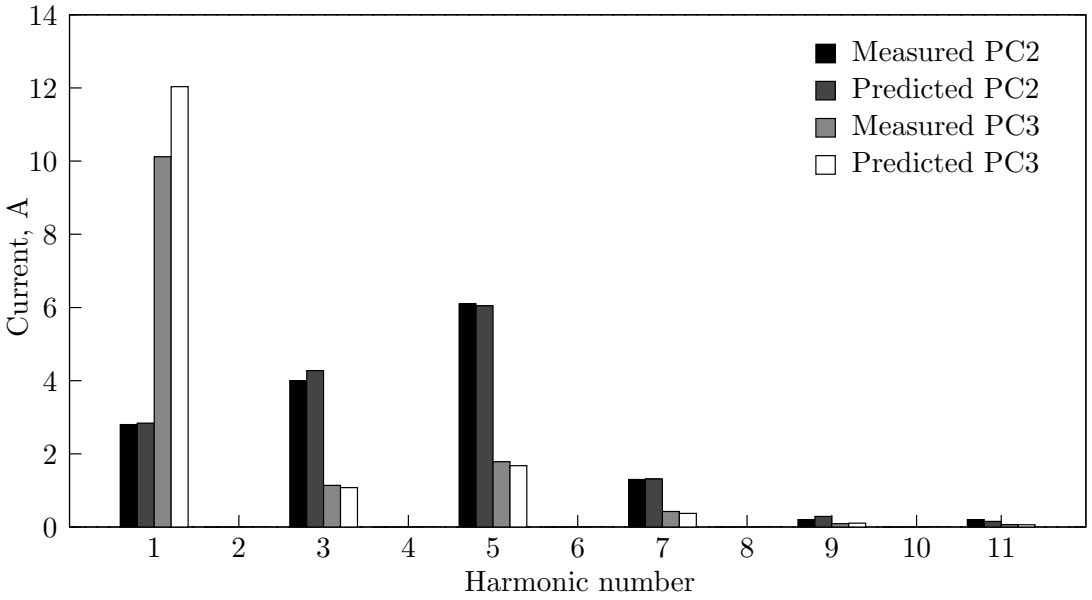

Figure 9.7 Measured and predicted harmonic currents for PC5 and PC6. Both devices were used to energise $C_l = 265$ nF to 10 kV from the same distorted voltage waveform.

impedance at harmonic frequencies and the output voltage can be filtered.

9.4.5 Voltage induced in unused tapping winding sections

With reference to Figure 9.2, PC4 was configured with the core centre-gap set to 12 mm and the high- and low-voltage winding taps set to a1-a3 and A2-A3, respectively. The load capacitance was 1.20 uF. Terminal a1 was the high-voltage end of the high-voltage winding, denoted V_s. Terminal a2, along with the terminals of the tapping section at the same end of the winding, {a3, a6, a7, a10, a11, a14, a15}, were earthed. Eqs. 6.6 & 6.7 of Section 6.4.2 and Eq. 6.32 of Section 6.9.1 were used to calculate the induced voltage at each terminal under loaded-circuit and short-circuit conditions. The results are shown in Table 9.3. The voltage magnitudes and phases were calculated to an accuracy of at least 1.1% and 5.5 degrees, respectively.

9.5 OTHER EXPERIMENTAL DATA

The thermal duty-cycle of the PCRTXs and an alternative core stacking technique are investigated experimentally in this section. Thermal and core loss models for the PCRTX have not yet been developed.

Loaded circuit						
Voltage	Magnitude, V			Phase, degrees		
	Measured	Predicted	Error, %	Measured	Predicted	Error, degrees
V_p	132.8	132.8	0.0	0.0	0.0	0.0
V_s	12210.0	12148.2	0.5	0.0	-1.9	1.9
V_{a4}	756.8	749.7	0.9	180.0	179.7	0.3
V_{a5}	753.7	745.6	1.1	0.0	-0.2	0.2
V_{a8}	823.2	822.3	0.1	180.0	179.8	0.2
V_{a9}	819.4	818.1	0.2	0.0	-0.2	0.2
V_{a12}	813.9	814.0	0.0	180.0	179.8	0.2
V_{a13}	810.3	809.8	0.1	0.0	-0.2	0.2
V_{a16}	805.0	805.7	-0.1	180.0	179.9	0.1
Short circuit						
Voltage	Magnitude, V			Phase, degrees		
	Measured	Predicted	Error, %	Measured	Predicted	Error, degrees
V_p	9.0	9.0	0.0	0.0	0.0	0.0
V_s	0.0	0.0	0.0	-	-	-
V_{a4}	8.3	8.3	-0.3	140.4	140.7	-0.3
V_{a5}	9.7	9.7	-0.1	-41.4	-42.1	0.7
V_{a8}	12.2	12.3	-0.8	138.6	135.9	2.7
V_{a9}	13.7	13.8	-0.9	-43.2	-45.6	2.4
V_{a12}	15.2	15.3	-0.9	138.6	133.1	5.5
V_{a13}	16.9	16.8	0.2	-48.6	-47.9	-0.7
V_{a16}	18.3	18.4	-0.4	135.0	131.2	3.8

Table 9.3 Measured and predicted voltages in the tapping winding sections of PC4 for a sample configuration.

9.5.1 Heat-run of mock-up inductor

Winding resistivity at temperature T_2°C is given by [Davies, 1990]:

$$\rho_{T_2} = (1 + \Delta\rho(T_2 - T_1))\rho_{T_1} \tag{9.1}$$

where $\Delta\rho$ is the thermal resistivity coefficient and ρ_{T_1} is the material resistivity at T_1°C.

Assuming a uniform temperature distribution throughout the winding, T_2 can be calculated from the measured winding resistance at temperatures T_1 and T_2 (since $R \propto \rho$) using:

$$T_2 = T_1 + \frac{R_{T_2}/R_{T_1} - 1}{\Delta\rho} \tag{9.2}$$

A mock-up winding was built to verify Eq. 9.2 before using it to measure the cooling characteristics of the PCRTXs, which have no embedded temperature sensors. A single-layer of 1.25 mm wire, having 193 turns and length 257 mm, was wound over a fibre-glass former, producing an air-core inductor having calculated wire resistance and inductance values of 2.18 Ω (at 20°C) and 6.52 mH, respectively. The former was an off-cut from one of the three one-metre lengths which were custom made for the PCRTXs. The wire, having the same grade as the first winding section of PC4, was held in place using the same fibre-glass tape which was wound over the low-voltage windings of each PCRTX.

The mock-up winding is shown in Figure 9.8.

Assuming zero radiation, convection and conduction losses, the winding temperature rise θ_m when a current-density J is applied for a time t is given by [Davies, 1990]:

$$\theta_m = J^2 \frac{\rho}{(C\gamma)} t \tag{9.3}$$

where $(C\gamma)$ is the volume specific heat.

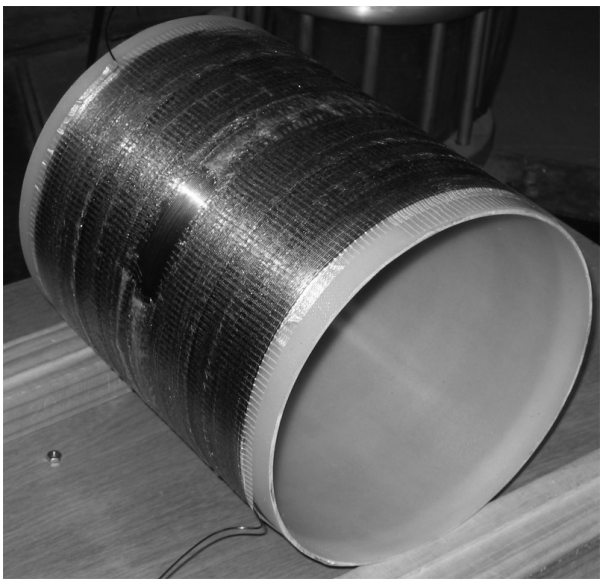

Figure 9.8 Mock-up winding used to verify the winding resistance / temperature relationship of Eq. 9.2.

The winding temperature was increased from an ambient of 22°C to 162.3°C over 8 minutes and 30 seconds by applying a current-density of 14.1 A/mm^2. The winding cooling characteristic was then measured for 28 minutes and 30 seconds. Temperature measurements were taken at the top of the centre of the winding and the bottom of the centre of the inside of the former during the heating and cooling periods using a Raytek Raynger MX heat-gun. It was necessary to adjust the variac over the heating period to maintain the current-density value as the winding resistance increased. The results of the heat-run are shown in Figure 9.9.

Initially, the measured winding temperature rise closely matches the value calculated using Eq. 9.3. The rate of temperature rise starts to reduce as convection losses to the air and conduction losses to the former become significant. The radiation losses are still insignificant at these temperatures. The thermal lag between the winding and inside former temperatures, present during the heating period, practically disappears over the cooling period. Resistance measurements of the winding terminals over the cooling period were used to calculate the winding temperature using Eq. 9.2. The calculated winding temperature is virtually indistinguishable from the values measured using the

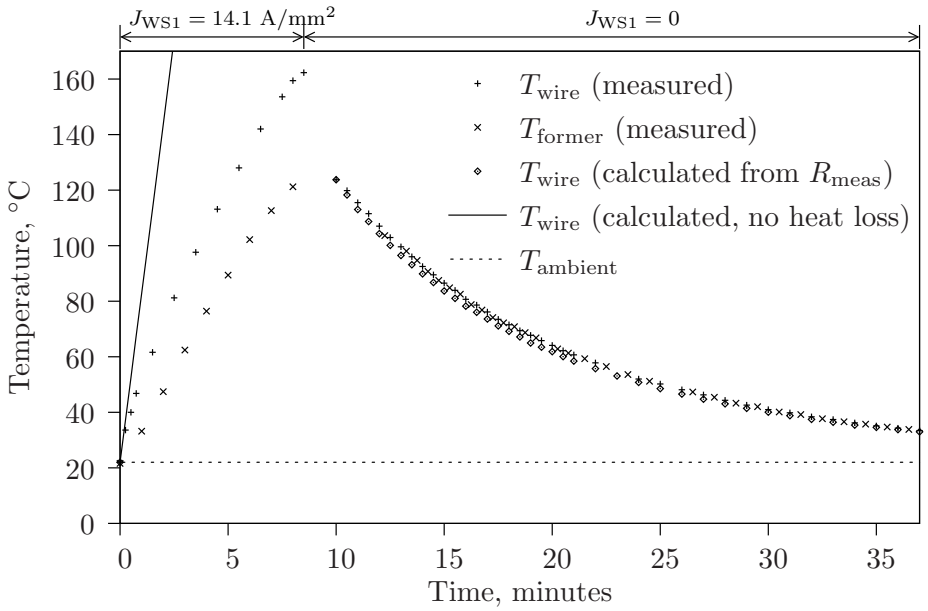

Figure 9.9 Heat-run test results of mock-up winding.

heat-gun. Confidence can thus be had in predicting the winding temperature of the PCRTXs by measuring the winding resistance.

9.5.2 Heat-run of PCRTXs

As discussed in Section 7.5.2, the PCRTXs were designed for a maximum winding temperature of 130°C, based on a worst-case temperature rise of 95°C and a maximum ambient temperature of 35°C. In testing the mock-up winding, it was noted that the fibre-glass tape started to deform at a winding temperature of approximately 150°C. The former and wire insulation remained intact throughout the heat-run. Furthermore, the winding inter-layer insulation and encapsulant, used in the PCRTXs but not in the mock-up winding, had temperature ratings of 180°C and 200°C, respectively. Confidence was thus held that the PCRTXs would survive the heat-run intact.

A three-minute heat-run of PC4 was performed using only the main winding section of the high-voltage winding. The applied current-density was 10.1 A/mm^2, equal to the design-value. The winding remained intact throughout the test. The cooling characteristic is shown in Figure 9.10.

Using Eq. 9.3, the winding temperature was calculated to be 109°C at the end of the heating period. The first winding resistance measurement, taken 2 minutes and 45 seconds into the cooling period, gave an estimated winding temperature of 96.0°C. Interpolating the measured cooling characteristic back to the end of the heating period, it appears that the actual winding temperature rise was only slightly below the calculated value. The good thermal insulating properties of the encapsulated winding meant that

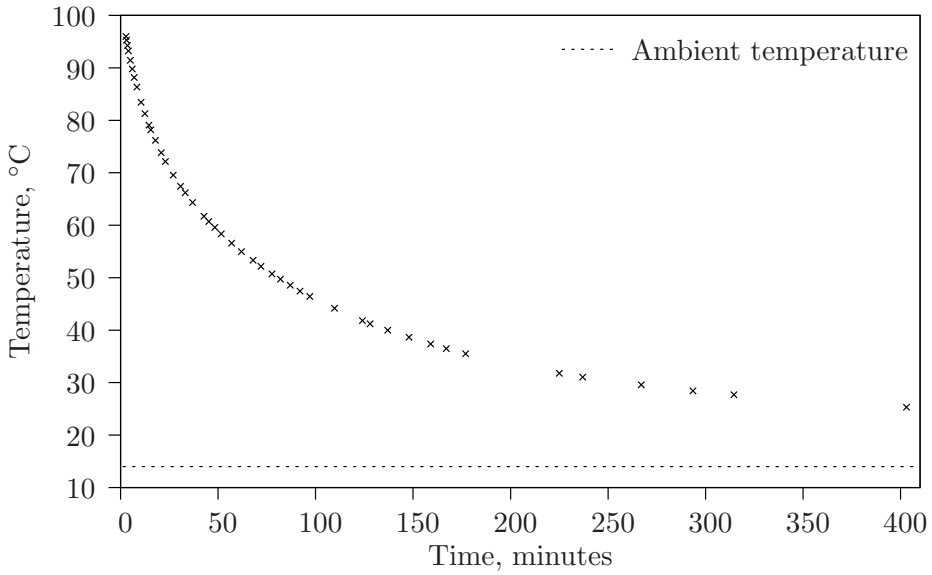

Figure 9.10 Secondary winding cooling characteristic of PC4 after a current-density of 10.1 A/mm^2 was applied for three minutes.

the radiation, convection and conduction losses were relatively insignificant over the three-minute heating period.

In stator insulation testing, the test voltage, typically equal to two times the rated phase-to-phase voltage + 1 kV, is applied for 60 seconds. The voltage must be ramped-up and ramped-down from the rated phase-to-ground voltage at a rate of 1 kV/s. This information was used to calculate an effective on-time at the test voltage V_t. For a given load capacitance C_l, $\theta_m \propto J^2 \propto \int V_s^2 dt$. Assuming that $V_t = 36$ kV and that the ramp-up and ramp-down starts at zero volts, giving some allowance for circuit tuning, the integral is equal to $V_s^2(\frac{2}{3}t_1 + (t_2 - t_1))$, where $t_1 = 36$ s and $(t_2 - t_1) = 60$ s. The effective on-time for a 60 second test at $V_t = 36$ kV is thus $(\frac{2}{3} \times 36 + 60)$ s = 84 s.

The measured cooling characteristic of PC4 was used to estimate the testing duty-cycle of the PCRTXs. The method is not exact because a thermal equilibrium between the core and windings was not reached during the three-minute heat-run and each PCRTX has a different winding thickness. Using Eq. 9.3, the calculated temperature rise for a current-density of 10.1 A/mm^2 and an on-time of 84 seconds was 43.5°C. Using Figure 9.10 and assuming that the winding temperature was equal to 100°C at the end of the heating period, the winding would take 57 minutes to cool down by this amount. A testing duty-cycle of one test per hour was thus assigned. This was applied to each PCRTX, using only the main winding section and maintaining the same current-density. The results are shown in Figure 9.11.

The winding temperature of PC4 stabilised to 107°C after 18 hours. The maximum temperature was 7 degrees above the estimated temperature at the end of the three-minute heat-run, but still considerably below the design-value of 130°C. The winding

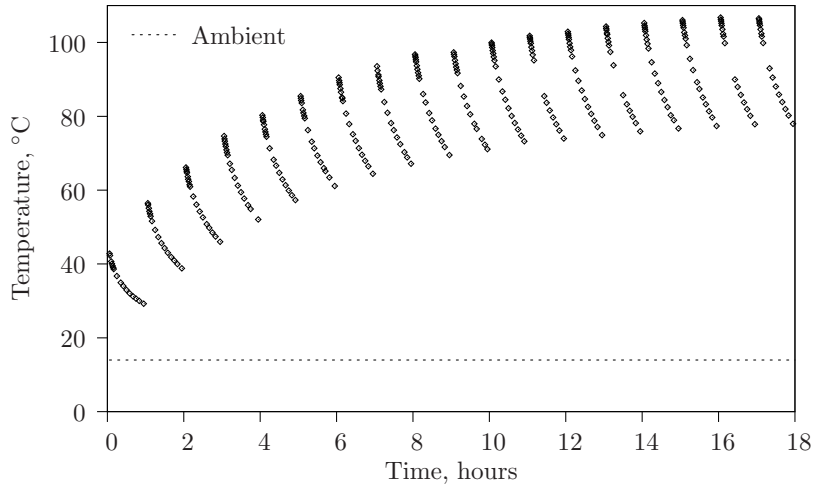

(a) PC4

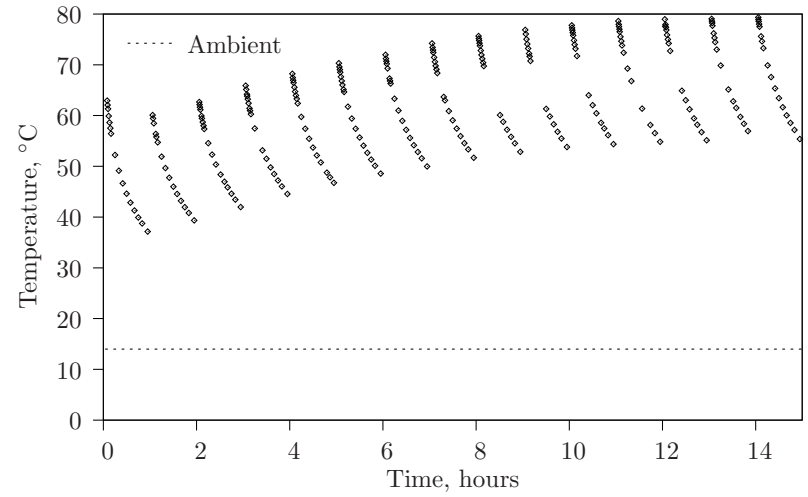

(b) PC5

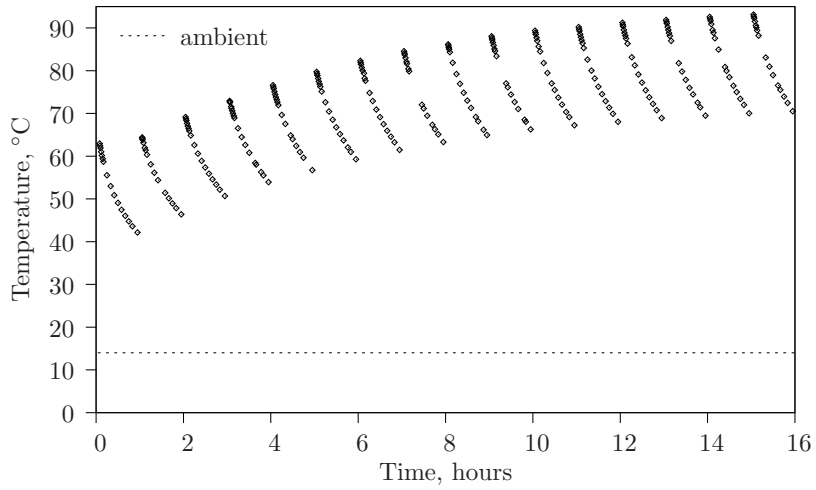

(c) PC6

Figure 9.11 Secondary winding temperatures of the PCRTXs after applying a current-density of 10.1 A/mm^2 for 84 seconds every hour.

temperature of PC5 and PC6 stabilised after 15 and 16 hours, although an initial on-time of 180 seconds was chosen to reduce the test duration. The maximum winding temperatures were 79°C and 93°C, respectively. The temperature rise per test of PC5 and PC6 was ∼23°C compared to ∼29°C for PC4. Both PC5 and PC6 have ∼12 kg less of copper in their main winding sections than PC4, but each PCRTX has the same former diameter and hence cross-sectional area for convection cooling. This may be the reason for the reduced temperature rise of PC5 and PC6.

These temperature rise measurements, along with Figures 9.10 & 9.11, show that if the windings were initially at an ambient temperature of ∼16°C, any PCRTX can be used to perform two consecutive tests and then one test every hour after that, without ever reaching a temperature which would cause damage. It also looks feasible to perform three tests, spaced 20 minutes apart, and then one test every hour after that. Assuming that the stator insulation remained intact, this duty-cycle would likely cause no undue delay when testing each phase separately in a three-phase generator. In the case of insulation failure, modifications to the stator assembly would likely take longer than the cooling period of the PCRTX.

In another experiment, the winding temperature of PC4 was increased to almost 135°C over 7 hours and 30 minutes by reducing the off-time to 45 minutes. The high wire tension and multiple layers, not present in the mock-up winding, stopped the former from expanding outwards with the temperature rise, causing several small cracks to form. While the device remained fully functional afterwards, this experiment indicated that a duty-cycle of less than one test per hour may be required for ambient temperatures significantly above the laboratory ambient of ∼16°C.

Lower test voltages and configurations involving the tapping winding sections will reduce the winding temperature rise, which can be calculated using Eq. 6.28 of Section 6.7. If cooling curves were then obtained for each winding configuration, it would be possible to increase the testing duty-cycle for other configurations. The above determined duty-cycle is relatively conservative and suitable for all of the designed winding configurations and secondary voltages up to 36 kV.

9.5.3 Core construction methods

The central limb of a full-core transformer is normally constructed by stacking the core laminations parallel to each other, with the widths stepped to make an approximate circle. The loss of cross-sectional area from the stepped lamination widths can be minimised for a given number of steps by adjusting the bundle height such that the difference in widths between any two adjacent bundles is constant. The four core sections of the kitset were constructed this way, with a total of 55 steps per core. The design and finished product are shown in Figures 9.12(a) & 9.12(c). A stacking factor

of 0.96 was assumed and this was almost achieved in practice.

It has been reported in the literature that eddy-current heating effects in cores with parallel-stacked laminations can be significant in full-core reactors, especially when the air-gaps are large [Meyerhans, 1958]. Eddy-current heating effects have also been observed in partial-core transformers with parallel-stacked laminations [Bodger and Enright, 2004].

The heating effects can be reduced by stacking the core laminations in the radial direction [Meyerhans, 1956]. A fifth core section was constructed with radially-stacked laminations so that the heating effects of each construction method could be compared. The design and finished product are shown in Figures 9.12(b) & 9.12(d).

A computer program was written to calculate the 9 lamination widths of each bundle 'A', 'B', 'C', 'D', 'E', 'F', 'G', 'H', 'I'. The widths are labelled in Figure 9.12(b) (in small font). The overall stacking factor was calculated to be 0.87, assuming a parallel stacking factor within each bundle of 0.96. The core was constructed by inserting one bundle at a time and the calculated stacking factor was achieved in practice. The loss of stacking factor over the parallel-stacked core will have some effect on the saturation flux-density. However, for reasons of linearity and operating noise, a reduced flux-density of 1.2 T was chosen for the kitset, meaning that the saturation characteristic cannot easily be measured. It took approximately the same time to stack the radial laminations as it did to stack the parallel laminations in the other core sections.

9.5.4 Comparison of parallel- and radially-stacked laminations

Three parallel- and one radially-stacked core sections were used to tune PC4 to $C_l = 1.1$ uF. A secondary voltage V_s of 30 kV was applied for three minutes. The input power was measured at the start of the test as 10.2 kW. The input power includes the winding losses, proximity losses, capacitor losses and core losses. At the end of the test the input power had increased to 11.9 kW. This was due to the increasing resistance of the secondary winding. The temperature profile of the four core sections was recorded using a thermal imager at the end of the test. The results are shown in Figure 9.13, where the indicated times are after the device was switched off.

Figure 9.13 shows that the heating effects are largest for the outside core section with parallel-stacked laminations. The maximum temperature rise above ambient was measured as 33.6°C, 164 seconds after the test was complete. In another test, a temperature rise of 48°C was measured when the rated voltage of $V_s = 36$ kV was applied for three minutes. In comparison, the maximum temperature rise of the outside core section with radially-stacked laminations was measured as 3.3°C, 224 seconds after the test was complete. The eddy-current heating effects have disappeared. A

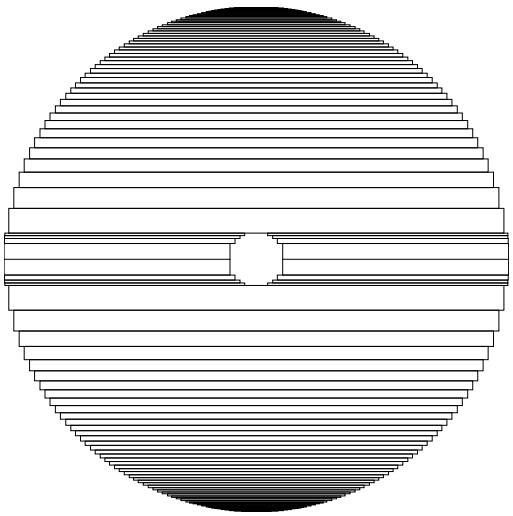

(a) Parallel-oriented laminations (theory)

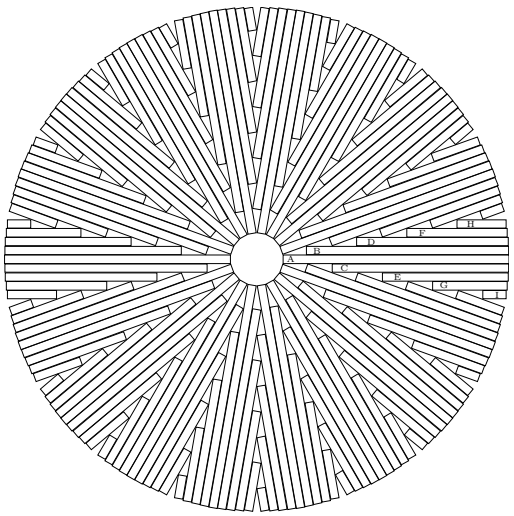

(b) Radially-oriented laminations (theory)

(c) Parallel-oriented laminations (practice)

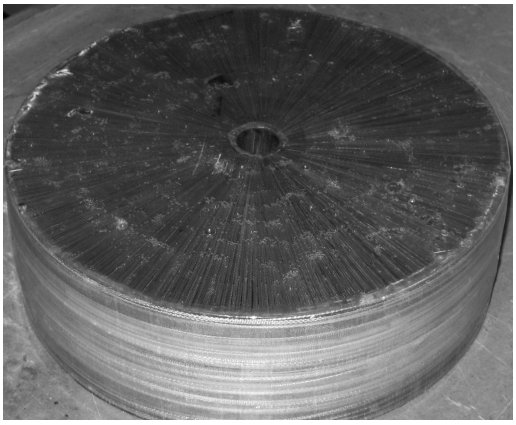

(d) Radially-oriented laminations (practice)

Figure 9.12 The two different methods of core construction used in the kitset.

radially-stacked core would be required in any continuously rated PCRTX, particularly for the outside core sections, which carry more inter-laminar flux.

After the core and winding sections had cooled down back to ambient temperature, the test was repeated using four parallel-stacked core sections. The input power was measured as 10.9 kW, 700 W more than for the previous test. The actual core losses cannot be obtained from the terminal conditions without having prior knowledge of the capacitor and proximity losses.

PC6 was configured for operation with only one core section. The inductance of the parallel- and radially-stacked core sections were separately measured, using the resonant tuning test, as 8.13 H and 8.22 H. The loss of stacking factor in the radially-stacked core did not reduce the inductance in this case, which was actually 1.1% larger than the core section with parallel-stacked laminations. In a radially-stacked core, the magnetic

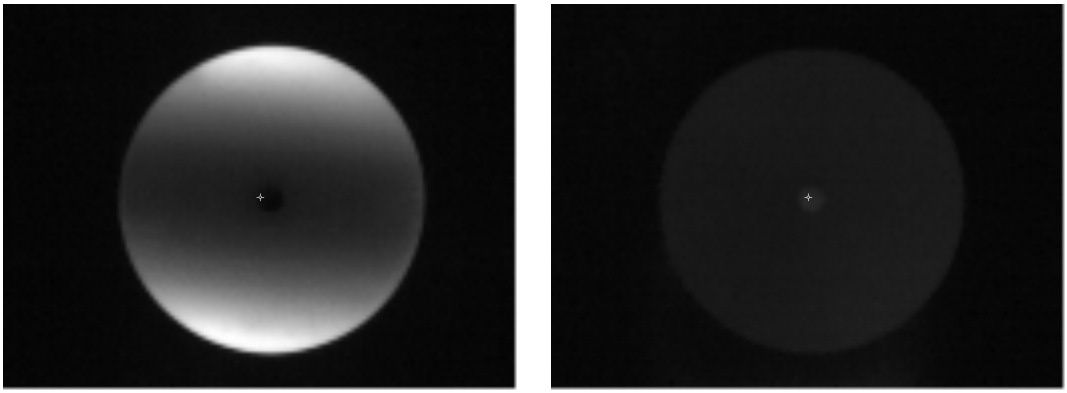

(a) Outside parallel-stacked core section, t = 164 s (b) Outside radially-stacked core section, t = 224 s

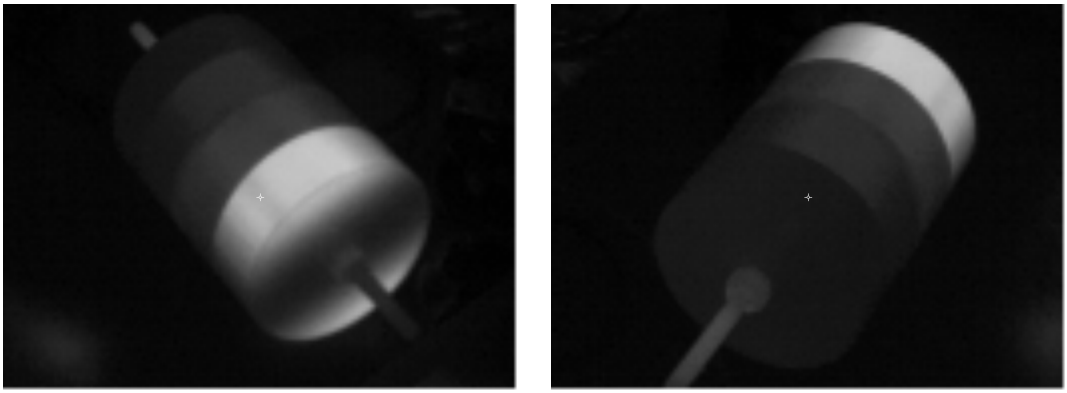

(c) All four core sections, t = 716 s (d) All four core sections, t = 730 s

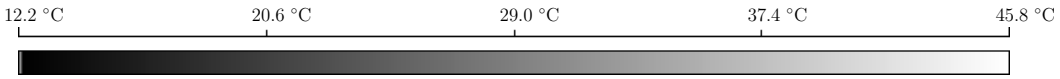

(e) Temperature scale

Figure 9.13 Comparison of eddy-current heating effects between core sections with parallel- and radially-stacked laminations in PC4 with V_s = 30 kV, C_l = 1.1 uF, t_{on} = 180 s.

flux remains within the lamination plane for all laminations. In a parallel-stacked core, the magnetic flux remains within the lamination plane for some laminations and travels normal to the lamination plane for others. The relative permeability of core steel in the direction normal to the lamination plane is greatly reduced, due to the inter-laminar insulation. If the stacking factor of the parallel-stacked and radially-stacked cores were then same, then, due to this effect, one would expect the radially-stacked core to produce a higher inductance value in a PCRTX. One plausible explanation for the increased inductance of the radially-stacked core is that this effect more than accounts for the loss of stacking factor.

9.6 CONCLUSIONS

A kitset for high-voltage testing of hydro-generator stators was designed, built and tested. Tests were performed in the laboratory to demonstrate performance. Good correlation between test and model results was obtained. The short-term rating of 448 kVAr was achieved with a shipping weight of 480 kg, giving a specific weight to kVAr ratio 1.1 kg/kVAr. This is a significant reduction over what is normally obtained using full-core variable inductors and a separate exciter transformer. The next step is to use the kitset in the field.

Chapter 10

FUTURE WORK

10.1 FOR THE PCRTX KITSET DESCRIBED IN CHAPTER 9

A good indication of the expected real-world performance of the PCRTX kitset was obtained from tests performed in the laboratory. The next step is to use the kitset in its intended application of high-voltage testing of hydro-generator stators. The benefits are not just limited to the industry exposure and financial gain of those involved. Technical expertise would also be obtained.

The capacitive tip-up of the stator winding under-test could be measured. Capacitive tip-up will reduce the input impedance of the resonant circuit, which is normally tuned to maximum impedance at a voltage well below the test voltage. It was difficult to measure the effect of capacitive tip-up on the input impedance of the resonant circuit when using earlier PCRTX designs because of core saturation effects, which also affect circuit tuning.

The real power at the primary winding could be measured when energising a stator winding. By comparing this value to the figure obtained when energising a low-loss capacitor in the laboratory of the same capacitance value, a measure of the quality factor of the insulation under-test could be obtained. This could be compared to the estimated value of 20.

Using the kitset in the field will also determine if the assigned thermal duty-cycle is overly restrictive, causing the testing schedule to be extended. The practicalities of the manual circuit tuning system, which requires repeated changing of winding taps and insertion and removal of the core pieces for air-gap adjustment, could be assessed.

To allow others to use the kitset without consulting this thesis, an instruction manual for the kitset could be written. This would contain the measured tuning characteristics, a procedure for circuit tuning, the thermal duty cycle and figures showing winding layout and terminal labels.

10.2 FURTHER INVESTIGATIONS INTO PCRTXs

10.2.1 Thermal model

A thermal model for the encapsulated high-voltage winding could be developed. This would allow for the duty-cycle of short-term rated devices to be calculated at the design-stage. It could also be used to calculate a suitable current-density for continuously rated devices. Reference paper [García et al., 2002], which contains a detailed thermal study of a 23 kV / 110 V, 45 kVA transformer with encapsulated windings, may be a good starting point for the model.

10.2.2 Stray magnetic field

The stray magnetic field from the partial-core induces eddy-currents in the winding wire. The theory described in [Sullivan, 2001] could be applied to the finite element model developed in Chapter 5 to calculate the associated losses in each turn. The theory could be extended to account for rectangular wire as well as circular wire. The loss calculations could be incorporated into the transformer design program. For continuously rated devices with large currents, the eddy-current heating effects may be significant enough to influence the design.

The stray magnetic field can also couple to nearby external conducting and ferromagnetic material, such as bus-bars and concrete reinforcing rods. This can create additional losses and potentially weaken the surrounding structures. Consideration to the clearances to these materials should be given when choosing an installation site for partial-core devices. Guidelines for air-core reactor installation, such as those given in Annex D of IEEE Std C57.16-1996 [IEEE Std C57.16-1996, 1997], could be modified for partial-core devices.

Consideration of the radiation exposure levels to nearby personnel could also be given. The reference level for occupational exposure to a 50 Hz time-varying magnetic field, set by the International Commission on Non-ionizing Radiation Protection [International commission on non-ionizing radiation protection, 1998], is 500 uT. Figure 10.1 shows that the calculated external magnetic field of PC4, at rated voltage and current, is well below the reference level at a perimeter of 10 times the device dimensions. The outside boundaries of the air-space, which were set to 100 times the device dimensions, are not shown in the figure. In testing performed to date, the operator has been located outside this perimeter. For future work, the calculated external magnetic field could be verified with measured data.

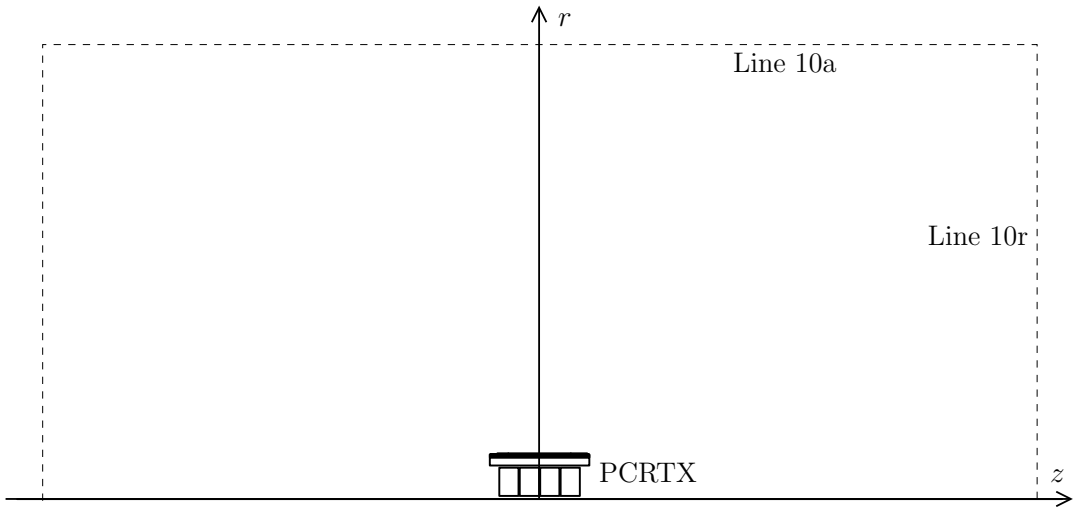

(a) Model geometry and sampling locations.

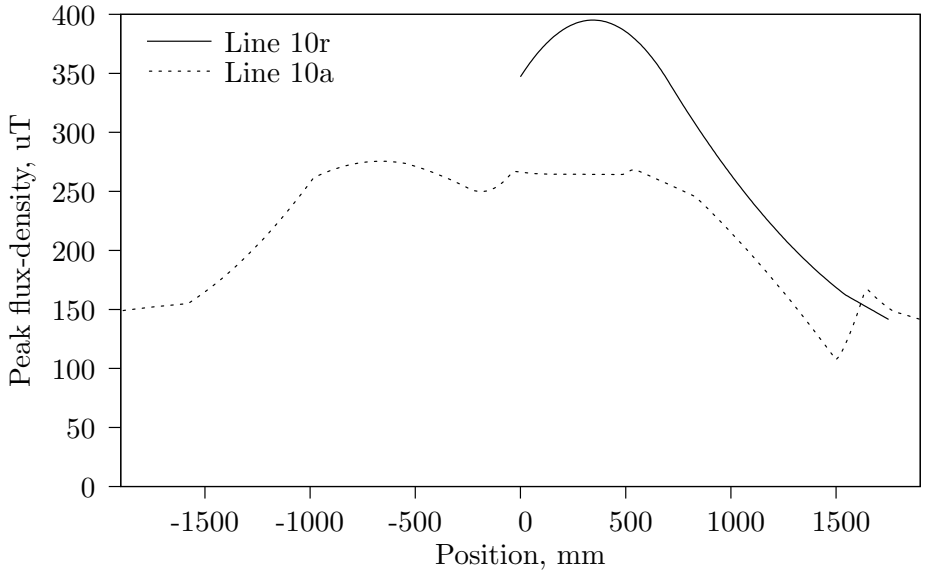

(b) Line plots.

Figure 10.1 Calculated external magnetic field surrounding PC4 at 36 kV, 448 kVAr.

10.2.3 Core loss model

A loss model for the partial-core with radially-stacked laminations could be developed. It is difficult to directly obtain the core losses in PCRTXs from the measured terminal power without having prior knowledge of the load quality factor, winding eddy-current losses and other proximity losses. Since the radially-stacked laminations are free of inter-laminar flux, the expected losses are equal to the figure given by the manufacturer, typically less than 1 W/kg @ 1.7 T, 50 Hz in grain-oriented steel [Qader and Basak, 1982]. A core loss model for partial-core inductors with radially-stacked laminations is given in [Friedrich, 1965]. This model may also be suitable for PCRTXs, since, for

circuit quality factors of Q > 10, the core flux-density and hence losses are mainly determined by the secondary winding.

10.2.4 Voltage distribution under impulse

Consideration could be given to the withstand capability of PCRTXs to power frequency and lightning impulse tests. The voltage distribution of the encapsulated high-voltage layer winding under impulse is unknown. In order to achieve a linear voltage distribution, the ratio of series capacitance to stray capacitance must be controlled. This may lead to an alternative winding cross-section design. Models for the series and stray capacitances of the high-voltage winding could be developed. These models have already been developed for a partial-core transformer with a different winding layout [Liew and Bodger, 2002]. They could be used as a starting point for the new models.

10.2.5 Measure partial-discharge levels

Partial-discharge (PD) measurements are often taken when energising stator and XLPE cable insulation. To obtain reliable data, background PD levels must be suitably low. The PD levels at the terminal of the high-voltage winding of PC4 could be measured at 36 kV when energising a high-voltage capacitor in the laboratory. This could be compared to the acceptable background level, set by IEC 60270 [IEC60270, 2000]. In case of non-compliance, an output filter may be required to reduce the background PD levels.

10.3 OTHER APPLICATIONS OF PCRTXS

10.3.1 Power supply for arc-signs

An arc-sign consists of a conducting back-plate, a sheet of insulation and one or more conducting front electrodes [Bell et al., 2007]. The front electrodes and the back-plate form the two terminals of the arc-sign. Mains frequency high-voltage, in the order of 10 - 20 kV, is applied across the terminals to produce visible corona and streamer discharge. The main purpose of the arc-sign is to create electrical artwork and signs. Electrically, arc-signs are similar to stator insulation under test. PCRTXs have also been used to energise large arc-signs [Lynch et al., 2007].

The design methodology of Chapter 7 could be applied to obtain an optimised PCRTX design for energising arc-signs. The main requirements are: operation from a standard 240 V, 10 A supply, easy circuit tuning (as insulation failure is a common occurrence) and an ability to energise arc-signs having capacitances of up to 100 nF (corresponding

to a front electrode cross-sectional area of $\sim$2.1 m^2), as well as operate under open-circuit conditions.

10.3.2 High-voltage testing of XLPE cables

High-voltage testing and off-line PD measurements are usually performed on XLPE cables after installation. The reactive power required to energise the cable capacitance can reach several 10s of MVAr. Resonant circuits are normally employed, with frequency-tuned systems becoming increasingly common. In 1997, CIGRE working group 21.09 defined a frequency range of 30 - 300 Hz to be "near power frequency" for the purposes of on-site cable testing [Schufft et al., 1999]. Test times can exceed 30 minutes and voltages of up to 500 kV are relatively common. Modern frequency-tuned resonant systems achieve specific weight to power ratios of 0.8 - 1.9 kg/kVAr. Without the need for a frequency converter and separate exciter transformer, a similar weight to power ratio could be achieved with a centre-gap tuned PCRTX. By operating at power frequency, a better representation of the in-service condition would be obtained.

Recently, a request for an investigation into the feasibility of a kitset having a 6 MVAr, 100 kV rating with a capacitive tuning range of 0.0095 - 1.9 uF at 50 Hz was made. A detailed study could be performed, to properly assess the technical and economic viability of the project. Starting with the methodology of Chapter 7, optimal designs utilising two and three devices with centre-gap tuning could be obtained. A motor-driven air centre-gap adjustment system could be designed. Particular attention would need to be given to the electric fields of the high-voltage winding, which may require the use of finite element analysis. The highest voltage obtained so far using the inter-layer insulation system with encapsulant is 80 kV. A 100 kV mock-up winding could be constructed and the PD levels could be measured to see if the existing construction method is viable. An alternative gaseous insulation medium such as SF_6 may be required for higher test voltages.

10.3.3 Partial-core resonant earthing coil

A resonant earthing coil (also known as a Peterson or arc-suppression coil) is a single-phase tunable reactor that is connected between the neutral of a transformer and ground, for the purpose of achieving a resonant neutral ground [Harlow, 2004]. In the event of a single-phase fault to ground, capacitive current flowing through the ground and into the two unfaulted phases can be compensated for with inductive current flowing through the ground and into the resonant earthing coil. The high impedance of the tuned parallel resonant circuit minimises any arcing at the fault location.

Tuning was achieved on earlier oil-filled designs with motorised adjustment of the central air-gap of a circular plunger core. The return for the magnetic circuit was via several

'C' sections [Meyerhans, 1956]. Modern arc-suppression coils are often dry-type and have fixed inductance. They are tuned via thyristor-switched capacitors, connected to tertiary windings [Jia et al., 2005]. Current injection into the neutral via a power converter, connected to another tertiary winding, can be used to compensate for the active and harmonic components of the fault current [Janssen et al., 2003]. This is known as residual current compensation (RCC).

Recently, a 635 kVAr resonant earthing coil with RCC was installed on the 11 kV network at the Darfield substation, located in the South Island of New Zealand [Scott, 2007]. The device has a full-core magnetic circuit, similar to a single-phase core-type transformer, but with a winding on each limb. The limbs have multiple air-gaps to ensure linearity. The high-voltage winding is rated at 6.35 kV, 100 A. The power converter and several low-voltage capacitors are connected to tertiary windings.

The voltage, kVAr and inductance values of this device are similar to that of PCRTXs. This brings about the possibility of designing a replacement resonant earthing coil with a partial-core. The main potential advantage is a significant reduction in weight and cost. The design methodology for fixed inductance PCRTXs of Chapter 7 could be used to design the replacement device. A detailed investigation could be performed, to properly assess the technical and economic viability of the project.

10.4 HIGH-TEMPERATURE SUPERCONDUCTING PARTIAL-CORE TRANSFORMER

The University of Canterbury has developed a prototype single-phase 230 V / 115 V, 15 kVA superconducting partial-core transformer (HTSPCTX). The device was designed using the reverse design method and a magnetic model based on circuit theory [Liew and Bodger, 2001]. The windings, made from first generation Bi-2223/Ag tape from American Superconductor and having a dc rating of 100 A under self-field, are immersed in liquid nitrogen. The partial-core remains in open air. Some preliminary test results have been obtained [Bodger et al., 2005]. A load test has not yet been performed, due to a crack in the fibre-glass cryostat, which is currently being repaired.

10.4.1 Apply finite element model to prototype HTSPCTX

The finite element model of Chapter 5 could be used as an alternative magnetic model for HTSPCTXs. As a preliminary model result, the open-circuit test results of the prototype HTSPCTX are compared to the finite element (FEM) and circuit theory (CTM) models in Table 10.1. Losses have not been modelled. No suitable model exists for core losses. Ac losses in the superconducting windings were assumed to be zero and

leadout losses were not calculated. Table 10.1 shows that the finite element model has accurately calculated the terminal conditions of the open-circuit test.

Parameter	Value		
	Measured	FEM	CTM
Primary voltage, V	230	230	230
Primary current, A	19	18.7	20.5
Secondary voltage, V	113	113.1	113.3
Tertiary voltage, V	111	111.3	-[a]
Primary power, W	200	0[b]	0[b]

[a]Cannot directly calculate this parameter using the circuit theory model.
[b]Losses have not been modelled.

Table 10.1 Preliminary open-circuit test results of prototype HTSPCTX compared to finite element and circuit theory models.

Accurate calculation of the magnetic fields within the winding window are required to evaluate the critical current and ac losses of the superconducting tape. A measured critical current characteristic for a sample of 50 A Bi-2223/Ag tape at liquid nitrogen temperature (77 K) is shown in Figure 10.2.

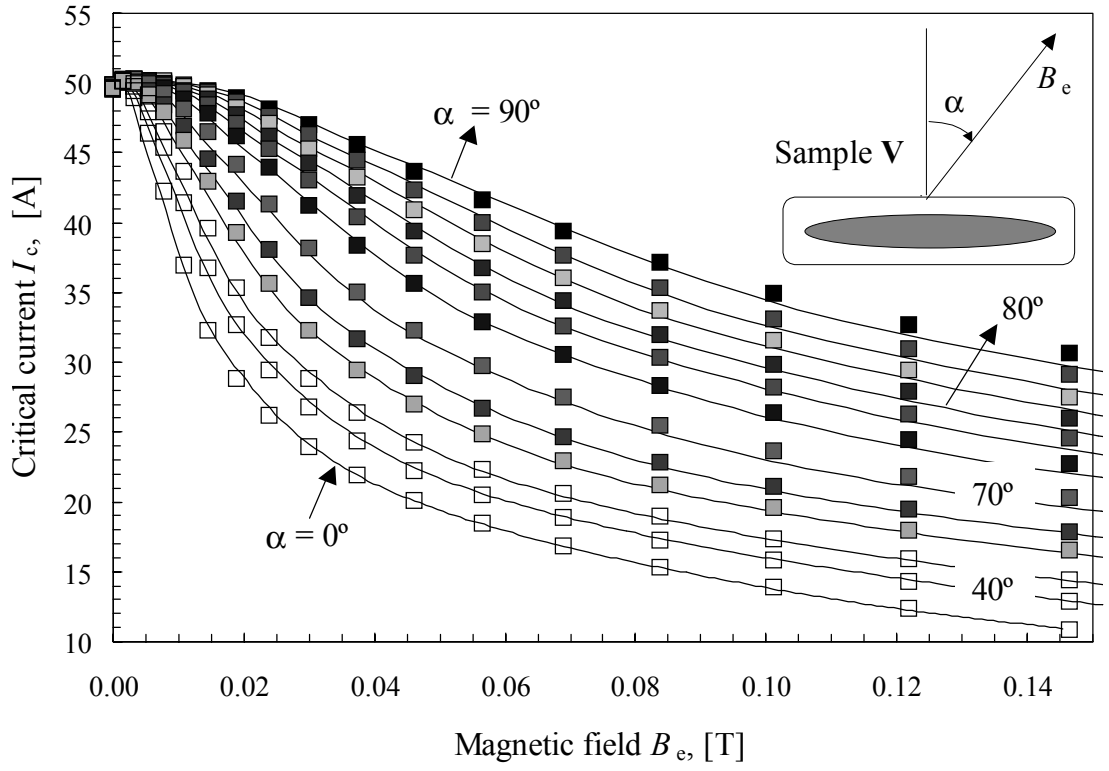

Figure 10.2 Critical current of the Bi-2223/Ag tape versus magnetic field amplitude B_e at 77 K for different angles $\alpha = 0°$; 40; 50; 60; 65; 70; 75; 77.5; 80; 82.5; 85 and 90° respectively. (taken from [Chevtchenko, 2002])

Figure 10.2 shows that the critical current of the tape can be significantly reduced by very low levels of radial magnetic field, which always occur in partial-core transformers. The critical current of the windings in the prototype HTSPCTX could be calculated using a characteristic curve similar to Figure 10.2 and then measured in the laboratory. Due to the non-uniform field over the winding window, the critical current of the windings may be difficult to measure. As the excitation currents are gradually increased, only the few turns most affected by the external field will stop superconducting. At first, there would be very little difference in the terminal conditions but the affected turns would experience rapid heating as the conduction starts to take place in the silver matrix, rather than in the superconducting ceramic. It was noted in [Ho, 2004] that very rapid boil-off of liquid nitrogen occurred when the open-circuit test voltage was increased above 200 V. This may indicate that the critical current of the primary winding was reached below the rated voltage of 230 V. Further investigations are required.

Once a model for the winding critical current has been developed, it could be used to investigate the effect of adding end-pieces to the partial-core on the winding critical current. Figure 10.3 shows that the radial flux in the winding window of the prototype HTSPCTX can be reduced with two core sections from the new PCRTX kitset of Chapter 9, placed at each end of the partial-core. A modified partial-core design may be arrived at, which increases the winding critical current but still maintains the advantages of the original partial-core design.

10.4.2 Investigate fault-current limiting capability

As noted in [Hornfeldt et al., 1993], a transformer with superconducting windings can have rather attractive fault-current limiting properties. The fault-current limiting properties of the prototype HTSPCTX could be investigated. The extra turns of wire in the partial-core transformer, required to reduce the heavy magnetising current of the open magnetic circuit, could provide enhanced fault-current limiting properties over an equivalent full-core transformer.

10.4.3 Develop a three-phase HTSPCTX

Three identical two-winding partial-core transformers could be connected together to form a three-phase transformer. By arranging the three devices close together in an equilateral triangle configuration, the magnetic flux of each partial-core would return through the remaining two cores, increasing the magnetising reactance values. The self- and mutual-inductance approach to calculating magnetising and leakage reactance values could still be employed. Making use of winding symmetry and the phase relations of three-phase circuits, the 6×6 inductance matrix $\mathbf{L}$ can be reduced to six unique

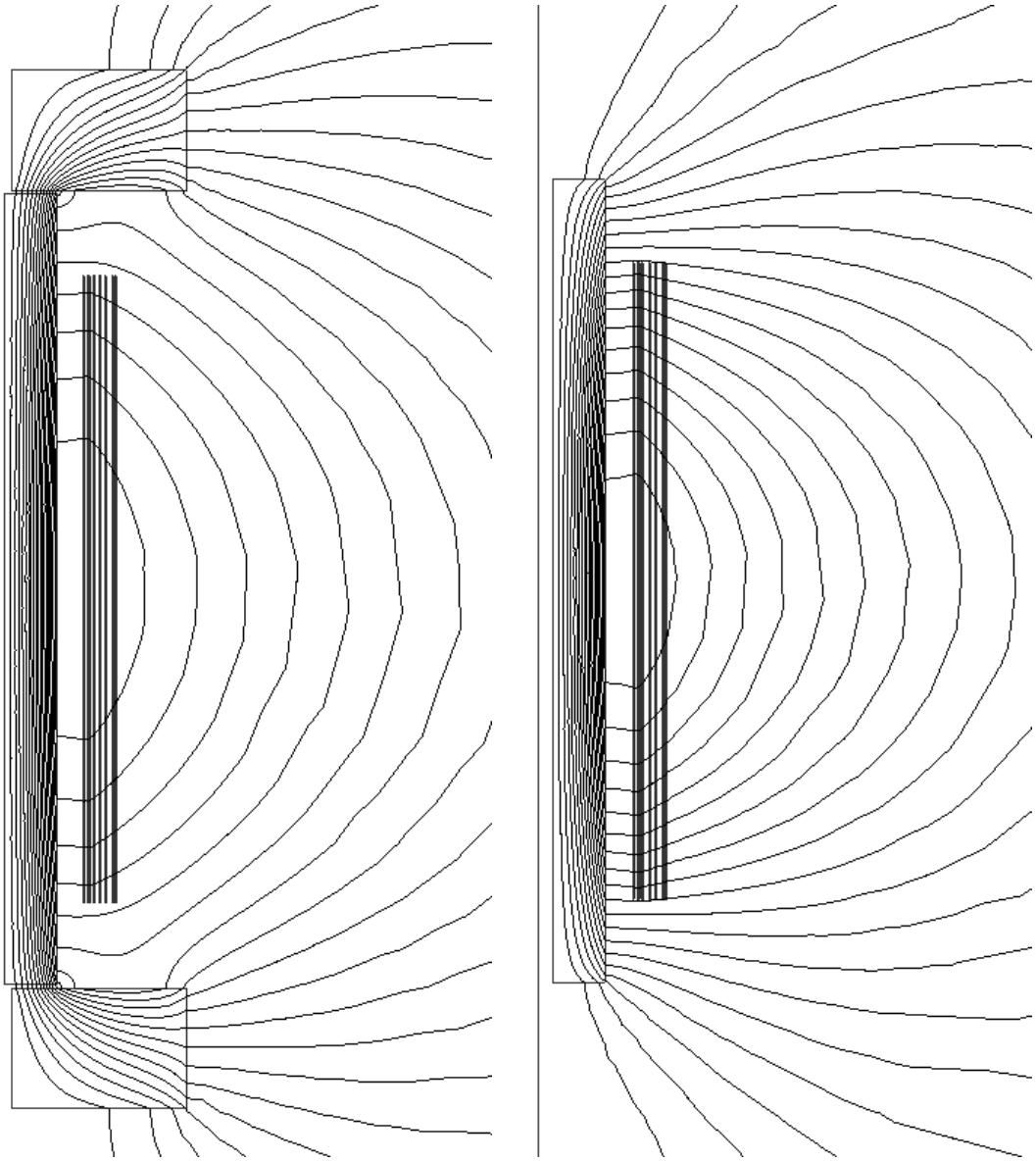

(a) With core end-pieces. (b) Without core end-pieces.

Figure 10.3 Open-circuit flux plot of prototype HTSPCTX with and without core end-pieces.

inductances for steady-state conditions, from which an equivalent single-phase circuit can be derived [Yamaguchi et al., 1999].

10.4.4 Use a radially-stacked core

A radially-stacked core could be built for the prototype HTSPCTX as a replacement for the parallel-stacked core. The heating effects and losses of the two designs could be compared.

Chapter 11

CONCLUSION

This thesis started by introducing the reverse method of transformer design. An existing magnetic model for full-core shell-type transformers, based on circuit theory, was summarised. A magneto-static finite element model was introduced and two sample transformers were analysed using both models. The magnetic model based on finite element analysis was shown to be more accurate than the model based on circuit theory, though at the expense of complexity of programming. The finite element magnetic model was also found to be more flexible, as it allowed for other transformer types, such as those based on air- or partial-core designs, to be modelled by only making changes to the model geometry. This removed the need for empirically derived factors.

Partial-core resonant transformers were then introduced and their characteristics were explained using an equivalent circuit model. A method of measuring the winding inductances under resonant operation was developed and used to investigate the characteristics of two different tuning methods. It was found that centre-gap tuning provided a larger inductance variation for the same air-gap over axial-offset tuning, as well as linearity to higher voltages. Another practical advantage of centre-gap tuning is that the forces between the core and windings are symmetric. The core is self-centering when the transformer is energised and mechanical core locking mechanisms are no longer required.

A finite element model of the partial-core resonant transformer was developed by adopting the model for full-core shell-type transformers. The model results accurately matched the measured inductance variation characteristics of three sample transformers and predicted the onset of core saturation in both axial-offset and centre-gap arrangements.

A new design of partial-core resonant transformer was arrived at, having an alternative core and winding layout, as well as multiple winding taps. The finite element model was extended to accommodate the new design and a framework of analysis tools was developed. A general design methodology for partial-core resonant transformers with fixed inductance was developed. A multiple design method was applied to obtain an optimal design for a given set of specifications and restrictions. The design methodology

was then extended to devices with variable inductance.

Three design examples of partial-core resonant transformers with variable inductance were presented. The first two design examples were replacement transformers for two of the previously tested sample devices. The device weights were significantly reduced and the saturation effects were removed. The third design example was a kitset for high-voltage testing, with the capability to test any hydro-generator stator in New Zealand. The kitset was built and tested in the laboratory, demonstrating design capability. Other significant test results, for which no models have yet been developed, were also presented. Heating effects in the core were reduced by adopting an alternative core construction method, where the laminations were stacked radially, rather than in the usual parallel direction. The new kitset is yet to be used in the field.

The general design methodologies developed in this thesis were successfully verified. They can now be used to design PCRTXs for testing the insulation integrity of other devices, such as cables, transformers and switch-gear. Other possible applications of the partial-core transformer were also presented.

REFERENCES

Allcock, R., McClelland, R., Holland, S. A., and Roué, A. (1995). Transformer design and analysis using finite element methods. In *IEE Colloquium on Computation in Electrostatics*, pages 8/1–8/3.

Alonso, G. and Antonio, J. (2001). A new method for calculating of leakage reactances and iron losses in transformers. In *Proceedings of the Fifth International Conference on Electrical Machines and Systems (ICEMS)*, volume 1, pages 178–181, Shenyang, China.

Andersen, O. W. (1967). Optimum design of electrical machines. *IEEE Transactions on Power Apparatus and Systems*, 86(6):707–711.

Asensi, R., Cobos, J. A., Garcia, O., Prieto, R., and Uceda, J. (1994). A full procedure to model high frequency transformer windings. In *Proc. IEEE Power Electronics Specialist Conference PESC'94*, volume 2, pages 856–863.

Bell, S. C., Enright, W. G., Tunstall, K. R., and Bodger, P. S. (2007). Lightning arc drawings - dielectric barrier discharges for artwork. In *15th International Symposium on High Voltage Engineering*, Ljubljana, Slovenia. Paper T9.305, CD-ROM.

Bendre, V. D., Bell, S. C., Enright, W. G., and Bodger, P. S. (2007). AC high potential testing of large hydro-generator stators using open core transformers. In *15th International Symposium on High Voltage Engineering*, Ljubljana, Slovenia. Paper T3.303, CD-ROM.

Bendre, V. D., Bodger, P. S., and Wood, A. R. (2008). Towards a practical partial core transformer - compensation of reactive power requirements with a VSC. In *IASTED International conference on Power and Energy Systems*, Gaborone, Botswana. CD-ROM.

Bernasconi, F., Zaengl, W. S., and Vonwiller, K. (1979). A new hv-series resonant circuit for dielectric tests. In *Third international symposium on high voltage engineering*, Milan, Italy. Paper 43.02.

Bettess, P. (1988). Finite element modelling of exterior electromagnetic problems. *IEEE Transactions on Magnetics*, 24(1):238–243.

Blachie, F., Keradec, J., and Cogitore, B. (1994). Stray capacitances of two winding transformers: equivalent circuit, measurements, calculation and lowering. In *Conference Record of the 1994 IEEE Industry Applications Society Annual Meeting*, volume 2, pages 1211–1217.

Bodger, P. S. and Enright, W. G. (2004). A resonant transformer for high voltage testing of generator stators. *Australian Journal of Electrical and Electronics Engineering*, 1(3):179–185.

Bodger, P. S., Enright, W. G., and Ho, V. (2005). A low voltage, mains frequency, partial core, high temperature, superconducting transformer. In *Australasian Universities Power Engineering Conference (AUPEC)*, volume 1, pages 73–78, Hobart, Australia.

Bodger, P. S. and Liew, M. C. (2002). Reverse as-built transformer design method. *International Journal of Electrical Engineering Education (IJEEE)*, 39(1):42–53.

Bomben, S., Sedding, H., DiPaul, J., and Glowacki, R. (2003). Experience with high potential testing hydro generator multi turn stator coils using 60 Hz AC, DC, and VLF (0.1 Hz). In *Electrical Insulation Conference and Electrical Manufacturing & Coil Winding Technology Conference*, pages 435–438.

Brauer, J. R. (1993). *What every engineer should know about finite element analysis*. Marcel Dekker, New York, 2nd edition.

Chen, Q. and Konrad, A. (1997). A review of finite element open boundary techniques for static and quasi-static electromagnetic field problems. *IEEE Transactions on Magnetics*, 33(1):663–676.

Chevtchenko, O. A. (2002). *On the application of high-T_c superconductors in power coils and transformers*. PhD thesis, University of Twente, The Netherlands.

Christoffel, M. (1967). The design and testing of EHV shunt reactors. *IEEE Transactions on Power Apparatus and Systems*, PAS-86(6):684–692.

Connelly, F. C. (1965). *Transformers: Their principles and design for light electrical engineers*. Sir Issac Putman & Sons Ltd, London, 1st edition.

Davies, E. J. (1990). *Conduction and induction heating*. P. Peregrinus Ltd, London, U.K., 1st edition.

Edwards, J. D. (2005). *An introduction to MagNet for Static 2D Modelling*. Infolytica Corporation.

Emery, F. T. (2004). Basics of power factor measurements on high voltage stator bars and stator windings. *IEEE Electrical Insulation Magazine*, 20(31):40–45.

Enright, W. and Arrillaga, J. (1998). A critique of Steinmetz model as a power transformer representation. *International Journal of Electrical Engineering Education (IJEEE)*, 35(4):370–375.

Enright, W. G., Bendre, V. D., Bell, S. C., and Bodger, P. S. (2008). Field experiences using a prototype open core resonating transformer for A.C. high potential testing of hydro-generator stators. In *Techcon Asia Pacific*, pages 265–277, Sydney, Australia.

Enright, W. G. and Bodger, P. S. (2004). Short time rated and protected high voltage ac testing of generator stators using parallel resonant circuits. In *Electricity Engineers Association Conference (EEA)*, Christchurch, New Zealand. CD-ROM.

Freeman, E. M. and Lowther, D. A. (1989). An open boundary technique for axisymmetric and three dimensional magnetic and electric field problems. *IEEE Transactions on Magnetics*, 25(5):4135–4137.

Friedrich, M. (1965). Der magnetische Kreis von Stabkerne. *Schweizerische technische Zeitschrift*, 46:929–943.

García, A., Espinosa-Paredes, G., and Hernández, I. (2002). A thermal study of an encapsulated electrical transformer. *Computers & Electrical Engineering*, 28(6):417–445.

Gerlach, H. G. (1991). Resonant power supply kit system for high voltage testing. *IEEE Transactions on Power Delivery*, 6(1):1–7.

Gillespie, M. T. G., Murchie, G. B., and Stone, G. C. (1989). Experience with a.c. highpot and partial discharge tests for commissioning generating station cables and switchgear. *IEEE Transaction on Energy Conversion*, 4(3):392–396.

Gupta, B. K. (1995). Use of a.c. and d.c. highpot tests to assess condition of stator insulation. In *Electrical and Electronics Insulation Conference*, pages 605–608, Chicago, Illinois.

Harlow, J. H. (2004). *Electric power transformer engineering*. CRC Press, Boca Raton, FL, 1st edition.

Hauschild, W., Coors, P., Schufft, W., Plath, R., Herrmann, U., and Polster, K. (2002). The technique of AC on-site testing of HV cables by frequency-tuned resonant test systems. *Cigre Report*, 33-304.

Ho, V. (2004). Superconducting partial core transformer. Final year project report, Department of Electrical and Computer Engineering, University of Canterbury, Christchurch, New Zealand.

Holland, S., O'Connell, G. P., and Haydock, L. (1992). Calculating stray losses in power transformers using surface impedance with finite elements. *IEEE Transactions on Magnetics*, 28(2):1355–1358.

Hong, J., Heyun, L., and Zihong, X. (2005). Three-dimensional finite element analysis of electric fields at winding ends of dry-type transformer. In *Proceedings of the Eighth International Conference on Electrical Machines and Systems (ICEMS)*, volume 3, pages 2136–2139.

Hornfeldt, S., Albertsson, O., Bonmann, D., and Konig, F. (1993). Power transformer with superconducting windings. *IEEE Transactions on Magnetics*, 29(6):3556–3558.

Hurley, W. G., Wölfle, W. H., and Breslin, J. G. (1998). Optimized transformer design: inclusive of high-frequency effects. *IEEE Transactions on Power Electronics*, 13(4):651–659.

IEC60034-1 (2004). Rotating electrical machines. Part 1: Ratings and performance.

IEC60060-1 (1989). High voltage test techniques. Part 1: General definitions and test requirements.

IEC60270 (2000). High voltage test techniques - Partial discharge measurements.

IEEE Std C57.16-1996 (1997). IEEE standard requirements, terminology, and test code for dry-type air-core series-connected reactors.

International commission on non-ionizing radiation protection (1998). Guidelines for limiting exposure to time-varying electric, magnetic, and electromagnetic fields (up to 300 GHz). *Health Physics*, 74(4):494–522.

Janssen, M., Kraemer, S., Schmidt, R., and Winter, K. (2003). Residual current compensation (RCC) for resonant grounded transmission systems using high performance voltage source inverter. In *Transmission and Distribution Conference and Exposition, 2003 IEEE PES*, volume 2, pages 574–578.

Jewell, W. T. (1990). Transformer design in the undergraduate power engineering laboratory. *IEEE Transactions on Power Systems*, 5(2):499–505.

Jia, Q., Wang, N., Lin, D., Zhang, H., and Han, X. (2005). A thyristor controlled neutral grounding reactor for medium voltage power networks. *Transmission and Distribution Conference and Exhibition: Asia and Pacific, 2005 IEEE/PES*, pages 1–4.

Johnstone, P. T. and Bodger, P. S. (1997). High voltage disinfection of liquids. *IPENZ Transactions*, 24(1):30–35.

Kuffel, E., Zaengl, W. S., and Kuffel, J. (2000). *High voltage engineering : fundamentals*. Newnes, Oxford, Boston, 2nd edition.

Kulkarni, S. V. and Khaparde, S. A. (2004). *Transformer engineering : design and practice*. Marcel Dekker, New York, 1st edition.

Lee, R. (1933). A practical analysis of parallel resonance. *Proceedings of the IRE*, 21(2):271–281.

Liew, M. C. (2001). *Reverse Design Transformer Modelling Technique with Particular Application to Partial Core Transformers*. PhD thesis, Department of Electrical and Computer Engineering, University of Canterbury, Christchruch, New Zealand.

Liew, M. C. and Bodger, P. S. (2001). Partial-core transformer design using reverse modelling techniques. *IEE Proceedings Electric Power Applications*, 148(6):513–519.

Liew, M. C. and Bodger, P. S. (2002). Incorporating capacitance into partial-core transformer models to determine first natural resonant frequencies. *IEE Proceedings Generation, Transmission and Distribution*, 149(6):746–752.

Liew, M. C., O'Neil, M. B., and Bodger, P. S. (2001). Operating partial core transformers under liquid nitrogen conditions. *IEE Proceedings Electric Power Applications*, 148(4):293–298.

Lindblom, A., Isberg, J., and Bernhoff, H. (2004). Calculating the coupling factor in a multilayer coaxial transformer with air core. *IEEE Transactions on Magnetics*, 40(5):3244–3248.

Lowdon, E. (1989). *Practical Transformer Design Handbook*. McGraw-Hill, New York, 2nd edition.

Ludwig, G. W. and El-Hamamsy, S.-A. (1991). Coupled inductance and reluctance models of magnetic components. *IEEE Transactions on Power Electronics*, 6(2):240–250.

Lynch, K., Bodger, P. S., Enright, W. G., and Bell, S. C. (2007). Partial core transformer for energization of high voltage arc-signs. In *15th International Symposium on High Voltage Engineering*, Ljubljana, Slovenia. Paper T3.304, CD-ROM.

MagNet (2007). MagNet 6.23. Infolytica Corporation. www.infolytica.com.

Margueron, X. and Keradec, J.-P. (2007). Design of equivalent circuits and characterization strategy for n-input coupled inductors. *IEEE Transactions on Industry Applications*, 43(1):14–22.

McLyman, W. T. (2004). *Transformer and Inductor Design Handbook*. Dekker, New York, 3rd edition.

Mechler, F. F. and Girgis, R. S. (1998). Calculation of spatial loss distribution in stacked power and distribution transformer cores. *IEEE Transactions on Power Delivery*, 13(2):532–537.

Meyerhans, A. (1945). New designs of transformers and choke coils. *The Brown Boveri Review*, 32(3):91–100.

Meyerhans, A. (1956). Radially laminated transformers and reactors. *The Brown Boveri Review*, 43(6):187–205.

Meyerhans, A. (1958). A new design for shunt reactors of high rating. *The Brown Boveri Review*, 45(9):407–410.

Moses, A. J. (1998). Comparison of transformer loss prediction from computed and measured flux density distribution. *IEEE Transactions on Magnetics*, 34(4):1186–1188.

Ong, C. M. (1998). *Dynamic simulation of electric machinery using matlab / simulink*. Prentice Hall, New Jersey, 1st edition.

Paul, C. R., Nasar, S. A., and Unnewehr, L. E. (1986). *Introduction to Electrical Engineering*. McGraw-Hill, Singapore, 1st edition.

Petkov, R. (1995). Design issues of high-power high-frequency transformer. In *Proc. 1995 International Conference on Power Electronics and Drive Systems*, volume 1, pages 401–410.

Pfützner, H., Bengtsson, C., Booth, T., Löffler, F., and Gramm, K. (1994). Three-dimensional flux distributions in transformer cores as a function of package design. *IEEE Transactions on Magnetics*, 30(5):2713–2727.

Preis, K., Biro, O., Friedrich, M., Gottvald, A., and Magele, C. (1991). Comparison of different optimization strategies in the design of electromagnetic devices. *IEEE Transactions on Magnetics*, 27(5):4154–4157.

Qader, A. A. and Basak, A. (1982). Building factor of a 100 KVA 3 phase distribution transformer core. *IEEE Transactions on Magnetics*, 18(6):1487–1489.

Rubaai, A. (1994). Computer aided instruction of power transformer design in the undergraduate power engineering class. *IEEE Transactions on Power Systems*, 9(3):1174–1181.

Saravolac, M. P. (1998). Use of advanced software techniques in transformer design. *Design Technology of T&D Plant (Digest No. 1998/287), IEE Colloquium on*, pages 9/1–9/11.

Schufft, W., Coors, P., Hauschild, W., and Spiegelberg, J. (1999). Frequency-tuned resonant test systems for on-site testing and diagnostics of extruded cables. In *Eleventh International Symposium on High Voltage Engineering*, volume 5, pages 335–339, London, United Kingdom.

Scott, T. (2007). The first application of resonant earthing with residual current compensation to a NZ distribution network. In *Electricity Engineers Association Conference (EEA)*, Auckland, New Zealand. CD-ROM.

Shahzad, F. and Shwehdi, M. H. (1997). Human-computer interaction of single/three phase transformer design and performance. In *Proc. Industrial and Commercial Power Systems Technical Conference*, pages 193–196.

Sherman, J. B. (1942). Some aspects of coupled and resonant circuits. *Proceedings of the IRE*, 30(11):505–510.

Shirkoohi, G. H. and Arikat, M. A. M. (1994). Anisotropic properties of high permeability grain-oriented 3.25% Si-Fe electrical steel. *IEEE Transactions on Magnetics*, 30(2):928–930.

Slemon, G. R. (1966). *Magnetoelectric Devices: Transducers, Transformers, and Machines*. John Wiley and Sons, Inc, USA, 1st edition.

Smith, D., Enright, W. G., and Bodger, P. S. (2007). A test circuit for long distance directional plasma discharge using the exploding wire technique. In *15th International Symposium on High Voltage Engineering*, Ljubljana, Slovenia. Paper T3.489, CD-ROM.

Stochniol, A., Freeman, E. M., and Lowther, D. A. (1992). A user oriented shell for electromagnetic CAD of axisymmetric devices. *IEEE Transactions on Magnetics*, 28(2):1782–1784.

Sullivan, C. R. (2001). Computationally efficient winding loss calculation with multiple windings, arbitrary waveforms, and two-dimensional or three-dimensional field geometry. *IEEE Transactions on Power Electronics*, 16(1):142–150.

Terman, F. E. (1947). *Radio Engineering*. McGraw-Hill, New York, 3rd edition.

Van den Bossche, A., Valchev, V. C., and Barudov, S. (2006). Practical wide frequency approach for calculating eddy current losses in transformer windings. In *IEEE International Symposium on Industrial Electronics*, volume 2, pages 1070–1074.

Warren, V. and Stone, G. (1998). Recent developments in diagnostic testing of stator windings. *IEEE Electrical Insulation Magazine*, 14(5):16–21.

Weishu, H. (1995). Lightweight and low-cost hv-testing system with power frequency. In *7th International Conference on Transmission and Distribution Construction and Live Line Maintenance*, pages 178–182.

Wirgau, K. A. (1976). Inductance calculation of an air-core disk winding. *IEEE Transactions on Power Apparatus and Systems*, 95(1):394–400.

Witulski, A. F. (1995). Introduction to modeling of transformers and coupled inductors. *IEEE Transactions on Power Electronics*, 10(3):349–357.

Yamada, S., Bessho, K., Iizuka, T., and Kimura, H. (1979). A method of calculating the characteristics of open-core-type reactors. *Electrical Engineering in Japan*, 99(5):105–113.

Yamaguchi, H., Kataoka, T., and Sato, Y. (1999). Analysis of a 3-phase air-core superconducting power transformer. *IEEE Transactions on Applied Superconductivity*, 9(2):1300–1303.

Yu, Q., Holmes, T. W., and Naishadham, K. (2002). RF equivalent circuit modeling of ferrite-core inductors and characterization of core materials. *IEEE Transactions on Electromagnetic Compatibility*, 44(1):258–262.

Zaengl, W. S. and Bernasconi, F. (1982). High voltage insulation testing system. United States Patent no. 4,338,561.

Appendix A

TRANSFORMER PROGRAM DOCUMENTATION

A.1 INTRODUCTION

TranModel is a transformer design and analysis program. It is based on the reverse design method and is coded specifically for dry-type transformers with silicone encapsulated layer windings. The program is particularly suited for transformers with a partial-core, although elementary models have also been developed for full-core shell-type transformers. The program takes supply conditions and the physical characteristics and dimensions of the core and windings to produce component values for the Steinmetz 'exact' transformer equivalent circuit of Figure 3.2. The equivalent circuit is used to calculate the steady-state performance of the transformer under open-circuit, short-circuit and loaded conditions. TranModel also has load and save capabilities.

The program is contained in a Microsoft Excel workbook (TranModel.xls) which is coupled to the commercial finite element analysis software package MagNet[1]. TranModel is an example of a user oriented shell for MagNet, a concept first proposed by Stochnoil [Stochniol et al., 1992]. The workbook contains several worksheets and three stand-alone modules. The modules are written in Visual Basic for Applications (VBA) code. The worksheets contain cell data (familiar to most Excel users) and VBA code.

The program interface consists of data, contained in several input and output worksheets, and command buttons, located in the **Main** and **Scripting** worksheets. The command buttons allow the user to execute the program code while the input and output worksheets allow the user to enter-in and read-out program data. The layout of the TranModel workbook is shown in Table A.1.

TranModel incorporates two magnetic models. The first model is based on magnetic circuit theory (variable prefix 'CTM'). For the partial-core transformer, this model also contains empirically derived factors. This model is described in [Liew and Bodger, 2001]. The second model is based on magneto-static finite element analysis (variable prefix 'FEM'). Equivalent circuit parameters and test results are available for each model.

[1] Trial version available to download for educational purposes at www.infolytica.com.

Worksheets	Modules
Main[a]	Main[b]
Design Data[c]	Scripting
Configuration Data[c]	Temp
Supply Conditions[c]	
Design Review[c]	
Load Conditions[c]	
Test Outputs 1[c]	
Test Outputs 2[c]	
Scripting[ac]	
Temp	
Program Log	

[a]Worksheet contains macros.
[b]Module contains global variables.
[c]Worksheet contains named ranges.

Table A.1 Top level layout of the TranModel workbook.

A.2 TRANSFORMER DESIGN CYCLE

A typical transformer design cycle using the reverse design method in TranModel is shown in Figure A.1. Input data is entered in the **Design Data**, **Configuration Data** and **Supply Conditions** worksheets. Then, either the 'Design Calculations' or 'Design Calculations (don't rerun FEM)' command button is executed from the **Main** worksheet. The former command button must be executed during the first iteration of a transformer design cycle. In subsequent iterations, the later command button may be used to reduce program execution time, provided that the transformer geometry and core configuration has not changed in the last iteration.

Next, the transformer design is reviewed in the **Design Review** worksheet. If the design review is not acceptable, then the transformer input data must be modified and the 'Design Calculations' or 'Design Calculations (don't rerun FEM)' command button re-executed. Once the design review is acceptable, the transformer loading conditions can be specified in the **Load Conditions** worksheet and the 'Test Calculations' command button is executed from the **Main** worksheet.

The transformer performance under the specified loading conditions is reviewed in the **Test Outputs 1** and **Test Outputs 2** worksheets. If the calculated performance is not acceptable, then the transformer input data must be modified and the design cycle must be repeated. Once acceptable performance is obtained, the magnetic field from the finite element model can be viewed to ensure that the flux-density is below the saturation value of the transformer steel.

The entire process is repeated for other core configurations, winding configurations and

supply conditions until satisfactory performance is obtained over the intended operating range of the transformer.

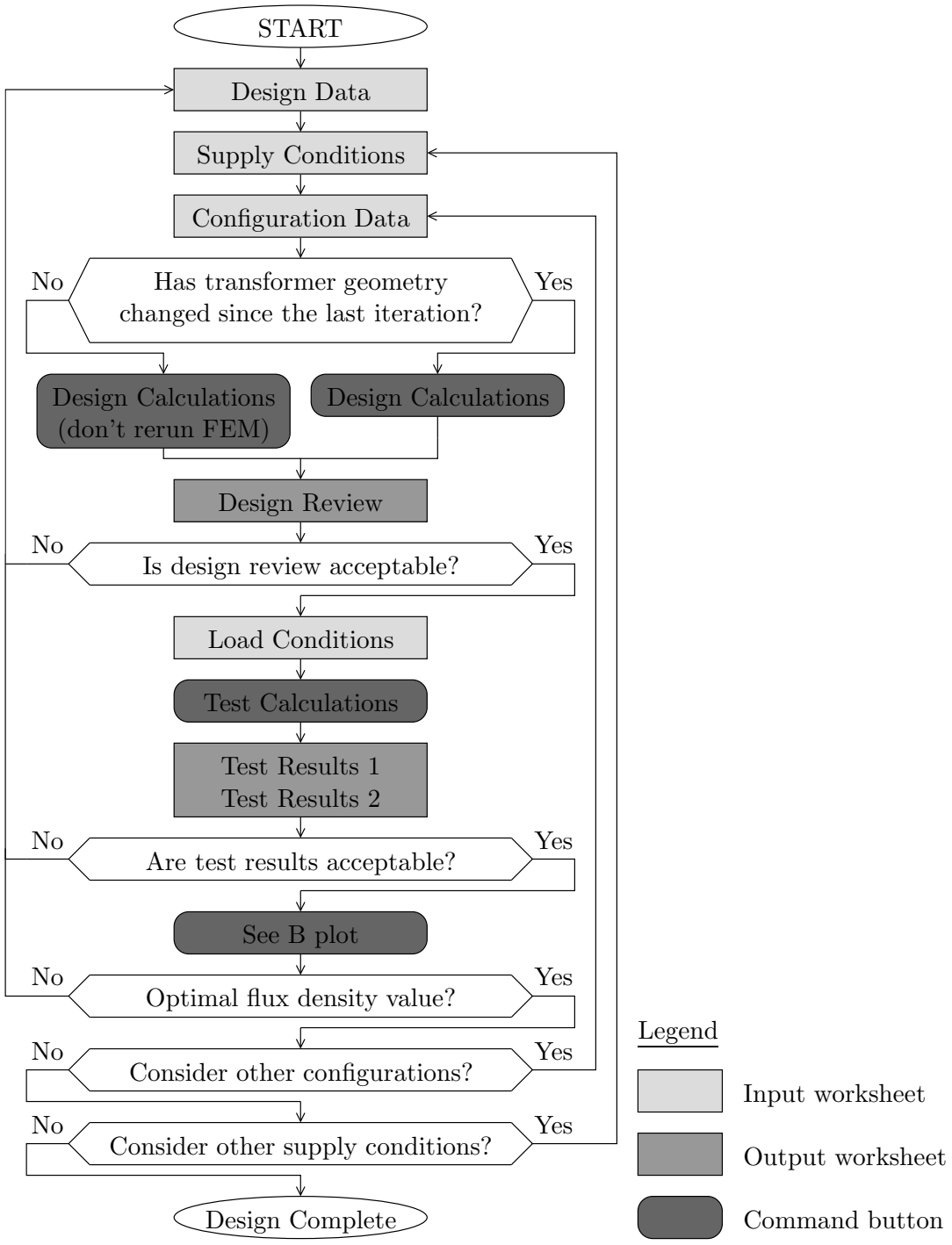

Figure A.1 Typical transformer design cycle in TranModel.

A.3 WORKSHEET SUMMARIES

This section describes the purpose and structure of each of the worksheets in TranModel. Some of the worksheets contain named ranges which correspond to either individual cell locations or one- or two-dimensional arrays of cells. The worksheets containing named ranges are specified in Table A.1.

For each named range, a corresponding global variable is declared in the **Main** module. This allows the named ranges to act as variables in the program memory. All named ranges are read into their corresponding variables on program execution. Similarly, when the program halts, the variables are written back to their corresponding named ranges. Each worksheet with named ranges contains the necessary VBA code to implement this functionality.

A.3.1 Main

The TranModel program is executed via command buttons. Most are located in the **Main** worksheet. These are summarised in Table A.2. The remaining command buttons are located in the **Scripting** worksheet. They are not documented.

Program command buttons	Read / Write command buttons
Design Calculations	Read Design Data
Design Calculations (don't rerun FEM)	Read Configuration Data
Test Calculations	Read Supply Conditions
See B plot (primary A-t excitation only)	Save Design Data
See B plot (secondary A-t excitation only)	Save Configuration Data
See B plot (prim / sec A-t excitation)	Save Supply Conditions

Table A.2 Command buttons located in **Main** worksheet.

The 'Design Calculations', 'Design Calculations (don't rerun FEM)' and 'Test Calculations' command buttons call driver functions to achieve their functionality. The driver functions, located in the **Main** worksheet, define a calling sequence for the execution of other functions, located in the **Main** module. The driver functions are summarised in Figure A.2. For the remaining command buttons, where the functionality is much simpler, the code associated with the command buttons directly call functions in the **Main** module, bypassing the driver functions. The calling sequence of these command buttons is shown in Figure A.3.

A.3.2 Design Data

The **Design Data** worksheet contains all of the design data for the transformer, including all core sections, winding sections, inter-layer and inter-section insulation and

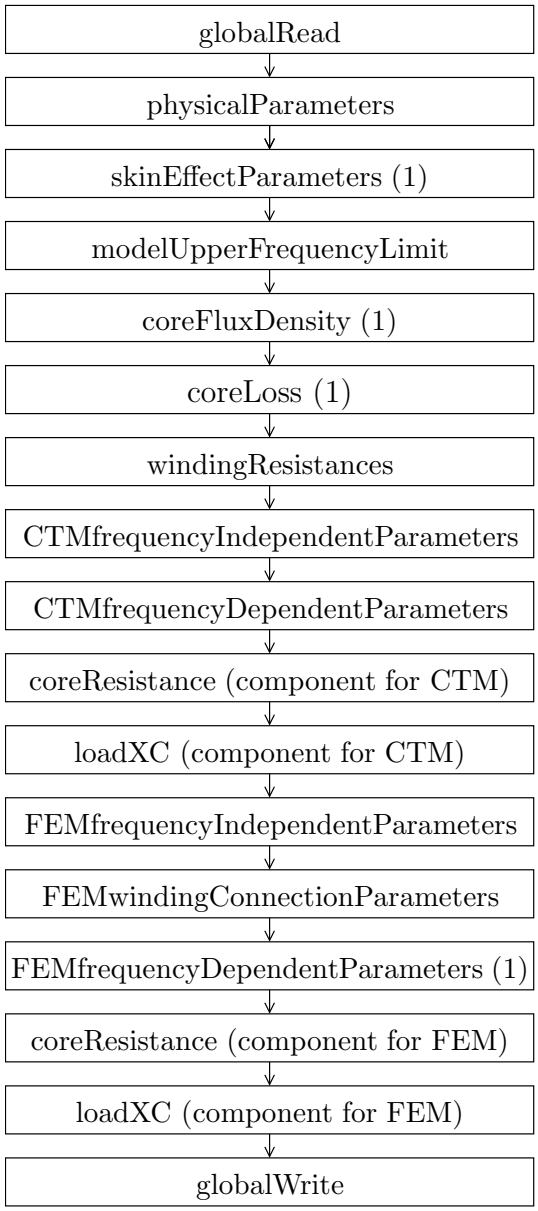

(a) Design Calculations.

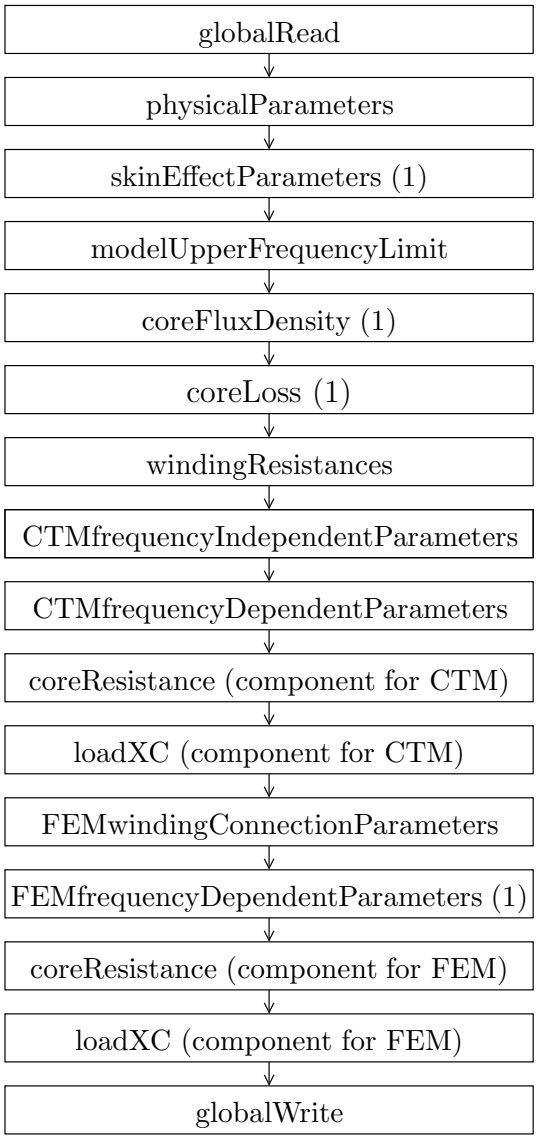

(b) Design Calculations (don't run FEM).

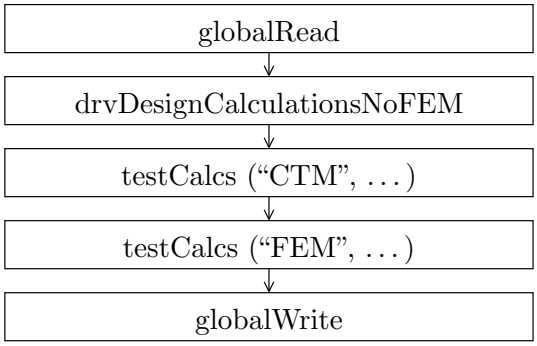

(c) Test Calculations.

Figure A.2 Function calling sequence of the command buttons in the **Main** worksheet which use driver functions. The calling sequence is located in the driver functions, and the functions called are located in the **Main** module.

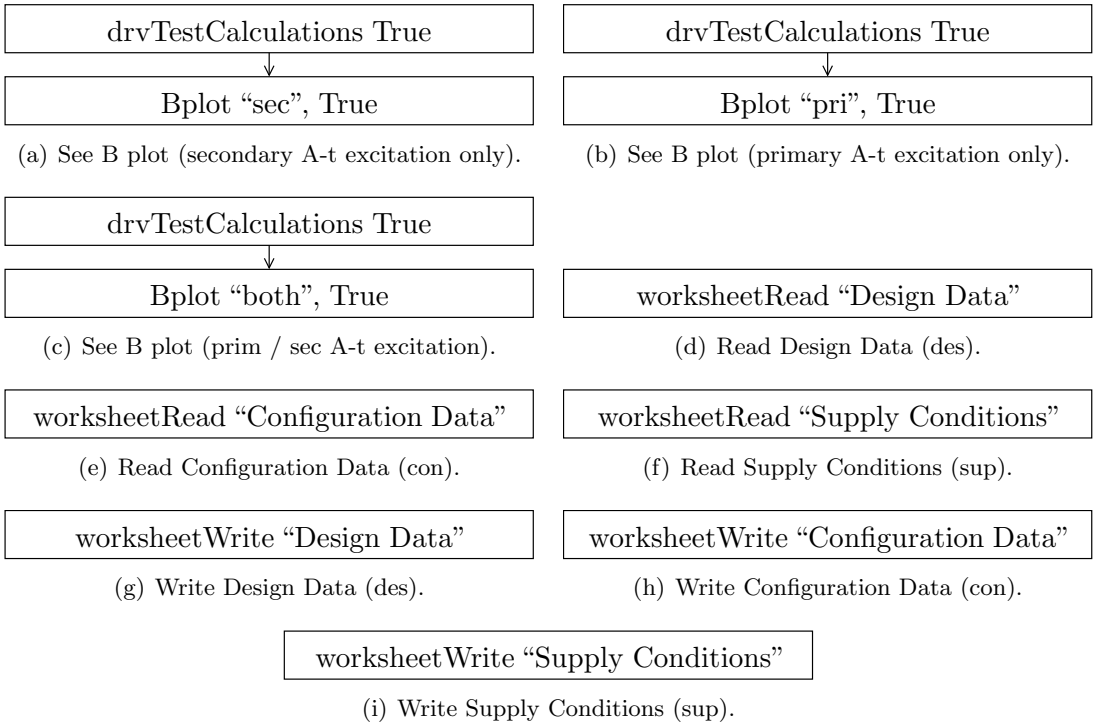

(a) See B plot (secondary A-t excitation only).

(b) See B plot (primary A-t excitation only).

(c) See B plot (prim / sec A-t excitation).

(d) Read Design Data (des).

(e) Read Configuration Data (con).

(f) Read Supply Conditions (sup).

(g) Write Design Data (des).

(h) Write Configuration Data (con).

(i) Write Supply Conditions (sup).

Figure A.3 Function calling sequence of the command buttons in the **Main** worksheet which do not use driver functions. The calling sequence is located in the code for the command button, and the functions called are located in the **Main** module.

encapsulant.

A.3.3 Supply Conditions

The **Supply Conditions** worksheet contains the supply frequency, as well as the fundamental and harmonic components of the supply voltage, up to the 15th harmonic. The fundamental component is expressed as an absolute value, while the harmonics are expressed as a percentage of the fundamental component. It is assumed that the harmonic components will scale linearly with the fundamental component. This allows the actions of an ideal variac to be modelled by changing only the fundamental component of voltage. The supply is assumed to be of zero impedance. A simple resistance / inductance $R + j\omega L$ branch could be placed in series with the supply voltage with very little programming effort.

A.3.4 Configuration Data

The **Configuration Data** worksheet contains configuration data for the core and winding sections. The axial offset of the winding sections can be specified as well as the combination of series-connected winding sections used to form the primary and

secondary windings. The core sections used, as well as any axial offsets and centre air-gaps are specified.

A.3.5 Design Review

The **Design Review** worksheet is divided into sections A - H. Section A contains the individual and overall dimensions, weights and costs of the transformer. Section B contains the transformer electrical parameters which are related to skin effect. Section C lists the upper-frequency for which the transformer model is valid. Section D estimates the transformer flux-density, using the 'transformer equation' (Eq. 3.11 of Section 3.4.2). Section E contains parameters for the magnetic model based on circuit theory. Section F contains parameters for the core loss model. Section G contains parameters for the finite element magnetic model. Section H lists the equivalent circuit parameters for both the circuit theory and finite element magnetic models.

A.3.6 Load Conditions

The **Load Conditions** worksheet is used to specify the load (open-circuit, short-circuit or loaded-circuit). Loaded-circuit parameters are specified as R + j α. The sign of α is used to determine how α scales with frequency. For $\alpha > 0$, α is defined as an inductance, and the reactance is calculated as $2\pi f\alpha$. For $\alpha < 0$, α is defined as a capacitance, and the reactance is calculated as $\frac{-1}{2\pi f\alpha}$.

A.3.7 Test Results 1

The **Test Results 1** worksheet is used to calculate the transformer terminal conditions for both the circuit theory and finite element magnetic models.

A.3.8 Test Results 2

The **Test Results 2** worksheet gives a detailed breakdown of the transformer performance, including harmonic voltages and currents for each winding section. The performance of both magnetic models is calculated.

A.3.9 Scripting

The **Scripting** worksheet is used to automate various processes, including calculating the effect of changing internal model parameters on model performance, optimal transformer design using the multiple design method, and executing multiple load-tests. In many cases, the outputs of the **Scripting** worksheet have been used to produce the graphs in this thesis.

A.3.10 Temp

The **Temp** worksheet is used to try out new ideas and is not documented.

A.4 WORKSHEET LAYOUT

A sample layout of the TranModel program worksheets for transformer PC5 is shown in Figure A.4. The worksheets show the program inputs and outputs, which were used to calculate the harmonic currents of Figure 9.7 of Section 9.4.4.

TranModel 1.0 - Design Data worksheet

Description	Name	Type	Value	Unit	Fig. ref	Symbol in latex
Section A - Material specifications						
Core type and material properties						
Type ("p" = partial-core, "f" = full-core shell type)	CTP	string	p	-	-	-
Shape ("c" = circular, "r" = rectangular) (*1)	CS	string	c	-	-	-
Lamination thickness	LT	double	0.23	mm	-	c_{l}
Stacking factor	CSF	double	0.96	-	-	s
Relative permeability	CUR	double	3000	-	-	\mu_{rc}
Resistivity at 20 °C	CR20	double	1.80E-07	ohm-m	-	\rho_{\unit{20}{\celsius}}
Thermal resistivity coefficient	CTRC	double	6.00E-03	ohm-m/°C	-	\delta \rho
Operating temperature	COT	double	50	°C	-	T_{c}
Material density	CMD	double	7870	kg/m^3	-	\gamma_{c}
Material cost	CMC	double	11	$/kg	-	C_{c}
Core dimensions						
Partial-core transformer (*2)						

	Section 1	Section 2	Section 3	Section 4	Section 5	Section 6	Section 7	Section 8	Section 9	Section 10
Length, mm (CSLar)	74	74	74	74						
(CS = "c") Inner radius, mm (CSR1ar) (*3)	12.5	12.5	12.5	12.5						
(CS = "c") Outer radius, mm (CSR2ar) (*3)	120	120	120	120						
(CS = "r") Width-1 (breadth), mm (CSW1ar) (*3)	0	0	0	0						
(CS = "r") Width-2 (depth), mm (CSW2ar) (*3)	0	0	0	0						
Full-core shell-type transformer										
Length	CFL	double	0	mm	-	c_{l}				
Central limb width	CFCW	double	0	mm	-	w_{1}				
Outer limb width (typically CFCW / 2)	CFOW	double	0	mm	-	w_{o}				
Yoke height (typically CFCW / 2)	CFYH	double	0	mm	-	y_{h}				
Depth	CFD	double	0	mm	-	w_{2}				
Former										
Thickness	FT	double	8.5	mm	-	FT				

Winding sections, numbered from the inside (winding section = one or more layer of the same wire type and size, with a consistent inter-layer insulation thickness) (*4)

	Section 1	Section 2	Section 3	Section 4	Section 5	Section 6	Section 7	Section 8	Section 9	Section 10	Section 11	Section 12	Section 13
Overall													
Estimate of length, mm (WSLEar)	408	408	408	408	408	408	408	408	390.1	36.5	57.3		
Layers (WSLSar)	16	1	1	1	1	1	1	1	1	1	1		
Wire													
Shape ("c" = circular, "r" = rectangular) (WSSar)	c	c	c	c	c	c	c	c	r	r	r		
(WSS = "c") Diameter, mm (WSWDar)	0.9	0.9	0.85	0.85	0.85	0.85	0.67	0.67	0	0	0	0	
(WSS = "r") Radial width, mm (WSWW1ar)	0	0	0	0	0	0	0	0	2.5	2.5	2.5	2.5	
(WSS = "r") Axial width, mm (WSWW2ar)	0	0	0	0	0	0	0	0	5	5	5	5	
Insulation thickness, mm (WSWITar)	0.04	0.04	0.04	0.04	0.04	0.04	0.04	0.04	0.1	0.1	0.1	0.1	
Stacking factor (axial direction) (WSSFar)	1	1	1	1	1	1	1	1	1	1	1	1	
Material ("c" = copper, "o" = other) (WSMar) (*5)	c	c	c	c	c	c	c	c	o	o	o	o	
(WSM = "o") Resistivity at 20 C, ohm-m (WSR20ar)	0.00E+00	0.00E+00	0.00E+00	0.00E+00	0.00E+00	0.00E+00	0.00E+00	0.00E+00	2.76E-08	2.76E-08	2.76E-08	2.76E-08	
(WSM = "o") Thermal resistivity coefficient, ohm-m/°C (WSTRCar)	0.00E+00	0.00E+00	0.00E+00	0.00E+00	0.00E+00	0.00E+00	0.00E+00	0.00E+00	4.30E-03	4.30E-03	4.30E-03	4.30E-03	
Volume specific heat at 20 °C, J/m^3-K (WSVSHar)	3.39E+06	3.39E+06	3.39E+06	3.39E+06	3.39E+06	3.39E+06	3.39E+06	3.39E+06	2.52E+06	2.52E+06	2.52E+06	2.52E+06	
Operating temperature, °C (WSOTar)	20	20	20	20	20	20	20	20	20	20	20	20	
Material density, kg/m^3 (WSMDar)	8960	8960	8960	8960	8960	8960	8960	8960	2700	2700	2700	2700	
Material cost, $/kg (WSMCar)	10	10	10	10	10	10	10	10	10	10	10	10	
Inter-layer insulation													
Thickness (build value), mm (WSILITar)	0.6	0.6	0.6	0.6	0.6	0.6	0.6	0.6	0	0	0	0	
Circumferal overlap, mm (WSILIOar)	50	50	50	50	50	50	50	50	0	0	0	0	
Winding-ends overlap, mm (WSILIWEOar)	25	25	25	25	25	25	25	25	0	0	0	0	
Material weight per CSA, kg/m^2 (WSILIMWar)	0.61	0.61	0.61	0.61	0.61	0.61	0.61	0.61	0	0	0	0	
Material cost per CSA, $/m^2 (WSILIMCar)	35	35	35	35	35	35	35	35	0	0	0	0	
Inter-section insulation (winding section n to n + 1)													
Thickness (build value), mm (WSISITar)	0.6	0.6	0.6	0.6	0.6	0.6	0.6	0.6	0	0	0	0	
Circumferal overlap, mm (WSISIOar)	50	50	50	50	50	50	50	50	0	0	0	0	
Winding ends overlap, mm (WSISIWEOar)	25	25	25	25	25	25	25	25	0	0	0	0	
Material weight per CSA, kg/m^2 (WSISIMWar)	0.61	0.61	0.61	0.61	0.61	0.61	0.61	0.61	0	0	0	0	
Material cost per CSA, $/m^2 (WSISIMCar)	35	35	35	35	35	35	35	35	0	0	0	0	
Encapsulant (*6)													

First encapsulated winding section	FEWS	integer	1	-	-	-
Last encapsulated winding section	LEWS	integer	8	-	-	-

(a) Design Data worksheet (page 1 of 2)

Figure A.4 TranModel sample layout for transformer PC5.

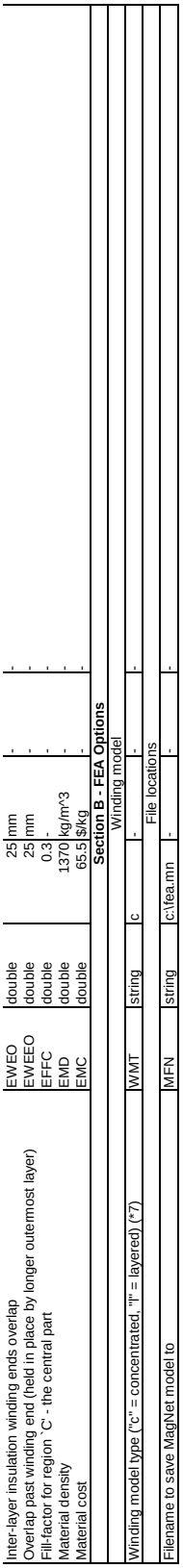

Inter-layer insulation winding ends overlap	EWEO	double	25	mm	-	-
Overlap past winding end (held in place by longer outermost layer)	EWEEO	double	25	mm	-	-
Fill-factor for region `C' - the central part	EFFC	double	0.3	-	-	-
Material density	EMD	double	1370	kg/m^3	-	-
Material cost	EMC	double	65.5	$/kg	-	-
Section B - FEA Options						
Winding model						
Winding model type ("c" = concentrated, "l" = layered) (*7)	WMT	string	c	-	-	-
File locations						
Filename to save MagNet model to	MFN	string	c:\fea.mn	-	-	-

Notes

*1 Rectangular core required for full-core shell-type transformer.
*2 Parameters for the circuit theory model are calculated using the first core section only.
*3 The core section with the largest outer radius must be placed in section 1 as this is used to calculate the coordinates of the windings. Only one core section allowed for a rectangular core.
*4 Inter-section insulation of the outer-most winding section is used to extend the winding window for a full-core shell-type transformer.
*5 A more accurate formula for calculating the resistivity variation with temperature is provided for copper.
*6 Circular core only. A single block of winding sections may be encapsulated. For circular wire, assume penetration throughout the winding wire. Assume penetration between inter-layer insulation at the winding ends overlap.
*7 Layer model not available yet. Would require n_winding_sections of dynamic matrices of size n_layers.

(b) Design Data worksheet (page 2 of 2)

Figure A.4 (Continued) TranModel sample layout for transformer PC5.

TranModel 1.0 - Supply Conditions worksheet

Name	Type	Value	Description	Unit	Fig. ref	Symbol in latex
Section A - Frequency						
F	double	50	Frequency	Hz	-	f
Section B - Fundamental voltage and harmonics						
PVPar(1, 1)	double	99.13398458	1st harmonic / fundamental voltage, RMS	V	-	V_{1}
PVPar(2, 1)	double	0	2nd harmonic, % fundamental	%	-	-
PVPar(3, 1)	double	1.1	3rd harmonic, % fundamental	%	-	-
PVPar(4, 1)	double	0	4th harmonic, % fundamental	%	-	-
PVPar(5, 1)	double	2.8	5th harmonic, % fundamental	%	-	-
PVPar(6, 1)	double	0	6th harmonic, % fundamental	%	-	-
PVPar(7, 1)	double	1	7th harmonic, % fundamental	%	-	-
PVPar(8, 1)	double	0	8th harmonic, % fundamental	%	-	-
PVPar(9, 1)	double	0.3	9th harmonic, % fundamental	%	-	-
PVPar(10, 1)	double	0	10th harmonic, % fundamental	%	-	-
PVPar(11, 1)	double	0.2	11th harmonic, % fundamental	%	-	-
PVPar(12, 1)	double	0	12th harmonic, % fundamental	%	-	-
PVPar(13, 1)	double	0	13th harmonic, % fundamental	%	-	-
PVPar(14, 1)	double	0	14th harmonic, % fundamental	%	-	-
PVPar(15, 1)	double	0	15th harmonic, % fundamental	%	-	-

User feedback (no named ranges used)

Test results using the finite element magnetic model

Desired V2, V	1.00E+04
Required V1, V	99.13398458
Desired I1, A	60
Required V1, V	739.4009853

Test results using the circuit theory magnetic model

Desired V2, V	3.60E+04
Required V1, V	301.0174723
Desired I1, A	60
Required V1, V	431.9258728

(c) Supply Conditions worksheet

TranModel 1.0 - Load Conditions worksheet

Name	Type	Value	Description	Unit	Fig. ref	Symbol in latex
LD	string	l	Load designation ("o" = open circuit, "s" = short circuit, "l" = loaded)	-	-	-
REZL	double	0	Resistive component (unreferred)	ohm	-	-
IMZL	double	-2.650E-07	Inductive (+ve) / Capacitive (-ve) component (unreferred) (*1)	ohm	-	-

Notes

*1 Example: IMZL = -10e-9 means a capacitive component of 10nF, IMZL = 25e-3 means an inductive component of 10mH.

(d) Load Conditions worksheet

Figure A.4 (Continued) TranModel sample layout for transformer PC5.

TranModel 1.0 - Configuration Data worksheet

Description	Name	Type	Value	Unit	Fig. ref	Symbol in latex													
Winding configuration																			
Winding section	Section 1	Section 2	Section 3	Section 4	Section 5	Section 6	Section 7	Section 8	Section 9	Section 10	Section 11	Section 12	Section 13						
Axial split with previous WS (yes / no) (WSCar) (*1)	no	no	no	no	no	no	no	no	no	no	yes								
Axial offset, mm (WCAOar) (*1, *2)		0	0	0	0	0	0	0	0	0	18.25								
Winding connections (*3)																			
Winding section	Section 1	Section 2	Section 3	Section 4	Section 5	Section 6	Section 7	Section 8	Section 9	Section 10	Section 11	Section 12	Section 13						
Primary winding																			
Connected* (yes / no) (PWCar)									yes	yes	yes								
Secondary winding																			
Connected* (yes / no) (SWCar)	yes	yes	yes	yes	yes	yes	yes	yes											
Core Sections (*4)																			
Position (numbered from top to bottom)	Position 1	Position 2	Position 3	Position 4	Position 5	Position 6	Position 7	Position 8	Position 9	Position 10									
Axial group 1																			
Core section used, (CSG1Car)		1	2	3	4														
Air gap from position i to position i + 1, (CSG1Gar) (*5)		4.2	15.5	4.6															
Group axial offset	CSG1O	double		0	mm	-													
Axial group 2																			
Core section used, (CSG2Car)																			
Air gap from position i to position i + 1, (CSG2Gar) (*5)																			
Group axial offset	CSG2O	double		0	mm	-													
Axial group 3																			
Core section used, (CSG3Car)																			
Air gap from position i to position i + 1, (CSG3Gar) (*5)																			
Group axial offset	CSG3O	double		0	mm	-													

Notes

*1 Circular core only. Circuit theory magnetic model assumes no axial split and zero axial offset. For an axial split all parameters for winding section i and i + 1 must be the same.
*2 Offset if that individual winding section was previously centered.
*3 One or more winding sections may be connected in series to form the complete winding. The accuracy of the circuit theory magnetic model is likely to be poor in this case. Autotransformer configuration no available yet.
*4 Not applicable to the circuit theory magnetic model.
*5 Leave unused gaps blank.

(e) Configuration Data worksheet

Figure A.4 (Continued) TranModel sample layout for transformer PC5.

TranModel 1.0 - Design Review worksheet

Description	Name	Type	Value	Unit	Fig. ref	Symbol in latex / further comments
Section A - Physical parameters (independent of frequency and configuration data)						
Core						
Type ("p" = partial-core, "f" = full-core)	CTP2	string	p	-	-	-
Resistivity	CRE	double	2.124E-07	ohm-m	-	\rho_{c}
Partial-core transformer						
	Section 1	Section 2	Section 3	Section 4	Section 5	Section 6	Section 7	Section 8	Section 9	Section 10	
Number of laminations, (CSLNar) (*1)	1001	1001	1001	1001		0	0	0	0	0	
CSA incl. stack fact but no skin depth considerations, m^2 (CSCAAar)	0.042958	0.042958	0.042958	0.042958		0	0	0	0	0	
Volume = CAA * CL, m^3 (CSCVar)	0.003178	0.003178	0.003178	0.003178		0	0	0	0	0	
Weight, kg (CSCWar)	25.01796	25.01796	25.01796	25.01796		0	0	0	0	0	
Cost, $ (CSCCar)	275.1975	275.1975	275.1975	275.1975		0	0	0	0	0	
Full-core transformer											
Number of laminations	FCLN	double	0	-	-						
CSA central limb - incl stack factor but no skin depth considerations	FCCLCAA	double	0	m^2	-						
CSA yoke - incl stack factor but no skin depth considerations	FCYCAA	double	0	m^2	-						
CSA outer limb - incl stack factor but no skin depth considerations	FCOLCAA	double	0	m^2	-						
Winding window width	FCWWW	double	-8.5	mm	-						
Mean path length - each limb	FCMPLL	double	0	mm	-						
Mean path length - yoke	FCMPLY	double	0	mm	-						
Total volume (no stacking factor considerations)	FCTV	double	0	m^3	-						
Total weight	FCTW	double	0	kg	-						
Total cost	FCTC	double	0	$	-						
Winding sections											
	Section 1	Section 2	Section 3	Section 4	Section 5	Section 6	Section 7	Section 8	Section 9	Section 10	Section 11	Section 12	Section 13
Overall													
Designation ("p" = primary, "s" = secondary, "n" = neither) (WSDar)	s	s	s	s	s	s	s	s	p	p	p	n	n
Layers (WSLS2ar)	16	1	1	1	1	1	1	1	1	1	1	0	0
Length, mm (WSLar)	408	408	408	408	408	408	408	408	390.1	36.5	57.3	0	0
Thickness, mm (WSTar)	24.68	0.98	0.93	0.93	0.93	0.93	0.75	0.75	2.7	2.7	2.7	0	0
Space factor (WSSPFar)	0.420846	0.662403	0.656087	0.656087	0.656087	0.656087	0.626782	0.626782	0.890313	0.890313	0.890313	0	0
Outside width-1, mm (WSW1ar)	306.36	309.52	312.58	315.64	318.7	321.76	324.46	327.16	333.76	339.16	339.16	0	0
Outside width-2, mm (WSW2ar)	306.36	309.52	312.58	315.64	318.7	321.76	324.46	327.16	333.76	339.16	339.16	0	0
Radial position of winding start (circular core), mm (WSCSar)	128.5	153.78	155.36	156.89	158.42	159.95	161.48	162.83	164.18	166.88	166.88	0	0
Radial position of winding end (circular core), mm (WSCEar)	153.18	154.76	156.29	157.82	159.35	160.88	162.23	163.58	166.88	169.58	169.58	0	0
1st radial position of winding start (rectangular core), mm (WSR1Sar)	0	0	0	0	0	0	0	0	0	0	0	0	0
1st radial position of winding end (rectangular core), mm (WSR1Ear)	0	0	0	0	0	0	0	0	0	0	0	0	0
2nd radial position of winding start (rectangular core), mm (WSR2Sar)	0	0	0	0	0	0	0	0	0	0	0	0	0
2nd radial position of winding end (rectangular core), mm (WSR2Ear)	0	0	0	0	0	0	0	0	0	0	0	0	0
Wire													
Turns per layer (WSTLar)	416	416	438	438	438	438	544	544	75	7	11	0	0
Turns total (WSTTar)	6656	416	438	438	438	438	544	544	75	7	11	0	0
Conductor CSA, mm^2 (WSCSAar)	0.636172	0.636173	0.567451	0.567451	0.567451	0.567451	0.352565	0.352565	12.5	12.5	12.5	0	0
Resistivity, ohm-m (WSRar)	1.7098E-08	1.7098E-08	1.7098E-08	1.7098E-08	1.7098E-08	1.7098E-08	1.7098E-08	1.7098E-08	2.76E-08	2.76E-08	2.76E-08	0	0
Length, m (WSWLar)	5890.052	403.2317	428.8358	433.0464	437.2571	441.4677	553.2289	557.8433	78.00417	7.399141	11.62722	0	0
Weight, kg (WSWar)	33.57392	2.298463	2.180353	2.201761	2.223169	2.244577	1.747641	1.762218	2.632641	0.249721	0.392418	0	0
Cost, $ (WSC2ar)	335.7392	22.98463	21.80353	22.01761	22.23169	22.44577	17.47641	17.62218	26.32641	2.497210	3.924188	0	0
Inter-layer insulation													
Length, m (WSILIar)	14.02386	0	0	0	0	0	0	0	0	0	0	0	0
Breadth, mm (WSILIBar)	458	458	458	458	458	458	458	458	0	0	0	0	0
Weight, kg (WSILIWar)	3.917985	0	0	0	0	0	0	0	0	0	0	0	0
Cost, $ (WSILICar)	224.8024	0	0	0	0	0	0	0	0	0	0	0	0
Inter-section insulation (winding section n to n + 1)													
Length, mm (WSISILar)	1.014343	1.024270	1.033883	1.043497	1.053110	1.062723	1.071206	1.079688	0	0	0	0	0
Breadth, mm (WSISIBar)	458	458	458	458	458	458	458	508	0	0	0	0	0
Weight, kg (WSISIWar)	0.283387	0.286160	0.288846	0.291533	0.294218	0.296903	0.299273	0.334573	0	0	0	0	0
Cost, $ (WSISICar)	16.25993	16.41905	16.57316	16.72726	16.88136	17.03546	17.17143	19.19686	0	0	0	0	0
Encapsulant													
Volume in end-caps (region with only outermost insulation layer)	EVEC	double	0.001609	m^3	-	-							
Volume in inter-layer insulation winding ends overlap	EVWE	double	0.001036	m^3	-	-							
Volume in winding region	EVWR	double	0.000526	m^3	-	-							
Total Volume	EV	double	0.003171	m^3	-	-							
Weight in end-caps (region with only outermost insulation layer)	EWEC	double	2.204965	kg	-	-							

(f) Design Review worksheet (page 1 of 4)

Figure A.4 (Continued) TranModel sample layout for transformer PC5.

Weight in inter-layer insulation winding ends overlap	EWWE	double	1.41956876	kg	-	-
Weight in winding region	EWWR	double	0.72106196	kg	-	-
Total Weight	EW	double	4.34559648	kg	-	-
Cost	EC	double	284.636569	$	-	-
Primary / secondary winding						
Primary winding total turns	PWTT	double	93	-	-	-
Secondary winding total turns	SWTT	double	9912	-	-	-
Average length of all primary windings	WAVLP	double	161.3		-	-
Average length of all secondary windings	WAVLS	double	408		-	-
Average length of primary and secondary windings	WAVL	double	284.65	mm	-	-
Winding thickness factor	WTF	double	43.78	-	Figure 2.1	\tau_{12}
Aspect ratio	AR	double	6.50182732	-	-	\beta_{a}
Perimeter about middle of interwinding space	PSP	double	1029.68841	mm	-	l_{ps}
Perimeter about middle of primary winding	PPW	double	1057.02026	mm	-	l_{iw} or l_{ow}
Perimeter about middle of secondary winding	PSW	double	917.596382	mm	-	l_{iw} or l_{ow}
Primary winding thickness	PWT	double	8.1	mm	-	d_{iw} or d_{ow}
Secondary winding thickness	SWT	double	35.08	mm	-	d_{iw} or d_{ow}
Primary / secondary insulation thickness	PST	double	0.6	mm	-	\delta d
Radial position of primary winding start (circular core)	PWCS	double	164.18	mm	-	-
Radial position of primary winding end (circular core)	PWCE	double	172.28	mm	-	-
1st radial position of primary winding start (rectangular core)	PWR1S	double	0	mm	-	-
1st radial position of primary winding end (rectangular core)	PWR1E	double	0	mm	-	-
2nd radial position of primary winding start (rectangular core)	PWR2S	double	0	mm	-	-
2nd radial position of primary winding end (rectangular core)	PWR2E	double	0	mm	-	-
Radial position of secondary winding start (circular core)	SWCS	double	128.5	mm	-	-
Radial position of secondary winding end (circular core)	SWCE	double	163.58	mm	-	-
1st radial position of secondary winding start (rectangular core)	SWR1S	double	0	mm	-	-
1st radial position of secondary winding end (rectangular core)	SWR1E	double	0	mm	-	-
2nd radial position of secondary winding start (rectangular core)	SWR2S	double	0	mm	-	-
2nd radial position of secondary winding end (rectangular core)	SWR2E	double	0	mm	-	-
Turns ratio						
Primary / secondary	PS	double	0.00938257	-	-	a
Secondary / primary	SP	double	106.580645	-	-	1 / a
Weight						
Winding	WTWS	double	51.5068909	kg	-	-
Core	WC	double	100.071842	kg	-	-
Insulation	WTI	double	6.2928812	kg	-	-
Encapsulant	WE	double	4.34559648	kg	-	-
Total	WT	double	162.21721	kg	-	-
Cost						
Winding	CTWS	double	515.068909	$	-	-
Core	CC2	double	1100.79026	$	-	-
Insulation	CTI	double	361.066954	$	-	-
Encapsulant	CE	double	284.636569	$	-	-
Total	CT	double	2261.56269	$	-	-

Section B - Parameters related to skin effect (calculated at fundamental frequency)													
Core													
Penetration depth at fundamental frequency	LPD	double	0.59889648	mm	-	\delta_{c}							
Maximum frequency for complete flux penetration, Hz	CMFCP	double	1356.05667	Hz	-	-							
Partial-core transformer													
	Section 1	Section 2	Section 3	Section 4	Section 5	Section 6	Section 7	Section 8	Section 9	Section 10			
CSA incl. sf & skin depth at fund frequency, m^2 (CSCASDar) (*2)	0.04295814	0.04295814	0.04295814	0.04295814	0	0	0	0	0	0			
Core effective volume = CSCASD * CL, m^3 (CSVEFFar)	0.0031789	0.0031789	0.0031789	0.0031789	0	0	0	0	0	0			
Full-core transformer													
CSA central limb - incl stack factor and ski depth consids at fund fq	FCCLASD	double	0	m^2	-								
CSA yoke - incl stack factor and ski depth consids at fund fq	FCYASD	double	0	m^2	-								
CSA outer limb - incl stack factor and ski depth consids at fund fq	FCOLASD	double	0	m^2	-								
Winding sections													
	Section 1	Section 2	Section 3	Section 4	Section 5	Section 6	Section 7	Section 8	Section 9	Section 10	Section 11	Section 12	Section 13
Penetration depth, mm (WSPDar)	9.30695868	9.30695868	9.30695868	9.30695868	9.30695868	9.30695868	9.30695868	9.30695868	11.8246875	11.8246875	11.8246875	0	0
Effective CSA with skin depth consids at fund fq, mm^2 (WSEAar)	0.63617251	0.63617251	0.56745017	0.56745017	0.56745017	0.56745017	0.56745017	0.35256524	12.5	12.5	12.5	0	0
Maximum fq for complete radial flux penetration, Hz (WSMFCRPar)	21387.5259	21387.5259	23977.7107	23977.7107	23977.7107	23977.7107	23977.7107	38591.8823	4474.34347	4474.34347	4474.34347	0	0
Maximum fq for complete axial flux penetration, Hz (WSMFCAPar)	21387.5259	21387.5259	23977.7107	23977.7107	23977.7107	23977.7107	23977.7107	38591.8823	1118.58587	1118.58587	1118.58587	0	0
Winding resistance, ohm (WSRESar)	158.30317	10.8373997	12.9213739	13.0482451	13.1751163	13.3019875	26.8293848	27.0531633	0.17223322	0.01633731	0.02567291	0	0
Section C - Model upper-frequency limit													

(g) Design Review worksheet (page 2 of 4)

Figure A.4 (Continued) TranModel sample layout for transformer PC5.

Maximum frequency for static finite element model	MFSFEM	double	1118.58587	Hz	-
Section D - Core flux density estimate (calculated at fundamental frequency, valid for a single core section only, for full-core transformer calculated for central limb only)					
Maximum flux density estimate from V1 at fundamental frequency	CMB	double	0.11170157	T	-
RMS flux density estimate from V1 at fundamental frequency	CRB	double	0.07898494	T	-

Section E - Parameters for circuit theory magnetic model					
Partial-core transformer					
Frequency independent parameters					
Leakage reactance correction factor	LF	double	0.78806552	-	-
Magnetising reactance correction factor	MF	double	0.89534862	-	-
Frequency dependent parameters (calculated at fundamental frequency)					
Core flux reluctance	CTMCRU	double	4.569E+02	1 / H	-
Air flux reluctance (at each core end)	CTMARU	double	1.124E+06	1 / H	-
Core effective relative permeability	CURE	double	0.55	-	-

Full-core transformer					
Frequency dependent parameters (calculated at fundamental frequency)					
Central limb reluctance	FCCLR	double	0	1 / H	-
Outer limb reluctance	FCOLR	double	0	1 / H	-
Yoke reluctance	FCYR	double	0	1 / H	-
Total reluctance	FCTR	double	0	1 / H	-

Section F - Parameters for circuit theory core loss model (frequency dependent, calculated at fundamental frequency, for full-core transformer apply central limb flux density to outer limbs and yokes)					
Core hysteresis loss	CHL	double	2.44	W	-
Eddy current loss resistance	RED	double	241913.281	ohm	-

Section G - Parameters for finite element magnetic model (frequency independent)					
Geometry and configuration dependent parameters (click 'design calculations' if transformer geometry and / or core configuration has changed)					
Leakage inductance calculation based on energy method (referred to primary winding, for current configuration only)					
L11 + a^2 * L12	FEMLTE	double	0.00041043	H	-
Geometry dependent parameters (click 'design calculations' if transformer geometry is changed)					

Permeance (unit-turn inductance) matrix, H (FEMPMar)													
	Section 1	Section 2	Section 3	Section 4	Section 5	Section 6	Section 7	Section 8	Section 9	Section 10	Section 11	Section 12	Section 13
Section 1	3.815E-07	3.786E-07	3.7704E-07	3.7552E-07	3.74E-07	3.7249E-07	3.7108E-07	3.6977E-07	3.7516E-07	4.4494E-07	4.4592E-07	0	0
Section 2	3.786E-07	4.0034E-07	3.991E-07	3.9743E-07	3.9577E-07	3.9413E-07	3.926E-07	3.9118E-07	3.9663E-07	4.6681E-07	4.6783E-07	0	0
Section 3	3.7704E-07	3.991E-07	4.0154E-07	4.003E-07	3.9862E-07	3.9696E-07	3.9541E-07	3.9397E-07	3.9943E-07	4.6962E-07	4.7064E-07	0	0
Section 4	3.7551E-07	3.9743E-07	4.003E-07	4.0273E-07	4.0149E-07	4.0011E-07	3.9881E-07	3.9742E-07	3.9823E-07	4.7242E-07	4.7345E-07	0	0
Section 5	3.74E-07	3.9577E-07	3.9862E-07	4.0149E-07	4.0395E-07	4.0271E-07	4.0112E-07	3.9964E-07	4.051E-07	4.7528E-07	4.763E-07	0	0
Section 6	3.7249E-07	3.9413E-07	3.9696E-07	3.998E-07	4.0271E-07	4.052E-07	4.0406E-07	4.0256E-07	4.0802E-07	4.7819E-07	4.7921E-07	0	0
Section 7	3.7108E-07	3.926E-07	3.9541E-07	3.9823E-07	4.0112E-07	4.0406E-07	4.0651E-07	4.0537E-07	4.1081E-07	4.8095E-07	4.8199E-07	0	0
Section 8	3.6977E-07	3.9117E-07	3.9397E-07	3.9677E-07	3.9964E-07	4.0256E-07	4.0537E-07	4.0767E-07	4.1348E-07	4.8359E-07	4.8463E-07	0	0
Section 9	3.7516E-07	3.9663E-07	3.9943E-07	4.0224E-07	4.051E-07	4.0802E-07	4.1081E-07	4.1348E-07	4.2574E-07	5.0228E-07	5.0341E-07	0	0
Section 10	4.4492E-07	4.668E-07	4.6961E-07	4.7242E-07	4.7527E-07	4.7817E-07	4.8094E-07	4.8358E-07	5.0227E-07	1.0304E-06	6.8471E-07	0	0
Section 11	4.4591E-07	4.6782E-07	4.7063E-07	4.7344E-07	4.763E-07	4.7921E-07	4.8198E-07	4.8462E-07	5.034E-07	6.8473E-07	9.3688E-07	0	0
Section 12	0	0	0	0	0	0	0	0	0	0	0	0	0
Section 13	0	0	0	0	0	0	0	0	0	0	0	0	0

Configuration dependent parameters - calculated from permeance matrix and winding connection data (click 'design calculations (no FEM)' if only winding connections are changed)													
Inductance matrix, H (FEMIMar) (fit integer number of turns into CSA of connected winding sections)													
	Section 1	Section 2	Section 3	Section 4	Section 5	Section 6	Section 7	Section 8	Section 9	Section 10	Section 11	Section 12	Section 13
Section 1	16.901503	1.04830947	1.0991977	1.09474994	1.09033123	1.0859404	1.34364594	1.33888972	0.18727882	0.02073049	0.03264819	0	0
Section 2	1.04830802	0.0692809	0.07271978	0.07241491	0.07211313	0.07181413	0.08884719	0.08852468	0.0123749	0.00135936	0.00214078	0	0
Section 3	1.09919482	0.07271928	0.07703258	0.07679588	0.0764737	0.07615481	0.09421554	0.09387193	0.0131213	0.00143984	0.00226753	0	0
Section 4	1.09474119	0.07241443	0.07679585	0.07726107	0.07702384	0.07670031	0.0948881	0.09454011	0.01321338	0.00144845	0.00228107	0	0
Section 5	1.09032252	0.07211265	0.07702384	0.07749548	0.07725783	0.09557514	0.09522247	0.0133074	0.00145721	0.00229483	0	0	
Section 6	1.08593357	0.07181362	0.07615446	0.07670013	0.07725757	0.07773557	0.09627661	0.09591897	0.01340338	0.00146613	0.00230885	0	0
Section 7	1.34363403	0.08884659	0.09421515	0.0948881	0.09557515	0.09627696	0.12029951	0.11996362	0.0167611	0.00183147	0.0028842	0	0
Section 8	1.33887768	0.08852405	0.09387145	0.09454008	0.09522246	0.09591911	0.11996369	0.12064279	0.01686993	0.00184151	0.0029	0	0
Section 9	0.18727752	0.01237486	0.01312121	0.01321343	0.01330745	0.0134033	0.01676114	0.01686999	0.00239477	0.0002637	0.00041531	0	0
Section 10	0.02072992	0.00135932	0.00143982	0.00144843	0.00145718	0.00146608	0.00183144	0.00184148	0.00026369	5.0489E-05	5.2723E-05	0	0
Section 11	0.03264764	0.00214074	0.0022675	0.00228105	0.00229482	0.00230881	0.00288418	0.00289998	0.00041531	5.2724E-05	0.00011336	0	0
Section 12	0	0	0	0	0	0	0	0	0	0	0	0	0
Section 13	0	0	0	0	0	0	0	0	0	0	0	0	0

Coupling matrix Kij (FEMKMar) (fit integer number of turns into CSA of connected winding sections)													
	Section 1	Section 2	Section 3	Section 4	Section 5	Section 6	Section 7	Section 8	Section 9	Section 10	Section 11	Section 12	Section 13
Section 1	1	0.9687687	0.96333183	0.95801413	0.95270314	0.94740009	0.9423023	0.93762993	0.93088082	0.70965909	0.74586634	0	0
Section 2	0.96876735	1	0.99542507	0.98978511	0.98416842	0.97857301	0.97320658	0.9682933	0.96073407	0.72682419	0.76388753	0	0
Section 3	0.96332931	0.99541817	1	0.99545202	0.9897755	0.98412488	0.97870855	0.97375085	0.96606784	0.73009681	0.76732587	0	0
Section 4	0.95800647	0.98977854	0.99545167	1	0.99542054	0.9897075	0.98423647	0.97923081	0.97140763	0.73337604	0.77076816	0	0
Section 5	0.95269553	0.98416189	0.98977368	0.99542059	1	0.99539265	0.98986238	0.98480577	0.97683894	0.73669516	0.77424288	0	0

(h) Design Review worksheet (page 3 of 4)

Figure A.4 (Continued) TranModel sample layout for transformer PC5.

Section 6	0.94739413	0.97856607	0.98412032	0.98970521	0.99538931	1	0.99558639	0.99047588	0.98236408	0.74005556	0.77776794	0	0		
Section 7	0.94229395	0.97319995	0.9787045	0.98423649	0.98986251	0.99558999	1	0.99578816	0.98750334	0.74314147	0.78101217	0	0		
Section 8	0.93766215	0.96828641	0.97374583	0.97923305	0.98480566	0.99047733	0.99578875	1	0.99250056	0.74615083	0.78417388	0	0		
Section 9	0.93087433	0.96073095	0.96606127	0.97141136	0.97684265	0.98235823	0.98750608	0.99250416	1	0.75836672	0.79709318	0	0		
Section 10	0.70963957	0.72680532	0.73008402	0.73336407	0.736679	0.74003016	0.74312722	0.7461386	0.75834368	1	0.69689411	0	0		
Section 11	0.74585376	0.76387451	0.76731634	0.77075939	0.77423899	0.77775652	0.78100692	0.78416703	0.79708396	0.69690756	1	0	0		
Section 12	0	0	0	0	0	0	0	0	0	0	0	0	0		
Section 13	0	0	0	0	0	0	0	0	0	0	0	0	0		
Primary winding / secondary winding reluctances (per total CSA of connected winding sections)															
Primary winding total flux reluctance	PWTFR	double	2.49E+02	1 / H	-										
Primary winding leakage flux reluctance	PWLFR	double	-2.75E+00	1 / H	-										
Secondary winding total flux reluctance	SWTFR	double	2.68E-02	1 / H	-										
Secondary winding leakage flux reluctance	SWLFR	double	2.70E-02	1 / H	-										
Primary / secondary mutual flux reluctance	PSMFR	double	2.72E+00	1 / H	-										
Primary winding / secondary winding inductances and coupling (fit integer number of turns into CSA of connected winding sections)															
Primary winding self inductance	PWSI	double	0.00402208	H	-										
Secondary winding self inductance	SWSI	double	37.337948	H	-										
Primary - secondary mutual inductance	MIPS	double	0.36762729	H	-										
Primary - secondary coupling	PSK	double	0.94865232	-	-	k_{ps}									
Mutual inductances - Primary and secondary windings to unused winding sections															
	Section 1	Section 2	Section 3	Section 4	Section 5	Section 6	Section 7	Section 8	Section 9	Section 10	Section 11	Section 12	Section 13		
Primary - winding section i mutual inductance (FEMPIar)	0	0	0	0	0	0	0	0	0	0	0	0	0		
Secondary - winding section i mutual inductance (FEMSIar)	0	0	0	0	0	0	0	0	0	0	0	0	0		
Section H - Equivalent circuit parameters at fundamental frequency															
Parameters common to both magnetic models															
Turns ratio (frequency independent)	a	double	0.00938257	-	-	a									
Primary resistance at fundamental frequency	R1	double	0.21424343	ohm	-	R_{1}									
Secondary resistance at fundamental frequency	R2	double	275.46984	ohm	-	R_{2}									
Secondary resistance at fundamental frequency referred to primary	aaR2	double	0.02425031	ohm	-	a^2 R_{2}									
Parameters specific to circuit theory magnetic model															
Hysteresis loss resistance	CTMRH	double	3226.71903	ohm	-	R_{h}									
Core loss resistance	CTMRC	double	3184.24651	ohm	-	R_{c}									
Primary leakage reactance	CTMX1	double	0.10808295	ohm	-	jX_{1}									
Secondary leakage reactance	CTMX2	double	1227.76116	ohm	-	jX_{2}									
Secondary leakage referred to primary	CTMaaX2	double	0.10808295	ohm	-	ja^2 X_{2}									
Total leakage reactance referred to primary	CTMXLT	double	0.21616591	ohm	-										
Magnetising reactance	CTMXM	double	1.08156254	ohm	-	jX_{m}									
Load capacitance for parallel resonant operation	CTMXC	double	2.714E-07	farad	-	C_{\textrm{resonant}}									
Parameters specific to finite element magnetic model															
Hysteresis loss resistance	FEMRH	double	2881.39354	ohm	-	R_{h}									
Core loss resistance	FEMRC	double	2847.47765	ohm	-	R_{c}									
Primary leakage reactance	FEMX1	double	0.17994858	ohm	-	jX_{1}									
Secondary leakage reactance	FEMX2	double	-579.31133	ohm	-	jX_{2}									
Secondary leakage referred to primary	FEMaaX2	double	-0.0509983	ohm	-	ja^2 X_{2}									
Total leakage reactance referred to primary, S & M induct method	FEMXLT	double	0.12895033	ohm	-	-									
Total leakage reactance referred to primary, energy method (*3)	FEMXLTE	double	0.12894171	ohm	-	-									
Difference between leakage inductance methods	FEMXLTD	double	0.00668226	%	-	=100 * (FEMXLT - FEMXLTE) / FEMXLT									
Magnetising reactance	FEMXM	double	1.08362562	ohm	-	jX_{m}									
Load capacitance for parallel resonant operation	FEMXC	double	2.714E-07	farad	-	C_{\textrm{resonant}}									

Notes

*1 Assume centre-hole radius = 0 and that the core width can be covered by a single lamination.
*2 Currently assume centre-hole radius = 0. This restricts the circuit theory magnetic model to having a centre-hole radius of zero too. This does not affect weight calculations, just electrical performance at higher frequencies.
*3 Unlike the parameters FEMX1, FEMX2, FEMXM, have to re-run `Design Calculations' if data in `Winding Configuration' worksheet is changed in order to obtain the updated value of FEMXLTE.

(i) Design Review worksheet (page 4 of 4)

Figure A.4 (Continued) TranModel sample layout for transformer PC5.

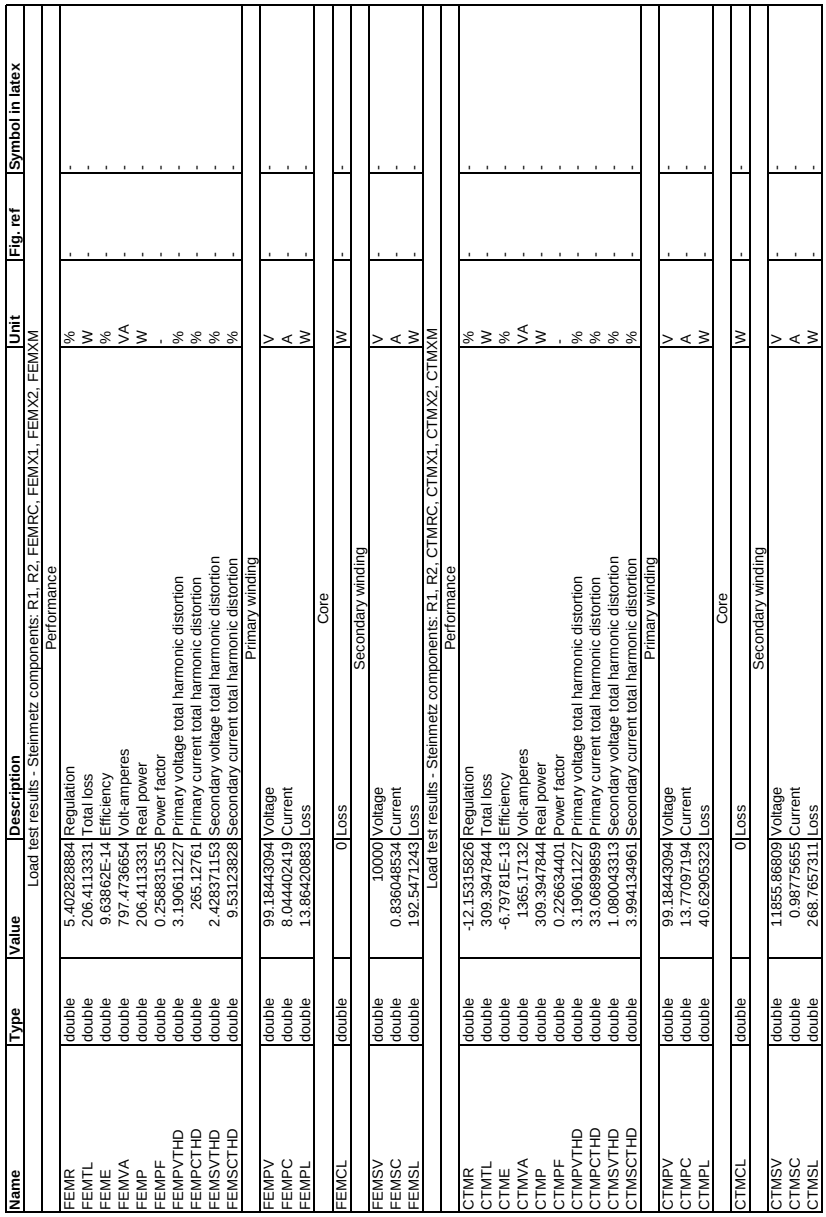

TranModel 1.0 - Test Results 1 worksheet

Name	Type	Value	Description	Unit	Fig. ref	Symbol in latex
Load test results - Steinmetz components: R1, R2, FEMRC, FEMX1, FEMX2, FEMXM						
Performance						
FEMR	double	5.402828884	Regulation	%	-	-
FEMTL	double	206.4113331	Total loss	W	-	-
FEME	double	9.63862E-14	Efficiency	%	-	-
FEMVA	double	797.4736654	Volt-amperes	VA	-	-
FEMP	double	206.4113331	Real power	W	-	-
FEMPF	double	0.258831535	Power factor	-	-	-
FEMPVTHD	double	3.190611227	Primary voltage total harmonic distortion	%	-	-
FEMPCTHD	double	265.12761	Primary current total harmonic distortion	%	-	-
FEMSVTHD	double	2.428371153	Secondary voltage total harmonic distortion	%	-	-
FEMSCTHD	double	9.53123828	Secondary current total harmonic distortion	%	-	-
Primary winding						
FEMPV	double	99.18443094	Voltage	V	-	-
FEMPC	double	8.044402419	Current	A	-	-
FEMPL	double	13.86420883	Loss	W	-	-
Core						
FEMCL	double	0	Loss	W	-	-
Secondary winding						
FEMSV	double	10000	Voltage	V	-	-
FEMSC	double	0.836048534	Current	A	-	-
FEMSL	double	192.5471243	Loss	W	-	-
Load test results - Steinmetz components: R1, R2, CTMRC, CTMX1, CTMX2, CTMXM						
Performance						
CTMR	double	-12.15315826	Regulation	%	-	-
CTMTL	double	309.3947844	Total loss	W	-	-
CTME	double	-6.79781E-13	Efficiency	%	-	-
CTMVA	double	1365.17132	Volt-amperes	VA	-	-
CTMP	double	309.3947844	Real power	W	-	-
CTMPF	double	0.226634401	Power factor	-	-	-
CTMPVTHD	double	3.190611227	Primary voltage total harmonic distortion	%	-	-
CTMPCTHD	double	33.06899859	Primary current total harmonic distortion	%	-	-
CTMSVTHD	double	1.080043313	Secondary voltage total harmonic distortion	%	-	-
CTMSCTHD	double	3.994134961	Secondary current total harmonic distortion	%	-	-
Primary winding						
CTMPV	double	99.18443094	Voltage	V	-	-
CTMPC	double	13.77097194	Current	A	-	-
CTMPL	double	40.62905323	Loss	W	-	-
Core						
CTMCL	double	0	Loss	W	-	-
Secondary winding						
CTMSV	double	1855.86809	Voltage	V	-	-
CTMSC	double	0.98775655	Current	A	-	-
CTMSL	double	268.7657311	Loss	W	-	-

(j) Test Results 1 worksheet

Figure A.4 (Continued) TranModel sample layout for transformer PC5.

TranModel 1.0 - Test Results 2 worksheet

Load test results - Steinmetz components: R1, R2, FEMRC, FEMX1, FEMX1, FEMXM

Terminal Conditions

Performance

Harmonics	Overall	1	2	3	4	5	6	7	8	9	10	11	12	13	14	15
Volt-amperes, VA (FEMVA2ar)	797.4737	281.4352	0	4.662967	0	16.77865	0	1.301521	0	0.085415	0	0.030087	0	0	0	0
Real power, W (FEMRP2ar)	206.4113	192.5404	0	4.539111	0	8.889031	0	0.417304	0	0.019932	0	0.005559	0	0	0	0
Power factor (FEMpf2ar)	0.258832	-0.68414	0	0.973438	0	-0.52978	0	-0.32063	0	-0.23335	0	-0.18477	0	0	0	0
Total loss, W (FEMTL2ar)	206.4113	192.5404	0	4.539111	0	8.889031	0	0.417304	0	0.019932	0	0.005559	0	0	0	0

Primary winding (positive current into the winding)

Harmonics	Overall	1	2	3	4	5	6	7	8	9	10	11	12	13	14	15
Voltage, V (FEMPVar2)	99.18443	99.13398	0	1.090474	0	2.775752	0	0.99134	0	0.297402	0	0.198268	0	0	0	0
Voltage angle, deg (FEMPVAar)	-	0	0	0	0	0	0	0	0	0	0	0	0	0	0	0
Current, A (FEMPCar)	8.044402	2.838938	0	4.276092	0	6.044723	0	1.312891	0	0.287205	0	0.15175	0	0	0	0
Ampere-turns, A-t (FEMPATar)	748.1294	264.0212	0	397.6766	0	562.1593	0	122.0989	0	26.71002	0	14.11278	0	0	0	0
Current angle, deg (FEMPCAar)	-	-46.8322	0	13.23522	0	-58.0093	0	-71.2991	0	-76.5056	0	-79.3524	0	0	0	0
Loss, W (FEMPLar)	13.86421	1.72671	0	3.917434	0	7.828172	0	0.369288	0	0.017672	0	0.004934	0	0	0	0

Secondary winding (positive current out of the winding)

Harmonics	Overall	1	2	3	4	5	6	7	8	9	10	11	12	13	14	15
Voltage, V (FEMSVar)	10000	9997.053	0	190.2078	0	149.0823	0	22.65488	0	3.822383	0	1.645465	0	0	0	0
Voltage angle, deg (FEMSVAar)	-	-1.19851	0	-76.2587	0	32.27135	0	18.8972	0	13.64585	0	10.77093	0	0	0	0
Current, A (FEMSCar)	0.836049	0.832277	0	0.047506	0	0.062057	0	0.013202	0	0.002864	0	0.001507	0	0	0	0
Ampere-turns, A-t (FEMSATar)	8286.913	8249.527	0	470.8761	0	615.1106	0	130.863	0	28.38793	0	14.93614	0	0	0	0
Current angle, deg (FEMSCAar)	-	88.80149	0	13.7413	0	-57.7287	0	-71.1028	0	-76.3541	0	-79.2291	0	0	0	0
Loss, W (FEMSLar)	192.5471	190.8137	0	0.621677	0	1.06086	0	0.048016	0	0.00226	0	0.000626	0	0	0	0

Core

Harmonics	Overall	1	2	3	4	5	6	7	8	9	10	11	12	13	14	15
emf E1, V (FEMCEMFar)	98.43001	98.34532	0	2.562222	0	3.089477	0	0.715703	0	0.176123	0	0.105606	0	0	0	0
emf angle, deg (FEMCEMFAar)	-	0.054828	0	-73.512	0	35.24726	0	21.62999	0	16.05467	0	12.88444	0	0	0	0
Loss, W (FEMCLar)	0	0	0	0	0	0	0	0	0	0	0	0	0	0	0	0

Winding sections (FEMRESULTSar)

Section 1

Designation ("p" = primary, "s" = secondary, "n" = neither / unconnected, "d" = does not exist) s

Harmonics	Overall	1	2	3	4	5	6	7	8	9	10	11	12	13	14	15
Volts / Section, V	0	0	0	0	0	0	0	0	0	0	0	0	0	0	0	0
Volts / Layer, V	0	0	0	0	0	0	0	0	0	0	0	0	0	0	0	0
Volts / Turn, V	0	0	0	0	0	0	0	0	0	0	0	0	0	0	0	0
Voltage angle, deg	0	0	0	0	0	0	0	0	0	0	0	0	0	0	0	0
Current, A	0.836049	0.832277	0	0.047506	0	0.062057	0	0.013202	0	0.002864	0	0.001507	0	0	0	0
Current density, A/mm^2	1.314185	1.308256	0	0.074674	0	0.097548	0	0.020753	0	0.004502	0	0.002369	0	0	0	0
Ampere-turns, A-t	5564.739	5539.634	0	316.1976	0	413.0525	0	87.8757	0	19.06276	0	10.02975	0	0	0	0
Loss, W	110.6503	109.6542	0	0.357257	0	0.60964	0	0.027593	0	0.001298	0	0.000359	0	0	0	0
Temp rise / minute (worst case), deg C	0.522649	0.517944	0	0.001687	0	0.00288	0	0.00013	0	6.13E-06	0	1.7E-06	0	0	0	0

Section 2

Designation ("p" = primary, "s" = secondary, "n" = neither / unconnected, "d" = does not exist) s

Harmonics	Overall	1	2	3	4	5	6	7	8	9	10	11	12	13	14	15
Volts / Section, V	0	0	0	0	0	0	0	0	0	0	0	0	0	0	0	0
Volts / Layer, V	0	0	0	0	0	0	0	0	0	0	0	0	0	0	0	0
Volts / Turn, V	0	0	0	0	0	0	0	0	0	0	0	0	0	0	0	0
Voltage angle, deg	0	0	0	0	0	0	0	0	0	0	0	0	0	0	0	0
Current, A	0.836049	0.832277	0	0.047506	0	0.062057	0	0.013202	0	0.002864	0	0.001507	0	0	0	0
Current density, A/mm^2	1.314185	1.308256	0	0.074674	0	0.097548	0	0.020753	0	0.004502	0	0.002369	0	0	0	0
Ampere-turns, A-t	347.7962	346.2271	0	19.76235	0	25.81578	0	5.492231	0	1.191422	0	0.62686	0	0	0	0
Loss, W	7.575095	7.506899	0	0.024458	0	0.041736	0	0.001889	0	8.89E-05	0	2.46E-05	0	0	0	0
Temp rise / minute (worst case), deg C	0.522649	0.517944	0	0.001687	0	0.00288	0	0.00013	0	6.13E-06	0	1.7E-06	0	0	0	0

Section 3

Designation ("p" = primary, "s" = secondary, "n" = neither / unconnected, "d" = does not exist) s

Harmonics	Overall	1	2	3	4	5	6	7	8	9	10	11	12	13	14	15
Volts / Section, V	0	0	0	0	0	0	0	0	0	0	0	0	0	0	0	0
Volts / Layer, V	0	0	0	0	0	0	0	0	0	0	0	0	0	0	0	0
Volts / Turn, V	0	0	0	0	0	0	0	0	0	0	0	0	0	0	0	0
Voltage angle, deg	0	0	0	0	0	0	0	0	0	0	0	0	0	0	0	0
Current, A	0.836049	0.832277	0	0.047506	0	0.062057	0	0.013202	0	0.002864	0	0.001507	0	0	0	0

(k) Test Results 2 worksheet (page 1 of 6)

Figure A.4 (Continued) TranModel sample layout for transformer PC5.

| | | |

Designation ("p" = primary, "s" = secondary, "n" = neither / unconnected, "d" = does not exist)							p								
Harmonics	Overall	1	2	3	4	5	6	7	8	9	10	11	12	13	14	15
Volts / Section, V	0	0	0	0	0	0	0	0	0	0	0	0	0	0	0	0
Volts / Layer, V	0	0	0	0	0	0	0	0	0	0	0	0	0	0	0	0
Volts / Turn, V	0	0	0	0	0	0	0	0	0	0	0	0	0	0	0	0
Voltage angle, deg	0	0	0	0	0	0	0	0	0	0	0	0	0	0	0	0
Current, A	8.044402	2.838938	0	4.276092	0	6.044723	0	1.312891	0	0.287205	0	0.15175	0	0	0	0
Current density, A/mm^2	0.643552	0.227115	0	0.342087	0	0.483578	0	0.105031	0	0.022976	0	0.01214	0	0	0	0
Ampere-turns, A-t	603.3302	212.9203	0	320.7069	0	453.3542	0	98.46681	0	21.54034	0	11.38128	0	0	0	0
Loss, W	11.14563	1.388125	0	3.149279	0	6.293174	0	0.296875	0	0.014207	0	0.003966	0	0	0	0
Temp rise / minute (worst case), deg C	0.272162	0.033896	0	0.076901	0	0.153671	0	0.007249	0	0.000347	0	9.68E-05	0	0	0	0
Section 10																
Designation ("p" = primary, "s" = secondary, "n" = neither / unconnected, "d" = does not exist)							p								
Harmonics	Overall	1	2	3	4	5	6	7	8	9	10	11	12	13	14	15
Volts / Section, V	0	0	0	0	0	0	0	0	0	0	0	0	0	0	0	0
Volts / Layer, V	0	0	0	0	0	0	0	0	0	0	0	0	0	0	0	0
Volts / Turn, V	0	0	0	0	0	0	0	0	0	0	0	0	0	0	0	0
Voltage angle, deg	0	0	0	0	0	0	0	0	0	0	0	0	0	0	0	0
Current, A	8.044402	2.838938	0	4.276092	0	6.044723	0	1.312891	0	0.287205	0	0.15175	0	0	0	0
Current density, A/mm^2	0.643552	0.227115	0	0.342087	0	0.483578	0	0.105031	0	0.022976	0	0.01214	0	0	0	0
Ampere-turns, A-t	56.31082	19.87257	0	29.93265	0	42.31306	0	9.190236	0	2.010432	0	1.062252	0	0	0	0
Loss, W	1.057226	0.131672	0	0.298727	0	0.596944	0	0.02816	0	0.001348	0	0.000376	0	0	0	0
Temp rise / minute (worst case), deg C	0.272162	0.033896	0	0.076901	0	0.153671	0	0.007249	0	0.000347	0	9.68E-05	0	0	0	0
Section 11																
Designation ("p" = primary, "s" = secondary, "n" = neither / unconnected, "d" = does not exist)							p								
Harmonics	Overall	1	2	3	4	5	6	7	8	9	10	11	12	13	14	15
Volts / Section, V	0	0	0	0	0	0	0	0	0	0	0	0	0	0	0	0
Volts / Layer, V	0	0	0	0	0	0	0	0	0	0	0	0	0	0	0	0
Volts / Turn, V	0	0	0	0	0	0	0	0	0	0	0	0	0	0	0	0
Voltage angle, deg	0	0	0	0	0	0	0	0	0	0	0	0	0	0	0	0
Current, A	8.044402	2.838938	0	4.276092	0	6.044723	0	1.312891	0	0.287205	0	0.15175	0	0	0	0
Current density, A/mm^2	0.643552	0.227115	0	0.342087	0	0.483578	0	0.105031	0	0.022976	0	0.01214	0	0	0	0
Ampere-turns, A-t	88.48843	31.22832	0	47.03702	0	66.49195	0	14.4418	0	3.15925	0	1.669254	0	0	0	0
Loss, W	1.661356	0.206913	0	0.469428	0	0.938054	0	0.044252	0	0.002118	0	0.000591	0	0	0	0
Temp rise / minute (worst case), deg C	0.272162	0.033896	0	0.076901	0	0.153671	0	0.007249	0	0.000347	0	9.68E-05	0	0	0	0
Section 12																
Designation ("p" = primary, "s" = secondary, "n" = neither / unconnected, "d" = does not exist)							d								
Harmonics	Overall	1	2	3	4	5	6	7	8	9	10	11	12	13	14	15
Volts / Section, V	0	0	0	0	0	0	0	0	0	0	0	0	0	0	0	0
Volts / Layer, V	0	0	0	0	0	0	0	0	0	0	0	0	0	0	0	0
Volts / Turn, V	0	0	0	0	0	0	0	0	0	0	0	0	0	0	0	0
Voltage angle, deg	0	0	0	0	0	0	0	0	0	0	0	0	0	0	0	0
Current, A	0	0	0	0	0	0	0	0	0	0	0	0	0	0	0	0
Current density, A/mm^2	0	0	0	0	0	0	0	0	0	0	0	0	0	0	0	0
Ampere-turns, A-t	0	0	0	0	0	0	0	0	0	0	0	0	0	0	0	0
Loss, W	0	0	0	0	0	0	0	0	0	0	0	0	0	0	0	0
Temp rise / minute (worst case), deg C	0	0	0	0	0	0	0	0	0	0	0	0	0	0	0	0
Section 13																
Designation ("p" = primary, "s" = secondary, "n" = neither / unconnected, "d" = does not exist)							d								
Harmonics	Overall	1	2	3	4	5	6	7	8	9	10	11	12	13	14	15
Volts / Section, V	0	0	0	0	0	0	0	0	0	0	0	0	0	0	0	0
Volts / Layer, V	0	0	0	0	0	0	0	0	0	0	0	0	0	0	0	0
Volts / Turn, V	0	0	0	0	0	0	0	0	0	0	0	0	0	0	0	0
Voltage angle, deg	0	0	0	0	0	0	0	0	0	0	0	0	0	0	0	0
Current, A	0	0	0	0	0	0	0	0	0	0	0	0	0	0	0	0
Current density, A/mm^2	0	0	0	0	0	0	0	0	0	0	0	0	0	0	0	0
Ampere-turns, A-t	0	0	0	0	0	0	0	0	0	0	0	0	0	0	0	0
Loss, W	0	0	0	0	0	0	0	0	0	0	0	0	0	0	0	0
Temp rise / minute (worst case), deg C	0	0	0	0	0	0	0	0	0	0	0	0	0	0	0	0

Load test results - Steinmetz components: R1, R2, CTMRC, CTMX1, CTMX1, CTMXM

Terminal Conditions																
Performance																
Harmonics	Overall	1	2	3	4	5	6	7	8	9	10	11	12	13	14	15

(m) Test Results 2 worksheet (page 3 of 6)

Figure A.4 (Continued) TranModel sample layout for transformer PC5.

Volt-amperes, VA (CTMVA2ar)	1365.171	1296.139	0	3.126305	0	8.729123	0	0.734428	0	0.049842	0	0.017849	0	0	0	0
Real power, W (CTMRP2ar)	309.3948	304.9617	0	1.963742	0	2.331897	0	0.128999	0	0.006593	0	0.001901	0	0	0	0
Power factor (CTMpf2ar)	0.226634	0.235285	0	-0.62813	0	-0.26714	0	-0.17565	0	-0.13228	0	-0.10652	0	0	0	0
Total loss, W (CTMTL2ar)	309.3948	304.9617	0	1.963742	0	2.331897	0	0.128999	0	0.006593	0	0.001901	0	0	0	0
Primary winding (positive current into the winding)																
Harmonics	Overall	1	2	3	4	5	6	7	8	9	10	11	12	13	14	15
Voltage, V (CTMPVar)	99.18443	99.13398	0	1.090474	0	2.775752	0	0.99134	0	0.297402	0	0.198268	0	0	0	0
Voltage angle, deg (CTMPVAar)	-	0	0	0	0	0	0	0	0	0	0	0	0	0	0	0
Current, A (CTMPCar)	13.77097	13.07462	0	2.866923	0	3.144778	0	0.740843	0	0.167591	0	0.090026	0	0	0	0
Ampere-turns, A-t (CTMPATar)	1280.7	1215.94	0	266.6239	0	292.4644	0	68.89844	0	15.58599	0	8.372451	0	0	0	0
Current angle, deg (CTMPCAar)	-	76.3916	0	-51.0873	0	-74.5059	0	-79.8838	0	-82.3988	0	-83.8854	0	0	0	0
Loss, W (CTMPLar)	40.62905	36.624	0	1.76092	0	2.118788	0	0.117587	0	0.006017	0	0.001736	0	0	0	0
Secondary winding (positive current out of the winding)																
Harmonics	Overall	1	2	3	4	5	6	7	8	9	10	11	12	13	14	15
Voltage, V (CTMSVar)	11855.87	11855.18	0	108.6432	0	66.81874	0	11.04427	0	1.929123	0	0.84477	0	0	0	0
Voltage angle, deg (CTMSVAar)	-	-3.21577	0	39.34463	0	15.73635	0	10.28613	0	7.73241	0	6.221519	0	0	0	0
Current, A (CTMSCar)	0.987757	0.98697	0	0.027134	0	0.027814	0	0.006436	0	0.001445	0	0.000774	0	0	0	0
Ampere-turns, A-t (CTMSATar)	9790.643	9782.843	0	268.9559	0	275.6927	0	63.79578	0	14.32714	0	7.668104	0	0	0	0
Current angle, deg (CTMSCAar)	-	86.78423	0	-50.6554	0	-74.2637	0	-79.7139	0	-82.2676	0	-83.7785	0	0	0	0
Loss, W (CTMSLar)	268.7657	268.3376	0	0.202821	0	0.213109	0	0.011411	0	0.000576	0	0.000165	0	0	0	0
Core																
Harmonics	Overall	1	2	3	4	5	6	7	8	9	10	11	12	13	14	15
emf E1, V (CTMCEMFar)	99.90095	99.89511	0	0.107616	0	0.977741	0	0.415706	0	0.13181	0	0.090125	0	0	0	0
emf angle, deg (CTMCEMFAar)	-	-1.7525	0	80.01359	0	11.51986	0	7.992736	0	6.108254	0	4.950258	0	0	0	0
Loss, W (CTMCLar)	0	0	0	0	0	0	0	0	0	0	0	0	0	0	0	0
Winding sections (CTMRESULTSar)																
Section 1																
Designation ("p" = primary, "s" = secondary, "n" = neither / unconnected, "d" = does not exist)							s									
Harmonics	Overall	1	2	3	4	5	6	7	8	9	10	11	12	13	14	15
Volts / Section, V (*1)	0	0	0	0	0	0	0	0	0	0	0	0	0	0	0	0
Volts / Layer, V	0	0	0	0	0	0	0	0	0	0	0	0	0	0	0	0
Volts / Turn, V	0	0	0	0	0	0	0	0	0	0	0	0	0	0	0	0
Voltage angle, deg	0	0	0	0	0	0	0	0	0	0	0	0	0	0	0	0
Current, A	0.987757	0.98697	0	0.027134	0	0.027814	0	0.006436	0	0.001445	0	0.000774	0	0	0	0
Current density, A/mm^2	1.552655	1.551418	0	0.042653	0	0.043721	0	0.010117	0	0.002272	0	0.001216	0	0	0	0
Ampere-turns, A-t	6574.508	6569.27	0	180.6064	0	185.1302	0	42.83946	0	9.620804	0	5.149203	0	0	0	0
Loss, W	111.0263	110.0268	0	0.358471	0	0.611712	0	0.027687	0	0.001303	0	0.000361	0	0	0	0
Temp rise / minute (worst case), deg C	0.729536	0.728374	0	0.000551	0	0.000578	0	3.1E-05	0	1.56E-06	0	4.48E-07	0	0	0	0
Section 2																
Designation ("p" = primary, "s" = secondary, "n" = neither / unconnected, "d" = does not exist)							s									
Harmonics	Overall	1	2	3	4	5	6	7	8	9	10	11	12	13	14	15
Volts / Section, V (*1)	0	0	0	0	0	0	0	0	0	0	0	0	0	0	0	0
Volts / Layer, V	0	0	0	0	0	0	0	0	0	0	0	0	0	0	0	0
Volts / Turn, V	0	0	0	0	0	0	0	0	0	0	0	0	0	0	0	0
Voltage angle, deg	0	0	0	0	0	0	0	0	0	0	0	0	0	0	0	0
Current, A	0.987757	0.98697	0	0.027134	0	0.027814	0	0.006436	0	0.001445	0	0.000774	0	0	0	0
Current density, A/mm^2	1.552655	1.551418	0	0.042653	0	0.043721	0	0.010117	0	0.002272	0	0.001216	0	0	0	0
Ampere-turns, A-t	410.9067	410.5794	0	11.2879	0	11.57064	0	2.677466	0	0.6013	0	0.321825	0	0	0	0
Loss, W	7.600836	7.532408	0	0.024541	0	0.041878	0	0.001895	0	8.92E-05	0	2.47E-05	0	0	0	0
Temp rise / minute (worst case), deg C	0.729536	0.728374	0	0.000551	0	0.000578	0	3.1E-05	0	1.56E-06	0	4.48E-07	0	0	0	0
Section 3																
Designation ("p" = primary, "s" = secondary, "n" = neither / unconnected, "d" = does not exist)							s									
Harmonics	Overall	1	2	3	4	5	6	7	8	9	10	11	12	13	14	15
Volts / Section, V (*1)	0	0	0	0	0	0	0	0	0	0	0	0	0	0	0	0
Volts / Layer, V	0	0	0	0	0	0	0	0	0	0	0	0	0	0	0	0
Volts / Turn, V	0	0	0	0	0	0	0	0	0	0	0	0	0	0	0	0
Voltage angle, deg	0	0	0	0	0	0	0	0	0	0	0	0	0	0	0	0
Current, A	0.987757	0.98697	0	0.027134	0	0.027814	0	0.006436	0	0.001445	0	0.000774	0	0	0	0
Current density, A/mm^2	1.740693	1.739306	0	0.047818	0	0.049016	0	0.011342	0	0.002547	0	0.001363	0	0	0	0
Ampere-turns, A-t	432.6374	432.2927	0	11.88485	0	12.18255	0	2.819063	0	0.6331	0	0.338845	0	0	0	0
Loss, W	9.062436	8.98085	0	0.02926	0	0.04993	0	0.00226	0	0.000106	0	2.94E-05	0	0	0	0
Temp rise / minute (worst case), deg C	0.916941	0.91548	0	0.000692	0	0.000727	0	3.89E-05	0	1.96E-06	0	5.62E-07	0	0	0	0
Section 4																
Designation ("p" = primary, "s" = secondary, "n" = neither / unconnected, "d" = does not exist)							s									
Harmonics	Overall	1	2	3	4	5	6	7	8	9	10	11	12	13	14	15

(n) Test Results 2 worksheet (page 4 of 6)

Figure A.4 (Continued) TranModel sample layout for transformer PC5.

Volts / Section, V (*1)	0	0	0	0	0	0	0	0	0	0	0	0	0	0	0	0	0	0	0	0	0	0	0	0	0
Volts / Layer, V	0	0	0	0	0	0	0	0	0	0	0	0	0	0	0	0	0	0	0	0	0	0	0	0	0
Volts / Turn, V	0	0	0	0	0	0	0	0	0	0	0	0	0	0	0	0	0	0	0	0	0	0	0	0	0
Voltage angle, deg	0	0	0	0	0	0	0	0	0	0	0	0	0	0	0	0	0	0	0	0	0	0	0	0	0
Current, A	0.987757	0.98697	0	0.027134	0	0.027814	0	0.006436	0	0.001445	0	0.000774	0	0.001445	0	0.000774	0	0.001445	0	0.000774	0	0.001445	0	0.000774	0
Current density, A/mm^2	1.740693	1.739306	0	0.047818	0	0.049016	0	0.011342	0	0.002547	0	0.001363	0	0.002547	0	0.001363	0	0.002547	0	0.001363	0	0.002547	0	0.001363	0
Ampere-turns, A-t	432.6374	432.2927	0	11.88485	0	12.18255	0	2.819063	0	0.6331	0	0.338845	0	0.6331	0	0.338845	0	0.6331	0	0.338845	0	0.6331	0	0.338845	0
Loss, W	9.151418	9.06903	0	0.029547	0	0.050421	0	0.002282	0	0.000107	0	2.97E-05	0	0.000107	0	2.97E-05	0	0.000107	0	2.97E-05	0	0.000107	0	2.97E-05	0
Temp rise / minute (worst case), deg C	0.916941	0.91548	0	0.000692	0	0.000727	0	3.89E-05	0	1.96E-06	0	5.62E-07	0	1.96E-06	0	5.62E-07	0	1.96E-06	0	5.62E-07	0	1.96E-06	0	5.62E-07	0

Section 5

Designation ("p" = primary, "s" = secondary, "n" = neither / unconnected, "d" = does not exist)							s																		
Harmonics	Overall	1	2	3	4	5	6	7	8	9	10	11	12	13	14	15									
Volts / Section, V (*1)	0	0	0	0	0	0	0	0	0	0	0	0	0	0	0	0									
Volts / Layer, V	0	0	0	0	0	0	0	0	0	0	0	0	0	0	0	0									
Volts / Turn, V	0	0	0	0	0	0	0	0	0	0	0	0	0	0	0	0									
Voltage angle, deg	0	0	0	0	0	0	0	0	0	0	0	0	0	0	0	0									
Current, A	0.987757	0.98697	0	0.027134	0	0.027814	0	0.006436	0	0.001445	0	0.000774	0	0.001445	0	0.000774									
Current density, A/mm^2	1.740693	1.739306	0	0.047818	0	0.049016	0	0.011342	0	0.002547	0	0.001363	0	0.002547	0	0.001363									
Ampere-turns, A-t	432.6374	432.2927	0	11.88485	0	12.18255	0	2.819063	0	0.6331	0	0.338845	0	0.6331	0	0.338845									
Loss, W	9.240399	9.157211	0	0.029834	0	0.050911	0	0.002304	0	0.000108	0	3E-05	0	0.000108	0	3E-05									
Temp rise / minute (worst case), deg C	0.916941	0.91548	0	0.000692	0	0.000727	0	3.89E-05	0	1.96E-06	0	5.62E-07	0	0.000727	0	0									

Section 6

Designation ("p" = primary, "s" = secondary, "n" = neither / unconnected, "d" = does not exist)							s																		
Harmonics	Overall	1	2	3	4	5	6	7	8	9	10	11	12	13	14	15									
Volts / Section, V (*1)	0	0	0	0	0	0	0	0	0	0	0	0	0	0	0	0									
Volts / Layer, V	0	0	0	0	0	0	0	0	0	0	0	0	0	0	0	0									
Volts / Turn, V	0	0	0	0	0	0	0	0	0	0	0	0	0	0	0	0									
Voltage angle, deg	0	0	0	0	0	0	0	0	0	0	0	0	0	0	0	0									
Current, A	0.987757	0.98697	0	0.027134	0	0.027814	0	0.006436	0	0.001445	0	0.000774	0	0.001445	0	0.000774									
Current density, A/mm^2	1.740693	1.739306	0	0.047818	0	0.049016	0	0.011342	0	0.002547	0	0.001363	0	0.002547	0	0.001363									
Ampere-turns, A-t	432.6374	432.2927	0	11.88485	0	12.18255	0	2.819063	0	0.6331	0	0.338845	0	0.6331	0	0.338845									
Loss, W	9.32938	9.245391	0	0.030122	0	0.051401	0	0.002326	0	0.000109	0	3.03E-05	0	0.000109	0	3.03E-05									
Temp rise / minute (worst case), deg C	0.916941	0.91548	0	0.000692	0	0.000727	0	3.89E-05	0	1.96E-06	0	5.62E-07	0	0.000727	0	0									

Section 7

Designation ("p" = primary, "s" = secondary, "n" = neither / unconnected, "d" = does not exist)							s																		
Harmonics	Overall	1	2	3	4	5	6	7	8	9	10	11	12	13	14	15									
Volts / Section, V (*1)	0	0	0	0	0	0	0	0	0	0	0	0	0	0	0	0									
Volts / Layer, V	0	0	0	0	0	0	0	0	0	0	0	0	0	0	0	0									
Volts / Turn, V	0	0	0	0	0	0	0	0	0	0	0	0	0	0	0	0									
Voltage angle, deg	0	0	0	0	0	0	0	0	0	0	0	0	0	0	0	0									
Current, A	0.987757	0.98697	0	0.027134	0	0.027814	0	0.006436	0	0.001445	0	0.000774	0	0.001445	0	0.000774									
Current density, A/mm^2	2.801628	2.799396	0	0.076963	0	0.07889	0	0.018255	0	0.0041	0	0.002194	0	0.0041	0	0.002194									
Ampere-turns, A-t	537.3396	536.9115	0	14.7611	0	15.13084	0	3.501302	0	0.786316	0	0.420848	0	0.786316	0	0.420848									
Loss, W	18.81685	18.64745	0	0.060754	0	0.103674	0	0.004692	0	0.000221	0	6.11E-05	0	0.000221	0	6.11E-05									
Temp rise / minute (worst case), deg C	2.375296	2.371513	0	0.001792	0	0.001883	0	0.000101	0	5.09E-06	0	1.46E-06	0	0	0	0									

Section 8

Designation ("p" = primary, "s" = secondary, "n" = neither / unconnected, "d" = does not exist)							s																		
Harmonics	Overall	1	2	3	4	5	6	7	8	9	10	11	12	13	14	15									
Volts / Section, V (*1)	0	0	0	0	0	0	0	0	0	0	0	0	0	0	0	0									
Volts / Layer, V	0	0	0	0	0	0	0	0	0	0	0	0	0	0	0	0									
Volts / Turn, V	0	0	0	0	0	0	0	0	0	0	0	0	0	0	0	0									
Voltage angle, deg	0	0	0	0	0	0	0	0	0	0	0	0	0	0	0	0									
Current, A	0.987757	0.98697	0	0.027134	0	0.027814	0	0.006436	0	0.001445	0	0.000774	0	0.001445	0	0.000774									
Current density, A/mm^2	2.801628	2.799396	0	0.076963	0	0.07889	0	0.018255	0	0.0041	0	0.002194	0	0.0041	0	0.002194									
Ampere-turns, A-t	537.3396	536.9115	0	14.7611	0	15.13084	0	3.501302	0	0.786316	0	0.420848	0	0.786316	0	0.420848									
Loss, W	18.97738	18.80299	0	0.061261	0	0.104538	0	0.004732	0	0.000223	0	6.16E-05	0	0.000223	0	6.16E-05									
Temp rise / minute (worst case), deg C	2.375296	2.371513	0	0.001792	0	0.001883	0	0.000101	0	5.09E-06	0	1.46E-06	0	0	0	0									

Section 9

Designation ("p" = primary, "s" = secondary, "n" = neither / unconnected, "d" = does not exist)							p																		
Harmonics	Overall	1	2	3	4	5	6	7	8	9	10	11	12	13	14	15									
Volts / Section, V (*1)	0	0	0	0	0	0	0	0	0	0	0	0	0	0	0	0									
Volts / Layer, V	0	0	0	0	0	0	0	0	0	0	0	0	0	0	0	0									
Volts / Turn, V	0	0	0	0	0	0	0	0	0	0	0	0	0	0	0	0									
Voltage angle, deg	0	0	0	0	0	0	0	0	0	0	0	0	0	0	0	0									
Current, A	13.77097	13.07462	0	2.866923	0	3.144778	0	0.740843	0	0.167591	0	0.090026	0	0	0	0									

(o) Test Results 2 worksheet (page 5 of 6)

Figure A.4 (Continued) TranModel sample layout for transformer PC5.

| | | |

Appendix B

TRANSFORMER DESIGN DATA

The Design Data worksheets of the transformer program TranModel for the transformers described in this thesis are presented here.

TranModel 1.0 - Design Data worksheet

Description	Name	Type	Value	Unit	Fig. ref	Symbol in latex
Section A - Material specifications						
Core type and material properties						
Type ("p" = partial-core, "f" = full-core shell type)	CTP	string	f	-	-	-
Shape ("c" = circular, "r" = rectangular) (*1)	CS	string	r	-	-	-
Lamination thickness	LT	double	0.5	mm	-	c_{l}
Stacking factor	CSF	double	0.95	-	-	s
Relative permeability	CUR	double	3000	-	-	\mu_{rc}
Resistivity at 20 °C	CR20	double	1.80E-07	ohm-m	-	\rho_{\unit{20}{\celsius}}
Thermal resistivity coefficient	CTRC	double	6.00E-03	ohm-m/°C	-	\delta \rho
Operating temperature	COT	double	50	°C	-	T_{c}
Material density	CMD	double	7870	kg/m^3	-	\gamma_{c}
Material cost	CMC	double	11	$/kg	-	C_{c}
Core dimensions						
Partial-core transformer (*2)						
	Section 1	Section 2	Section 3	Section 4	Section 5	Section 6	Section 7	Section 8	Section 9	Section 10		
Length, mm (CSLar)												
(CS = "c") Inner radius, mm (CSR1ar) (*3)												
(CS = "c") Outer radius, mm (CSR2ar) (*3)												
(CS = "r") Width-1 (breadth), mm (CSW1ar) (*3)												
(CS = "r") Width-2 (depth), mm (CSW2ar) (*3)												
Full-core shell-type transformer												
Length	CFL	double	68	mm	-	c_{l}						
Central limb width	CFCW	double	51	mm	-	w_{1}						
Outer limb width (typically CFCW / 2)	CFOW	double	25.5	mm	-	w_{o}						
Yoke height (typically CFCW / 2)	CFYH	double	25.5	mm	-	y_{h}						
Depth	CFD	double	44	mm	-	w_{2}						
Former												
Thickness	FT	double	2	mm	-	FT						
Winding sections, numbered from the inside (winding section = one or more layer of the same wire type and size, with a consistent inter-layer insulation thickness) (*4)												
	Section 1	Section 2	Section 3	Section 4	Section 5	Section 6	Section 7	Section 8	Section 9	Section 10	Section 11	Section 12	Section 13
Overall													
Estimate of length, mm (WSLEar)	66	66											
Layers (WSLSar)	5	20											
Wire													
Shape ("c" = circular, "r" = rectangular) (WSSar)	c	c											
(WSS = "c") Diameter, mm (WSWDar)	0.8	0.125											
(WSS = "r") Radial width, mm (WSWW1ar)	0	0											
(WSS = "r") Axial width, mm (WSWW2ar)	0	0											
Insulation thickness, mm (WSWITar)	0	0											
Stacking factor (axial direction) (WSSFar)	1	1											
Material ("c" = copper, "o" = other) (WSMar) (*5)	o	o											
(WSM = "o") Resistivity at 20 C, ohm-m (WSR20ar)	1.76E-08	1.76E-08											
(WSM = "o") Thermal resistivity coefficient, ohm-m/°C (WSTRCar)	3.90E-03	3.90E-03											
Volume specific heat at 20 °C, J/m^3-K (WSVSHar)	3.39E+06	3.39E+06											
Operating temperature, °C (WSOTar)	50	50											
Material density, kg/m^3 (WSMDar)	8960	8960											
Material cost, $/kg (WSMCar)	12	12											
Inter-layer insulation													
Thickness (build value), mm (WSILITar)	0.5	0.5											
Circumferal overlap, mm (WSILIOar)	0	0											
Winding-ends overlap, mm (WSILIWEOar)	0	0											
Material weight per CSA, kg/m^2 (WSILIMWar)	0	0											
Material cost per CSA, $/m^2 (WSILIMCar)	0												
Inter-section insulation (winding section n to n + 1)													
Thickness (build value), mm (WSISITar)	0.7	1											
Circumferal overlap, mm (WSISIOar)	0	0											
Winding ends overlap, mm (WSISIWEOar)	0	0											
Material weight per CSA, kg/m^2 (WSISIMWar)	0	0											
Material cost per CSA, $/m^2 (WSISIMCar)	0	0											
Encapsulant (*6)													
First encapsulated winding section	FEWS	integer	1	-	-	-							
Last encapsulated winding section	LEWS	integer	1	-	-	-							

(a) Page 1 of 2

Figure B.1 TranModel Design Data worksheet for transformer FC1.

Inter-layer insulation winding ends overlap	EWEO	double	0	mm	-
Overlap past winding end (held in place by longer outermost layer)	EWEEO	double	0	mm	-
Fill-factor for region `C' - the central part	EFFC	double	0	-	-
Material density	EMD	double	0	kg/m^3	-
Material cost	EMC	double	0	$/kg	-
Section B - FEA Options					
Winding model					
Winding model type ("c" = concentrated, "l" = layered) (*7)	WMT	string	c	-	-
File locations					
Filename to save MagNet model to	MFN	string	c:\fea.mn	-	-

Notes

*1 Rectangular core required for full-core shell-type transformer.
*2 Parameters for the circuit theory model are calculated using the first core section only.
*3 The core section with the largest outer radius must be placed in section 1 as this is used to calculate the coordinates of the windings. Only one core section allowed for a rectangular core.
*4 Inter-section insulation of the outer-most winding section is used to extend the winding window for a full-core shell-type transformer.
*5 A more accurate formula for calculating the resistivity variation with temperature is provided for copper.
*6 Circular core only. A single block of winding sections may be encapsulated. For circular wire, assume penetration throughout the winding wire. Assume penetration between inter-layer insulation at the winding ends overlap.
*7 Layer model not available yet. Would require n_winding_sections of dynamic matrices of size n_layers.

(b) Page 2 of 2

Figure B.1 (Continued) TranModel Design Data worksheet for transformer FC1.

TranModel 1.0 - Design Data worksheet

Description	Name	Type	Value	Unit	Fig. ref	Symbol in latex
Section A - Material specifications						
Core type and material properties						
Type ("p" = partial-core, "f" = full-core shell type)	CTP	string	f	-	-	-
Shape ("c" = circular, "r" = rectangular) (*1)	CS	string	r	-	-	-
Lamination thickness	LT	double	0.5	mm	-	c_{l}
Stacking factor	CSF	double	0.95	-	-	s
Relative permeability	CUR	double	3000	-	-	\mu_{rc}
Resistivity at 20 °C	CR20	double	1.80E-07	ohm-m	-	\rho_{\unit{20}{\celsius}}
Thermal resistivity coefficient	CTRC	double	6.00E-03	ohm-m/°C	-	\delta \rho
Operating temperature	COT	double	50	°C	-	T_{c}
Material density	CMD	double	7870	kg/m^3	-	\gamma_{c}
Material cost	CMC	double	11	$/kg	-	C_{c}
Core dimensions						
Partial-core transformer (*2)						
	Section 1	Section 2	Section 3	Section 4	Section 5	Section 6
Length, mm (CSLar)						
(CS = "c") Inner radius, mm (CSR1ar) (*3)						
(CS = "c") Outer radius, mm (CSR2ar) (*3)						
(CS = "r") Width-1 (breadth), mm (CSW1ar) (*3)						
(CS = "r") Width-2 (depth), mm (CSW2ar) (*3)						
Full-core shell-type transformer						
Length	CFL	double	114	mm	-	c_{l}
Central limb width	CFCW	double	44	mm	-	w_{1}
Outer limb width (typically CFCW / 2)	CFOW	double	22	mm	-	w_{o}
Yoke height (typically CFCW / 2)	CFYH	double	22	mm	-	y_{h}
Depth	CFD	double	152	mm	-	w_{2}
Former						
Thickness	FT	double	3.25	mm	-	FT
Winding sections, numbered from the inside (winding section = one or more layer of the same wire type and size, with a consistent inter-layer insulation thickness) (*4)						
	Section 1	Section 2	Section 3	Section 4	Section 5	Section 6
Overall						
Estimate of length, mm (WSLEar)	114	114				
Layers (WSLSar)	1	20				
Wire						
Shape ("c" = circular, "r" = rectangular) (WSSar)	c	c				
(WSS = "c") Diameter, mm (WSWDar)	3.55	0.212				
(WSS = "r") Radial width, mm (WSWW1ar)	0	0				
(WSS = "r") Axial width, mm (WSWW2ar)	0	0				
Insulation thickness, mm (WSWITar)	0	0				
Stacking factor (axial direction) (WSSFar)	1	1				
Material ("c" = copper, "o" = other) (WSMar) (*5)	o	o				
(WSM = "o") Resistivity at 20 C, ohm-m (WSR20ar)	1.76E-08	1.76E-08				
(WSM = "o") Thermal resistivity coefficient, ohm-m/°C (WSTRCar)	3.90E-03	3.90E-03				
Volume specific heat at 20 °C, J/m^3-K (WSVSHar)	3.39E+06	3.39E+06				
Operating temperature, °C (WSOTar)	50	50				
Material density, kg/m^3 (WSMDar)	8960	8960				
Material cost, $/kg (WSMCar)	12	12				
Inter-layer insulation						
Thickness (build value), mm (WSILITar)	0	0.09				
Circumferal overlap, mm (WSILIOar)	0	0				
Winding-ends overlap, mm (WSILIWEOar)	0	0				
Material weight per CSA, kg/m^2 (WSILIMWar)	0	0				
Material cost per CSA, $/m^2 (WSILIMCar)	0	0				
Inter-section insulation (winding section n to n + 1)						
Thickness (build value), mm (WSISITar)	6.5	1				
Circumferal overlap, mm (WSISIOar)	0	0				
Winding ends overlap, mm (WSISIWEOar)	0	0				
Material weight per CSA, kg/m^2 (WSISIMWar)	0	0				
Material cost per CSA, $/m^2 (WSISIMCar)	0	0				
Encapsulant (*6)						
First encapsulated winding section	FEWS	integer	1	-	-	-
Last encapsulated winding section	LEWS	integer	1	-	-	-

(a) Page 1 of 2

Figure B.2 TranModel Design Data worksheet for transformer FC2.

Inter-layer insulation winding ends overlap	EWEO	double	0	mm	-
Overlap past winding end (held in place by longer outermost layer)	EWEEO	double	0	mm	-
Fill-factor for region `C' - the central part	EFFC	double	0	-	-
Material density	EMD	double	0	kg/m^3	-
Material cost	EMC	double	0	$/kg	-
Section B - FEA Options					
Winding model					
Winding model type ("c" = concentrated, "l" = layered) (*7)	WMT	string	c	-	-
File locations					
Filename to save MagNet model to	MFN	string	c:\fea.mn	-	-

Notes

*1 Rectangular core required for full-core shell-type transformer.
*2 Parameters for the circuit theory model are calculated using the first core section only.
*3 The core section with the largest outer radius must be placed in section 1 as this is used to calculate the coordinates of the windings. Only one core section allowed for a rectangular core.
*4 Inter-section insulation of the outer-most winding section is used to extend the winding window for a full-core shell-type transformer.
*5 A more accurate formula for calculating the resistivity variation with temperature is provided for copper.
*6 Circular core only. A single block of winding sections may be encapsulated. For circular wire, assume penetration throughout the winding wire. Assume penetration between inter-layer insulation at the winding ends overlap.
*7 Layer model not available yet. Would require n_winding_sections of dynamic matrices of size n_layers.

(b) Page 2 of 2

Figure B.2 (Continued) TranModel Design Data worksheet for transformer FC2.

TranModel 1.0 - Design Data worksheet

Description	Name	Type	Value	Unit	Fig. ref	Symbol in latex
Section A - Material specifications						
Core type and material properties						
Type ("p" = partial-core, "f" = full-core shell type)	CTP	string	p	-	-	-
Shape ("c" = circular, "r" = rectangular) (*1)	CS	string	c	-	-	-
Lamination thickness	LT	double	0.5	mm	-	c_{l}
Stacking factor	CSF	double	0.96	-	-	s
Relative permeability	CUR	double	3000	-	-	\mu_{rc}
Resistivity at 20 °C	CR20	double	1.80E-07	ohm-m	-	\rho_{\unit{20}{\celsius}}
Thermal resistivity coefficient	CTRC	double	6.00E-03	ohm-m/°C	-	\delta \rho
Operating temperature	COT	double	50	°C	-	T_{c}
Material density	CMD	double	7870	kg/m^3	-	\gamma_{c}
Material cost	CMC	double	11	$/kg	-	C_{c}
Core dimensions						
Partial-core transformer (*2)						

	Section 1	Section 2	Section 3	Section 4	Section 5	Section 6	Section 7	Section 8	Section 9	Section 10	
Length, mm (CSLar)	715										
(CS = "c") Inner radius, mm (CSR1ar) (*3)	0										
(CS = "c") Outer radius, mm (CSR2ar) (*3)	62.5										
(CS = "r") Width-1 (breadth), mm (CSW1ar) (*3)											
(CS = "r") Width-2 (depth), mm (CSW2ar) (*3)											
Full-core shell-type transformer											
Length	CFL	double	0	mm	-	c_{l}					
Central limb width	CFCW	double	0	mm	-	w_{1}					
Outer limb width (typically CFCW / 2)	CFOW	double	0	mm	-	w_{o}					
Yoke height (typically CFCW / 2)	CFYH	double	0	mm	-	y_{h}					
Depth	CFD	double	0	mm	-	w_{2}					

Thickness	FT	double	8.5	mm	-	FT					
Winding sections, numbered from the inside (winding section = one or more layer of the same wire type and size, with a consistent inter-layer insulation thickness) (*4)											
	Section 1	Section 2	Section 3	Section 4	Section 5	Section 6	Section 7	Section 8	Section 9	Section 10	Section 11	Section 12	Section 13
Overall													
Estimate of length, mm (WSLEar)	735	735	735	735	680								
Layers (WSLSar)	1	2	1	9	1								
Wire													
Shape ("c" = circular, "r" = rectangular) (WSSar)	c	c	c	c	r								
(WSS = "c") Diameter, mm (WSWDar)	1	1	1	1	0								
(WSS = "r") Radial width, mm (WSWW1ar)	0	0	0	0	2.5								
(WSS = "r") Axial width, mm (WSWW2ar)	0	0	0	0	10								
Insulation thickness, mm (WSWITar)	0.04	0.04	0.04	0.04	0.2								
Stacking factor (axial direction) (WSSFar)	1	1	1	1	1								
Material ("c" = copper, "o" = other) (WSMar) (*5)	o	o	o	o	o								
(WSM = "o") Resistivity at 20 C, ohm-m (WSR20ar)	1.76E-08	1.76E-08	1.76E-08	1.76E-08	2.76E-08								
(WSM = "o") Thermal resistivity coefficient, ohm-m/°C (WSTRCar)	3.90E-03	3.90E-03	3.90E-03	3.90E-03	4.30E-03								
Volume specific heat at 20 °C, J/m^3-K (WSVSHar)	3.39E+06	3.39E+06	3.39E+06	3.39E+06	2.52E+06								
Operating temperature, °C (WSOTar)	50	50	50	50	50								
Material density, kg/m^3 (WSMDar)	8960	8960	8960	8960	2700								
Material cost, $/kg (WSMCar)	10	10	10	10	10								
Inter-layer insulation													
Thickness (build value), mm (WSILITar)	0.88	0.88	0.88	0.88	0								
Circumferal overlap, mm (WSILIOar)	25	25	25	25	0								
Winding-ends overlap, mm (WSILIWEOar)	100	100	100	100	0								
Material weight per CSA, kg/m^2 (WSILIMWar)	0.61	0.61	0.61	0.61	0								
Material cost per CSA, $/m^2 (WSILIMCar)	35	35	35	35	0								
Inter-section insulation (winding section n to n + 1)													
Thickness (build value), mm (WSISITar)	0.88	0.88	0.88	0.88	0								
Circumferal overlap, mm (WSISIOar)	25	25	25	25	0								
Winding ends overlap, mm (WSISIWEOar)	100	100	100	100	0								
Material weight per CSA, kg/m^2 (WSISIMWar)	0.61	0.61	0.61	0.61	0								
Material cost per CSA, $/m^2 (WSISIMCar)	35	35	35	35	0								

Encapsulant (*6)					
First encapsulated winding section	FEWS	integer	1	-	-
Last encapsulated winding section	LEWS	integer	4	-	-

(a) Page 1 of 2

Figure B.3 TranModel Design Data worksheet for transformer PC1.

Inter-layer insulation winding ends overlap	EWEO	double	0	mm	-
Overlap past winding end (held in place by longer outermost layer)	EWEEO	double	0	mm	-
Fill-factor for region `C' - the central part	EFFC	double	0	-	-
Material density	EMD	double	0	kg/m^3	-
Material cost	EMC	double	0	$/kg	-
Section B - FEA Options					
Winding model					
Winding model type ("c" = concentrated, "l" = layered) (*7)	WMT	string	c	-	-
File locations					
Filename to save MagNet model to	MFN	string	c:\fea.mn	-	-

Notes

*1 Rectangular core required for full-core shell-type transformer.
*2 Parameters for the circuit theory model are calculated using the first core section only.
*3 The core section with the largest outer radius must be placed in section 1 as this is used to calculate the coordinates of the windings. Only one core section allowed for a rectangular core.
*4 Inter-section insulation of the outer-most winding section is used to extend the winding window for a full-core shell-type transformer.
*5 A more accurate formula for calculating the resistivity variation with temperature is provided for copper.
*6 Circular core only. A single block of winding sections may be encapsulated. For circular wire, assume penetration throughout the winding wire. Assume penetration between inter-layer insulation at the winding ends overlap.
*7 Layer model not available yet. Would require n_winding_sections of dynamic matrices of size n_layers.

(b) Page 2 of 2

Figure B.3 (Continued) TranModel Design Data worksheet for transformer PC1.

TranModel 1.0 - Design Data worksheet

Description	Name	Type	Value	Unit	Fig. ref	Symbol in latex
Section A - Material specifications						
Core type and material properties						
Type ("p" = partial-core, "f" = full-core shell type)	CTP	string	p	-	-	-
Shape ("c" = circular, "r" = rectangular) (*1)	CS	string	c	-	-	-
Lamination thickness	LT	double	0.5	mm	-	c_{l}
Stacking factor	CSF	double	0.96	-	-	s
Relative permeability	CUR	double	3000	-	-	\mu_{rc}
Resistivity at 20 °C	CR20	double	1.80E-07	ohm-m	-	\rho_{\unit{20}{\celsius}}
Thermal resistivity coefficient	CTRC	double	6.00E-03	ohm-m/°C	-	\delta \rho
Operating temperature	COT	double	50	°C	-	T_{c}
Material density	CMD	double	7870	kg/m^3	-	\gamma_{c}
Material cost	CMC	double	11	$/kg	-	C_{c}
Core dimensions						
Partial-core transformer (*2)						
	Section 1	Section 2	Section 3	Section 4	Section 5	Section 6	Section 7	Section 8	Section 9	Section 10	
Length, mm (CSLar)	1200										
(CS = "c") Inner radius, mm (CSR1ar) (*3)	0										
(CS = "c") Outer radius, mm (CSR2ar) (*3)	87.5										
(CS = "r") Width-1 (breadth), mm (CSW1ar) (*3)											
(CS = "r") Width-2 (depth), mm (CSW2ar) (*3)											
Full-core shell-type transformer											
Length	CFL	double	0	mm	-	c_{l}					
Central limb width	CFCW	double	0	mm	-	w_{1}					
Outer limb width (typically CFCW / 2)	CFOW	double	0	mm	-	w_{o}					
Yoke height (typically CFCW / 2)	CFYH	double	0	mm	-	y_{h}					
Depth	CFD	double	0	mm	-	w_{2}					
Former											
Thickness	FT	double	12.5	mm	-	FT					
Winding sections, numbered from the inside (winding section = one or more layer of the same wire type and size, with a consistent inter-layer insulation thickness) (*4)											
	Section 1	Section 2	Section 3	Section 4	Section 5	Section 6	Section 7	Section 8	Section 9	Section 10	Section 11	Section 12	Section 13
Overall													
Estimate of length, mm (WSLEar)	920	875											
Layers (WSLSar)	9	1											
Wire													
Shape ("c" = circular, "r" = rectangular) (WSSar)	c	r											
(WSS = "c") Diameter, mm (WSWDar)	1.8	0											
(WSS = "r") Radial width, mm (WSWW1ar)	0	3.55											
(WSS = "r") Axial width, mm (WSWW2ar)	0	13.9											
Insulation thickness, mm (WSWITar)	0.016	0.1											
Stacking factor (axial direction) (WSSFar)	1	1											
Material ("c" = copper, "o" = other) (WSMar) (*5)	o	o											
(WSM = "o") Resistivity at 20 C, ohm-m (WSR20ar)	1.76E-08	2.76E-08											
(WSM = "o") Thermal resistivity coefficient, ohm-m/°C (WSTRCar)	3.90E-03	4.30E-03											
Volume specific heat at 20 °C, J/m^3-K (WSVSHar)	3.39E+06	3.39E+06											
Operating temperature, °C (WSOTar)	50	50											
Material density, kg/m^3 (WSMDar)	8960	2700											
Material cost, $/kg (WSMCar)	10	10											
Inter-layer insulation													
Thickness (build value), mm (WSILITar)	0.733	0											
Circumferal overlap, mm (WSILIOar)	25	0											
Winding-ends overlap, mm (WSILIWEOar)	100	0											
Material weight per CSA, kg/m^2 (WSILIMWar)	0.61	0											
Material cost per CSA, $/m^2 (WSILIMCar)	35	0											
Inter-section insulation (winding section n to n + 1)													
Thickness (build value), mm (WSISITar)	0.733	0											
Circumferal overlap, mm (WSISIOar)	25	0											
Winding ends overlap, mm (WSISIWEOar)	100	0											
Material weight per CSA, kg/m^2 (WSISIMWar)	0.61	0											
Material cost per CSA, $/m^2 (WSISIMCar)	35	0											
Encapsulant (*6)													
First encapsulated winding section	FEWS	integer	1	-	-	-							
Last encapsulated winding section	LEWS	integer	1	-	-	-							

(a) Page 1 of 2

Figure B.4 TranModel Design Data worksheet for transformer PC2.

Inter-layer insulation winding ends overlap	EWEO	double	0	mm	-
Overlap past winding end (held in place by longer outermost layer)	EWEEO	double	0	mm	-
Fill-factor for region `C' - the central part	EFFC	double	0	-	-
Material density	EMD	double	0	kg/m^3	-
Material cost	EMC	double	0	$/kg	-
Section B - FEA Options					
Winding model					
Winding model type ("c" = concentrated, "l" = layered) (*7)	WMT	string	c	-	-
File locations					
Filename to save MagNet model to	MFN	string	c:\fea.mn	-	-

Notes

*1 Rectangular core required for full-core shell-type transformer.
*2 Parameters for the circuit theory model are calculated using the first core section only.
*3 The core section with the largest outer radius must be placed in section 1 as this is used to calculate the coordinates of the windings. Only one core section allowed for a rectangular core.
*4 Inter-section insulation of the outer-most winding section is used to extend the winding window for a full-core shell-type transformer.
*5 A more accurate formula for calculating the resistivity variation with temperature is provided for copper.
*6 Circular core only. A single block of winding sections may be encapsulated. For circular wire, assume penetration throughout the winding wire. Assume penetration between inter-layer insulation at the winding ends overlap.
*7 Layer model not available yet. Would require n_winding_sections of dynamic matrices of size n_layers.

(b) Page 2 of 2

Figure B.4 (Continued) TranModel Design Data worksheet for transformer PC2.

TranModel 1.0 - Design Data worksheet

Description	Name	Type	Value	Unit	Fig. ref	Symbol in latex
Section A - Material specifications						
Core type and material properties						
Type ("p" = partial-core, "f" = full-core shell type)	CTP	string	p	-	-	-
Shape ("c" = circular, "r" = rectangular) (*1)	CS	string	c	-	-	-
Lamination thickness	LT	double	0.5	mm	-	c_{l}
Stacking factor	CSF	double	0.96	-	-	s
Relative permeability	CUR	double	3000	-	-	\mu_{rc}
Resistivity at 20 °C	CR20	double	1.80E-07	ohm-m	-	\rho_{\unit{20}{\celsius}}
Thermal resistivity coefficient	CTRC	double	6.00E-03	ohm-m/°C	-	\delta \rho
Operating temperature	COT	double	50	°C	-	T_{c}
Material density	CMD	double	7870	kg/m^3	-	\gamma_{c}
Material cost	CMC	double	11	$/kg	-	C_{c}
Core dimensions						
Partial-core transformer (*2)						

	Section 1	Section 2	Section 3	Section 4	Section 5	Section 6	Section 7	Section 8	Section 9	Section 10	
Length, mm (CSLar)	300	300									
(CS = "c") Inner radius, mm (CSR1ar) (*3)	0	0									
(CS = "c") Outer radius, mm (CSR2ar) (*3)	36	36									
(CS = "r") Width-1 (breadth), mm (CSW1ar) (*3)	0	0									
(CS = "r") Width-2 (depth), mm (CSW2ar) (*3)	0	0									
Full-core shell-type transformer											
Length	CFL	double	0	mm	-	c_{l}					
Central limb width	CFCW	double	0	mm	-	w_{1}					
Outer limb width (typically CFCW / 2)	CFOW	double	0	mm	-	w_{o}					
Yoke height (typically CFCW / 2)	CFYH	double	0	mm	-	y_{h}					
Depth	CFD	double	0	mm	-	w_{2}					

Former											
Thickness	FT	double	7.5	mm	-	FT					
Winding sections, numbered from the inside (winding section = one or more layer of the same wire type and size, with a consistent inter-layer insulation thickness) (*4)	Section 1	Section 2	Section 3	Section 4	Section 5	Section 6	Section 7	Section 8	Section 9	Section 10	Section 11	Section 12	Section 13
Overall													
Estimate of length, mm (WSLEar)	700	600	600										
Layers (WSLSar)	37	1	1										
Wire													
Shape ("c" = circular, "r" = rectangular) (WSSar)	c	r	r										
(WSS = "c") Diameter, mm (WSWDar)	0.375	0	0										
(WSS = "r") Radial width, mm (WSWW1ar)	0	3.55	3.55										
(WSS = "r") Axial width, mm (WSWW2ar)	0	7.1	7.1										
Insulation thickness, mm (WSWITar)	0.03125	0.2	0.2										
Stacking factor (axial direction) (WSSFar)	1	1	1										
Material ("c" = copper, "o" = other) (WSMar) (*5)	c	0	0										
(WSM = "o") Resistivity at 20 C, ohm-m (WSR20ar)	0.00E+00	2.76E-08	2.76E-08										
(WSM = "o") Thermal resistivity coefficient, ohm-m/°C (WSTRCar)	0.00E+00	4.30E-03	4.30E-03										
Volume specific heat at 20 °C, J/m^3-K (WSVSHar)	3.39E+06	2.52E+06	2.52E+06										
Operating temperature, °C (WSOTar)	50	50	50										
Material density, kg/m^3 (WSMDar)	8960	2700	2700										
Material cost, $/kg (WSMCar)	10	10	10										
Inter-layer insulation													
Thickness (build value), mm (WSILITar)	0.77	0	0										
Circumferal overlap, mm (WSILIOar)	50	0	0										
Winding-ends overlap, mm (WSILIWEOar)	100	0	0										
Material weight per CSA, kg/m^2 (WSILIMWar)	0.61	0	0										
Material cost per CSA, $/m^2 (WSILIMCar)	35	0	0										
Inter-section insulation (winding section n to n + 1)													
Thickness (build value), mm (WSISITar)	0.77	0	0										
Circumferal overlap, mm (WSISIOar)	50	0	0										
Winding ends overlap, mm (WSISIWEOar)	100	0	0										
Material weight per CSA, kg/m^2 (WSISIMWar)	0.61	0	0										
Material cost per CSA, $/m^2 (WSISIMCar)	35	0	0										

Encapsulant (*6)					
First encapsulated winding section	FEWS	integer	1	-	-
Last encapsulated winding section	LEWS	integer	1	-	-

(a) Page 1 of 2

Figure B.5 TranModel Design Data worksheet for transformer PC3.

Inter-layer insulation winding ends overlap	EWEO	double	0	mm	-
Overlap past winding end (held in place by longer outermost layer)	EWEEO	double	0	mm	-
Fill-factor for region `C' - the central part	EFFC	double	0	-	-
Material density	EMD	double	0	kg/m^3	-
Material cost	EMC	double	0	$/kg	-
Section B - FEA Options					
Winding model					
Winding model type ("c" = concentrated, "l" = layered) (*7)	WMT	string	c	-	-
File locations					
Filename to save MagNet model to	MFN	string	c:\fea.mn	-	-

Notes

*1 Rectangular core required for full-core shell-type transformer.
*2 Parameters for the circuit theory model are calculated using the first core section only.
*3 The core section with the largest outer radius must be placed in section 1 as this is used to calculate the coordinates of the windings. Only one core section allowed for a rectangular core.
*4 Inter-section insulation of the outer-most winding section is used to extend the winding window for a full-core shell-type transformer.
*5 A more accurate formula for calculating the resistivity variation with temperature is provided for copper.
*6 Circular core only. A single block of winding sections may be encapsulated. For circular wire, assume penetration throughout the winding wire. Assume penetration between inter-layer insulation at the winding ends overlap.
*7 Layer model not available yet. Would require n_winding_sections of dynamic matrices of size n_layers.

(b) Page 2 of 2

Figure B.5 (Continued) TranModel Design Data worksheet for transformer PC3.

TranModel 1.0 - Design Data worksheet

Description	Name	Type	Value	Unit	Fig. ref	Symbol in latex
Section A - Material specifications						
Core type and material properties						
Type ("p" = partial-core, "f" = full-core shell type)	CTP	string	p	-	-	
Shape ("c" = circular, "r" = rectangular) (*1)	CS	string	c	-	-	
Lamination thickness	LT	double		0.23	mm	-	c_{l}
Stacking factor	CSF	double		0.96	-	-	s
Relative permeability	CUR	double		3000	-	-	\mu_{rc}
Resistivity at 20 °C	CR20	double		1.80E-07	ohm-m	-	\rho_{\unit{20}{\celsius}}
Thermal resistivity coefficient	CTRC	double		6.00E-03	ohm-m/°C	-	\delta \rho
Operating temperature	COT	double		50	°C	-	T_{c}
Material density	CMD	double		7870	kg/m^3	-	\gamma_{c}
Material cost	CMC	double		11	$/kg	-	C_{c}
Core dimensions						
Partial-core transformer (*2)						

	Section 1	Section 2	Section 3	Section 4	Section 5	Section 6	Section 7	Section 8	Section 9	Section 10
Length, mm (CSLar)	74	74	74	74						
(CS = "c") Inner radius, mm (CSR1ar) (*3)	12.5	12.5	12.5	12.5						
(CS = "c") Outer radius, mm (CSR2ar) (*3)	120	120	120	120						
(CS = "r") Width-1 (breadth), mm (CSW1ar) (*3)	0	0	0	0						
(CS = "r") Width-2 (depth), mm (CSW2ar) (*3)	0	0	0	0						
Full-core shell-type transformer										
Length	CFL	double	0	mm	-	c_{l}				
Central limb width	CFCW	double	0	mm	-	w_{1}				
Outer limb width (typically CFCW / 2)	CFOW	double	0	mm	-	w_{o}				
Yoke height (typically CFCW / 2)	CFYH	double	0	mm	-	y_{h}				
Depth	CFD	double	0	mm	-	w_{2}				

Former

Thickness	FT	double	8.5	mm	-	FT							
Winding sections, numbered from the inside (winding section = one or more layer of the same wire type and size, with a consistent inter-layer insulation thickness) (*4)	Section 1	Section 2	Section 3	Section 4	Section 5	Section 6	Section 7	Section 8	Section 9	Section 10	Section 11	Section 12	Section 13
Overall													
Estimate of length, mm (WSLEar)	380	380	380	380	380	380	380	380	239.3	41.7	62.5		
Layers (WSLSar)	16	1	1	1	1	1	1	1	1	1	1		
Wire													
Shape ("c" = circular, "r" = rectangular) (WSSar)	c	c	c	c	c	c	c	c	r	r	r		
(WSS = "c") Diameter, mm (WSWDar)	1.25	1.25	1.25	1.12	1.12	1.12	1.12	1.12	0	0	0	0	
(WSS = "r") Radial width, mm (WSWW1ar)	0	0	0	0	0	0	0	0	2.5	2.5	2.5		
(WSS = "r") Axial width, mm (WSWW2ar)	0	0	0	0	0	0	0	0	5	5	5		
Insulation thickness, mm (WSWITar)	0.04	0.04	0.04	0.04	0.04	0.04	0.04	0.04	0.1	0.1	0.1		
Stacking factor (axial direction) (WSSFar)	1	1	1	1	1	1	1	1	1	1	1		
Material ("c" = copper, "o" = other) (WSMar) (*5)	c	c	c	c	c	c	c	c	o	o	o		
(WSM = "o") Resistivity at 20 C, ohm-m (WSR20ar)	-	-	-	-	-	-	-	-	2.76E-08	2.76E-08	2.76E-08		
(WSM = "o") Thermal resistivity coefficient, ohm-m/°C (WSTRCar)	-	-	-	-	-	-	-	-	4.30E-03	4.30E-03	4.30E-03		
Volume specific heat at 20 °C, J/m^3-K (WSVSHar)	3.39E+06	3.39E+06	3.39E+06	3.39E+06	3.39E+06	3.39E+06	3.39E+06	3.39E+06	2.52E+06	2.52E+06	2.52E+06		
Operating temperature, °C (WSOTar)	70	70	70	70	70	70	70	70	50	50	50		
Material density, kg/m^3 (WSMDar)	8960	8960	8960	8960	8960	8960	8960	8960	2700	2700	2700		
Material cost, $/kg (WSMCar)	10	10	10	10	10	10	10	10	10	10	10		
Inter-layer insulation													
Thickness (build value), mm (WSILITar)	0.6	0.6	0.6	0.6	0.6	0.6	0.6	0.6	0	0	0	0	
Circumferal overlap, mm (WSILIOar)	25	25	25	25	25	25	25	25	0	0	0	0	
Winding-ends overlap, mm (WSILIWEOar)	25	25	25	25	25	25	25	25	0	0	0	0	
Material weight per CSA, kg/m^2 (WSILIMWar)	0.61	0.61	0.61	0.61	0.61	0.61	0.61	0.61	0	0	0	0	
Material cost per CSA, $/m^2 (WSILIMCar)	35	35	35	35	35	35	35	35	0	0	0	0	
Inter-section insulation (winding section n to n + 1)													
Thickness (build value), mm (WSISITar)	0.6	0.6	0.6	0.6	0.6	0.6	0.6	0.6	0	0	0	0	
Circumferal overlap, mm (WSISIOar)	25	25	25	25	25	25	25	25	0	0	0	0	
Winding ends overlap, mm (WSISIWEOar)	25	25	25	25	25	25	25	50	0	0	0	0	
Material weight per CSA, kg/m^2 (WSISIMWar)	0.61	0.61	0.61	0.61	0.61	0.61	0.61	0.61	0	0	0	0	
Material cost per CSA, $/m^2 (WSISIMCar)	35	35	35	35	35	35	35	35	0	0	0	0	

Encapsulant (*6)

First encapsulated winding section	FEWS	integer	1	-	-	-
Last encapsulated winding section	LEWS	integer	8	-	-	-

(a) Page 1 of 2

Figure B.6 TranModel Design Data worksheet for transformer PC4.

Inter-layer insulation winding ends overlap	EWEO	double	25	mm	-
Overlap past winding end (held in place by longer outermost layer)	EWEEO	double	25	mm	-
Fill-factor for region 'C' - the central part	EFFC	double	0.3	-	-
Material density	EMD	double	1370	kg/m^3	-
Material cost	EMC	double	65.5	$/kg	-
Section B - FEA Options					
Winding model					
Winding model type ("c" = concentrated, "l" = layered) (*7)	WMT	string	c	-	-
File locations					
Filename to save MagNet model to	MFN	string	c:\fea.mn	-	-

Notes

*1 Rectangular core required for full-core shell-type transformer.
*2 Parameters for the circuit theory model are calculated using the first core section only.
*3 The core section with the largest outer radius must be placed in section 1 as this is used to calculate the coordinates of the windings. Only one core section allowed for a rectangular core.
*4 Inter-section insulation of the outer-most winding section is used to extend the winding window for a full-core shell-type transformer.
*5 A more accurate formula for calculating the resistivity variation with temperature is provided for copper.
*6 Circular core only. A single block of winding sections may be encapsulated. For circular wire, assume penetration throughout the winding wire. Assume penetration between inter-layer insulation at the winding ends overlap.
*7 Layer model not available yet. Would require n_winding_sections of dynamic matrices of size n_layers.

(b) Page 2 of 2

Figure B.6 (Continued) TranModel Design Data worksheet for transformer PC4.

TranModel 1.0 - Design Data worksheet

Description	Name	Type	Value	Unit	Fig. ref	Symbol in latex
Section A - Material specifications						
Core type and material properties						
Type ("p" = partial-core, "f" = full-core shell type)	CTP	string	p	-	-	
Shape ("c" = circular, "r" = rectangular) (*1)	CS	string	c	-	-	
Lamination thickness	LT	double		0.23 mm	-	c_{l}
Stacking factor	CSF	double		0.96 -	-	s
Relative permeability	CUR	double		3000 -	-	\mu_{rc}
Resistivity at 20 °C	CR20	double		1.80E-07 ohm-m	-	\rho_{\unit{20}{\celsius}}
Thermal resistivity coefficient	CTRC	double		6.00E-03 ohm-m/°C	-	\delta \rho
Operating temperature	COT	double		50 °C	-	T_{c}
Material density	CMD	double		7870 kg/m^3	-	\gamma_{c}
Material cost	CMC	double		11 $/kg	-	C_{c}
Core dimensions						
Partial-core transformer (*2)						

	Section 1	Section 2	Section 3	Section 4	Section 5	Section 6	Section 7	Section 8	Section 9	Section 10	
Length, mm (CSLar)	74	74	74	74							
(CS = "c") Inner radius, mm (CSR1ar) (*3)	12.5	12.5	12.5	12.5							
(CS = "c") Outer radius, mm (CSR2ar) (*3)	120	120	120	120							
(CS = "r") Width-1 (breadth), mm (CSW1ar) (*3)	0	0	0	0							
(CS = "r") Width-2 (depth), mm (CSW2ar) (*3)	0	0	0	0							
Full-core shell-type transformer											
Length	CFL	double	0	mm	-	c_{l}					
Central limb width	CFCW	double	0	mm	-	w_{1}					
Outer limb width (typically CFCW / 2)	CFOW	double	0	mm	-	w_{o}					
Yoke height (typically CFCW / 2)	CFYH	double	0	mm	-	y_{h}					
Depth	CFD	double	0	mm	-	w_{2}					

Former												
Thickness	FT	double	8.5	mm	-	FT						
Winding sections, numbered from the inside (winding section = one or more layer of the same wire type and size, with a consistent inter-layer insulation thickness) (*4)												
	Section 1	Section 2	Section 3	Section 4	Section 5	Section 6	Section 7	Section 8	Section 9	Section 10	Section 11	Section 12	Section 13
Overall													
Estimate of length, mm (WSLEar)	408	408	408	408	408	408	408	408	390.1	36.5	57.3		
Layers (WSLSar)	16	1	1	1	1	1	1	1	1	1	1		
Wire													
Shape ("c" = circular, "r" = rectangular) (WSSar)	c	c	c	c	c	c	c	c	r	r	r		
(WSS = "c") Diameter, mm (WSWDar)	0.9	0.9	0.85	0.85	0.85	0.85	0.67	0.67	0	0	0	0	
(WSS = "r") Radial width, mm (WSWW1ar)	0	0	0	0	0	0	0	0	2.5	2.5	2.5		
(WSS = "r") Axial width, mm (WSWW2ar)	0	0	0	0	0	0	0	0	5	5	5		
Insulation thickness, mm (WSWITar)	0.04	0.04	0.04	0.04	0.04	0.04	0.04	0.04	0.1	0.1	0.1		
Stacking factor (axial direction) (WSSFar)	1	1	1	1	1	1	1	1	1	1	1		
Material ("c" = copper, "o" = other) (WSMar) (*5)	c	c	c	c	c	c	c	c	o	o	o		
(WSM = "o") Resistivity at 20 C, ohm-m (WSR20ar)	0.00E+00	0.00E+00	0.00E+00	0.00E+00	0.00E+00	0.00E+00	0.00E+00	0.00E+00	2.76E-08	2.76E-08	2.76E-08	2.76E-08	
(WSM = "o") Thermal resistivity coefficient, ohm-m/°C (WSTRCar)	0.00E+00	0.00E+00	0.00E+00	0.00E+00	0.00E+00	0.00E+00	0.00E+00	0.00E+00	4.30E-03	4.30E-03	4.30E-03	4.30E-03	
Volume specific heat at 20 °C, J/m^3-K (WSVSHar)	3.39E+06	3.39E+06	3.39E+06	3.39E+06	3.39E+06	3.39E+06	3.39E+06	3.39E+06	2.52E+06	2.52E+06	2.52E+06	2.52E+06	
Operating temperature, °C (WSOTar)	70	70	70	70	70	70	70	70	50	50	50	50	
Material density, kg/m^3 (WSMDar)	8960	8960	8960	8960	8960	8960	8960	8960	2700	2700	2700	2700	
Material cost, $/kg (WSMCar)	10	10	10	10	10	10	10	10	10	10	10	10	
Inter-layer insulation													
Thickness (build value), mm (WSILITar)	0.6	0.6	0.6	0.6	0.6	0.6	0.6	0.6	0	0	0	0	
Circumferal overlap, mm (WSILIOar)	50	50	50	50	50	50	50	50	0	0	0	0	
Winding-ends overlap, mm (WSILIWEOar)	25	25	25	25	25	25	25	25	0	0	0	0	
Material weight per CSA, kg/m^2 (WSILIMWar)	0.61	0.61	0.61	0.61	0.61	0.61	0.61	0.61	0	0	0	0	
Material cost per CSA, $/m^2 (WSILIMCar)	35	35	35	35	35	35	35	35	0	0	0	0	
Inter-section insulation (winding section n to n + 1)													
Thickness (build value), mm (WSISITar)	0.6	0.6	0.6	0.6	0.6	0.6	0.6	0.6	0	0	0	0	
Circumferal overlap, mm (WSISIOar)	50	50	50	50	50	50	50	50	0	0	0	0	
Winding ends overlap, mm (WSISIWEOar)	25	25	25	25	25	25	25	25	0	0	0	0	
Material weight per CSA, kg/m^2 (WSISIMWar)	0.61	0.61	0.61	0.61	0.61	0.61	0.61	0.61	0	0	0	0	
Material cost per CSA, $/m^2 (WSISIMCar)	35	35	35	35	35	35	35	35	0	0	0	0	

Encapsulant (*6)				
First encapsulated winding section	FEWS	integer	1	-
Last encapsulated winding section	LEWS	integer	8	-

(a) Page 1 of 2

Figure B.7 TranModel Design Data worksheet for transformer PC5.

Inter-layer insulation winding ends overlap	EWEO	double	25	mm	-
Overlap past winding end (held in place by longer outermost layer)	EWEEO	double	25	mm	-
Fill-factor for region `C' - the central part	EFFC	double	0.3	-	-
Material density	EMD	double	1370	kg/m^3	-
Material cost	EMC	double	65.5	$/kg	-
Section B - FEA Options					
Winding model					
Winding model type ("c" = concentrated, "l" = layered) (*7)	WMT	string	c	-	-
File locations					
Filename to save MagNet model to	MFN	string	c:\fea.mn	-	-

Notes

*1 Rectangular core required for full-core shell-type transformer.
*2 Parameters for the circuit theory model are calculated using the first core section only.
*3 The core section with the largest outer radius must be placed in section 1 as this is used to calculate the coordinates of the windings. Only one core section allowed for a rectangular core.
*4 Inter-section insulation of the outer-most winding section is used to extend the winding window for a full-core shell-type transformer.
*5 A more accurate formula for calculating the resistivity variation with temperature is provided for copper.
*6 Circular core only. A single block of winding sections may be encapsulated. For circular wire, assume penetration throughout the winding wire. Assume penetration between inter-layer insulation at the winding ends overlap.
*7 Layer model not available yet. Would require n_winding_sections of dynamic matrices of size n_layers.

(b) Page 2 of 2

Figure B.7 (Continued) TranModel Design Data worksheet for transformer PC5.

TranModel 1.0 - Design Data worksheet

Description	Name	Type	Value	Unit	Fig. ref	Symbol in latex
Section A - Material specifications						
Core type and material properties						
Type ("p" = partial-core, "f" = full-core shell type)	CTP	string	p	-	-	
Shape ("c" = circular, "r" = rectangular) (*1)	CS	string	c	-	-	
Lamination thickness	LT	double		0.23	mm	-	c_{l}
Stacking factor	CSF	double		0.96	-	-	s
Relative permeability	CUR	double		3000	-	-	\mu_{rc}
Resistivity at 20 °C	CR20	double		1.80E-07	ohm-m	-	\rho_{\unit{20}{\celsius}}
Thermal resistivity coefficient	CTRC	double		6.00E-03	ohm-m/°C	-	\delta \rho
Operating temperature	COT	double		50	°C	-	T_{c}
Material density	CMD	double		7870	kg/m^3	-	\gamma_{c}
Material cost	CMC	double		11	$/kg	-	C_{c}
Core dimensions						
Partial-core transformer (*2)						

	Section 1	Section 2	Section 3	Section 4	Section 5	Section 6	Section 7	Section 8	Section 9	Section 10	
Length, mm (CSLar)	74	74	74	74							
(CS = "c") Inner radius, mm (CSR1ar) (*3)	12.5	12.5	12.5	12.5							
(CS = "c") Outer radius, mm (CSR2ar) (*3)	120	120	120	120							
(CS = "r") Width-1 (breadth), mm (CSW1ar) (*3)	0	0	0	0							
(CS = "r") Width-2 (depth), mm (CSW2ar) (*3)	0	0	0	0							
Full-core shell-type transformer											
Length	CFL	double	0	mm	-	c_{l}					
Central limb width	CFCW	double	0	mm	-	w_{1}					
Outer limb width (typically CFCW / 2)	CFOW	double	0	mm	-	w_{o}					
Yoke height (typically CFCW / 2)	CFYH	double	0	mm	-	y_{h}					
Depth	CFD	double	0	mm	-	w_{2}					

Former													
Thickness	FT	double	8.5	mm	-	FT							
Winding sections, numbered from the inside (winding section = one or more layer of the same wire type and size, with a consistent inter-layer insulation thickness) (*4)	Section 1	Section 2	Section 3	Section 4	Section 5	Section 6	Section 7	Section 8	Section 9	Section 10	Section 11	Section 12	Section 13
Overall													
Estimate of length, mm (WSLEar)	350	350	350	350	350	350	350	350	348.5	343.3	171.7	166.5	
Layers (WSLSar)	29	1	1	1	1	1	1	1	1	1	1	1	
Wire													
Shape ("c" = circular, "r" = rectangular) (WSSar)	c	c	c	c	c	c	c	c	r	r	r	r	
(WSS = "c") Diameter, mm (WSWDar)	0.6	0.475	0.475	0.475	0.355	0.355	0.355	0.355	0	0	0	0	0
(WSS = "r") Radial width, mm (WSWW1ar)	0	0	0	0	0	0	0	0	2.5	2.5	2.5	2.5	2.5
(WSS = "r") Axial width, mm (WSWW2ar)	0	0	0	0	0	0	0	0	5	5	5	5	5
Insulation thickness, mm (WSWITar)	0.04	0.04	0.04	0.04	0.04	0.04	0.04	0.04	0.1	0.1	0.1	0.1	0.1
Stacking factor (axial direction) (WSSFar)	1	1	1	1	1	1	1	1	1	1	1	1	1
Material ("c" = copper, "o" = other) (WSMar) (*5)	c	c	c	c	c	c	c	c	o	o	o	o	
(WSM = "o") Resistivity at 20 C, ohm-m (WSR20ar)	0.00E+00	0.00E+00	0.00E+00	0.00E+00	0.00E+00	0.00E+00	0.00E+00	0.00E+00	2.76E-08	2.76E-08	2.76E-08	2.76E-08	2.76E-08
(WSM = "o") Thermal resistivity coefficient, ohm-m/°C (WSTRCar)	0.00E+00	0.00E+00	0.00E+00	0.00E+00	0.00E+00	0.00E+00	0.00E+00	0.00E+00	4.30E-03	4.30E-03	4.30E-03	4.30E-03	4.30E-03
Volume specific heat at 20 °C, J/m^3-K (WSVSHar)	3.39E+06	3.39E+06	3.39E+06	3.39E+06	3.39E+06	3.39E+06	3.39E+06	3.39E+06	2.52E+06	2.52E+06	2.52E+06	2.52E+06	2.52E+06
Operating temperature, °C (WSOTar)	70	70	70	70	70	70	70	70	50	50	50	50	50
Material density, kg/m^3 (WSMDar)	8960	8960	8960	8960	8960	8960	8960	8960	2700	2700	2700	2700	2700
Material cost, $/kg (WSMCar)	10	10	10	10	10	10	10	10	10	10	10	10	10
Inter-layer insulation													
Thickness (build value), mm (WSILITar)	0.6	0.6	0.6	0.6	0.6	0.6	0.6	0.6	0	0	0	0	0
Circumferal overlap, mm (WSILIOar)	50	50	50	50	50	50	50	50	0	0	0	0	0
Winding-ends overlap, mm (WSILIWEOar)	25	25	25	25	25	25	25	25	0	0	0	0	0
Material weight per CSA, kg/m^2 (WSILIMWar)	0.61	0.61	0.61	0.61	0.61	0.61	0.61	0.61	0	0	0	0	0
Material cost per CSA, $/m^2 (WSILIMCar)	35	35	35	35	35	35	35	35	0	0	0	0	0
Inter-section insulation (winding section n to n + 1)													
Thickness (build value), mm (WSISITar)	0.6	0.6	0.6	0.6	0.6	0.6	0.6	0.6	0	0	0	0	0
Circumferal overlap, mm (WSISIOar)	50	50	50	50	50	50	50	50	0	0	0	0	0
Winding ends overlap, mm (WSISIWEOar)	25	25	25	25	25	25	25	25	0	0	0	0	0
Material weight per CSA, kg/m^2 (WSISIMWar)	0.61	0.61	0.61	0.61	0.61	0.61	0.61	0.61	0	0	0	0	0
Material cost per CSA, $/m^2 (WSISIMCar)	35	35	35	35	35	35	35	35	0	0	0	0	0

Encapsulant (*6)					
First encapsulated winding section	FEWS	integer	1	-	-
Last encapsulated winding section	LEWS	integer	8	-	-

(a) Page 1 of 2

Figure B.8 TranModel Design Data worksheet for transformer PC6.

Inter-layer insulation winding ends overlap	EWEO	double	25	mm	-
Overlap past winding end (held in place by longer outermost layer)	EWEEO	double	25	mm	-
Fill-factor for region `C' - the central part	EFFC	double	0.3	-	-
Material density	EMD	double	1370	kg/m^3	-
Material cost	EMC	double	65.5	$/kg	-
Section B - FEA Options					
Winding model					
Winding model type ("c" = concentrated, "l" = layered) (*7)	WMT	string	c	-	-
File locations					
Filename to save MagNet model to	MFN	string	c:\fea.mn	-	-

Notes

*1 Rectangular core required for full-core shell-type transformer.
*2 Parameters for the circuit theory model are calculated using the first core section only.
*3 The core section with the largest outer radius must be placed in section 1 as this is used to calculate the coordinates of the windings. Only one core section allowed for a rectangular core.
*4 Inter-section insulation of the outer-most winding section is used to extend the winding window for a full-core shell-type transformer.
*5 A more accurate formula for calculating the resistivity variation with temperature is provided for copper.
*6 Circular core only. A single block of winding sections may be encapsulated. For circular wire, assume penetration throughout the winding wire. Assume penetration between inter-layer insulation at the winding ends overlap.
*7 Layer model not available yet. Would require n_winding_sections of dynamic matrices of size n_layers.

(b) Page 2 of 2

Figure B.8 (Continued) TranModel Design Data worksheet for transformer PC6.

TranModel 1.0 - Design Data worksheet

Description	Name	Type	Value	Unit	Fig. ref	Symbol in latex
Section A - Material specifications						
Core type and material properties						
Type ("p" = partial-core, "f" = full-core shell type)	CTP	string	p	-	-	-
Shape ("c" = circular, "r" = rectangular) (*1)	CS	string	c	-	-	-
Lamination thickness	LT	double	0.5	mm	-	c_{l}
Stacking factor	CSF	double	0.96	-	-	s
Relative permeability	CUR	double	3000	-	-	\mu_{rc}
Resistivity at 20 °C	CR20	double	1.80E-07	ohm-m	-	\rho_{\unit{20}{\celsius}}
Thermal resistivity coefficient	CTRC	double	6.00E-03	ohm-m/°C	-	\delta \rho
Operating temperature	COT	double	50	°C	-	T_{c}
Material density	CMD	double	7870	kg/m^3	-	\gamma_{c}
Material cost	CMC	double	11	$/kg	-	C_{c}
Core dimensions						
Partial-core transformer (*2)						

	Section 1	Section 2	Section 3	Section 4	Section 5	Section 6	Section 7	Section 8	Section 9	Section 10
Length, mm (CSLar)	484									
(CS = "c") Inner radius, mm (CSR1ar) (*3)	8.2									
(CS = "c") Outer radius, mm (CSR2ar) (*3)	40									
(CS = "r") Width-1 (breadth), mm (CSW1ar) (*3)	0									
(CS = "r") Width-2 (depth), mm (CSW2ar) (*3)	0									
Full-core shell-type transformer										
Length	CFL	double	0	mm	-	c_{l}				
Central limb width	CFCW	double	0	mm	-	w_{1}				
Outer limb width (typically CFCW / 2)	CFOW	double	0	mm	-	w_{o}				
Yoke height (typically CFCW / 2)	CFYH	double	0	mm	-	y_{h}				
Depth	CFD	double	0	mm	-	w_{2}				

Former												
Thickness	FT	double	16.7	mm	-	FT						
Winding sections, numbered from the inside (winding section = one or more layer of the same wire type and size, with a consistent inter-layer insulation thickness) (*4)	Section 1	Section 2	Section 3	Section 4	Section 5	Section 6	Section 7	Section 8	Section 9	Section 10	Section 11	Section 12	Section 13
Overall													
Estimate of length, mm (WSLEar)	384	384	384	384	384	384	384	384					
Layers (WSLSar)	1	1	1	1	1	1	1	1					
Wire													
Shape ("c" = circular, "r" = rectangular) (WSSar)	r	r	r	r	r	r	r	r					
(WSS = "c") Diameter, mm (WSWDar)	0	0	0	0	0	0	0	0					
(WSS = "r") Radial width, mm (WSWW1ar)	0.7	0.7	0.7	0.7	0.7	0.7	0.7	0.7					
(WSS = "r") Axial width, mm (WSWW2ar)	4.65	4.65	4.65	4.65	4.65	4.65	4.65	4.65					
Insulation thickness, mm (WSWITar)	0.04	0.04	0.04	0.04	0.04	0.04	0.04	0.04					
Stacking factor (axial direction) (WSSFar)	0.99	0.99	0.99	0.99	0.99	0.99	0.99	0.99					
Material ("c" = copper, "o" = other) (WSMar) (*5)	o	o	o	o	o	o	o	o					
(WSM = "o") Resistivity at 20 C, ohm-m (WSR20ar)	0.00E+00	0.00E+00	0.00E+00	0.00E+00	0.00E+00	0.00E+00	0.00E+00	0.00E+00					
(WSM = "o") Thermal resistivity coefficient, ohm-m/°C (WSTRCar)	0.00E+00	0.00E+00	0.00E+00	0.00E+00	0.00E+01	0.00E+00	0.00E+00	0.00E+00					
Volume specific heat at 20 °C, J/m^3-K (WSVSHar)	0.00E+00	0.00E+00	0.00E+00	0.00E+00	0.00E+00	0.00E+00	0.00E+00	0.00E+00					
Operating temperature, °C (WSOTar)	20	20	20	20	20	20	20	20					
Material density, kg/m^3 (WSMDar)	8960	8960	8960	8960	8960	8960	8960	8960					
Material cost, $/kg (WSMCar)	10	10	10	10	10	10	10	10					
Inter-layer insulation													
Thickness (build value), mm (WSILITar)	0	0	0	0	0	0	0	0					
Circumferal overlap, mm (WSILIOar)	0	0	0	0	0	0	0	0					
Winding-ends overlap, mm (WSILIWEOar)	0	0	0	0	0	0	0	0					
Material weight per CSA, kg/m^2 (WSILIMWar)	0	0	0	0	0	0	0	0					
Material cost per CSA, $/m^2 (WSILIMCar)	0	0	0	0	0	0	0	0					
Inter-section insulation (winding section n to n + 1)													
Thickness (build value), mm (WSISITar)	1.8	0.2	1.45	3.45	2.75	3.2	1.45	0					
Circumferal overlap, mm (WSISIOar)	25	25	25	25	25	25	25	25					
Winding ends overlap, mm (WSISIWEOar)	25	25	25	25	25	25	25	25					
Material weight per CSA, kg/m^2 (WSISIMWar)	0.61	0.61	0.61	0.61	0.61	0.61	0.61	0.61					
Material cost per CSA, $/m^2 (WSISIMCar)	35	35	35	35	35	35	35	35					

Encapsulant (*6)					
First encapsulated winding section	FEWS	integer	1	-	-
Last encapsulated winding section	LEWS	integer	1	-	-

(a) Page 1 of 2

Figure B.9 TranModel Design Data worksheet for transformer HTSPC1.

Inter-layer insulation winding ends overlap	EWEO	double	0	mm	-
Overlap past winding end (held in place by longer outermost layer)	EWEEO	double	0	mm	-
Fill-factor for region `C' - the central part	EFFC	double	0	-	-
Material density	EMD	double	0	kg/m^3	-
Material cost	EMC	double	0	$/kg	-
Section B - FEA Options					
Winding model					
Winding model type ("c" = concentrated, "l" = layered) (*7)	WMT	string	c	-	-
File locations					
Filename to save MagNet model to	MFN	string	c:\fea.mn	-	-

Notes

*1 Rectangular core required for full-core shell-type transformer.
*2 Parameters for the circuit theory model are calculated using the first core section only.
*3 The core section with the largest outer radius must be placed in section 1 as this is used to calculate the coordinates of the windings. Only one core section allowed for a rectangular core.
*4 Inter-section insulation of the outer-most winding section is used to extend the winding window for a full-core shell-type transformer.
*5 A more accurate formula for calculating the resistivity variation with temperature is provided for copper.
*6 Circular core only. A single block of winding sections may be encapsulated. For circular wire, assume penetration throughout the winding wire. Assume penetration between inter-layer insulation at the winding ends overlap.
*7 Layer model not available yet. Would require n_winding_sections of dynamic matrices of size n_layers.

(b) Page 2 of 2

Figure B.9 (Continued) TranModel Design Data worksheet for transformer HTSPC1.